# A STUDY OF THE ADSORBATE COMPOSITION AND MECHANISM OF BUTANE STEAM REFORMING ON NICKEL CATALYSTS

A thesis submitted to the University of Manchester Institute of Science and Technology for the degree of Doctor of Philosophy

by

**Andrzej Kalczewski**

Department of Chemistry

September 1998

# Declaration

All of the work described in this thesis is the original work of the author, except where acknowledged by reference or special recognition. No portion of the work referred to in this thesis has been submitted in support of an application for another degree or qualification of this or any other university, or other institution of learning.

signed.....

## Abstract

During the last four decades, steam reforming has grown into one of the world's most important catalytic processes. It converts hydrocarbons into mixtures of $H_2$, CO and $CO_2$ - so called synthesis gas. The catalyst is an alumina supported nickel and the process typically operates between 723 and 1023 K and at 30 atm pressure. The major difficulty confronting steam reforming is the formation of filamentous carbon. It can lead to severe operational difficulties since it completely disintegrates the catalyst particle. Its formation must therefore be suppressed and this is usually achieved by adding alkali or rare earth promoters to the catalyst.

Nine $NiO/\alpha\text{-}Al_2O_3$ catalysts were prepared containing 15wt% NiO. Three were promoted with added $Al_2O_3$ (1, 5 and 10wt% of the NiO loading), three with added MgO (1, 5 and 10wt% of the NiO loading) and three with added $La_2O_3$ (1, 5 and 10wt% of the NiO loading). Characterisation by X-ray diffraction (XRD) and Temperature-Programmed Reduction (TPR) revealed that the promoters had a profound effect on the nature of the NiO precursor. The total surface area of the catalysts was determined by $N_2$ adsorption at 77 K, giving values ranging from 2.4 to 2.9 $m^2\ g^{-1}$.

Temperature-Programmed Reaction (TPRn) of 2% n-butane up to 1023 K on each catalyst provided information relating to the kinetics and mechanism of butane decomposition. The kinetics of butane decomposition were remarkably similar for each catalyst. This indicated that although the promoters had a marked effect on the nature of the NiO precursors, they had little effect on the dehydrogenational activity of Ni once formed after reduction. In each case the promoter had a negligible effect on suppressing the formation of carbon. Calculation of the activation energy for the production of hydrogen gave values in good agreement with those in the literature for the diffusion of carbon through nickel (125 - 155 kJ $mol^{-1}$) which is considered to be the rate determining step for the formation of carbon filaments. Transmission Electron Microscopy (TEM) confirmed that carbon filaments were formed during the butane TPRn.

Temperature-Programmed Oxidation (TPO) of the carbon deposited by the butane decomposition was found to result in a redispersion of the Ni on the support which resulted in a completely different Ni surface morphology. As a result the kinetics of butane decomposition were dramatically altered when the butane TPRn was repeated on the regenerated catalysts. The amount of carbon formed on regenerated catalysts was also considerably less. The redistribution of Ni crystallographic faces on the surface was believed to be such so as to inhibit the adsorption and subsequent decomposition of butane. A redispersion of the promoters following oxidation was also found to play a major role in suppressing the formation of carbon by blocking specific Ni ensembles required for the formation of ethylidyne intermediate. Of the three promoters, $Al_2O_3$ was found to be most effective for inhibiting the formation of carbon.

The nature of the carbonaceous species formed on the catalysts by butane TPRn at various temperatures were characterised by their reactivity with $O_2$ and $H_2$ during Temperature-Programmed Surface Reaction (TPSR) and by TEM. These revealed that at 673 K nickel particles are encapsulated by a film consisting of two types of carbon. At 773 K short filaments are the dominant carbon species, which are partially amorphous and consist of one type of carbon. These filaments undergo a transition into tubular carbon filaments at 873 K which consist of a duplex structure of an outer carbon skin and an inner carbon channel.

Butane TPRn revealed that addition of 3wt% potassium to the 5wt% $Al_2O_3$ promoted catalyst facilitated a reduced accumulation of carbon by decreasing the rate of hydrocarbon decomposition. This was attributed to the potassium blocking specific nickel ensembles required for the adsorption of n-butane and subsequent formation of ethylidyne.

# Acknowledgements

I would like to express utmost thanks to my supervisors, Professor Kenneth Waugh and Dr Bahij Sakakini, for the unfailing support, help and guidance they have afforded throughout the course of this work.

Thank you also to all my labmates whose friendship I will always value - Mohammad Al-Dosari, David Coultas, Andrew Cowap, Andrew Elliott, Hadi Farrokhnia, Matthew Hague, Philippe Marenne, Nicholas Moffat, Irmawati Ramli, Sharbanu Setayesh, Javad Tabatabaei, Yun Hin Taufiq-Yap, Reza Torbati, Sabaithip Tungkamani and Fessehaye Zemicael.

Many thanks are also due to Mr Jim Holden, Mr Peter Kenway, Dr Max Parrott and Mr Stuart Vaudrey for the expert technical assistance they provided throughout this project.

I would also like to express sincere thanks to Dr Martin Fowles for all the helpful advice he provided.

Financial support from EPSRC and ICI Katalco are gratefully acknowledged.

Finally, very special thanks go to my mother, father, sister and brother, without whose love and support none of this would have been possible.

This thesis is dedicated to my beloved parents, my mother Zofia and late father Tadeusz....

Mama, I am forever indebted to you for all you have done for me.
Tata, although you're not here I know that you can see this. Love and miss you always.

# Contents

# 1

# INTRODUCTION

## 1.1 Surface Catalysis

In the early 1800's, when many significant discoveries in chemistry and physics were being made, it was observed that certain chemical reactions were affected by trace amounts of substances that were not consumed in the reaction. As early as 1817, for example, Sir Humphry Davey [1] observed that when a hot platinum or palladium wire was exposed to mixtures of air and hydrogen or ethylene, a flameless combustion was observed. In 1823 Döbereiner discovered that platinum could bring about the oxidation of hydrogen and used this reaction to successfully develop a 'lighter' or portable flame source before the availability of matches. Michael Faraday [2] also demonstrated that the oxidation of ethanol vapour was sustained by platinum sponge, which glowed white-hot from the heat produced. Thus the discovery of heterogeneous catalysis was complete thanks to such studies, although it was not until 1836 that J.J.Berzelius [3] attempted to rationalise these startling findings. He was the first to use the term *catalysis*, describing a catalyst as 'a substance which can bring about chemical reaction, apparently without itself undergoing any change'. He also suggested the existence of a 'catalytic force' associated with the actions of catalysts.

The study of heterogeneous catalysis itself has been stimulated by its industrial importance. Many sections of the chemical and allied industries rely on processes for which catalysts are essential. Catalysed chemistry-based technologies first appeared in the latter half of the $19^{th}$ century. One of the first industrial processes, which oxidised hydrochloric acid to chlorine, was discovered in 1860 and was known as the Deacon Process. Soon after in 1875 the oxidation of $SO_2$ to $SO_3$ was discovered by Messel. In the early $20^{th}$ century Ostwald developed the process of ammonia oxidation to form nitric oxide, the precursor to nitric acid manufacture. Badische Anilin & Soda Fabric (BASF) successfully introduced the catalytic process for ammonia synthesis in 1913

where nitrogen and hydrogen were reacted over an iron catalyst containing alumina and potassium oxide. In 1923 they used the catalysed reactions of CO and $H_2$ over zinc oxide/chromia to produce methanol [4].

During the 1930-50 period the production of motor fuels became one of the main aims of catalysis. The cracking of long chain hydrocarbons to produce lower molecular weight products was achieved over oxide catalysts, composed mostly of alumina and silica. The early 1950's saw the discovery of abundant and inexpensive oil in Arabia which focussed the development of catalytic processes to convert petrolium crude to fuels and chemicals. Thus the establishment of the petrochemical industry gave rise to many major catalytic processes. One such process is the steam reforming of hydrocarbons.

### 1.2 The Steam Reforming reaction

Catalytic steam reforming has grown during the last four decades into one of the world's great catalytic processes. Here hydrocarbons and steam react over a catalyst to produce mixtures of hydrogen, carbon monoxide and carbon dioxide in various proportions, known as synthesis or syn gas. Synthesis gas is of enormous value since it forms the feed for a number of other significant industrial processes. It is used in the petrochemical industry to produce methanol and for oxo-synthesis. It is also used in the Fischer-Tropsch reaction for the synthesis of hydrocarbons. Syn gas is the major source of hydrogen used in ammonia synthesis and in oil refinery processes which consume hydrogen, such as hydrodesulphurisation and hydrocracking. Furthermore, syn gas is also used for direct reduction of iron ore in steel production. Carbon monoxide itself is used in the production of paints, plastics, foams, pesticides and insecticides.

The old commercial method used to make syn gas involved the *water gas* reaction. Here steam was passed over red-hot coke, where the following simple exothermic reactions occurred:

$$C + H_2O = H_2 + CO \qquad (1.1)$$

$$C + 2H_2O = 2H_2 + CO_2 \qquad (1.2)$$

In order to sustain the reaction temperature steam was intermittently cut off and air was introduced to re-heat the bed of coke by the following exothermic reactions:

$$C + {}^1/_2O_2 = CO \qquad (1.3)$$

$$C + O_2 = CO_2 \qquad (1.4)$$

Steam was then re-introduced and the reaction continued in this cyclical manner.
An unattractive feature of this process, however, was that the hydrogen produced came solely from the water and so a process more economic than that based on coal was required. Hydrocarbon feedstocks are rich in hydrogen (the hydrogen-to-carbon ratio varying from 4 in the case of methane to about 2 for longer chain hydrocarbons). It was therefore realised that additional molecules of hydrogen could be formed by reacting hydrocarbons with steam over a suitable catalyst. As a result this newer process, known as steam reforming, has supplanted the water gas reaction and is today responsible for some 90% of the world's hydrogen production [5].

### 1.3 Historical Aspects

The catalytic interaction between hydrocarbons and metals was already observed in 1817 by Humphrey Davey [1] during the development of the mine safety lamp. Davey also observed that 'a thin film of carbonaceous matter destroys the igniting power of platinum', and thereby already recognised the detrimental action of carbon, which causes severe problems in steam reforming (Section 1.9). In 1824, whilst carrying out similar experiments to those of Davey, Gibert [6] also reported an inflammable combustion when nickel was exposed to mixtures of air and hydrogen. The interaction

between olefins and nickel was reported in 1842 by Marchand [7] who observed that a carbon layer was formed containing a few percent of metallic nickel.

In 1868 Tessie du Motay and Maréchal [8] described a process for conversion of hydrocarbons into hydrogen in the presence of steam. The hydrocarbons and steam were passed over calcium oxide resulting in the formation of calcium carbonate and hydrogen. A two-step process to produce hydrogen by passing hydrocarbons and steam over nickel was carried out in 1889 by Mond and Langer [9]. In a first step carbon monoxide or hydrocarbons were decomposed over nickel at 623-723 K:

$$2CO + Ni_x = Ni_xC + CO_2 \qquad (1.5)$$

$$CH_n + Ni_x = Ni_xC + {}^{n}/_{2}H_2 \qquad (1.6)$$

The second step involved oxidation of the carbide with steam at the same temperatures:

$$Ni_xC + 2H_2O = Ni_x + CO_2 + 2H_2 \qquad (1.7)$$

In 1920 Sabatier [10] published a book summarising his comprehensive studies of reactions on nickel catalysts. However he failed to mention steam reforming, even though industrial interest was reflected earlier by the patents of Dieffenbach and Moldenhauer [11] and by BASF in 1912 [12].

1924 saw Neumann and Jacob [13] publish what is believed to be the first detailed study of the catalytic reactions between methane and steam. This generated interest into how the reforming reaction could be utilised to convert natural gas or methane-rich gases industrially into hydrogen or synthesis gas.

A 1926 steam reforming patent claimed low operating temperatures by using catalysts of iron, cobalt or nickel promoted with chromia, vanadia, alkali or alkali earths [14]. Fischer and Tropsch [15] also screened a large number of catalysts for the steam-methane and $CO_2$-methane reactions at temperatures of 1140-1250 K and found that supported nickel or cobalt rated as the best preparations. A patent issued in 1930 by I.G.Farben [16] described a process where the catalyst was placed in externally heated tubes of alloy steel.

### 1.4 Industrial Advances

1930 saw the first industrial steam reformer installed at Baton Rouge by Standard Oil of New Jersey [17]. The plant was used to produce hydrogen from off-gases for a coal hydrogenation plant and the steam reforming took place over catalyst in vertical tubes, supported in parallel rows in a radiant furnace. In 1936 the first Imperial Chemical Industries (ICI) reforming plant was commissioned at Billingham [18]. The ICI technology was subsequently used in the development of plants in North America during the War. All used natural gas which contained mainly methane with low concentrations of higher hydrocarbons.

Unlike in the United States, natural gas was not a readily available feedstock in the U.K. and Europe. However as more refineries were built during the 30's, other hydrocarbons such as $C_3$-$C_7$ light distillate naphthas became increasingly available and became an economical feedstock for steam reforming. In 1959 ICI started up the first naphtha reforming plants and the process was used exclusively for the production of synthesis gas for ammonia manufacture [19]. In 1962 ICI also successfully developed a process for the steam reforming of naphtha at higher pressures (~15atm) which gave rise to over 400 plants world wide for the production of ammonia, methanol and hydrogen [18]. The naphtha process was also extended to produce Town Gas in countries lacking natural gas. The gas produced had a calorific value of 500 Btu $ft^{-3}$, hence the process became known as The ICI 500 Process [20].

Another route to naphtha reforming was followed by the British Gas Council, where in 1957 Dent et al [21] described a process for adiabatic gasification of naphtha to produce methane. The first plant based on these principles, known as the Catalytic Rich Gas or CRG process, was commissioned in 1964 [22]. A year later the first Topspe reformer using naphtha as feed was started and two years later, a Topspe reformer operating at a pressure of 40atm was installed [23].

Today, more than 80% of the world ammonia production is based on the on the steam reforming of hydrocarbons. Natural gas, which alone counts for 70%, is the preferred feedstock in most new plants. Increased demands for desulphurisation and hydrocracking have seen oil refineries using more and more hydrogen [24]. As a result the deficit in available hydrogen is being filled by the steam reforming of naphtha and off-gases. Reforming of natural gas has found a new application in the manufacture of reducing gas for steel production [25]. Plants of this type are being constructed particularly in countries where cheap natural gas is available. Conversely, in the United States where it is likely that cheap natural gas will not be easily available in the future, the steam reforming of naphtha looks likely to be utilised for the production of substitute natural gas (SNG) [26].

### 1.5 Feedstocks

Feedstocks for catalytic steam reforming can vary widely in composition. In principle, any hydrocarbon can be used and broken down into hydrogen and carbon oxides, although in practice methane and naphtha are most commonly employed. Regional availability is a major factor which determines the nature of the feedstock used.

The simplest feedstock, methane, occurs as natural gas and usually contains other saturated hydrocarbons of low molecular weight as well as nitrogen, carbon dioxide and organic and inorganic sulphur compounds. Before being used as a feedstock for steam reforming, liquid condensates must be removed to ensure a constant gas composition and any solid suspension must be removed by filtration. Sulphur is a severe poison for

steam reforming catalysts and so all sulphur compounds must be removed by hydrogenolysis and absorption in a bed of zinc oxide. Natural gas is the primary feedstock used in the U.S. and most of western Europe.

In countries not so adequately endowed with natural gas, e.g. Japan and India, naphtha is still an important feedstock. Naphtha fractions with a final boiling point of less than 500K are normally used for steam reforming. To avoid the possibility of aromatisation in the hydrodesulphurisation process, no more than 40% of the feedstock must consist of naphthenes since this would increase the aromatic content of the feed to the reformer. Olefinic compounds in the feed gas should be in amounts of less than 1% and contaminants such as sulphur and chlorine must be reduced to less than 0.5ppm and 1ppm respectively. Any arsenic which may be present must be completely removed.

## 1.6 Chemistry of Steam Reforming

### 1.6.1 Natural gas Reforming

The steam reforming of natural gas is based on two simple reversible reactions:

$$CH_4 + H_2O = CO + 3H_2 \qquad (\Delta H = +206 \text{ kJ mol}^{-1}) \qquad (1.8)$$

$$CO + H_2O = CO_2 + H_2 \qquad (\Delta H = -41 \text{ kJ mol}^{-1}) \qquad (1.9)$$

The steam reforming reaction (1.8) is today more commonly termed 'reforming' and should not be confused with the well known process for improvement of the octane number of gasoline. The reforming reaction is strongly endothermic so the forward reaction is favoured by a high temperature as well as by low pressure. Reaction (1.9), known as the shift reaction, is exothermic and is thus favoured by low temperature but is largely unaffected by changes in pressure. Depending upon the end use, operating

conditions in a steam reforming plant are adjusted so as to optimise the composition of the emergent gas.

For methane, the stoichiometric requirement for steam per carbon atom is 1.0. However, this is not practicable since all catalysts developed to the present day tend to promote undesired carbon forming reactions under steam reforming conditions (See Section 1.9). An excess of steam is required to suppress carbon formation and promote the reforming reaction, so the resulting minimum steam to carbon ratio is in the region of 1.7:1 [20]. In practice the steam ratios utilised are in the range 2.5-3.5 [19]. Despite the thermodynamics of the process, reformers operate at high pressure to optimise the overall economics of the process.

### 1.6.2 Naphtha Reforming

The reforming of saturated naphthas of general formula $C_nH_{2n+2}$ is based on three reactions:

$$C_nH_{2n+2} + nH_2O \rightarrow nCO + (2n+1)H_2 \qquad (\Delta H > 0) \qquad (1.10)$$

$$CO + H_2O = CO_2 + H_2 \qquad (\Delta H = -41 \text{ kJ mol}^{-1}) \qquad (1.11)$$

$$CO + 3H_2 = CH_4 + H_2O \qquad (\Delta H = -206 \text{ kJ mol}^{-1}) \qquad (1.12)$$

Reaction (1.10) is strongly endothermic, whereas both the shift reaction (1.11) and methanation reaction (1.12) evolve heat. The overall heat of reactions (1.10)-(1.12) however, may be positive, zero or negative depending on process conditions. The naphtha reforming reaction is regarded as irreversible at normal conditions. Intermediates will then come to equilibrium via the shift and methanation reactions.

The use of stoichiometric ratios of carbon and steam may again give rise to carbon formation on catalysts, even more so than with methane, as illustrated in Fig.1.7. It is therefore even more important to ensure an excess of steam to promote reaction. Higher steam to carbon ratios than those for methane are employed, usually 3.5-4.5:1, with the minimum practical ratio being about 2.2:1 [20]. The various gas compositions which can be obtained from reactions (1.10)-(1.12) are determined by the steam to carbon ratio and the catalyst exit temperature, since the pressure is normally fixed. At low catalyst exit temperatures, for example, and low steam to carbon ratios the overall reaction is exothermic and the methanation reaction dominates. This is reflected by a high methane content in the product gas which can then be used for Town Gas or as a step in the preparation of SNG. In contrast, hydrogen and synthesis gases with lower methane contents in the reformer effluent are produced at high temperature and a high steam to carbon ratio, where the overall reaction becomes endothermic. Fig.1.1 illustrates some typical reforming conditions for various applications.

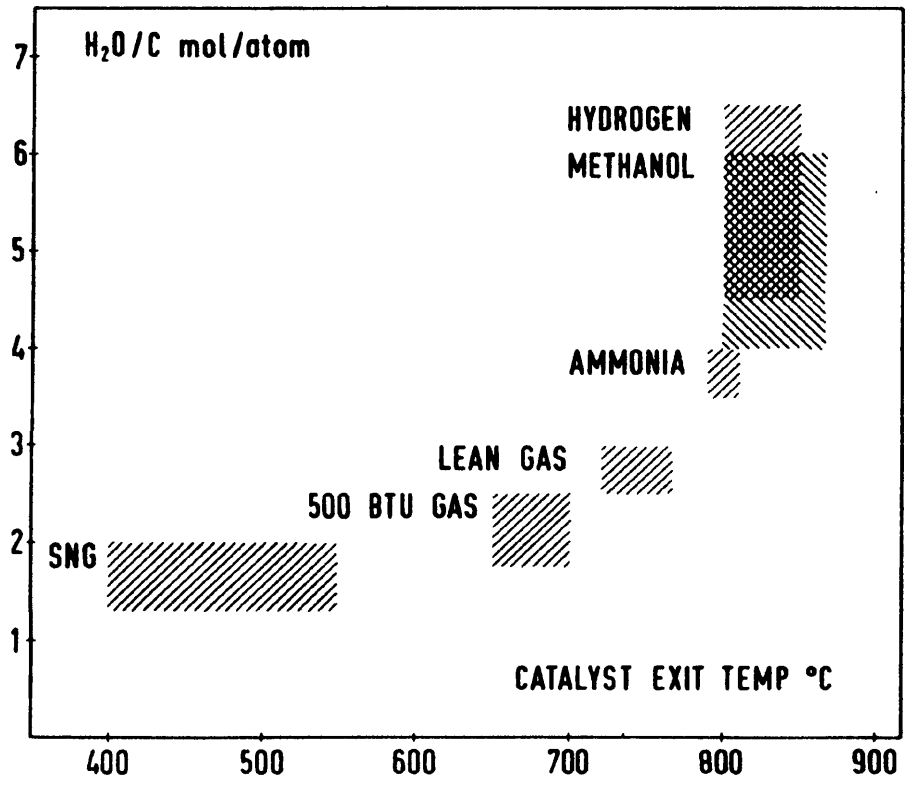


Fig.1.1 Typical reforming conditions for various applications [24]

## 1.7 The Tubular Reformer

In order to supply the heat for the overall endothermic steam reforming reaction, the catalyst is loaded into a number of high-alloy tubes placed inside a furnace equipped with burners, as shown in Fig.1.2. Such a reactor is known as a Tubular Reformer. Typical inlet temperatures are 720-920 K and the product gas leaves the reformer at 970-1220 K, depending on the applications.

The primary reformer consists essentially of two sections: the furnace and the convection section. Depending on output, the furnace can contain anything from 40 to 650 tubes, the internal diameter ranging from 70-160mm and with an overall length of 6-12m. The fuel used to provide energy input to the reformer is usually the same as the hydrocarbon feed. In a typical tubular reformer furnace, about 50% of the heat produced by combustion in the burners is transferred through the reformer tube walls and absorbed by the process [27]. The other half of the fired duty is available in the hot flue gas and is recovered in the waste heat or convection section of the reformer for preheat duties and for steam production. In this way the overall thermal efficiency of the reformer approaches 95%.

The reformer tubes are made from high alloy nickel chromium steel (typically Cr 25%, Ni 20%, Co 4%) and are subject to very large stresses since they operate at high temperatures with very large temperature gradients. The maximum allowable stress value in the tubes is strongly influenced by the maximum tube wall temperature and maximum heat flux. Even a slight increase in the maximum tube wall temperature may result in a serious reduction of the expected life of the tubes. Reformer tubes are normally designed for an average expected lifetime of 100 000 hours.

### 1.7.1 Secondary reforming

The reforming process in an ammonia plant is divided into two stages, so that the necessary nitrogen can be added to the process. Nitrogen is introduced as air into a secondary reformer. This is a catalyst filled vessel in which a highly exothermic

reaction between oxygen and hydrogen takes place, liberating heat and raising the temperature of the product gases from the primary as high as construction materials will allow. Typical temperatures achieved are in the region of 1273 K. In this way as much methane as possible is converted into hydrogen and carbon oxides.

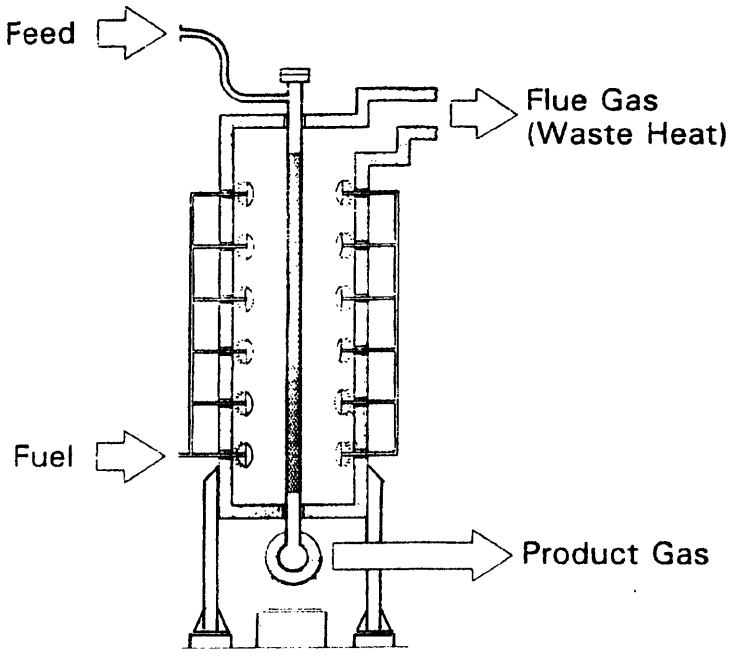


Fig.1.2 The tubular reformer

## 1.8 Nickel as a catalyst

### 1.8.1 Introduction

Nickel is a very important metal to industry. The vast majority of nickel consumption is in the production of stainless steels and other alloys such as cupro-nickel for coin manufacture, nickel-iron thermal expansion alloys for bimetallic strips in switches and steels for cryogenic use. Other major uses include electroplating for corrosion resistance and also the production of batteries. Surprisingly, in terms of volume, a very minor use of nickel is in catalysis. It was in 1897 that Sabatier [10], during his studies

on catalytic hydrogenation, attempted to synthesise $Ni(C_2H_4)$ only to observe that passing ethene over heated nickel produced ethane, rather than the volatile nickel compound. Mixing ethene with hydrogen and then passing the mixture over the metal gave a greater yield of ethane. Sabatier found that nickel acted as an efficient hydrogenation catalyst. Alkenes gave the corresponding alkanes. Alkynes also produced alkanes. Aromatic hydrocarbons (e.g. benzene, methylbenzenes etc.) gave the corresponding hexahydro derivatives. Carbon monoxide and carbon dioxide both gave methane and this eventually led to the methanation process, where syn gas is converted to methane (Town gas) over a supported nickel catalyst. The hydrogenation of alkenes, particularly unsaturated fatty acids, is presently a very important commercial process utilising nickel catalysts.

### 1.8.2 Nickel as a steam reforming catalyst

Undoubtedly the most important application of nickel catalysts today is their use in steam reforming. In fact nickel has long been recognised as the most suitable metal for the reaction. As early as 1928 Fischer and Tropsch [15] described screening tests on many catalysts from which they concluded that nickel was among the best catalysts for the steam reforming reaction. Only five years later in 1933, Fujimoto [28] reported one of the first uses of a supported nickel catalyst, 90% $Ni/Al_2O_3$, for the steam reforming of methane over the temperature range 673-1273 K at atmospheric pressure.

In general, the metals of group VIII of the periodic table are active for the steam reforming reaction. However, nickel is invariably the active metal used in industrial catalysts [24]. Iron and cobalt are not stable under the process conditions and the precious metals, although considerably more active per unit weight than nickel, are too expensive to use commercially. The steam reforming reaction can generally be thought of as non-selective since the products required are the most thermodynamically stable under the conditions used. Therefore there is no major advantage to be gained by using more expensive metals since nickel is sufficiently active to catalyse the reactions.

### 1.8.3 Catalyst requirements and properties

It is essential that an industrial catalyst for steam reforming duty promotes the desired reaction and be inactive as possible towards unwanted side-reactions, particularly those forming carbon. Developments in catalyst modification by the addition of specific promoters to combat the problem of carbon formation are discussed in detail in Section 1.11. Thermal stability of the catalyst is crucial, which must be able to maintain its activity under the demanding process conditions. It must also be strong enough to withstand the general handling it receives, from manufacture to charging into the reformer as well as the stresses generated by the process conditions.

The physical shape of the catalyst must be suitable to provide an appropriate geometric surface area to give a sufficient activity per unit volume of packed bed, whilst possessing acceptably low pressure-drop characteristics. Original reforming catalysts were crude 'cubes' of material until ICI pioneered the use of the first catalyst 'shape' – the Raschig ring (Fig.1.3(a)) – which met the required criteria and dominated the reforming catalyst market for some 50 years [29]. During the 1980's however, ICI Katalco successfully developed a 4-hole catalyst shape – the 'Optimised ring' (Fig.1.3(b)) – which gave the following improvements over the Raschig ring in reformer operation:

i) improved catalyst activity
ii) reduced pressure drop
iii) better heat transfer properties

This new shape is able to reduce the maximum tube wall temperature by some 20K which can effectively double the life of tubes [19]. Not surprisingly then, the Optimised ring has steadily supplanted the use of Raschig rings in reformers world wide.

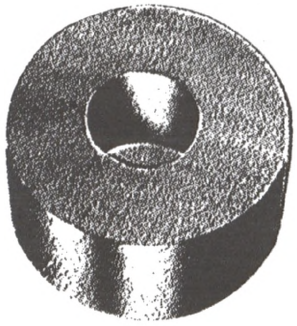

Typical dimensions:
Length: 6 - 17mm
Diameter: 14 - 17mm

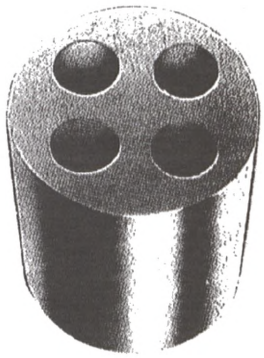

Typical dimentions:
Length: 13 - 17mm
Diameter: 10 - 14mm

Fig.1.3 (a) The 'Raschig ring' (b) The 'Optimised ring'

### 1.8.4 Catalyst preparation and activation

The reforming reaction takes place in a thin layer close to the catalyst surface. The size of this layer is described as the 'effectiveness' factor. A typical value would be 1 - 2% [19]. The activity of reforming catalyst is then a function of the micromeritics of the catalytic material which determine the depth of the layer where the reaction occurs. It is also a function of the shape of the catalyst which is designed to give the maximum area of this layer by maximising the external or 'geometric' surface area of the catalyst per unit volume of the tube.

In order to produce the maximum stable nickel surface area available to the reactants, reforming catalysts are manufactured by dispersing the nickel as small crystallites on a

refractory support. The support must be sufficiently porous to allow access by the gas to the nickel surface. This is usually achieved by either of two methods:

i) Co-precipitation

In this procedure the nickel compound and the support are simultaneously precipitated from the same solution. For example, a nickel/alumina catalyst is produced by treating a solution of the metal nitrates (ie. nickel nitrate and aluminium nitrate) with an alkali (eg. sodium carbonate) to produce the co-precipitate. The co-precipitate is then filtered, washed and dried before being calcined in air to produce the oxide form [30]. This procedure is illustrated in Fig.1.4(a). Co-precipitated $Ni/Al_2O_3$ catalysts were first prepared by Zelinsky in 1924 [31].

ii) Impregnation

In this method the nickel is incorporated by simply impregnating a preformed catalyst support with a solution of a nickel salt, which is subsequently decomposed to the oxide by heating [32]. This is illustrated in Fig.1.4(b).

In order to activate the catalyst, the nickel oxide produced must be reduced to the zero-valent metal, $Ni^{(0)}$, by reduction of $Ni^{2+}$ with a suitable reducing agent. In industrial plants these can include hydrogen, ammonia, methanol and hydrocarbons added to steam [33]. The reduction using hydrogen is shown below:

$$NiO + H_2 = Ni + H_2O \qquad (\Delta H = -1.2 \text{ kJ mol}^{-1}) \qquad (1.13)$$

Industrial activation is often carried out by means of the feed stream of steam and hydrocarbons at a high steam to carbon ratio (5-10) and at a low pressure. The hydrocarbons crack thermally and the resulting hydrogen acts as an initiator for the

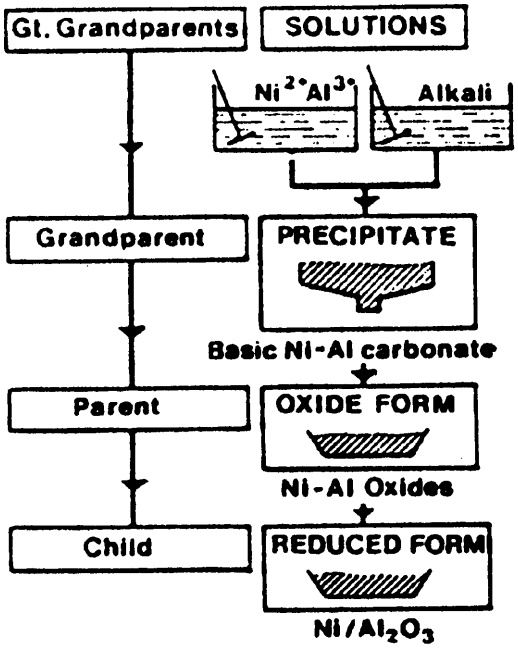


Fig.1.4 (a) Scheme showing each stage in the preparation of a co-precipitated nickel/alumina catalyst

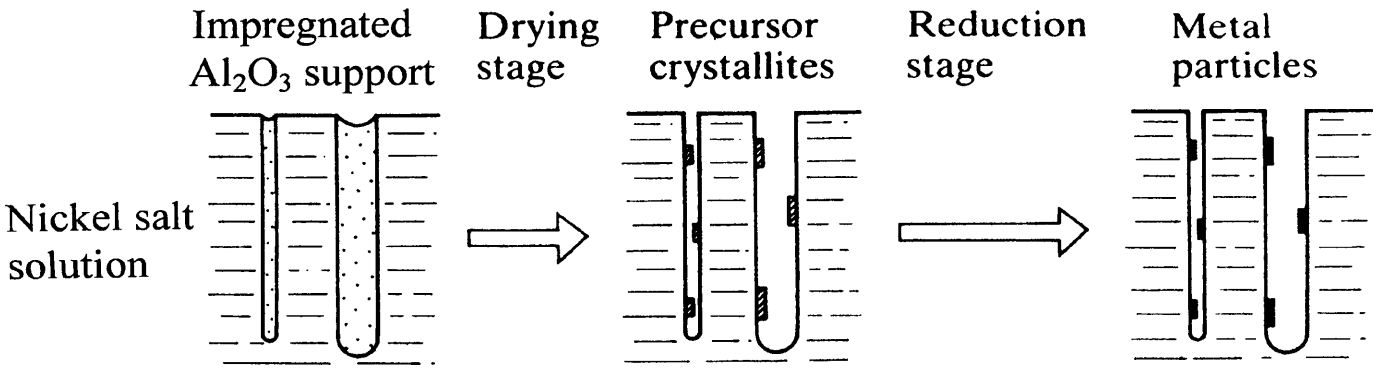


(b) Illustration of the stages in the preparation of a nickel/alumina catalyst by the impregnation method. The pores of the support are initially impregnated with a solution of the metal salt

reduction process. As soon as metallic nickel is available, the steam reforming process will produce sufficient hydrogen for a quick reduction of the catalyst.

Steam reforming catalysts differ in the ease with which they reduce and the extent of reduction is influenced by the chemical nature of the catalyst support, the reduction temperature and time and the composition of the reducing gas. Numerous studies [34] [35] have reported that the activation procedure influences the size of the resulting nickel surface and hence the activity of the catalyst. It has been observed that the highest nickel surface area is obtained when the reduction is done using dry hydrogen (rather than steam and hydrogen) and when the reduction temperature is about 873 K [20]. Below this temperature reduction can be slow and incomplete, whereas above 873 K there is danger of sintering which lowers the nickel surface area. The longer the reduction period, the further the sintering process proceeds to give even lower surface areas.

The presence of steam during activation may also cause a decrease of the resulting nickel area. Rostrup-Nielsen [33] explained this effect by the assumption that steam oxidises the smallest nuclei of nickel or prevents their formation. Consequently, the number of nuclei and the resulting number of crystals is decreased which means a smaller area.

### 1.8.5 Sintering

Sintering of nickel crystals results in a loss of surface area and, in principle, recrystallisation may change the nickel ensembles available and also cause a decrease of the specific activity. Rostrup-Nielsen [36] carried out a study on the effect of heat treatment on nickel crystals on a stable low area ceramic support. The results are shown in Fig.1.5. No sintering was observed at 820 K over a period of 1000 hours, whereas the nickel surface area dropped to around 40 and 25% over the same period at 970 K and 1120 K respectively. The result corresponded to the rule of Tammann [37] which states that sintering is expected above 0.5 times the melting point of the metal ie. 864 K for nickel.

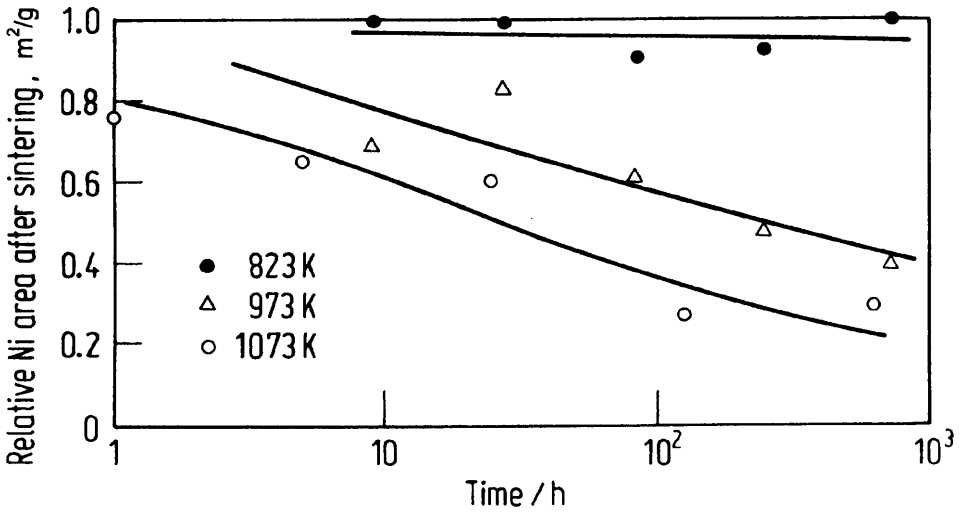


Fig.1.5. Sintering of nickel surface of a ceramic reforming catalyst. $P_{H2O}/P_{H2}$ = 3, $P$ = 0.1 MPa [36].

### 1.8.6 Performance and activity

The performance and strength of nickel reforming catalysts are determined by their formulation. In general impregnated catalysts are stronger than co-precipitated catalysts, although both find widespread use in industry. The activity of a steam reforming catalyst in service is related to the available surface area of the nickel metal and the access the reactants have to it [20]. Of course under normal reforming conditions, the nickel surface area of both impregnated and co-precipitated catalysts decreases as sintering of nickel crystallites occurs, with sintering proceeding more rapidly as the temperature increases. Not surprisingly therefore, for both catalyst types, activity is a function of the overall nickel content. The nickel surface area is generally increased with higher nickel contents in the catalyst [38] [39], but the dispersion of the nickel tends to decrease with increasing nickel content.

It has been demonstrated that with both impregnated and co-precipitated catalysts there is an optimum beyond which an increase in nickel content does not produce any further significant increase in activity. These optima are approximately 15wt% for impregnated catalysts and up to about 20wt% for co-precipitated catalysts. However, this does depend on the nature and physical properties of the actual support [20].

### 1.8.7 The role of the support

In addition to the catalytic function, the mechanical properties of the catalyst are critical and as a result much attention has been given to the selection of suitable supports which remain stable for prolonged periods. The temperature and the steam and hydrogen partial pressures during steam reforming restrict the choice of support material. Most importantly the support must be stable to all conditions which will be seen during its period in the reformer, be suitable for the dispersion of nickel crystallites and allow access of the reacting species without interfering with their activity. It is essential that the support does not catalyse side reactions, especially those forming carbonaceous deposits.

Most industrial catalysts for tubular reforming are based on ceramic oxides or oxides stabilised by a hydraulic cement. Typical ceramic supports are α-alumina ($Al_2O_3$), magnesium aluminium spinel ($MgAl_2O_4$), magnesia (MgO) and zirconia ($ZrO_2$) fired at temperatures well above 1270K. Supports derived from a mixture of alumina and a hydraulic cement processed to a porous calcium aluminate ($CaAl_2O_4$) are also particularly useful since they are less acidic than α-alumina and are therefore less susceptible to carbon formation initiated by hydrocarbon cracking reactions (see Fig.1.7).

Silaceous Portland cement is no longer favourable as a support since in the presence of steam at high temperatures it is volatile as orthosilicic acid ($Si(OH)_4$) and this leads to progressive weakness [5]. Care must also be taken when using magnesia. While resistant to high temperature steaming, magnesia-based catalysts are sensitive to steaming at low temperatures because of the risk of hydration:

$$MgO + H_2O = Mg(OH)_2 \qquad (\Delta H = -81.3 \text{ kJ mol}^{-1}) \qquad (1.14)$$

$Mg(OH)_2$ formed during the reaction has a molar volume almost twice that of MgO which may result in a dramatic weakening of the support and the consequent breakdown of the catalyst [33].

High area supports such as γ-alumina and chromia ($CrO_2$) are suitable for low temperature adiabatic reforming, however at temperatures above 770 K they suffer from substantial sintering and weakening. This deterioration is further accelerated by high steam partial pressures [40].

## 1.9 Carbon Formation

### 1.9.1 Introduction

The deactivation of supported nickel catalysts due to the formation of carbon is a problem of enormous magnitude in steam reforming. Severe operational difficulties in the reformer are introduced since carbon formation causes fouling of the metal surface, blockage of catalyst pores and physical disintegration of the catalyst support [41]. Consequently, the complete breakdown of the catalyst coupled with the accumulation of carbon cause partial or total blockage of reformer tubes, leading to an unequal gas distribution and therefore local overheating [33]. This results in the development of hot spots, hot bands or totally hot tubes (Fig.1.6) which dramatically shorten tube life.

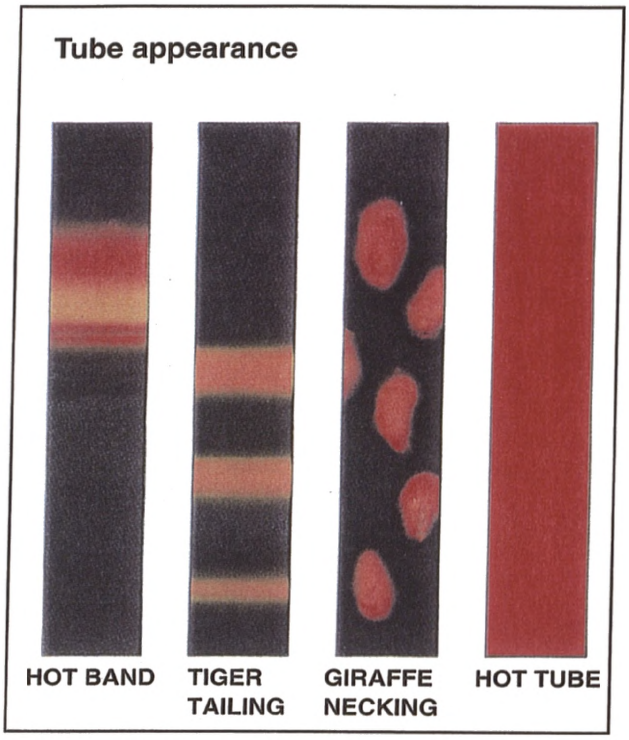


Fig.1.6 The various appearance of hot tubes

1.9.2 Carbon formation during Methane Reforming

All hydrocarbons decompose spontaneously at reforming temperatures, in the absence of steam, to form carbon and hydrogen:

$$CH_4 = C + 2H_2 \qquad (\Delta H = 75 \text{ kJ mol}^{-1}) \quad \text{Methane cracking} \quad (1.15)$$

In the presence of steam, and in particular with less than the stoichiometric amount of steam, carbon may also be formed by the Boudouard reaction:

$$2CO = C + CO_2 \qquad (\Delta H = -172 \text{ kJ mol}^{-1}) \qquad (1.16)$$

It is particularly important that the two above equilibria are kept well to the left so that the deposition of carbon is avoided. This is usually achieved by employing excess steam to react with the hydrocarbon in the feed to ensure a sufficiently high $CO_2$-to-CO and $H_2$-to-$CH_4$ ratio [42].

Carbon formed by methane cracking can be removed by reaction with steam (1.17) or $CO_2$ (1.18), provided that the rate of carbon removal is faster than the rate of formation. This is usually true at temperatures below about 920 K [42]. Above 920 K sufficient hydrogen will have been formed for the methane cracking reaction to be on the carbon removing side of the equilibrium.

$$C + H_2O = CO + H_2 \qquad (1.17)$$

$$C + CO_2 = 2CO \qquad (1.18)$$

### 1.9.3 Carbon formation during Naphtha Reforming

The decomposition of naphtha to form carbon is more complex than the decomposition of methane. Higher hydrocarbons have a greater tendency to form carbon than methane, since carbon can be formed by polymerisation of unsaturated intermediates as well as by feedstock cracking. Overall reaction takes place in several successive stages and can follow parallel routes, as shown in Fig.1.7. Initial deposition takes place catalytically above about 770 K and thermally above 920 K. Intermediates consisting of olefins and saturated hydrocarbons of low molecular weight are produced [43]. The intermediates react with steam catalytically to give product gas, but they can also polymerise and dehydrogenate to produce carbon, depending on their concentrations on the catalyst surface. This concentration is critical in influencing the delicate balance between carbon-forming and carbon-removing reactions. Carbon can also be produced directly by catalytic or thermal cracking of the feedstock [44].

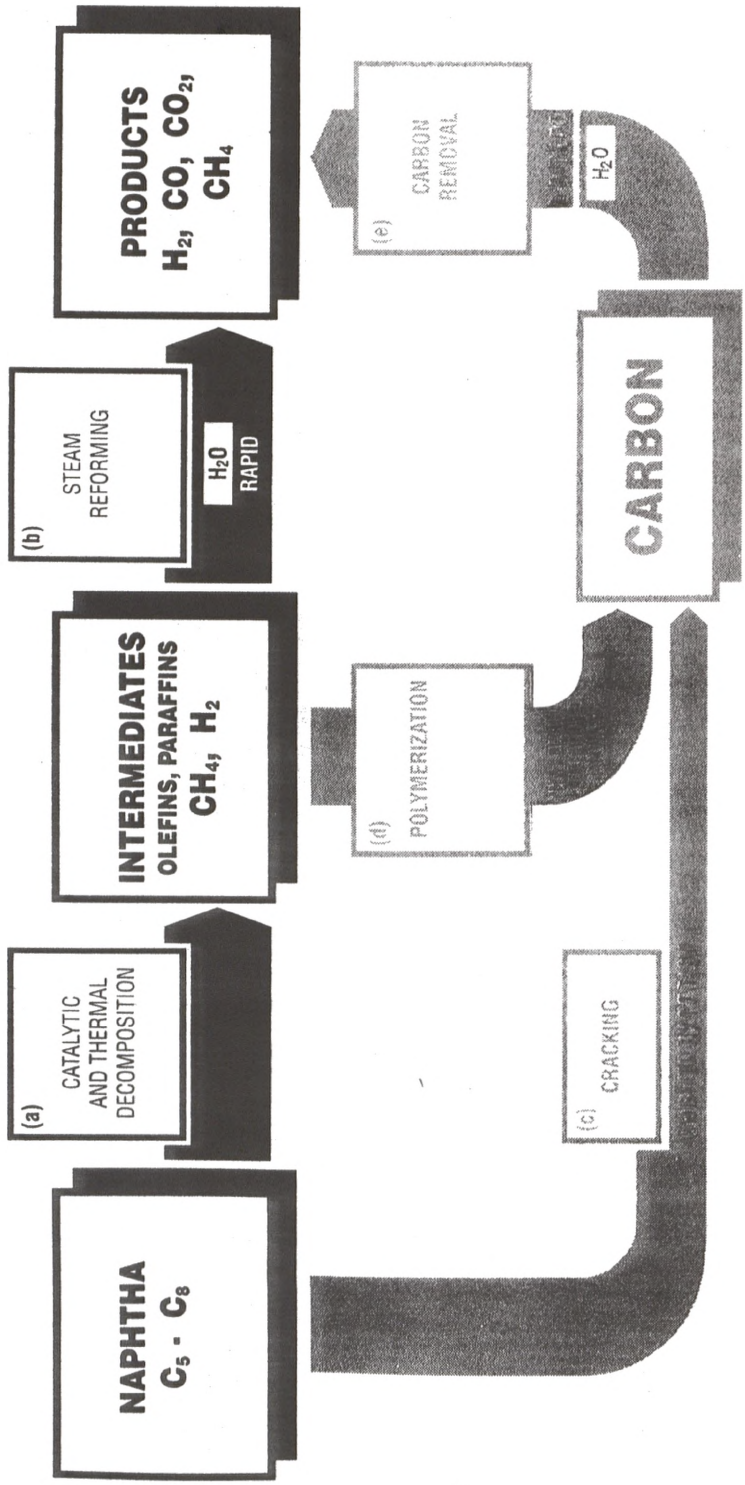


Fig.1.7 Flow scheme representing the formation of carbon from naphtha reforming

The different routes via which carbon may be formed influences the morphology of the carbon. Rostrup-Nielsen [33] described three different types of carbon species which can be formed in hydrocarbon steam reforming: filamentous (whisker) carbon formed at $T > 720$ K, encapsulating carbon films formed by polymerisation at $T < 770$ K and pyrolytic carbon formed by the cracking of hydrocarbons at $T > 870$ K. Both encapsulating and pyrolytic carbon lead to deactivation of the catalyst since the Ni particles become totally encapsulated by the carbon. Filamentous carbon does not deactivate the catalyst since the metal surface remains accessible to reagents. However, filamentous carbon can instigate the plugging of catalyst pores and reactor voids, lowering the conversion and increasing the pressure drop and channelling effects. Due to its high mechanical strength, filamentous carbon is also capable of completely disintegrating the catalyst support structure making all attempts at regeneration futile [45].

## 1.10 Filamentous carbon – a detailed study

### 1.10.1 Introduction

The formation of carbon on steam reforming catalysts has been studied extensively for many years. Much of this study has been focussed on the formation of filamentous carbon because of its particularly detrimental effect during the reforming process. Filamentous carbon is known to form from the reaction of hydrocarbons as well as carbon monoxide over transition metals. Nickel and iron are the most active metals for the formation of carbon filaments. However, emphasis will be placed upon the formation of filaments on nickel and the general mechanism by which they are formed will be portrayed.

### 1.10.2 General mechanism of carbon filament formation

Based on Controlled Atmosphere Electron Microscopy (CAEM) studies involving the catalysed decomposition of acetylene on transition metals, Baker [46] formulated

common qualitative characteristics of carbon filament formation on Ni, Fe and Co. The metal particle is always situated at the growing end of the filament and is carried away from the support surface by the growth process. The diameter of the filament is very close to that of the metal crystal at its head and the crystal is very often pear-shaped with the base pointing in the direction of growth. Active particles show that part of the surface is protected by the filament and part is exposed to the gas phase. Deactivated particles are totally covered in encapsulating carbon. The filaments themselves are tubular with a co-axial channel. A controlled oxidation of the filaments revealed the duplex structure consists of an inner core of easily oxidisable carbon surrounded by a skin of more oxidation resistant material.

Lobo et al [47] and Figuerido et al [48] studied the formation of carbon filaments on both nickel foils and supported Ni catalysts. During carbon formation from acetylene on Ni foils between 673 and 873 K, Lobo observed that there was an induction period, followed by an acceleratory period, and finally a steady state period at which there was a constant rate of carbon deposition. Figuerido reported similar findings when depositing carbon from a propylene/hydrogen mixture on nickel foils and catalysts. A common feature of carbon filament formation on foils and supported catalysts is the presence of an extended period of carbon formation at a constant rate, during which large amounts of bulk carbon are deposited. This suggests that carbon does not immediately deactivate the catalyst but is removed from the active sites to grow elsewhere.

These facts, coupled with the observation of carbon filaments by electron microscopy, led to a general mechanism for the formation of filamentous carbon on transition metals to be postulated [49] [50] [51]. The steps of the mechanism are shown schematically in Figs.1.8(a-b). Firstly chemisorbed carbon atoms are produced from the decomposition of adsorbed hydrocarbon molecules at the leading face of the metal particle. This is followed by dissolution of carbon in the bulk of the metal and subsequent diffusion to the trailing faces, where carbon is precipitated from solution to form the filament. The upper surface of the metal remains accessible for continued reaction with the gas phase

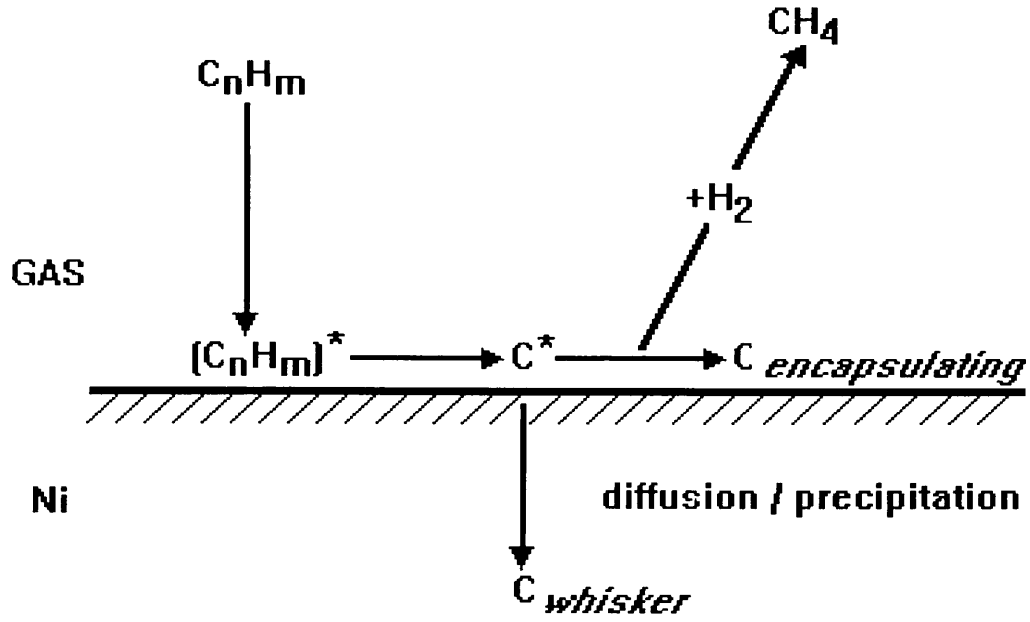


Fig.1.8 (a) The various steps in the mechanism of carbon filament formation

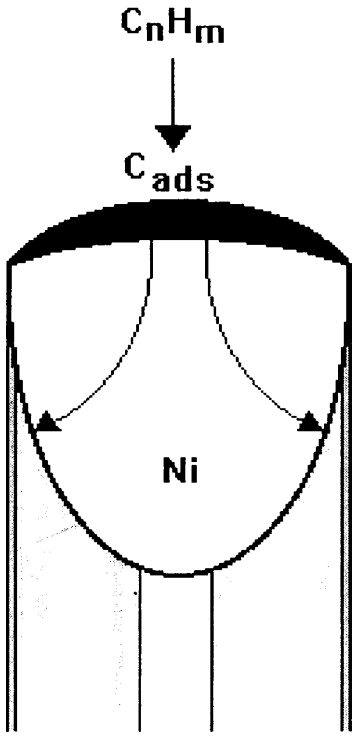


(b) Schematic representation of the mechanism of carbon filament formation

and no immediate deactivation takes place. Encapsulation of the leading face by carbon causes deactivation.

Although the above model is still generally considered to provide a realistic description of the catalytic growth of carbon filaments, the details of the mechanism are still the subject of much debate.

### 1.10.3 Thermodynamics of carbon filament formation

The deviation of the thermodynamic equilibrium for the Boudouard reaction (1.16) and the methane cracking reaction (1.15) from the equilibrium predicted on the basis of thermodynamic data for graphite was first observed by Dent et al [52]. They found that experimentally determined equilibrium constants for both processes were smaller than those based on graphite data. This meant that gas mixtures with a higher CO or $CH_4$ content (or lower $CO_2$ and $H_2$ content) could be maintained without any carbon deposition occurring, than would be expected based on graphite.

Similarly, Rostrup-Nielsen [53] found the equilibrium constants for CO and $CH_4$ decomposition between 723 and 973 K on various nickel catalysts deviated from constants based on graphite data. Examination in the electron microscope showed the presence of carbon as filaments. Estimates of the entropy change for the Boudouard and methane cracking reactions showed that the entropy of carbon filaments was higher than that of graphite, indicating a more disordered structure. The greatest deviation from graphite data was observed for catalysts with the smallest crystallites. Rostrup-Nielsen thus suggested that the deviation from the graphite equilibrium may be explained by the more disordered structure of the carbon formed and by a higher surface energy depending on the filament diameter.

Manning et al [54] studied the rate of growth of carbon and the equilibrium of carbon formation in a gas mixture of CO, $CO_2$, $CH_4$ and $H_2O$ over a $Ni/Al_2O_3$ catalyst and Co metal particles in the temperature range 700 - 900 K. They observed that the carbon deposition rate became zero under conditions where there was still an affinity for

graphite formation, and that the deviation from graphite decreased with increasing temperature. They concluded that the observed deviation from the graphite equilibrium was due to the formation of a metastable carbide intermediate which continuously decomposed into carbon and nickel or carbon and cobalt. The formation of this intermediate carbide phase has been questioned however [55], specifically at temperatures of 773 K and greater since nickel carbide is known to decompose at reasonable rates at temperatures higher than approximately 623 K [56]. Furthermore, X-ray diffraction experiments carried out by Manning et al failed to reveal the presence of a carbide phase.

De Bokx and co-workers [57] also studied the thermodynamics of filamentous carbon formed from CO and $CH_4$ on Ni and Fe catalysts in the temperature range 650 – 1000 K. Deviation from graphite equilibrium was again observed. Based on results obtained using Temperature Programmed Hydrogenation (TPH) and Thermomagnetic Analysis (TMA) they concluded that metastable carbides are present during the different stages of carbon deposition, leading to filamentous carbon on decomposition.

In a detailed description of the thermodynamics of the carbon filament formation process, Snoeck et al [55] described a condition referred to as the 'coking threshold', where no carbon deposition or gasification occurs. At the coking threshold, the rates of the surface reaction, the diffusion and the precipitation which operate in series, become zero. Since filamentous carbon has a structure which differs from that of graphite, its thermodynamic properties are evidently different. Therefore they suggested that the thermodynamic properties of the final product, i.e. filamentous carbon, determine the gas-phase composition at the coking threshold, since it determines the chemical potentials of carbon dissolved in nickel and that of surface carbon. At equilibrium, the chemical potential of carbon dissolved in nickel, just below the selvedge, and that of surface carbon are equal. The selvedge itself is created because of the segregation behaviour of carbon in nickel (see Fig.1.9). Isolated surface carbon atoms dissolve into the nickel particle at its front and diffuse to the rear. At the front of the nickel particle a segregation/dissolution equilibrium exists between adsorbed carbon and carbon dissolved in the bulk, just below the selvedge. The surface is enriched with carbon and

the carbon concentration decreases from the surface concentration to the bulk concentration of interstitially dissolved carbon over a number of atomic layers.

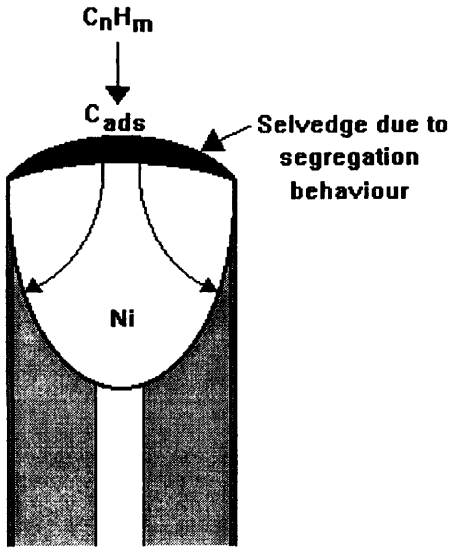


Fig.1.9 Schematic representation of carbon filament formation

### 1.10.4 The morphology of carbon filaments

High resolution electron microscopy studies have provided much information about the detailed structure of carbon filaments. Boellard et al [58] studied the microstructure of carbon filaments on supported Ni and Fe catalysts, formed from a mixture of $CO/H_2$ at 850 K. Filaments characterised by Transmission Electron Microscopy (TEM) exhibited relatively electron-transparent canals along their axes and an inhomogeneously streaked nature. Metal particles at the tip of these filaments exhibited a cone-shaped appearance. Selected Area Electron Diffraction (SAED) and dark-field imaging indicated that carbon filaments exhibit a very distinct carbon microstructure consisting of graphite layers and that the structure is determined by the shape of the particle at the tip of the filament. Boellard et al described the microstructure as a fishbone-like arrangement of the graphite basal planes demonstrating an almost cylindrical symmetry. The graphite layers are conically ordered thus possessing a mechanical strength capable of destroying the catalyst support structure.

A growth mechanism, although admittedly speculative, was also proposed highlighting three possibilities. Firstly, complete cones could be made up by graphite layers which are excreted consecutively from the metal particle, without slippages of the already formed graphite layers over one another (Fig.1.10(a)). Contrary to observations made however, this would cause an increase in filament diameter. Fig.1.10(b) illustrates the situation if slippage was allowed. Graphite layers successively excreted push the metal particle in the direction of the filament axis and the diameter of the filament would not change. However in this case dark-field images would not exhibit a streaked texture, but the diffraction due to perfectly parallel graphitic carbon layers would be exhibited homogeneously. So it was proposed that the rate of carbon excretion is not uniform over the entire metal cone surface (Fig.1.10(c)). Consequently, sites at the metal/carbon interface near the metal/gas interface (ie. the cone circumference) receive higher fluxes of carbon atoms than sites further from the metal/gas interface, so that different numbers of graphite layers are produced in a given period of time.

High Resolution Electron Microscopy (HREM) was used by Zaikovskii et al [59] to study the morphology of filamentous carbon formed on Ni and Fe from benzene at 923 K or butadiene at 723 K. They observed that filaments were formed with a hollow channel and metallic inclusions and that the metal particle at the top had a 'dropwise' shape. The deposited carbon was graphitic with layers which were approximately concentric on the filament axis. Regions with a pronounced disordering of graphite layers were also present. Like Boellard et al [58], Zaikovskii et al attributed the observed morphology and ordering of graphite layers to carbon emerging perpendicular to the metal surface and slippage of carbon layers.

Boellard et al [58] described a distinction between different types of filamentous carbon formed on supported Ni catalysts. According to them, primary filamentous carbon can be characterised by a filament diameter equal to that of the metal particle at the tip. These may possess a narrow electron-transparent canal, as shown in Fig.1.11(a), or a wider canal which effectively makes them a tube (Fig.1.11(b)). Pyrolytic filamentous carbon however, formed by thermal cracking of hydrocarbons at temperatures above

870 K, is recognised by diameters greatly exceeding the diameter of the original metal particle (Fig.1.11(c)). The particle of the original primary filament is trapped within the pyrolytic carbon.

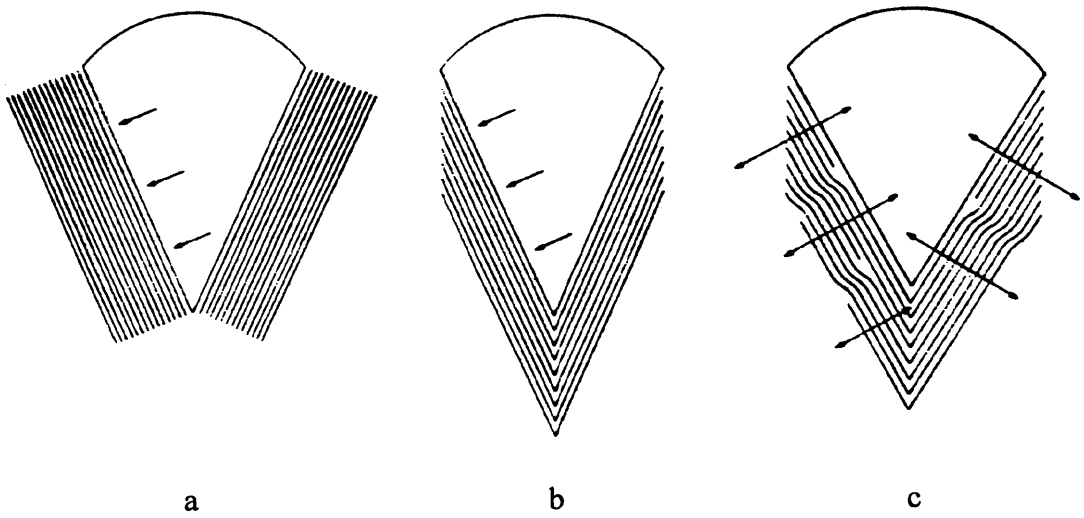


Fig.1.10 Cross section of conical graphite layers excreted in a direction perpendicular to the metal carbon interface (a) without slippage of the graphitic cones; (b) with slippage of the graphitic cones over one another; (c) with slippage of the graphitic cones over one another and with carbon excretion rates not uniform over the metal-carbon interface, introducing edge dislocations [58]

Tracz et al [60] used HREM to study the structure of carbon filaments deposited on $Ni/Al_2O_3$ and Ni/MgO catalysts during the steam reforming of n-butane in the temperature range 673–953 K. Three types of deposit were found on both catalysts. These were described as 'true' filaments (filaments possessing no hollow channel), tubes and shells. All three are shown in Figs.1.12(a)-(c). It was found that the forms created and their degree of graphitisation depended on the reaction temperature. At a temperature < 773 K for Ni/MgO and < 873 K for $Ni/Al_2O_3$, true filaments were

generated (Fig.1.12(a)). These filaments often had carbon layers aligned perfectly to the shape of the nickel particles.

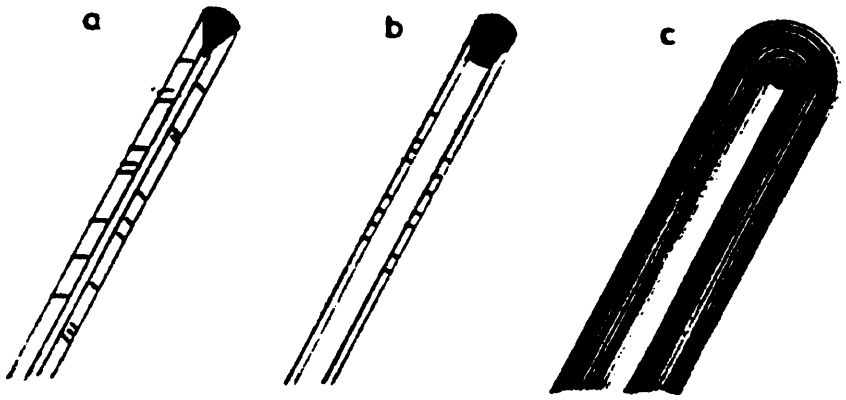


Fig.1.11 Different types of filamentous carbon: (a) primary carbon filament with a metal particle at the tip and a narrow electron-transparent canal; (b) primary carbon filament with a metal particle at the tip and a wide canal (tube); (c) pyrolytic filamentous carbon, where the metal particle of the original primary filament is trapped within the pyrolytic carbon [58]

At the lowest reaction temperature (673 K) the first indications of carbon layer stacking appeared perpendicular to the filament axis. At higher temperatures (≥ 873 K for Ni/MgO and 953 K for $Ni/Al_2O_3$) tubes with carbon layers nearly parallel to the tube axis and closed shells were created (Fig.1.12(b)). Comparison of the filament structures obtained at different temperatures indicated a continuous increase in graphitisation and a transitory stage between the true filament and the tube (Fig.1.12(c)). Here the filaments showed a widened core where only a part of the carbon layers crossed the tube. Shells were formed mainly on the Ni/MgO catalyst at

high temperature and showed a high degree of graphitisation. These shells were found to have a deactivating character.


Fig.1.12(a) Structure of a full (true) carbon filament formed on $Ni/Al_2O_3$ at 873 K [60]


Fig.1.12 (b) Typical structure of a carbon tube obtained on Ni/MgO at 873 K [60]

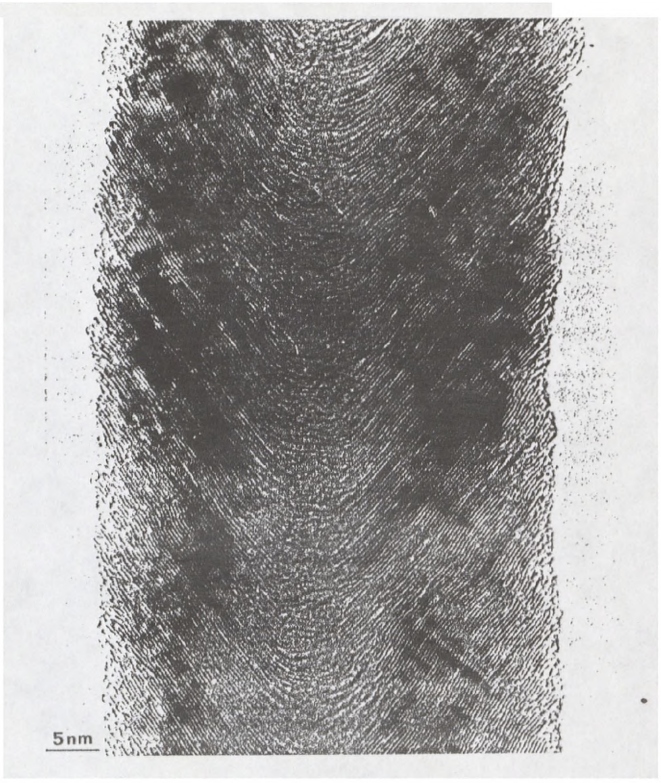


Fig.1.12 (c) Carbon filament formed on Ni/MgO at 823 K. The structure is an intermediate state between a true filament and a tube [60].

Baker et al [61] used TEM to examine carbon filaments formed on a range of iron/nickel catalyst powders. Carbon was deposited from the decomposition of CO ($CO/H_2$ mixture 4:1) at 873 K. It was found that the carbon structure of the filamentous carbon was dependent on the initial catalyst powder. Filaments formed on pure iron powder possessed a well defined and ordered 'platelet' structure, where the graphite layers were stacked on top of each other in a perpendicular direction with respect to the fiber axis, reminiscent of a 'deck of cards' (Fig.1.13(a)). Addition of 10% nickel to the iron, however, introduced a subtle change in the characteristics of the carbon filaments. They still possessed the well ordered crystalline form as previously, but growth now tended to occur by a bidirectional process with the metal particle entrenched within the filament. The filament now acquired a 'herring-bone' structure, shown schematically in Fig.1.13(b)., where the graphite platelets were aligned at an angle to the fiber axis.

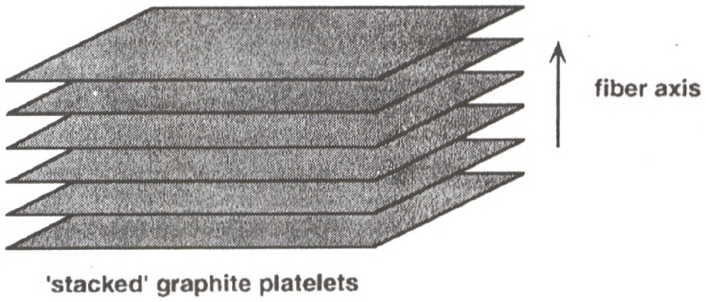


Fig.1.13 (a) Schematic representation of the graphite platelet stacking arrangement in a carbon filament

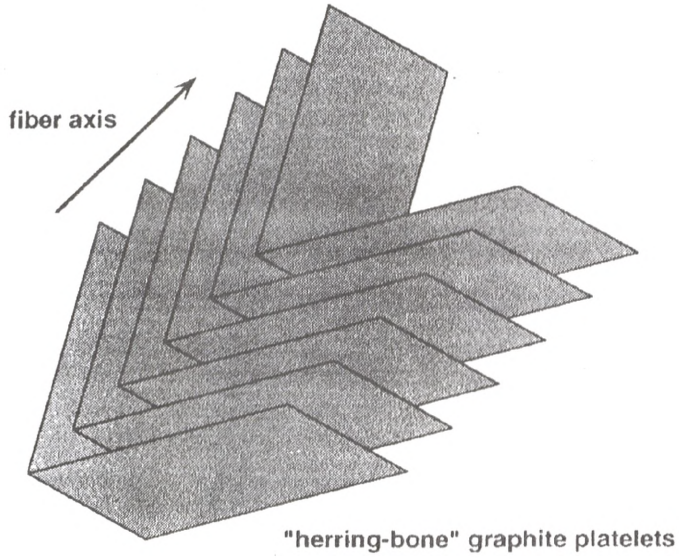


Fig.1.13 (b) Schematic representation of the 'herring-bone' graphite platelet stacking arrangement in a carbon filament

The most outstanding modification in the carbon filament characteristics was observed from a comparison of filaments grown on Fe-Ni (30:70) and Fe-Ni (25:75) powders under the same conditions. By merely adding an extra 5% Ni to the catalyst, the structural conformation of the filaments tended to change from one where the graphite platelets were oriented in a 'herring-bone' arrangement to one where the platelets were aligned parallel to the fibre axis and the filaments taking the form of 'tubules' (Fig.1.13(c)). As the nickel content was increased further, then the tubular conformation became the exclusive filament growth form.

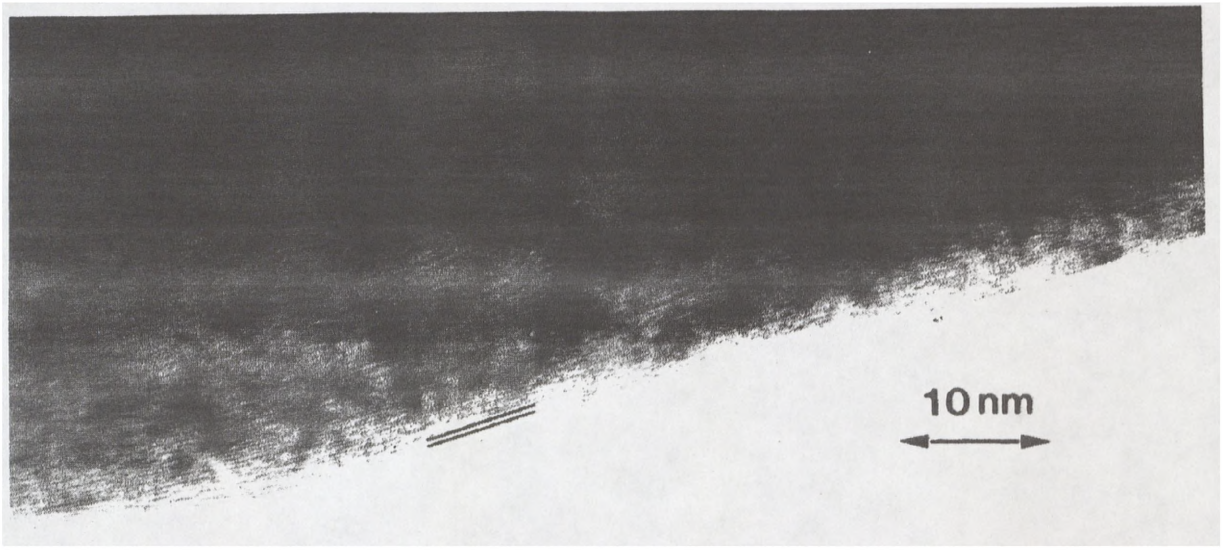


Fig.1.13 (c) High resolution electron micrograph showing the appearence of graphite platelets aligned in a direction parallel to the fiber axis giving rise to a filament 'tubule' [61]

### 1.10.5 Nucleation of carbon filaments

There is general agreement that the nucleation of filamentous carbon requires a supersaturation of carbon in nickel. However, it is still unclear how such supersaturation occurs. Rostrup-Nielsen et al [51] suggested that precipitation of carbon and filament growth is initiated at screw dislocations at the rear of the particle, due to a supersaturated solution of carbon in nickel.

Other authors [57] [62] [63] have reported that the initiation period involves the formation of carbide intermediates, the decomposition of which leads to filament formation. Indeed De Bokx et al [57] claimed that the ability of a metal to form carbides was a requirement for the formation of filaments. They suggested that metals which have a low affinity for carbide formation, such as Ru, be used to suppress filament formation. This was however challenged by Baker et al [64] who studied carbon formation on supported Ru catalysts. They found that even though Ru does not form bulk carbides under normal reaction conditions, it was a very active catalyst for filament formation.

Kock et al [65] carried out in-situ magnetisation measurements to monitor the carbidic content during the early stages of filament growth. Caburisation was carried out with methane in the temperature range 573-613 K. They proposed that an observed decrease in magnetisation was due to the formation of a bulk carbide prior to nucleation of filamentous carbon. The increase in magnetisation which followed indicated that after nucleation, the carbon content was significantly lower than in the early stages of carburisation. Kock et al concluded that the initiation period was the time required for the formation of a carbide phase of high nickel content, the incubation time associated with the decomposition of this phase and the nucleation of the filaments. Nucleation occurs via precipitation of graphite layers near the support-metal interface causing the metal particle to lift from the support.

The results of various surface spectroscopic investigations have provided further information about the initiation of filament growth.

Blakely et al [66] studied the segregation and precipitation of carbon on a number of nickel single crystal surfaces. They observed that on Ni(110), (311) and (111) faces a condensed carbon monolayer was formed upon cooling of a carbon doped crystal. This occurred at a temperature up to 373 K higher than the precipitation temperature. The monolayer was found to be stable upon further cooling until the saturation temperature was reached. Multilayer graphite precipitated and was accompanied by the

reconstruction of the Ni surfaces to mainly (111) and (311) faces, providing epitaxial fits with the graphite phase.

Based on the observations of Blakely et al [66], Alstrup [67] proposed that during the induction period, the Ni particles become supersaturated with carbon. When the supersaturation reaches the (111) facets at the support-metal interface, a considerable reconstruction is triggered strongly extending the (111) facets. At the same time graphite layers segregate out forming the carbon filament in the subsequent steady-state period (Fig.1.14).

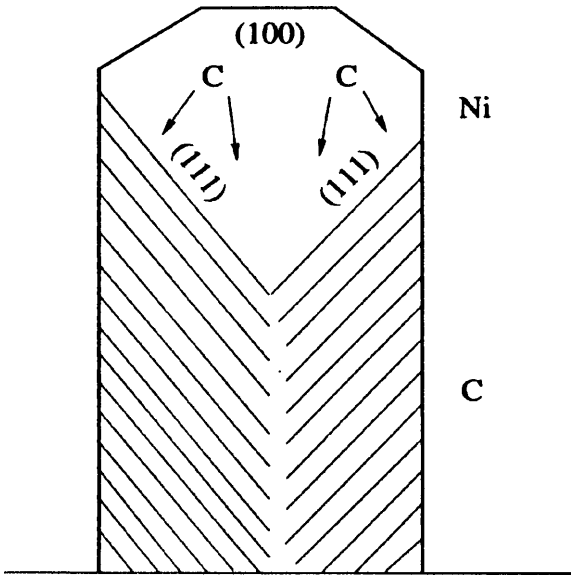


Fig.1.14 Schematic representation of filamentous carbon growth showing the facets of the nickel crystallite (arrow points to the direction of filament growth)

Yang et al [68] also studied the segregation process during the growth of carbon filaments. They used Selected Area Electron Diffraction (SAED) to identify the crystallographic faces at the metal-graphite and metal-gas interfaces. The (111) and (311) faces were mainly observed at the metal-carbon interface while (100) and (110) faces were most abundant at the metal-gas interface. Extended Hückel Molecular

Orbital (EHMO) calculations indicated that the Ni (111) and (311) faces, most abundant at the metal-carbon interface, provided the strongest epitaxial covalent bonds with the basal plane of graphite. The Ni(100) and (110) faces, most abundant at the metal-gas interface, were the most active for hydrocarbon decomposition.

Based on their findings, Yang et al [68] proposed the following mechanism for carbon filament formation. Carbon forms on the (100) and (110) faces of nickel, most abundant at the metal-gas interface, and diffuses in the bulk to the rear of the particle. A surface reconstruction then occurs upon graphite precipitation at the Ni(111) faces at the rear of the particle. The final step is then steady-state filament growth involving hydrocarbon decomposition at the metal-gas interface and precipitation at the metal-carbon interface.

### 1.10.6 Nature of the driving force for carbon diffusion

The general consensus is that the reaction mechanism of carbon filament growth involves bulk diffusion of carbon through the metal particle. However there is still debate as to the nature of the driving force for this diffusion.

Baker et al [49] suggested that the exothermic surface reaction (decomposition of acetylene) resulted in a temperature gradient across the metal particle working as a driving force for filament growth. Carbon diffuses along the thermal gradient to the cold rear of the particle where the solubility is smaller. This model however has been questioned, since the decomposition of some of the carbon forming gases (butylene, methane) is endothermic [51]. Moreover, calculations by Holstein [69] indicated the absence of any significant temperature difference (<0.1 K) between a metal particle and its support as a result of catalytic reaction on the metal.

Alternative explanations as to the driving force for bulk carbon diffusion suggested the existence of a concentration gradient across the metal particle. Rostrup-Nielsen et al [51] proposed that carbon species of different origin have different solubility. Therefore carbon species at the metal/gas interface originating from hydrocarbon

decomposition reactions have a higher solubility than carbon originating from graphite. Thus the resulting force for diffusion was believed to be a carbon concentration gradient arising from a difference in carbon activities. This is illustrated in Fig.1.15.

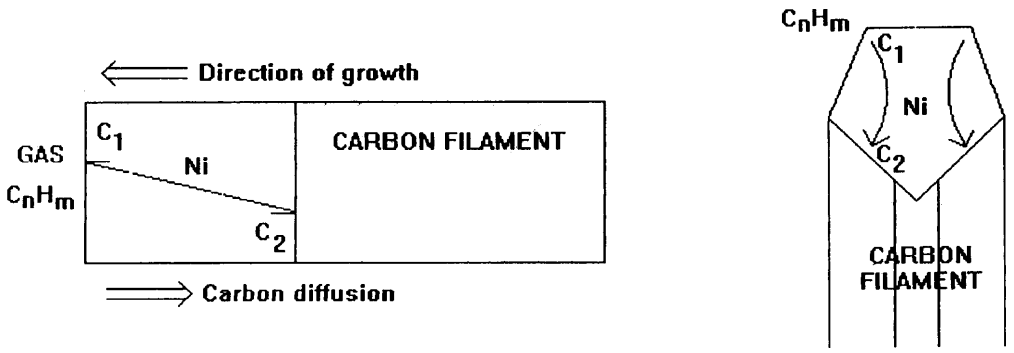


Fig.1.15. Model representing carbon transport through the nickel particle [51]

Schouten et al [70] studied the diffusion of carbon (deposited by methane cracking) through Ni (110) and (100) surfaces. They found that this diffusion could be quantitatively described by assuming a constant planar source below the surface, maintained by a much faster diffusion through the crystal selvedge in which the carbon concentration strongly exceeds the equilibrium solubility of carbon in bulk nickel. This selvedge with high carbon content is referred to as a 'surface carbide'.

Based on the findings of Schouten et al [70], Alstrup [67] proposed a new model explaining carbon filament growth on Ni, Fe and Ni-Cu alloy catalysts. According to Alstrup, the carbon atoms entering the selvedge create an unstable 'surface carbide' which subsequently decomposes into filamentous carbon or metal. However, he suggested the surface carbide is still present after the decomposition and carbon atoms produced by the surface reaction diffuse rapidly through during the steady-state growth period, maintaining a constant carbon concentration just below the selvedge. A

concentration gradient is thus maintained causing diffusion of carbon atoms to the rear end of the particle where they segregate on the filament/particle interface.

Kock et al [65] and De Bokx et al [57] identified the presence of metastable carbides during filament formation using TPH and TMA. They assigned one peak in the TPH spectrum, with a peak temperature of 400 K and a carbon content of 1.5-6 at%, to a substoichiometric bulk nickel carbide. This was supported by measurements of the saturation magnetisation before and after carburisation and quenching at room temperature. They concluded that a substoichiometric bulk carbide was present under steady state conditions and that carbon filaments grew by continuous decomposition of this metastable carbide intermediate. According to Kock et al [65] the driving force for bulk carbon diffusion is the gradient in carbon content of substoichiometric carbides, whereby the carbon content decreases in the direction of the metal/carbon interface, causing the transport of carbon atoms.

### 1.10.7 Gasification of filamentous carbon

Baker et al [49] carried out the oxidation of carbon filaments, formed on nickel catalysts from acetylene, at different temperatures. They found that at 970 K the central core of the filaments was oxidised first, leaving a more dense and relatively oxidation resistant tube. At 1100 K the outer tube or 'skin' of the filaments was also oxidised together with the encapsulating carbon surrounding deactivated nickel particles. If acetylene was reintroduced, filaments continued to grow even on previously deactivated nickel particles.

Figueiredo et al [50] used a microbalance unit to study the gasification of carbon filaments with $H_2$ and $H_2O$ in the temperature range 820-1020 K. The rate of gasification was measured on both nickel foils and supported nickel catalysts. In both cases gasification proceeded at constant rates up to about 60-70% burn off. It was found that with nickel foils the gasification rates were almost proportional to the amount of carbon originally present, whereas for supported nickel catalysts the rates of gasification were independent of the amount of carbon present. Chemical analysis of

the carbon deposits for nickel revealed that on nickel foils the amount of nickel present in the carbon was nearly proportional to the weight of carbon deposited. This was ascribed to the fact that the foil is effectively an 'infinite' source of nickel and that new filaments are continuously formed with time with nickel particles spread throughout the carbon. Conversely, on supported nickel catalysts, the amount of nickel present in carbon deposits was found to be independent of the weight of carbon. It was calculated that 50-60% of the nickel originally present in the catalyst was contained in the deposit. Figueiredo et al also found that the gasification by steam was zero order and concluded that the rate determining step was the diffusion of carbon through the nickel. By plotting the rate of gasification versus $^{1}/_{T}$, an activation energy of 33 kcal $mol^{-1}$ was determined which corresponded well with the activation energy observed for the diffusion of carbon through nickel (vide infra - Chapter 4). Gasification with $H_2$ was found to be considerably slower than with steam and the reaction was found to be second order in $H_2$. It was concluded that the rate of reaction on the surface was rate determining with $H_2$.

Figueiredo et al [71] also studied the gasification of filamentous carbon by $H_2$ and $H_2O$ using Controlled Atmosphere Electron Microscopy (CAEM). Continuous observation of filaments gasified by $H_2$ at around 970 K revealed that the nickel particle retraced its original path, removing the core component and leaving the outer, more structurally ordered skin. When acetylene was reintroduced after gasification at 970 K, the direction of the nickel particles was reversed and the inner core region once again proceeded to be filled with deposited carbon. It was not possible to determine whether there was any appreciable thickening of the filament skin during this second deposition cycle. Fig.1.16. schematically illustrates this reversible gasification of carbon filaments.

A different behaviour was observed when filaments were gasified with $H_2O$. In this case the reaction started at 900 K and was characterised by attack along the sides of the filament at particular regions where small particles were located, probably left as fragments during the growth process. No evidence was found under these conditions

for the nickel particles located at the tips of the filaments to exhibit the type of reversal behaviour observed in the presence of hydrogen.

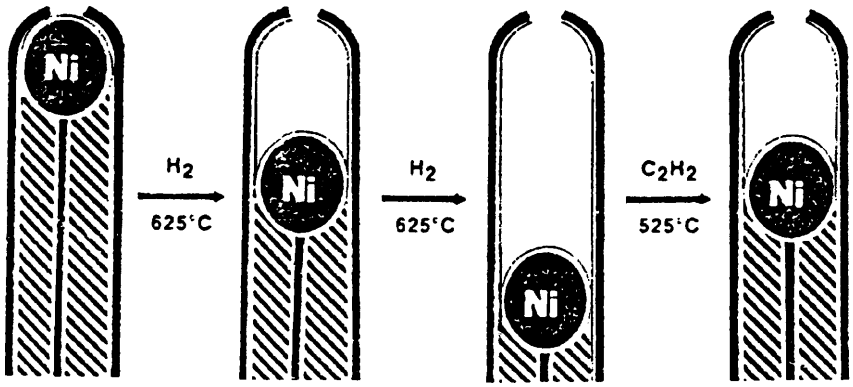


Fig.1.16. The reversible gasification and growth of carbon filaments

Based on CAEM observations and from kinetic studies of filament gasification, a mechanism for carbon filament gasification was proposed [71] [72]. The mechanism is essentially the reverse of that for filament formation. The preliminary step is the dissociative adsorption of the reacting gas at the exposed face of the nickel particles. This is followed by a surface reaction between the adsorbed gaseous species and the adsorbed carbon species. Carbon atoms are supplied to the exposed surface by dissolution of carbon from the filament core at the rear of the particle and diffusion through the metal particle to the front of it. As a result the direction of the movement of the metal particle is reversed as the core of the filament is gradually removed. Diffusion of carbon through the metal particle is a common step in both filament formation and gasification. However the concentration gradient in the metal particle is reversed.

### 1.10.8 Surface carbon and its characterisation by Temperature-Programmed Surface Reaction (TPSR)

The surface reactions of hydrocarbons or carbon monoxide which take place at the front of the nickel particle ie. metal/gas interface, initially lead to the formation of surface carbon. These isolated surface carbon atoms formed then either dissolve into the nickel, are gasified or combine on the surface to form encapsulating carbon. Carbon atoms which dissolve in the nickel diffuse to the back of the particle and ultimately the formation of a carbon filament takes place.

Temperature Programmed Surface Reaction (TPSR) has proved a very useful technique for the characterisation of surface carbon, providing useful information about the morphology of deposited carbon and its chemical nature ie. surface carbide, filaments etc. TPSR also indicates how reactive deposited carbon is towards gasification by gases such as $O_2$, $H_2$ and $H_2O$.

McCarty et al [73] carried out a comprehensive study of the nature of carbon deposits formed on a $Ni/Al_2O_3$ catalyst using TPSR. The catalyst was exposed to ethylene at varying temperatures ($T_d$) and the different types of carbon formed were characterised by their reactivity with $H_2$, together with electron microscopy and X-ray diffraction measurements. Different states of carbon were identified by maxima present in a plot of $CH_4$ production rate versus temperature (Fig.1.17). The temperature of the rate maxima ($T_p$) were characteristic of the reactive state of carbon in a deposit. Depending primarily on the temperature during deposition, $T_d$, McCarty et al identified seven reactive carbon states during the TPSR.

Exposure of the catalyst to ethylene at low temperature (573K) produced several very reactive states of carbon. A small amount of the carbon deposit, with less than 1 monolayer coverage, was named the $\alpha$'-state and had a peak temperature $T_p$ of 400 K. A larger peak at 495 K represented the $\alpha$-carbon state, populated up to about one monolayer below 600 K. These $\alpha$' and $\alpha$ states of carbon were identified as individual carbon atoms probably chemisorbed on two different sites ie. a terrace and ledge or step site. These states have metal-carbon bonds rather than carbon-carbon bonds.

At very high $C_2H_4$ exposure the γ-carbon state was formed ($T_p$ = 500 K) which obscured the α' and α peaks. This γ-state could be populated to an extent equivalent to 10 monolayers and was attributed to bulk nickel carbide. Since $Ni_3C$ is known to decompose above 600 K [56], it was not surprising that this state was not observed at 773 K. Another form of carbon, the β-carbon state, was also observed following $C_2H_4$ exposure at low temperature. The β-state had a $T_p$ which increased from 660 K at low coverage to 740 K at high coverage and the amount of carbon deposited was observed not to exceed 4 monolayers. Although not conclusively identified, the β-state was attributed to an amorphous carbon film or a polymeric hydrocarbon surface film.

A number of less reactive forms of carbon were produced following exposure of the catalyst to $C_2H_4$ at 773 – 1273 K. Two bulk forms of carbon, the δ' and δ-states, were produced with peak temperatures $T_p$ of 875 K and 960 K respectively. At a deposition temperature of 773 K only the δ'-state was observed. However, at higher deposition temperatures the presence of the δ-state was more prominent and at $T_d$ = 1073 K the δ'-state was not observed at all – only the δ-state was present. Electron microscopy studies identified the δ' and δ-states with filamentous carbon. At a deposition temperature of 1073 K many metal particles appeared to be completely encapsulated by carbon films. McCarty et al therefore postulated that the δ'-carbon state was the soft, more reactive carbon which occupies the core of filaments, whereas the δ-state was the harder outer shell of the filaments and also possibly the encapsulating carbon often observed surrounding nickel particles during high temperature exposure to hydrocarbons. These findings mirror those of Tracz et al [60] who studied the morphology of filaments formed on Ni catalysts at various temperatures and observed that at low temperature, full filaments were formed whereas at high temperatures, tubes and shells were formed.

At deposition temperatures greater than 873 K, McCarty et al [73] observed that yet another form of carbon was produced, the ε-carbon state, which possessed a very low characteristic reactivity with hydrogen ($T_p$=1120 K). This ε-state, amounting to several monolayers carbon, was believed to represent a film of 'platelet' carbon, a highly graphitised form of carbon often observed following precipitation from carbon

dissolved in large specimens of metallic nickel. This identification, however, was not conclusive.

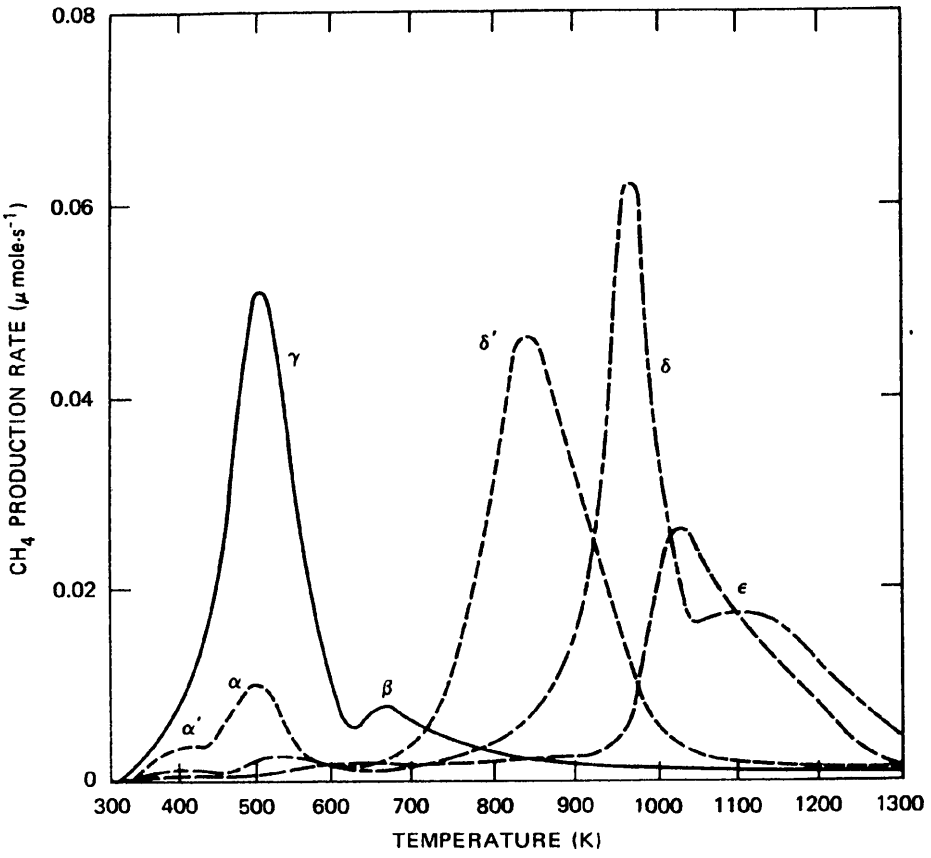


Fig.1.17 Hydrogen TPSR of carbon deposited on a $Ni/Al_2O_3$ catalyst by exposure to ethylene. Key to deposition temperature: ——, 573K; – – –, 773K; ——1073K; ———,1273K [73]

De Bokx et al [57] also performed TPSR experiments on carbon deposited on a $Ni/SiO_2$ catalyst by exposure to $CH_4$ at 750 K. Temperature Programmed Hydrogenation (TPH) of the carburised catalyst revealed the presence of different types of carbon species. As in the experiments of McCarty et al [73] the different carbon states were identified by peak maxima ($T_p$) in the rate of $CH_4$ production. At 400 K a small peak was observed which De Bokx et al attributed to an intermediate $Ni_3C$ phase, corresponding to the γ-carbon state described by McCarty et al. A high temperature peak at $T_p$ 825 K, which

increased with increasing carburisation time, was attributed to filamentous carbon and was identified as such by electron microscopy. This peak corresponded to the δ-state in McCarty's experiment. A small shoulder on the low-temperature side of the filamentous carbon peak was attributed, somewhat uncertainly, to amorphous carbon - β-carbon according to McCarty. De Bokx et al [57] explained the fact that the peak temperatures observed during their TPH experiments were significantly lower than the temperatures of similarly labelled peaks reported by McCarty et al was due to the low heating rate they used (11 mK $s^{-1}$) compared to 1 K $s^{-1}$ used by McCarty et al.

In a recent study Efstathiou et al [74] characterised the carbonaceous species formed during the reforming of $CH_4$ with $CO_2$ at 1023 K over Ni/CaO-$Al_2O_3$ catalysts. The amounts and kinds of carbonaceous deposits formed were determined using Temperature Programmed Oxidation (TPO). Two kinds of carbon species (free of chemically bound hydrogen) were mainly found to accumulate on the catalyst surface, differing in their structure and reactivity towards oxidation. It was found that both the amount and reactivity of the deposited carbon was strongly dependent on the support composition. The $CaO/Al_2O_3$ ratio was believed to influence the the nickel particle morphology and its size distribution which in turn controlled the origin, kinetics and reactivity of carbon deposition under reforming reaction conditions. $CaO/Al_2O_3$ ratios of 1/2 and 12/7 were used and in both cases the carbon species formed after 5 mins of the reforming reaction gave rise to a high temperature $CO_2$ peak on oxidation (973 K for $CaO/Al_2O_3$ ratio 1/2; 1008 K for $CaO/Al_2O_3$ ratio 12/7). This first type of carbon was suggested to be of an amorphous and/or graphitic form. A lower temperature $CO_2$ peak was also observed on oxidation (883 K for $CaO/Al_2O_3$ ratio 1/2; 873 K for $CaO/Al_2O_3$ ratio 12/7) and this carbon oxidised at lower temperatures was proposed to be filamentous in nature.

## 1.11 Promotion of catalysts to suppress carbon formation

### 1.11.1 Introduction

Earlier in Section 1.6 it was shown that thermodynamically, a steam to carbon ratio of 1:1 is all that is needed for the reforming reaction to proceed. In practice however, higher ratios than these are used in order to suppress the formation of carbon; ~1.7:1 for methane reforming and ~3.5:1 for naphtha reforming. Of course the lowest possible steam to carbon ratio (called the 'critical ratio') is desirable in economic terms but unfortunately this increases the possibility of carbon formation on the catalyst. As a result it was discovered that the introduction of specific promoters into the catalyst formulation was a convenient method of increasing the catalyst's resistivity to carbon formation, whilst still maintaining sufficiently low steam to carbon ratios.

### 1.11.2 Alkali promotion

The effect of alkali upon heterogeneous catalysts was first described more than 100 years ago. In 1845 Döbereiner [75] discovered that the 'effectiveness of platinum sponge is increased to such an extent when it is moistened with caustic soda or caustic potash that – like platinum black – it acts upon alcohol and wood spirit even at room temperature. In the case of platinum black the increase is so great that one can decompose any fermentable sugar with it to carbon dioxide and water.

In many industrial processes today, the addition of small amounts of alkali ions to supported metal catalysts can increase their activity or selectivity and can also prolong the effective lifetime of the catalyst. The positive effect of alkali doping has long been known for such reactions as ammonia synthesis, the Fischer-Tropsch synthesis, the oxidation of sulphur dioxide to sulphur trioxide and the production of ethylene oxide. Steam reforming catalysts benefit greatly from promotion with alkali since it suppresses the formation of carbon.

In steam reforming the most difficult feed from the carbon formation viewpoint are naphthas, as illustrated in Fig.1.7. In 1954 however, ICI [20] discovered that the introduction of alkali to nickel catalysts allowed continuous and economic reformer operation. Today this is still the most common method emplyed to prevent the formation of carbon.

In general the alkali is incorporated by mixing with the catalyst, usually by the addition of a suitable alkali metal salt-solution, eg. KOH. The alkali can also be present as an alkaline support, eg. $CaAl_2O_4$.

### 1.11.3 The function of the alkali

The presence of alkali in the catalyst formulation is believed to play several roles:

i) Let us firstly consider the acidity in the support and the effect it has on the formation of carbon. α-alumina, for example, is acidic in nature. It is dehydrated during preparation as follows:

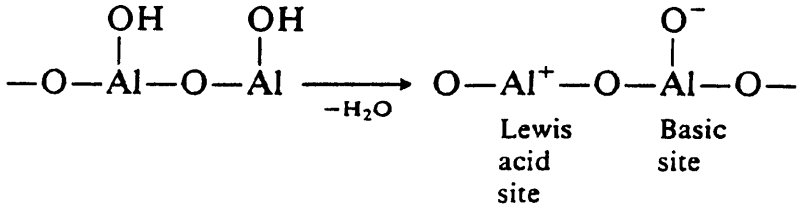


There is, however, always sufficient adsorbed water present on the catalyst surface to give

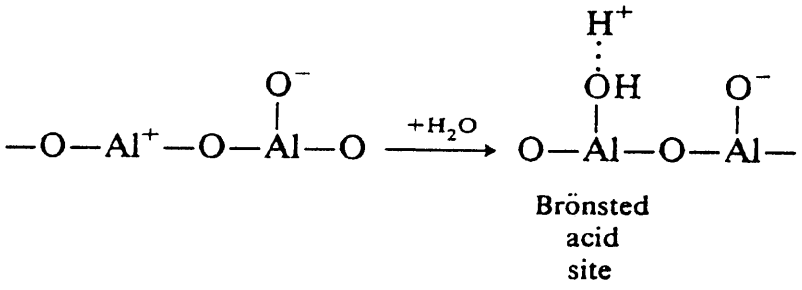

The acid sites on the catalyst support promote undesirable side reactions, such as cracking and polymerisation (see Fig.1.7) which lead to the formation of carbon. Doping with alkali neutralises support acidity, thereby retarding cracking and polymerisation and reducing the rate of carbon formation.

ii) Secondly, the alkali functions by increasing the rate of the steam gasification of carbon:

$$C + H_2O = CO + H_2 \qquad (1.17)$$

This ability of the alkali was reported as early as 1921 by Taylor and Neville [76]. It is believed that the alkali increases the amount of water adsorbed onto the catalyst surface and thereby ensures that the rate of carbon removal by (1.17) is higher than the rate of carbon formation. A more in-depth study of the function of alkali is presented in the following section.

### 1.11.4 Function of the alkali - a detailed study

Rostrup-Nielsen [77] observed that the addtion of potassium to nickel catalysts affected their activity for methane and ethane steam reforming, without affecting the apparent activation energy. He concluded that the effect of alkali was not an electronic one, but that the alkali doping influenced the number of sites available for the reforming reactions. Based on simple power law expressions, Rostrup Nielsen concluded that alkali enhances steam adsorption, mainly on the carrier material. This explained the decrease in the rate of carbon formation when alkali was present.

Hadden et al [78] investigated the effect of adding a potassium promoter to a $NiO/\alpha Al_2O_3$ steam reforming catalyst, in an attempt to describe a mechanism by which alkali provides resistance to carbon formation on nickel. Potassium was added by post-impregnation of the catalyst with a solution of potassium hydroxide. It was observed

that the presence of alkali reduced the rate of hydrocarbon cracking on the nickel component of the catalyst. They also observed a strengthening in $H_2O$ adsorption on both the nickel component and the alumina support, due to the formation of water clusters around adsorbed alkali species. In addition, the amount of water adsorbed on the alkalised catalyst was some 5 times larger than on an unpromoted catalyst. Hadden et al found that the rate of steam gasification of filamentous carbon was increased on the alkalised catalyst. This was attributed to the large number of water adsorption sites created by the presence of potassium which increased the surface coverage of molecular water on the nickel component of the catalyst and led to an increase in the pre-exponential factor in the gasification rate equation.

Chai and Falconer [79] investigated the effect of potassium promotion for CO hydrogenation on supported nickel catalysts. The influence of the support ($SiO_2$, $SiO_2.Al_2O_3$), the promoter (0.05-4% K), the alkali salt (KCl, $K_2CO_3$, $K_2C_2O_4$, KOH, $KNO_3$) and the method of preparation (pre-, co- and post-impregnation) were studied. The catalyst support and the promoter concentration were found to be the major factors influencing the activity and selectivity of alkali promoted catalysts. The method of preparation and the potassium salt made little difference for the same promoter loading. $H_2$ chemisorption revealed that with low potassium content (0.25%) a maximum percentage of nickel was exposed, which decreased sharply with higher potassium loadings for both supports.

Campbell et al [80] reported similar findings and concluded that much of the potassium is located on the support. Only at high potassium loadings was a significant portion of the nickel surface covered by the alkali. Campbell et al also proposed that the support influences the effect of potassium promotion because of the preferential reaction of potassium with acidic sites on the support, with most of the potassium located on the support at low loadings. They concluded that the acidity of the support appears to influence the coverage of alkali on the metal surface.

Demicheli et al [81] studied the influence of potassium on the hydrogenolysis of cyclopentane and the simultaneous carbon formation over a series of nickel/alumina

catalysts. They found that with increasing potassium loadings at temperatures where either a deactivating two-dimensional carbon or a filamentary carbon was formed (693-733 K), the catalytic activity passed through a maximum and then decreased. In the presence of steam, at relatively high K doses, the growth of filamentous carbon was largely reduced. Characterisation of the carbided catalyst by TPO and SEM disclosed quite different roles of the alkali. At lower contents, associated with alumina, potassium facilitated the formation of filamentous carbon and minimised the generation of carbon precursors. It was suggested that the potassium ions modify the metal-support interaction, reducing the adhesion strength between the nickel particles and the alumina matrix and therefore activating the formation of carbon filaments from these particles. The potassium, being a basic agent, also neutralises the acidic sites of alumina necessary for the generation of carbon precursors. At high K/Ni ratios the potassium acted as an inhibitor for both hydrogenolysis and carbon forming reactions, due to potassium adatoms blocking specific nickel ensembles for these reactions. It was found in all cases that the alkali promoted the catalytic oxidation of the carbon deposits and this was related to the specific localisation of the alkali between the nickel particle and the carbon tube of the filament.

It has also been reported that alkali atoms modify the electronic properties of the metal phase, as concluded from various studies on CO adsorption, CO disproportionation and CO hydrogenation reactions.

Kiskinova et al [82] and Campbell et al [83] both observed that the addition of alkali reinforced the metal-CO bond and weakened the C-O bond strength, evident from the increase in rate of CO disproportionation. The weakening of the C-O bond strength was confirmed by the decrease of the stretching frequency of CO adsorbed on Ni from 2060-1935$cm^{-1}$ to 1700$cm^{-1}$ on addition of potassium.

Luftman et al [84] explained these effects by the electropositive nature of the alkali atoms which donate a large fraction of their valence electrons to the metal. The bonding of CO on transition metals is believed to take place by an electron donation

from the CO 5σ molecular orbital into the partially unoccupied d orbitals of the metal and a concurrent back donation from the d orbitals into the CO antibonding 2π* orbital. The additional electron density on the transition metal surface results in an enhancement of the back donation from the d orbitals of the transition metal into the CO antibonding 2π* orbital, resulting in an increased metal-CO bond strength and a decrease in C-O bond strength.

Several authors have reported that the addition of potassium to nickel catalysts strongly affects their activity and selectivity towards the CO-hydrogenation reaction and that the effect is dependent on the type of support used [79] [80] [85]. The addition of alkali resulted in a decrease of the total activity of the catalyst (mainly on a $SiO_2$ support) and an increase in the selectivity to higher hydrocarbons and olefins. Campbell et al [82] also observed using Auger Electron Spectroscopy (AES) that the addition of alkali resulted in a marked increase of the steady-state level of carbidic carbon, probably by increasing the rate of CO dissociation. The increased carbide coverage results in an increase in the supply of reactants for chain growth, explaining the increase of the selectivity towards higher hydrocarbons upon alkali addition.

Campbell et al [83] suggested that the similar effect of alkali on Ni single crystals and supported Ni indicates that the mechanism by which potassium additives alter the catalysts' activity and selectivity is not related to the support material but is a consequence of direct K-Ni interactions. Bailey et al [85] however concluded that the effect of potassium depends on the $K/(Ni+Al_2O_3)$ ratio rather than on the K/Ni ratio.

### 1.11.5 Industrial potassium promoted catalysts

During the development of their naphtha reforming catalysts, ICI found that the most effective alkali was potash ($K_2O$) and most reformers today running on naphtha feedstocks use this alkalised catalyst system. The presence of potash is the basis of ICI's naphtha reforming catalysts known as series 46-1 [19].

The potassium is effective by being mobile on the catalyst surface. Accurate formulation combines the potash with the support to form a complex potassium alumina-silicate called kalsilite ($K_2O.Al_2O_3.SiO_2$). The complex structure of the support is involved in the mechanism which releases alkali to control carbon removal, shown schematically in Fig.1.18. As kalsilite decomposes, other compounds such as gehlenite and monticellite are formed and potassium is liberated at a very slow rate as involatile $K_2CO_3$. The $K_2CO_3$ is hydrolysed as fast as it is formed producing KOH, which is very mobile on the catalyst surface and is the effective carbon-removing agent. Potassium is therefore lost from the catalyst into the product gases, but the rate of evolution is very slow, being kinetically controlled by its release from the kalsilite compounds. The higher the temperature and the higher the feedstock throughput, the more rapid is the potassium depletion. Careful formulation of the catalyst ensures that lives of several years are obtained in most reformers [20].

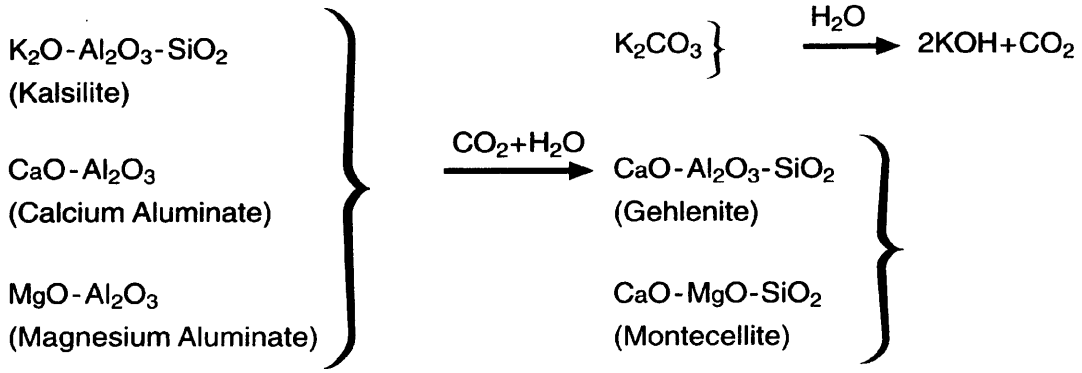


Fig.1.18 Scheme showing the hydrolysis of Kalsilite leading to the liberation of potassium

It should be noted however, that excessive quantities of alkali can also be counterproductive and more than cancel out the positive effect. It has been observed that higher concentrations of alkali in $Ni/Al_2O_3$ catalysts can accelerate the recrystallisation of the $Al_2O_3$ support and thereby reduce the effective lifetime of the catalyst in consequence of the decrease in the active surface area [86].

### 1.11.6 Prevention of carbon formation using MgO

The use of basic oxides such as MgO in place of acidic support oxides for catalysts has gained importance for reactions where acidity of the catalyst leads to undesired side reactions [87]. The presence of magnesium in nickel catalysts has been found to reduce the formation of carbon in hydrocarbon steam reforming reactions.

Borowiecki [88] reported that catalysts manifesting a high resistance to carbon formation were obtained by mixing coprecipitated mixtures of nickel and magnesium oxides of varied composition (called concentrates) with $\alpha$-$Al_2O_3$. He found that the amount of MgO incorporated in the catalysts ultimately influenced the size of the Ni crystallites and results obtained indicated that carbon formation was depressed when smaller nickel crystallites were used.

Rostrup-Nielsen [24] also reported that a common property of magnesia-supported nickel catalysts was the presence of a solid solution of nickel- and magnesium-oxide in the unreduced state. As the two oxides form ideal solid solutions, nickel is effectively distributed in the catalyst and the solid solution acts as a 'precursor' for the formation of small nickel crystallites by reduction of the catalyst. In addition he found that by supporting nickel on MgO, carbon deposition was delayed due to the enhancement of the adsorptive capacity of the catalyst to steam in the presence of the promoter.

In a paper describing preparative techniques of nickel catalysts, Choudhary et al [89] claimed the beneficial effect of precoating the $Al_2O_3$ support with MgO before depositing nickel oxide on the support. They found that because of the coating there was a very large increase in the methane-to-syngas conversion activity / selectivity of

the supported catalyst due to the elimination or drastic reduction in the formation of catalytically inactive $NiAl_2O_4$, resulting from the chemical interactions of NiO and $Al_2O_3$ at high temperatures. It is believed that the MgO forms a stable protective layer of $MgAl_2O_4$ between the support surface and the active nickel catalyst.

### 1.11.7 Industrial magnesia promoted catalysts

The use of magnesia as a promoter for industrial reforming catalysts is hardly as widespread as the use of potassium. This said, however, Haldor-Topsøe catalysts for industrial reforming are based on the presence of magnesia as a component in the catalyst formulation [90]. These catalysts are claimed to have various possible uses depending on formulation, ranging from town gas production at temperatures of 623-1023 K to hydrogen-rich synthesis gas production at 873-1273 K. The formulation of 2 Topsøe catalysts are shown in Table1.1. Both catalysts are prepared by coprecipitation and the patent claims that the material formed prior to the final calcination stage is a solid mixed phase of MgO and NiO together with a solid phase of alumina. During the calcination the alumina reacts at the grain boundaries with the MgO of the mixed phase to form $MgAl_2O_4$, which is evenly distributed through the bulk of the catalyst and so imparts exceptional mechanical strength. Catalyst R67 is used for reforming of natural gas and feedstocks where carbon deposition is minimal. For naphtha reforming, catalyst RKNR is used in which the excess of MgO acts as a promoter and, it is claimed, prohibits the formation of carbon deposits.

| CATALYST | NiO | $Al_2O_3$ | MgO |
|---|---|---|---|
| Topsøe R67 | 28 | 57 | 15 |
| Topsøe RKNR | 29 | 15 | 56 |

Table 1.1 Formulation of Topsøe reforming catalysts (wt% of components as oxides)

### 1.11.8 The use of rare-earths as promoters.

Recently there has been a growing interest concerning the promotion of nickel/alumina catalysts with rare-earth oxides, particularly $La_2O_3$, as a means of providing prolonged resistance to carbon formation. This is due mainly to the fact that, unlike alkali, $La_2O_3$ has been found to be effective without deactivating the catalyst [91]. Several authors have reported the ability of $La_2O_3$-promoted nickel catalysts to resist carbon deposition [91] [92] [93]. However, research regarding the definitive function of the $La_2O_3$ is still in its infancy and therefore the role of $La_2O_3$ in the prevention of carbon deposition has yet to be clearly defined.

There seems to be some concensus that, like alkali, $La_2O_3$ increases the amount of water adsorbed onto the catalyst surface and thereby accelerates the gasification of carbon with steam. Song et al [94] comparatively investigated the adsorption of steam on unpromoted nickel/alumina catalysts and ones promoted with $La_2O_3$ using Temperature Programmed Desorption. They found that the adsorptive capacity to steam on nickel catalysts promoted with >1.3 wt% rare-earth was substantially larger than on unpromoted catalyst, and as a result the gasification rate of surface carbon was enhanced.

Similarly Liu et al [95] studied what effect the addition of of $La_2O_3$ to nickel/alumina catalysts had on the properties of adsorbed water and the reaction of deposited carbon with steam. They found that the total amount of adsorbed water and the maximum reaction rate of deposited carbon with steam at 513 K were increased by 35% and 192% respectively on a $NiO\text{-}La_2O_3/Al_2O_3$ catalyst compared to the unpromoted material.

Tingrui et al [96] studied the effect of nickel crystal size distribution on the anticoking property of La-modified $Ni/\alpha\text{-}Al_2O_3$ catalysts. These consisted of a modified support - $\alpha\text{-}Al_2O_3$ impregnated with $La(NO_3)_3$ solution which was dried and calcined to $La_2O_3$. The crystal size distribution of unmodified and modified catalysts was determined by small angle x-ray scattering and the carbon-resistant behaviour of the catalysts was determined by the steam reforming of n-heptane. From their findings Tingrui et al concluded that in the steam reforming of hydrocarbons, the nickel crystal size

distribution of the $Ni/La_2O_3$-$Al_2O_3$ catalysts has a considerable effect on their resistance to carbon formation. Of the three crystal size fractions defined in the study, they found that the large size fraction plays the main role in controlling resistance to carbon formation. Reducing the large nickel crystallites into smaller ones by the appropriate addition of $La_2O_3$ was found to depress the rate of carbon formation by 78%.

As of yet, there is no $La_2O_3$-promoted nickel catalyst system in use for industrial reforming applications.

## References


[1] Davy, H., Phil. *Trans. Roy. Soc. London*, **107**, 77, 1817.

[2] Berzelius, J., Jahres - Bericht über die Fortschritte der Physichen Wissenschafen, Volume **15**, H. Laupp, Tübingen, 1836.

[3] Faraday, M., *Philos. Trans.*, **124**, 55, 1834.

[4] Somorjai, G.A., in 'Introduction to Surface Chemistry and Catalysis', John Wiley and Sons, Inc., 1994.

[5] Bond., G.C., in 'Heterogeneous Catalysis', Oxford Science Publications, 1990.

[6] Gilbert, L.W., *Ann. Phys. Gilbert*, **76**, 101, 1824.

[7] Marchand, R.F., *J. Prakt. Chem.*, **26**, 478, 1842.

[8] Tessie du Motay, M.M. and Maréchal, *Bull. Soc. Chim. France*, **9**, 334, 1868.

[9] DRP 51572, 1889 (Mond, L. And Langer, C.), *Chem. Zentralbl.* **II**, 32, 1890.

[10] Sabatier, P., La Catalyse en Chimie Organique, Librarie Polytéchnique, Paris, 1920.

[11] DRP 229406, 1909, (Dieffenbach, O. and Molderhauer, W.).

[12] DRP 296866, 1912, (BASF(Mittasch, A. and Schneider, C.)).

[13] Neumann, B. and Jacob, K., *Z. Elektrochem.*, **30**, 557, 1924.

[14] Brit. Pat. 267535, 1926 (I.G. Farben).

[15] Fischer, F. And Tropsch, H., *Brennst.-Chem.*, **9**, 39, 1928.

[16] U.S. Pat. 1934836, 1927, (I.G. Farben, (Wietzel, G., Haller, W.and Hennicke, W.)).

[17] Byrne, Jr. P.J., Gohr, R.J. and Haslam, R.T., *Ind. Eng. Chem.*, **24**, 1129, 1952.

[18] Gard, N.R., *Nitrogen*, **39**, 25, 1966.

[19] Barton, I.R. and Roberts, M.P., 'Shaped Reforming Catalysts', ICI Katalco Technical Papers, 292W/025/0/REF.

[20] Twigg, M.V., in 'Catalyst Handbook', (2nd ed.), Wolfe Publishing, London, 1989.

[21] Brit. Pat. 820527, 1958, (Gas Council, (Dent, F.J., Cockerham, R.G. and Percival, G.)).

[22] Cockerham, R.G. and Percival, G., *Trans. Inst. Gas. Eng.*, **107**, 390, 1956/57.

[23] Cockerham, R.G. , Percival, G. and Yarwood, T.A., *Inst. Gas. Eng. J.*, **5**, 109, 1965.

[24] Rostrup-Nielsen, J.R., in 'Steam Reforming Catalysts', Teknisk Forlag A/S, (Danish Technical Press Inc.), Copenhagen, 1975.

[25] Maisley, J., *Metals Bull.*, **49**, Dec. 1981.

[26] Chem. Eng., (New York), Apr.2, 24, 1993.

[27] Rostrup-Nielsen, J.R., *Catalysis Today*, **18**, 305, 1993.

[28] Fujimoto, H., *J. Soc. Chem. Ind. Jpn., Suppl.*, **36**, 147, 1933.

[29] Cromarty, B.J., Proc. Nitrogen 91 Conference, Copenhagen 5th June, 115, 1991.

[30] Puxley, D.C., Kitchener, I.J., Komodromos, C. and Parhuis, N.D., in 'Preparation of Catalysts III', (Poncelet, G. and Grange, P., eds.), Elsevier, Amsterdam, 1979.

[31] Zielinsky, N. and Kommarewsky, *W., Chem. Ber.*, **57**, 667, 1924.

[32] Zielinski, J., *J. Catal.*, **76**, 157, 1982.

[33] Rostrup-Nielsen, J.R., in 'Catalytic Steam Reforming', Springer-Verlag, 1984.

[34] Alzarmora, L.E., Ross, J.R.H., Kruissink, E.C. and Van Reijnen, L.L., *J. Chem. Soc. Faraday Trans. I*, **77**, 665, 1981.

[35] Shephard, F.E., *J. Catal.*, **14**, 148, 1969.

[36] Rostrup-Nielsen, J.R., *J. Catal.*, **21**, 171, 1971.

[37] Gregg, S.J., in 'The Surface Chemistry of Solids', Chapman and Hall, London, 1965.

[38] Williams, A., Butler, G.A. and Hammonds, J., *J. Catal.*, **24**, 352 1972.

[39] Erekson, E.J., Sughrue, E.L. and Bartholomew, C.H., *Fuel Process Technol.*, **5**, 91, 1981.

[40] Pedersen, K., Skov, A. and Rostrup-Nielsen, J.R., *Prepr. ACS Div. Fuel Chem.*, **25** (2), 89, 1980.

[41] Baker, R.T.K., Alonzo, J.R., Dumesic, J.A. and Yates, D.J.C., *J. Catal.*, **77**, 74, 1982.

[42] ICI Katalco, 'Steam Reforming Catalysts', Information brochure, 142W/074/1/CATPREF.

[43] Bridger, G.W., *The Oil and Gas Journal*, Feb.16, 73, 1976.

[44] Bridger, G.W. and Wyrwas, W., *Chemical and Process Engineering*, p.101, Sept. 1967.

[45] Bartholomew, C.H., *Catal. Rev. Sci. Eng.*, **24**, 67, 1982.

[46] Baker, R.T.K., *Catal. Rev. Sci. Eng.*, **19**, 161, 1979.

[47] Lobo, L.S. and Trimm, D.L., *J. Catal.*, **29**, 15, 1973.

[48] Figueiredo, J.L. and Trimm, D.L., *J. Catal.*, **40**, 154, 1975.

[49] Baker, R.T.K., Barber, M.A., Harris, P.S., Feates, F.S. and Waite, R.J., *J. Catal.*, **26**, 51, 1972.

[50] Figueiredo, J.L., in 'Progress in Catalyst Deactivation, Nato Advanced Study Institute Series, 45, 1982.

[51] Rostrup-Nielsen, J.R. and Trimm, D.L., *J. Catal.*, **48**, 155, 1977.

[52] Dent, F.J., Moignard, L.A., Eastwood, L.A., Blackburn, W.H. and Hebdon, D., *Trans. Inst. Gas. Eng.*, **602** (1945-1946).

[53] Rostrup-Nielsen, J.R., *J. Catal.*, **27**, 343, 1972.

[54] Manning, M.P., Garmirian, J.E. and Reid, R.C., *Ind. Eng. Chem. Process Des. Dev.*, **21**, 404, 1982.

[55] Snoeck, J.-W., Froment, G.F. and Fowles, M., *J. Catal.*, **169**, 240, 1997.

[56] Nagakura, S., *J. Phys. Soc. Jpn.*, **12**, 482, 1957.

[57] De Bokx, P.K., Kock, A.J.H.M., Boellard, E., Klop, W. and Geus, J.W., *J. Catal.*, **96**, 454, 1985.

[58] De Bokx, P.K., Kock, A.J.H.M., Boellard, E., Klop, W. and Geus, J.W., *J. Catal.*, **96**, 481, 1985.

[59] Zaikovski, V.I., Chesnokov, V.V. and Buyanov, R.A., *Appl. Catal.*, **38**, 41, 1988.

[60] Tracz, E., Scholtz, R. and Borowiecki, T., *Appl. Catal.*, **66**, 133, 1990.

[61] Park, C., Rodriguez, N.M. and Baker, R.T.K., *J. Catal.*, **169**, 212, 1997.

[62] Buyanov, R.A., *Kinetika i Kataliz*, **21**, 237, 1980.

[63] Sacco, A., Thaker, P., Chang, T.N. and Chaing, A.T.S., *J. Catal.*, **85**, 224, 1984.

[64] Baker, R.T.K. and Chludzinski, J.J., *J. Phys. Chem.*, **90**, 4734, 1986.

[65] Kock, A.J.H.M., De Bokx, P.K., Boellard, E., Klop, W. And geus, J.W., *J. Catal.*, **96**, 468, 1985.

[66] Eizenberg, M. and Blakely, J.M., *Surf. Sci.*, **82**, 228, 1979.

[67] Alstrup, I., *J. Catal.*, **109**, 241, 1988.

[68] Yang, R.T. and Chen, J.P., *J. Catal.*, **115**, 52, 1989.

[69] Holstein, W.L. and Boudart, M., *Rev. Latino-am. Ing. Quim. Apl.*, **13**, 107, 1983.

[70] Schouten, F.C., Gijzeman, O.L.J. and Bootsma, G.A., *Surf. Sci.*, **87**, 1, 1979.

[71] Figueiredo, J.L., Bernardo, C.A., Chludzinski, J.J. and Baker, R.T.K., *J. Catal.*, **110**, 127, 1988.

[72] Baker, R.T.K., in 'Catalyst Deactivation', (Bartholomew, C.H. and Butt, J.B., eds.), 1991.

[73] McCarty, J.G., Hou, P.Y., Sheridan, D. And Wise, H., in 'Coke Formation on metal Surfaces', (Albright, L.F. and baker, R.T.K., eds.), ACS Symposium Series 202, p.253., Am. Chem. Soc., Washington, D.C., 1982.

[74] Goula, M.A., Lemonidou, A.A. and Efstathiou, A.M., *J. Catal.*, **161**, 626, 1996.

[75] Döbereiner, W., *Pogg. Ann.*, **64**, 94, 1845.

[76] Taylor, H.S. and Neville, H.A., *J. Amer. Chem. Soc.*, **43**, 2055, 1921.

[77] Rostrup-Nielsen, J.R., *J. Catal.*, **31**, 173, 1973.

[78] Hadden, R.A., Howe, J.C. and Waugh, K.C., in 'Catalyst Deactivation 1991', (Bartholomew, C.H. and Butt, J.B., eds.), Elsevier Science Publishers B.V., Amsterdam, p.177.

[79] Chai, G.Y. and Falconer, J.L., *J. Catal.*, **93**, 152, 1985.

[80] Campbell, T.K. and Falconer, J.L., *Appl. Catal.*, **50**, 189, 1989.

[81] Demicheli, M.C., Duprez, D., Barbier, J., Ferretti, O.A. and Ponzi, E.N., *J. Catal.*, **145**, 437, 1994.

[82] Kiskinova, M.P., *Studies in Surface Science and Catal.* Vol. **70**, 1992.

[83] Campbell, T.K. and Goodman, D.W., *Surf. Sci.*, **123**, 413, 1982.

[84] Luftman, H.S. and White, J.M., *Surf. Sci.*, **139**, 369, 1984.

[85] Bailey, K.M., Campbell, T.K. and Falconer, J.L., *Appl. Catal.*, **54**, 159, 1989.

[86] Mross, W.D., *Catal. Rev. Sci. Eng.*, **25**, 591, 1983.

[87] Narayanan, S. and Sreekanth, G., *J. Chem. Soc. Faraday Trans.*, **89** (6), 943, 1993.

[88] Borowiecki, T., *Appl. Catal.*, **4**, 223, 1982.

[89] Choudhary, V.R., Uphade, B.S. and Mamman, A.S., *Catal. Lett.*, **32**, 387, 1995.

[90] U.S. Pat. 3791993, 1974, (Rostrup-Nielsen, J.R.).

[91] Kneale, B. and Ross, J.R.H., *Faraday Discuss. Chem. Soc.*, **72**, 157, 1981.

[92] U.S. Pat. 4215998, 1980, (Futami, A.).

[93] Cao, L., Chen, Y. and Li, W., Studies in Surface Science and Catalysis, Elsevier Science B.V., Vol.107, 467, 1997.

[94] Song, R.J., Zhang, L.Q. and Guo, S.D., *J. Nat. Gas. Chem.*, **4**, 352, 1992.

[95] Lui, G., Qui, F. and Guo, S., *Cuihua Xuebao*, **11** (1), 45, 1990.

[96] Tingrui, C., Huifang, P., Zailong, Z., Biao, W. and Huaiping, W., *Chinese J. Chem. Eng.*, **1** (3), 141, 1993.

# 2

# EXPERIMENTAL

## 2.1 Catalyst Preparation

### 2.1.1 15% NiO on α-alumina promoted with $Al_2O_3$, MgO and $La_2O_3$

Nine differently promoted α-alumina supported nickel catalysts containing 15% NiO were prepared by the technique of co-impregnation. Three were promoted with $Al_2O_3$ (1, 5 and 10wt% of the NiO loading), three with added MgO (1, 5 and 10wt% of the NiO loading) and three with added $La_2O_3$ (1, 5 and 10wt% of the NiO loading). A 3.3M nickel nitrate solution was prepared by dissolving $Ni(NO_3)_2.6H_2O$ (3700 g) in deionised water (3000 $cm^3$) and the solution divided to give nine 250 $cm^3$ portions. To three portions the following was added: $Al(NO_3)_3.9H_2O$ (2.3 g, 11.5 g and 23 g). To another three $Mg(NO_3)_2.6H_2O$ (4.0 g, 19.9 g and 39.8 g) and to the final three $La(NO_3)_3.6H_2O$ (0.8 g, 4.2 g and 8.3 g). 20 α-alumina 'optimised rings' (10mm diameter, 14mm high, ICI) fired at 1273 K were then dipped in each solution for 30 minutes, after which they were filtered and calcined in air at 823 K for 6 hours. When completely cool the rings were again dipped for a further 30 minutes and the calcination procedure repeated. Prior to charging in the reactor, the pellets were crushed and sieved and the 300-350 micron finings retained.

### 2.1.2 15% NiO/α-$Al_2O_3$ + 5% $Al_2O_3$ promoted with 3wt% K

15% NiO/α-$Al_2O_3$ + 5% $Al_2O_3$ as prepared above was crushed retaining the 300-350μm finings. The finings (3.0 g) were dipped in a solution of potassium carbonate (0.2 g) in deioinised water (250 $cm^3$), to give a potassium loading of 3wt%. After dipping for 30 minutes, the finings were filtered and calcined in air at 823K for 6 hours.

## 2.2 Gases and Reagents

1. Helium was from British Oxygen Company (BOC), 99.995% pure and was passed through an oxygen trap (Oxyclear) and a molecular sieve (Phase Sep)
2. Hydrogen (5.00% in helium) was from Electrochem Ltd. (ECM), 99.995% pure and was passed through a molecular sieve (Phase Sep)
3. *n*-butane (2.00% in helium) was from BOC, 99.998% pure
4. Nitrogen was from ECM, 99.999% pure
5. Oxygen (5.00% in helium) was from BOC, 99.99% pure
6. $Ni(NO_3)_2.6H_2O$ was from Aldrich, 99.99%
7. $Al(NO_3)_3.9H_2O$ was from Aldrich, 99.99%
8. $Mg(NO_3)_2.6H_2O$ was from Aldrich, 99.99%
9. $La(NO_3)_3.6H_2O$ was from Aldrich, 99.98%
10. $K_2CO_3$ was from from Aldrich, 99.99%

## 2.3 Apparatus

### 2.3.1 X-ray Diffraction (XRD)

X-ray diffraction (XRD) analysis was carried out on a SCINTAG employing $CuK_\alpha$ radiation to generate diffraction patterns from powder crystalline samples at ambient temperature. The diffractometer was controlled by a computer installed with a DMS2000 SCINTAG software package.

### 2.3.2 Electron Microscopy

Transmission electron microscopy (TEM) was carried out on a Philips CM 200 microscope with motor driven copustage.

### 2.3.3 The Microreactor System

A multipurpose microreactor was specially constructed on which various temperature programmed techniques could be carried out. These included temperature-programmed reduction (TPR), temperature-programmed reaction spectroscopy (TPRS), temperature-programmed desorption (TPD) and in-situ surface area measurements. Fig.2.1 shows a schematic representation of the microreactor. The system basically comprised of a gas handling panel, a tubular reactor and a quadrupole mass spectrometer.

The gas handling system allowed any mixture of up to three separate gases to be passed over the catalyst at a pressure of 101 kPa. However, since the pressure inside the chamber was not to exceed $1x10^{-4}$Pa (the limit for the mass spectrometer filament), only a small fraction of the gas stream was admitted.

The reactor itself was constructed from stainless steel tubing, approximately 20cm in length, an internal diameter of 4mm and a wall thickness of 1.5mm. The reactor was positioned vertically inside a small furnace which also housed a pair of 1kW cartridge heating elements (Fig.2.2). Typically 0.5 g of catalyst was loaded into the reactor (300-350 micron finings) and held in the correct position by stainless steel plugs. In order to obtain accurate temperature readings, a $^1/_{16}$ inch diameter, chromel-alumel K-type thermocouple was secured inside the reactor, as close to the catalyst bed as possible.

The temperature of the sample was controlled over the temperature range 77 K to 1273 K by a Newtronics temperature controller (MICRO 96 TP5), which was connected to the heating elements and thermocouple. The Newtronics also controlled the opening of a solenoid valve which allowed liquid nitrogen to pass through holes in the heating block, cooling the reactor tube to 77 K when required.

The outlet of the reactor tube was connected to the mass spectrometer via a $^1/_{32}$ inch stainless steel capillary mounted inside an armoured PTFE flexible hosing. The quadrupole mass spectrometer (HPR 20, Hiden Analytical, Warrington) was capable of following the partial pressures of up to 16 masses in the range 1-200 atomic mass units (a.m.u.). A trend analysis was most commonly performed in which the selected masses

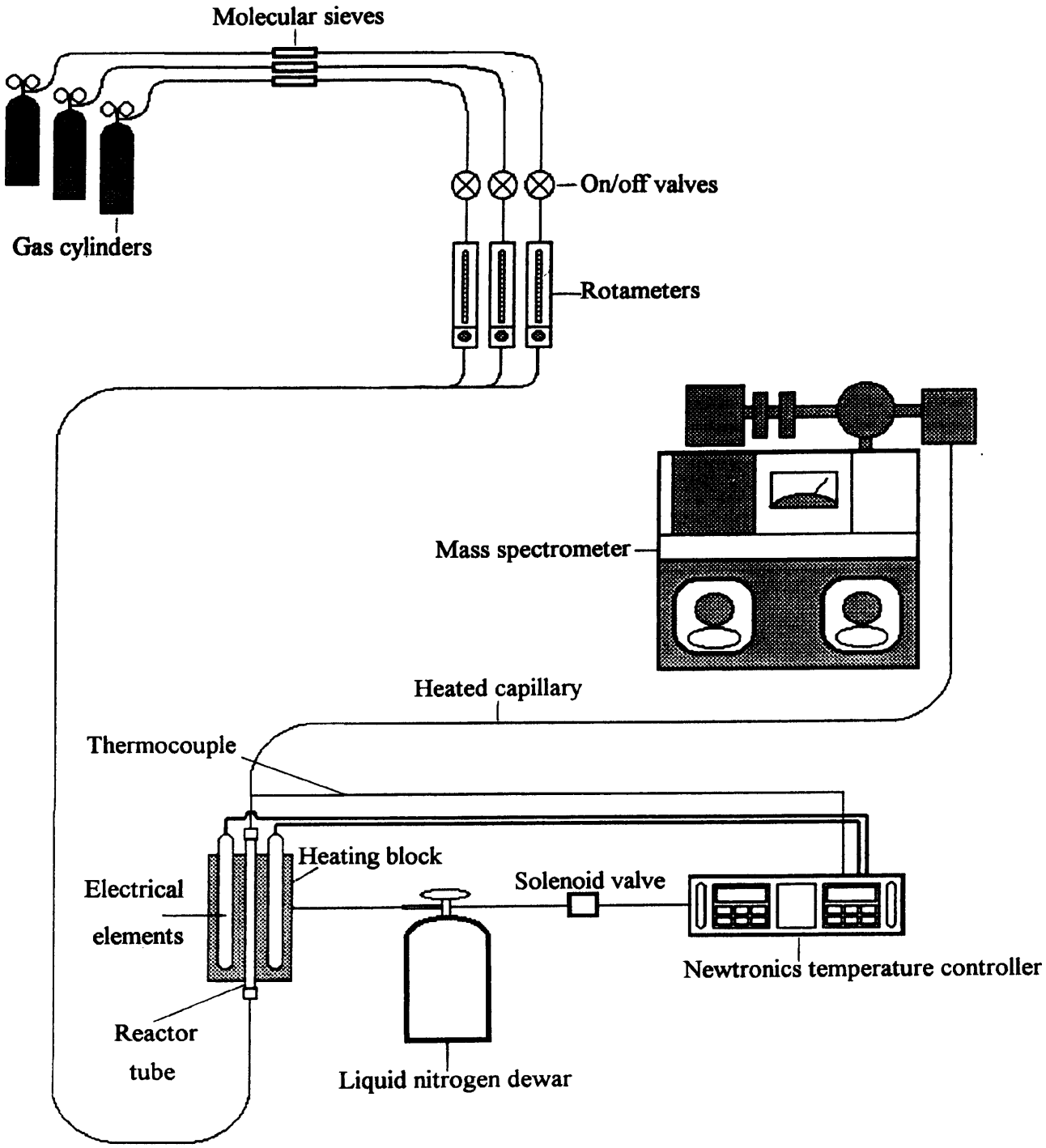


Fig.2.1 Schematic representation of the multi-purpose microreactor

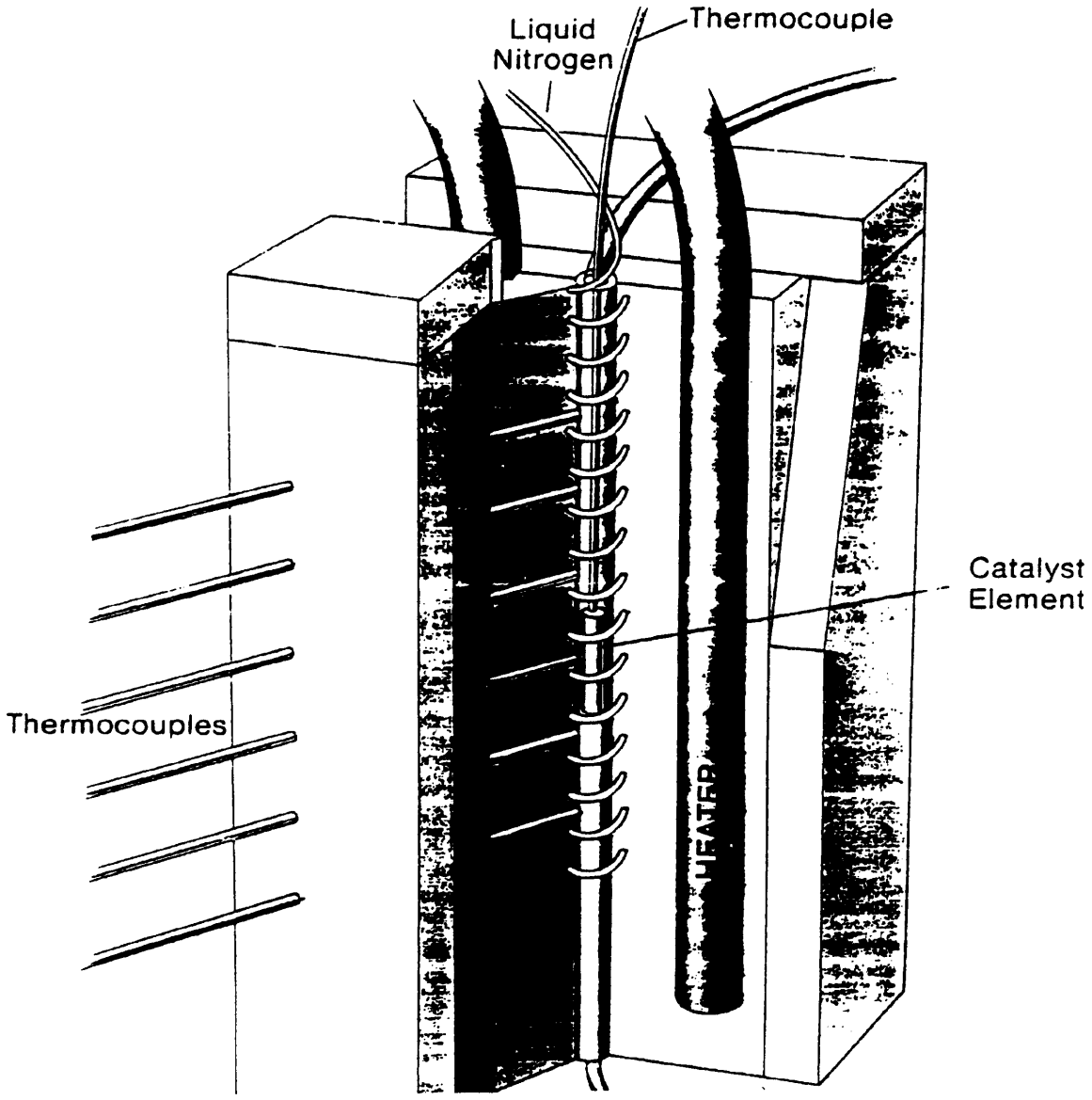


Fig.2.2 Reactor designed to allow cooling to 77 K and temperature programming up to 1273 K

were repeatedly scanned, their partial pressures recorded as a function of time. With the aid of a computer, manipulation of data allowed several peaks to be observed simultaneously as a function of temperature.

## 2.4 Techniques

### 2.4.1 Temperature-Programmed Reduction (TPR)

Temperature-programmed reduction is a widely used technique for the characterisation of supported metal catalysts. The main feature of this method is its capability of continuously monitoring the consecutive reactions of reducible species at increasing temperatures. It can therefore provide information about the dispersion states of the metallic component as well as the metal-support and metal-metal interactions in catalysis, since all of these affect reduction behaviour [1].

Reduction is an important step in the activation of metallic catalysts. It is also a critical step, because if not done correctly, the catalyst may sinter or may not reach its optimum state of reduction. The reduction of a metal oxide $MO_n$ by $H_2$, a commonly used reducing agent, is described by the equation

$$MO_n + nH_2 \rightarrow M + nH_2O \qquad (2.1)$$

Thermodynamics predict the conditions under which a catalyst can be reduced, and the reduction will proceed when the change in Gibbs free energy, $\Delta G$, has a negative value. Equation (2.2) shows how $\Delta G$ depends on pressures and temperature:

$$\Delta G = \Delta G^{o} + nRT \ln(P_{H2O}/P_{H2}) \qquad (2.2)$$

where

$\Delta G$ is the change in Gibbs free energy for the reduction

$\Delta G^{o}$ is the same under standard conditions

n is the stoichiometric coefficient of reaction (2.1)

R is the gas constant

T is the temperature

P is the partial pressure

If the catalyst is reduced under flowing hydrogen, the reaction product water is removed effectively and the second term in (2.2) is therefore always negative. For many oxides, such as those of nickel and the noble metals, $\Delta G^{o}$ is already negative and so reduction is thermodynamically feasible. All one has to do is find a temperature where the kinetics are rapid enough to achieve complete reduction. Oxides such as $Fe_2O_3$ and $SnO_2$, however, have a positive $\Delta G^{o}$ so now the second term in (2.2) determines whether $\Delta G$ is negative or not. In order to see if reduction is thermodynamically feasible, (2.2) is written in the form

$$\Delta G = nRT \ln[(P_{H2O}/P_{H2})/(P_{H2O})/(P_{H2})_{eq}] \qquad (2.3)$$

where the symbols are defined as above and the subscript 'eq' is for the equilibrium ratio. Thus $\Delta G$ is negative when the ratio $P_{(H2O)}/P_{(H2)}$ is smaller than the equlibrium value and the efficiency with which water is removed from the reactor becomes the decisive factor.

The reduction activation energy can be determined from the temperature of the maximum rate of reduction by solving the following equation at that temperature

$$E_r/RT^2_m - [H_2]\, A_r/\beta\, e^{-Er/RTm} = 0 \qquad (2.4)$$

where $E_r$ is the reduction activation energy, $A_r$ is the reduction pre-exponential factor, $T_m$ is the temperature of the maximum reduction rate, $\beta$ is the heating rate, R is the Boltzmann constant and $[H_2]$ is the gas phase concentration of hydrogen.

### 2.4.2 Temperature-Programmed Surface Reaction (TPSR)

Temperature-programmed surface reaction refers to the study of reactions under temperature programming. In this type of study two gases can be coadsorbed on the catalyst, usually sequentially, with heating carried out in an inert carrier. Another possibility is when a reactive carrier gas is used and the 'adsorbed' species is the result of decomposition of another molecule; the 'adsorbed' species cannot desorb under the conditions employed [2].

A wealth of information can be obtained from TPSR experiments if all the reaction products are detected. Several sites of different activity can exist on the catalyst surface which can increase or decrease with change in catalyst properties. Such changes cannot be predicted by steady state kinetic measurements and may be observed using temperature programmed analysis. This approach is very useful for the study of reactions such as oxidation, hydrogenation and carburisation.

## 2.5 X- ray Diffraction (XRD)

X-rays have wavelengths in the Ångstrøm range, are sufficiently energetic to penetrate solids and are well suited to probe their internal structure. XRD can be used to identify bulk phases, to monitor the kinetics of bulk transformations and to estimate particle sizes. An attractive feature is that the technique can be applied in situ.

A conventional X-ray source consists of a metal target which is bombarded with high energy electrons. When the electrons plunge into the material two contributions to the overall X-radiation are generated. First there is a continuous background of radiation

spanning a range of wavelengths. This continuum is called the *Bremsstrahlung* and arises from the rapid deceleration of the electrons when they sink into the material. Superimposed on this continuum are characteristic, narrow lines of high intensity. The Cu Kα line, with an energy of 8.04 keV and a wavelength of 0.154 nm, arises because a primary electron creates a core hole in the K shell, which is filled by an electron from the L shell under emission of an X-ray quantum. Kβ radiation is emitted when the K-hole is filled from the M-shell, and so on.

X-ray diffraction is the elastic scattering of X-ray photons by atoms in a periodic lattice. When monochromatic X-rays are scattered by the ordered environment in a crystal, inteference (both constructive and destructive) takes place among the scattered rays because the distances between the scattering centres are of the same order of magnitude as the wavelength of the radiation. When an X-ray beam strikes a crystal surface at a certain angle θ, a portion is scattered by the layer of atoms at the surface. The unscattered portion of the beam penetrates to the second layer of atoms where again a fraction is scattered, and the remainder passes on to the third layer, as shown in Fig.2.3. The cumulative effect of this scattering from regularly spaced centres of the crystal is a diffraction of the beam.

In 1912, W.L.Bragg [3] treated the diffraction of X-rays by crystals as shown in Fig.2.3. Here, a narrow beam strikes the crystal surface at angle θ; scattering occurs as a consequence of interaction of the radiation with atoms located at O, P and R. If the distance

$$AP + PC = n\lambda$$

where n is an interger, the scattered radiation will be in phase at OCD and the crystal will appear to reflect the X-radiation. But it is readily seen that

$$AP = PC = d \sin \theta$$

where d is the distance between two lattice planes. Thus we may write that the conditions for constructive interference of the beam at angle θ are

$$n\lambda = 2d \sin \theta \qquad (2.12)$$

This is called the Bragg equation and is of fundamental importance. X-rays appear only to be reflected from the crystal only if the angle of incidence satisfies the condition that

$$\sin \theta = n\lambda / 2d \qquad (2.13)$$

At all other angles, destructive interference occurs.

The XRD pattern of a powdered sample is measured with a stationary X-ray source (usually Cu Kα) and a moveable detector which scans the intensity of the diffracted radiation as a function of 2θ between the incoming and the diffracted beams. When working with powdered samples, an image of diffraction lines occurs because a small fraction of the powder particles will be oriented such that by chance a certain crystal plane is at the right angle θ with the incident beam for constructive interference.

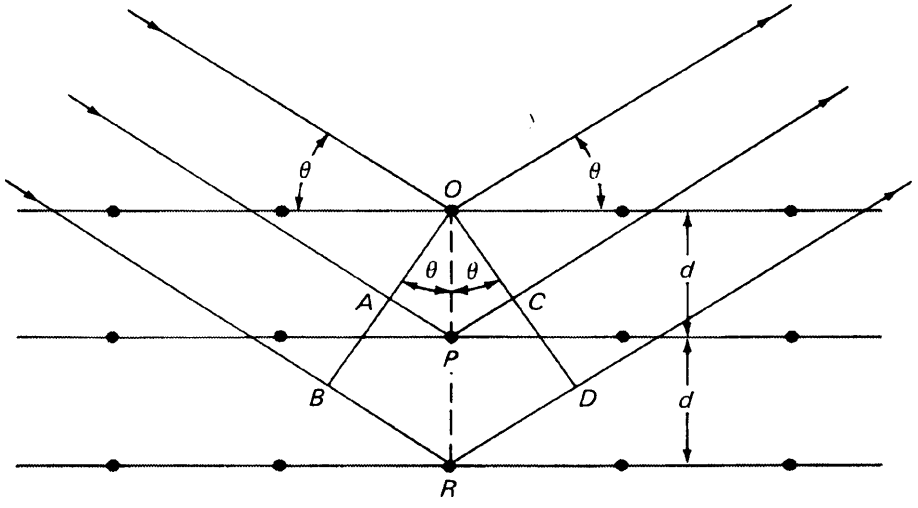


Fig.2.3 X-rays scattered by atoms in an ordered lattice interfere constructively in directions given by Braggs law. Diffractograms are measured as a function of the angle 2θ.

## 2.6 Transmission Electron Microscopy (TEM)

### 2.6.1 Introduction

Seeing the surface of a catalyst and any species present on it, in atomic detail, is an ideal in catalytic chemistry. Unfortunately, optical microscopy is of no use in this case since the rather long wavelength of visible light (a few hundred nanometres) does not allow the detection of features smaller than about one micron. Electron beams, however, offer better opportunities. Development over the past 40 years has resulted in electron microscopes which routinely achieve magnifications of the order of one million times and reveal details with a resolution of about 0.1 nm [4]. Therefore the technique has become very popular in catalysis, enabling the size and shape of supported particles to be determined.

### 2.6.2 Theory

When a beam of electrons is passed through a thin solid specimen, each electron has a number of possible fates. The most significant of these are:

i) it is undeflected (ie. transmitted without interacting with any atom)
ii) it is deflected but loses no energy (ie. elastically scattered)
iii) it loses a significant amount of energy and is probably deflected (ie. inelastically scattered). As a result of the transfer of energy, secondary electrons or X-rays may be excited.

If all these types of electrons (we shall call them i, ii and iii) are allowed to carry on down the microscope they will all contribute to the image and all regions of the specimen will look identical. There would be no contrast between areas of different composition or thickness. Therefore the scattered electrons (ii and/or iii) must be separated from the unscattered electrons (i) by means of an objective lens aperture in order to create contrast in the image (see Fig.2.4(e)).

Fig.2.4 schematically illustrates the fate of each 100 electrons falling on a hypothetical sample. Region (a) consists of 10nm of amorphous carbon. Being a light atom this scatters electrons very weakly so we can assume that only 10 of the 100 electrons will be deflected by $0.5^{\circ}$ or more, but no more than a few degrees. Region (b) is an area twice as thick as (a) and scatters slightly more strongly; we can assume 20 electrons are significantly deflected. Region (c) is the same thickness as (b) but consists of amorphous nickel. Here the majority of electrons are deflected but still only through a small angle. Finally, region (d) consists of the same thickness of crystalline nickel. Here diffraction can take place and the scattered electron beam will be reinforced in certain directions but cancelled in others. This results in most of the scattered electrons travelling in specific directions at the Bragg angle $\theta_B$ to the unscattered beam. The number of electrons emerging from the specimen in the unscattered and diffracted beams depends critically on the thickness and orientation of the specimen and may be anything from almost zero to 100 in each case.

If all 100 electrons are allowed to travel down the microscope, the image produced by the lenses will show no difference between each of the regions (a) – (d). There will be no contrast. If, however, those electrons which have been scattered through more than $0.5^{\circ}$ are stopped by inserting an aperture below the specimen (Fig.2.4.(e)), then regions (a) – (d) will look markedly different. The brightness of the image of each region is proportional to the number of unscattered electrons which pass through the aperture, so regions (a), (b) and (c) will appear to have brightness in the ratio 90:80:5. The nickel will therefore be clearly visible as a dark region, whereas thickness variations in the carbon region will give only faint contrast.

### 2.6.3 The major components of the Transmission Electron Microscope

The optical system of the TEM is shown schematically in Fig.2.5. There must be a source of illumination, a condenser system to collimate the illumination onto the specimen, an objective lens to provide a preliminary focussed image, a projector system to magnify this image to its final size, a screen on which to view the image and finally a

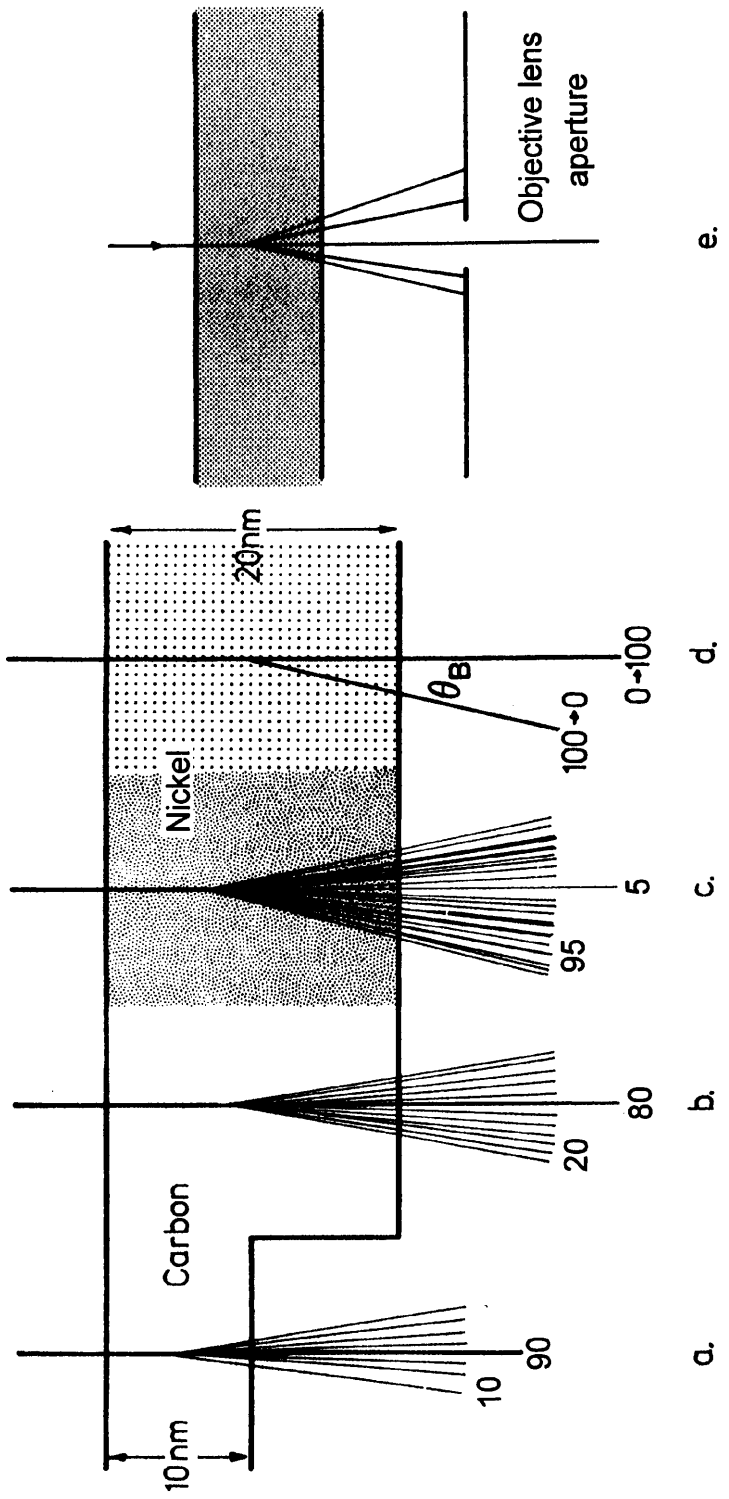


Fig.2.4 The fate of 100 electrons falling on four different regions of a hypothetical specimen. The numbers shown are those scattered through more than 0.5° and those unscattered. The regions are: (a) 10 nm of amorphous carbon; (b) 20 nm of amorphous carbon; (c) 20 nm of amorphous nickel; (d) 20 nm of crystalline nickel; (e) the effect of inserting an objective aperture to stop all electrons scattered through more than about 0.5°.

camera with which to record it. In the following section the two fundamental components, the electron gun and the typical electromagnetic lens, are discussed in more detail.

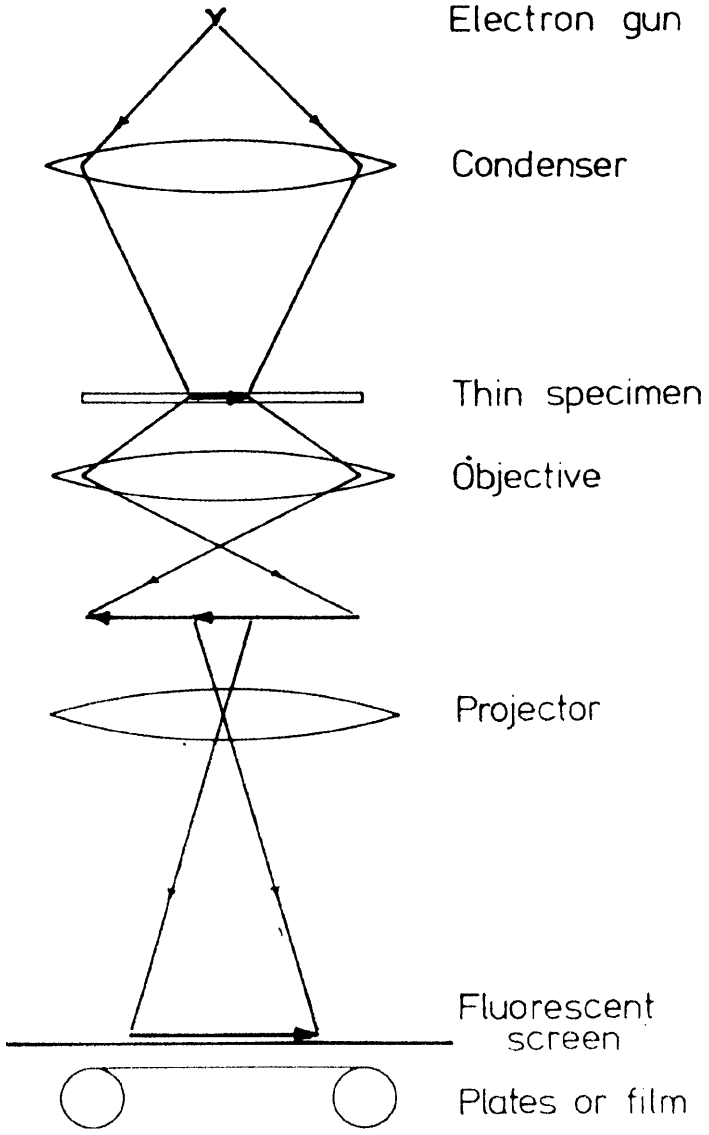


Fig.2.5 The major components of the optical system of the TEM

### 2.6.4 The Thermionic Electron Gun (TEG)

Almost all TEMs use a thermionic triode electron gun. It serves a dual purpose as a source of accelerated electrons and as a preliminary 'condenser lens'. It therefore produces an intense beam of high energy electrons which is directed down the

microscope column. The structure of a TEG is shown in Fig.2.6. A filament (usually tungsten or lanthanum hexaboride ($LaB_6$)) is heated to white heat and emits many thermionic electrons. These are accelerated towards an anode and pass through a hole in its centre to the condenser system of the microscope. The accelerating voltage itself is widely variable in steps from 20 or 40kV to the maximum of which the instrument is capable, usually up to 300kV. A bias applied to the Wehnelt cap causes the gun to act as a triode valve and as an electrostatic lens. The electrons are thus only emitted from a limited region of the filament and their trajectories cross over on their way to the anode hole. Looking from the point of view of the microscope, all the electrons appear to come from the cross-over point C, which is often called the 'virtual source'.

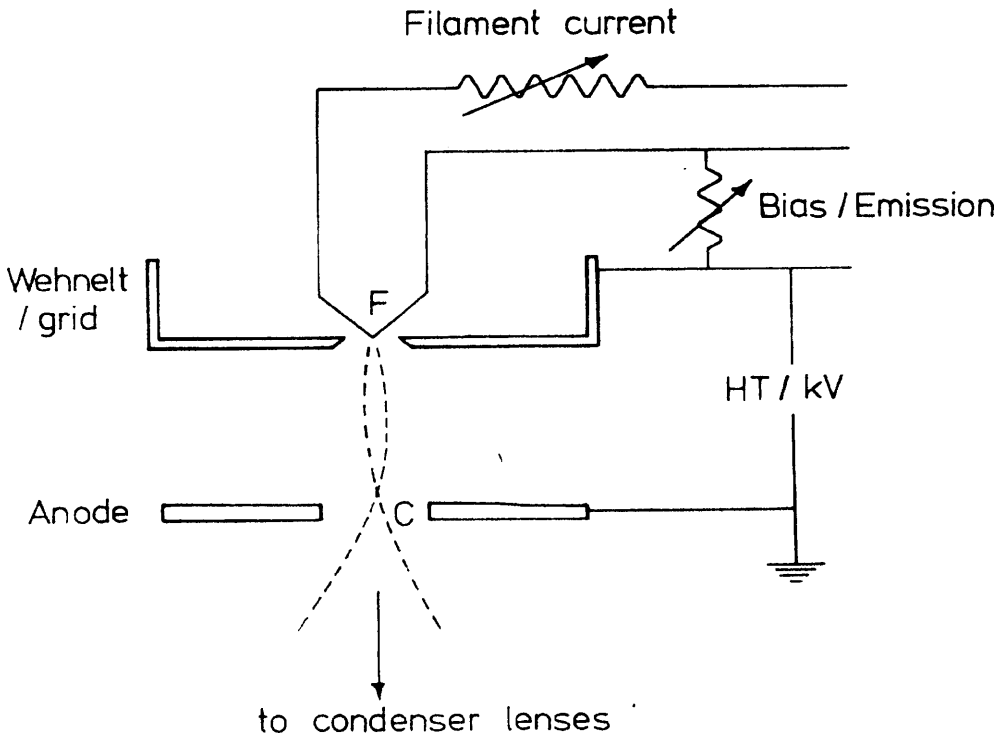


Fig.2.6 The thermionic electron gun

### 2.6.5 The Electromagnetic Lens

All of the lenses in a modern TEM operate in the same way. Basically, they set up an electromagnetic field symmetrically around the optical axis of the microscope. This is easily done using a simple coil wound round the optical axis (Fig.2.7(a)) but in practice the extent of the field needs to be restricted so that the field acts as a 'thin lens' in optical terms. This is achieved using a steel yoke and pole piece, (Fig.2.7(b)). Fig.2.8 illustrates how such a field acts as a converging lens.

An electron, A, travels down the optical axis of the microscope. A experiences no force and continues undeflected. However, an off-axis electron of velocity **v** experiences a force e(B**x**v), ie. of magnitude $evB\sin\theta$ in the direction perpendicular to both v and B (into the paper in Fig.2.8). This sends the electron spiralling around the optical axis. Once the electron has a component of velocity in a circumferential direction (into the paper), say $\mathbf{v_c}$, then it also experiences a force e(B**x**$\mathbf{v_c}$) pulling it towards the axis. The electron thus follows a spiral path such as that illustrated in Fig.2.8(b). The envelope of this path (shown by the broken line in Fig.2.7(b)) is analogous to the familiar ray in the conventional optical diagram (Fig.2.8(c)), but in addition the electron rotates through a number of turns of the spiral while traversing the lens. This number is rarely an integer and therefore the electromagnetic lens acts not only to invert the image but to rotate it about the optical axis by an amount depending on the strength of the lens. Since the great advantage of electron lenses is that their strength (and hence focal length) is easily changed by varying the current through their coil, it follows that any variation of the imaging lenses will result in rotation of the image.

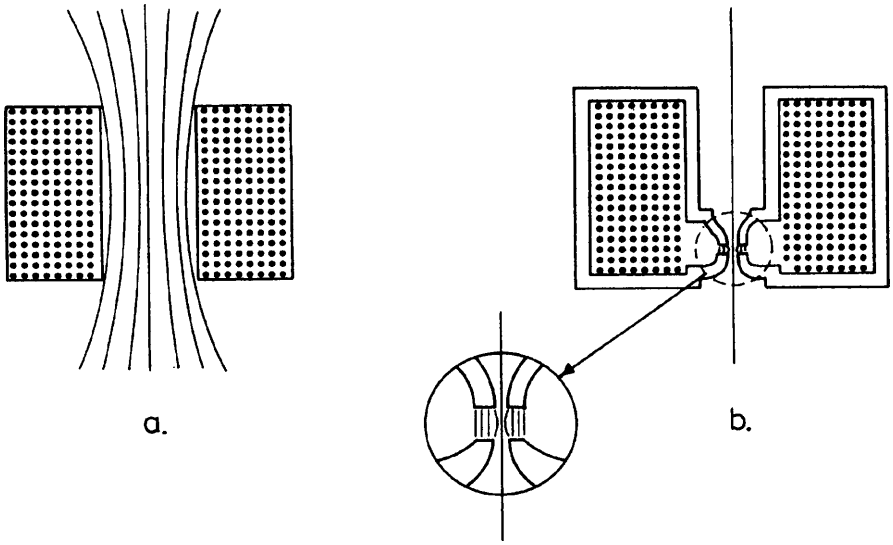


Fig.2.7 (a) The field from a simple electromagnet. (b) The field is restricted to the small 'lens' region by the addition of an iron yoke and pole pieces

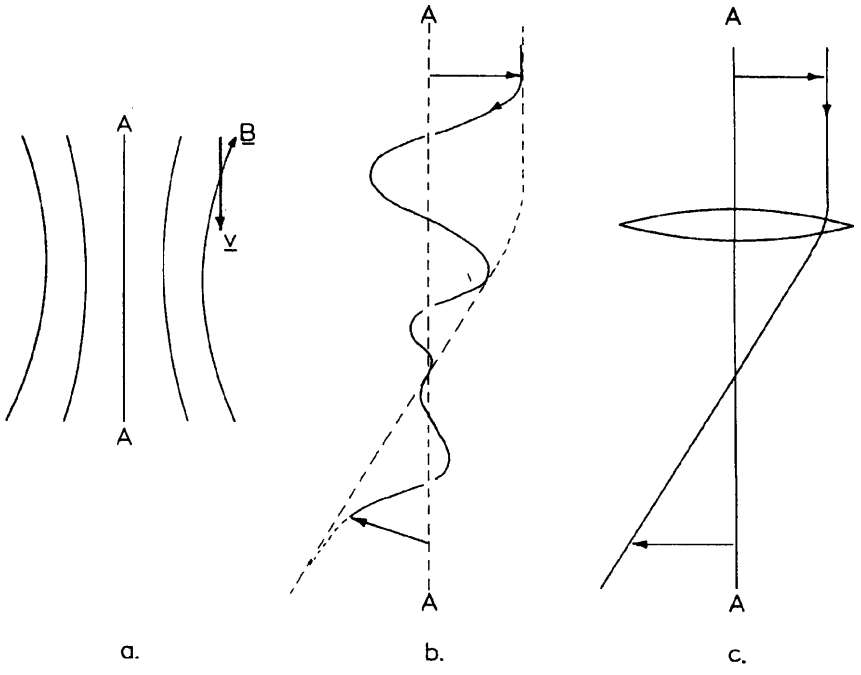


Fig.2.8 The action of the electromagnetic lens. (a) The electron with velocity **v** experiences a force e(B**x**v) into the paper. (b) This results in the electron spiralling round the optical axis. It's envelope, shown by the broken line, can be compared with the conventional ray diagram (c).

## References


[1] Huang, Y. J., Xue, J. and Schwarz, J. A., *J. Catal.*, **111**, 59, 1988.

[2] Bhatia, S., Beltramini, J. and Do, D.D., *Catalysis Today*, **7** (3), 309, 1990.

[3] Skoog, D.A., in 'Principles of Instrumental Analysis', 3rd edn., Saunders College Publishing, 1985.

[4] Goodhew, P.J. and Humphreys, F.J., in 'Electron Microscopy and Analysis', 2nd edn., Taylor and Francis Inc., London, 1988.

# 3

# PRE-TREATMENT AND CHARACTERISATION OF $NiO/Al_2O_3$ CATALYSTS PROMOTED WITH $Al_2O_3$, MgO AND $La_2O_3$

## 3.1 Introduction

As described in Chapter 1, preferred steam reforming catalysts contain nickel supported on refractory materials such as α-alumina, frequently combined with promoters to increase the catalyst's resistance to carbon formation. Since α-alumina is formulated at high temperatures and has a low surface area (~$3m^2\ g^{-1}$), the most convenient method for depositing the active component is impregnation followed by calcination to oxide precursors.

The impregnation method was used to prepare nine $NiO/\alpha\text{-}Al_2O_3$ catalysts, each promoted with amounts of $Al_2O_3$, MgO and $La_2O_3$ equivalent to 1, 5 and 10 wt% of the NiO loading. A detailed description of the preparation method can be found in Section 2.1, Chapter 2.

For convenience all nine catalysts have been assigned a name, AK1- AK9, and each will be referred to by their label in the remainder of this thesis. Each catalyst consisted of 15% NiO on $\alpha\text{-}Al_2O_3$ promoted as follows:

**Catalysts promoted with $Al_2O_3$:**

**AK1** - $Al_2O_3$ equivalent to 1wt% of the NiO loading

**AK2** - $Al_2O_3$ equivalent to 5wt% of the NiO loading

**AK3** - $Al_2O_3$ equivalent to 10wt% of the NiO loading

**Catalysts promoted with MgO:**

**AK4** - MgO equivalent to 1wt% of the NiO loading

**AK5** - MgO equivalent to 5wt% of the NiO loading

**AK6** - MgO equivalent to 10wt% of the NiO loading

**Catalysts promoted with $La_2O_3$:**

**AK7** - $La_2O_3$ equivalent to 1wt% of the NiO loading

**AK8** - $La_2O_3$ equivalent to 5wt% of the NiO loading

**AK9** - $La_2O_3$ equivalent to 10wt% of the NiO loading

### 3.2 Catalyst Pre-treatment and Characterisation

It is well known that the activity and stability of supported nickel catalysts are affected not only by factors such as method of preparation, calcination temperature and nature of support etc., but also by the conditions of pre-treatment. It is therefore imperative that catalyst activation is carried out correctly in order to achieve the proper catalyst structure and thus the optimum performance.

The aim of this section is to provide a systematic study of the pre-treatment of the prepared NiO/$\alpha$-$Al_2O_3$ catalysts and to describe their characterisation using various techniques. Pretreatment consisted of heating catalyst samples in helium followed by reduction in hydrogen. XRD analysis was carried out on unreduced samples to provide information about the crystalline phases which may have been formed during preparation. The total surface areas of the catalysts were measured by nitrogen adsorption at 77 K. Samples were cooled down to liquid nitrogen temperatures by pumping liquid nitrogen around the reactor.

### 3.3 X-ray analysis

X-ray diffraction was carried out on the powdered, calcined catalysts in their unreduced state. Comparison of the diffractogram with a library of XRD data files (known as a JCPDS file) quantitatively showed which crystalline phases were present in the sample. The results are illustrated for each series of promoted catalysts in the following section.

i) Catalysts promoted with $Al_2O_3$ (AK1 - AK3)

A typical X-ray diffraction pattern obtained for samples AK1 - AK3 is shown in Fig.3.1. For each of the 3 samples the diffractogram exhibited identical features. In each case the presence of NiO was identified by peaks occurring at $2\theta = 36.6^o$, $42.6^o$ and $62.4^o$. The presence of $\alpha$-$Al_2O_3$ (corundum) was also confirmed with main peaks at $2\theta = 34.5^o$, $42.6^o$ and $56.7^o$. There was no indication of NiO-$Al_2O_3$ compound formation in any of the samples and no separate phases with added $Al_2O_3$ were observed, suggesting that they were too finely divided to be detected by X-ray diffraction.

ii) Catalysts promoted with MgO (AK4 - AK6)

Fig.3.2 shows the X-ray diffraction pattern obtained for samples AK4 - AK6. Again for each sample the diffractogram exhibited identical features. In this case peaks at $2\theta = 36.5^o$, $42.6^o$ and $62.3^o$ suggested the presence of both $MgNiO_2$ and $Mg_{.4}Ni_{.6}O$ phases, although these peak positions differed only very slightly from those observed for free NiO. Peaks corresponding to MgO were not observed. Temperature-programmed reduction profiles obtained for the MgO promoted samples (Figs.3.6(a)-(c)) did however confirm that an interaction between NiO and MgO had occurred and therefore it is likely that these phases were present. A crystalline $\alpha$-$Al_2O_3$ phase was again identified by main peaks ocurring at $2\theta = 34.5^o$, $42.6^o$ and $56.7^o$.

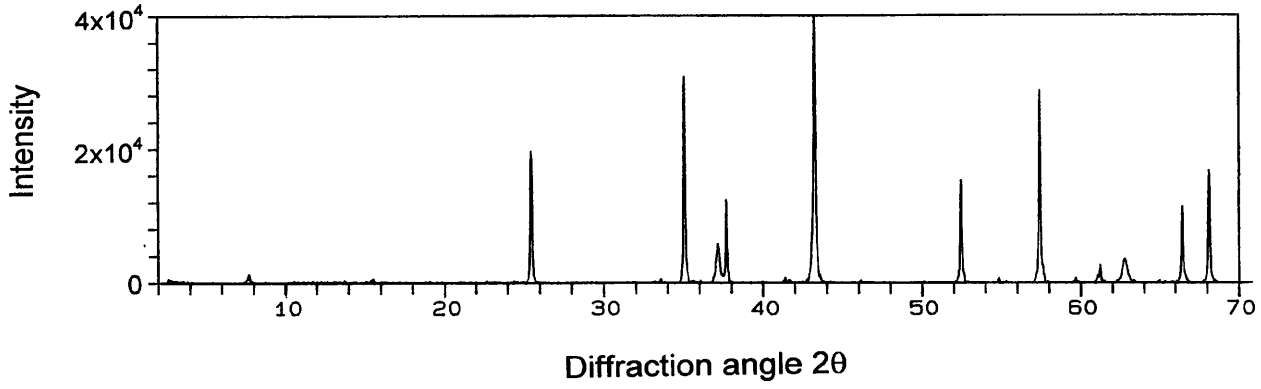


Fig.3.1 X-ray diffraction pattern of samples promoted with $Al_2O_3$ (AK1 - AK9)

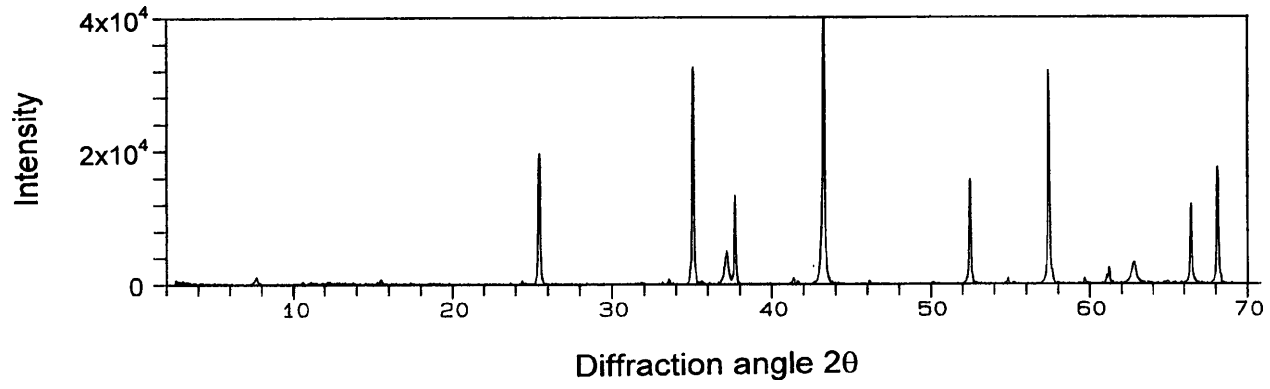


Fig.3.2 X-ray diffraction pattern of samples promoted with MgO (AK4 - AK6)

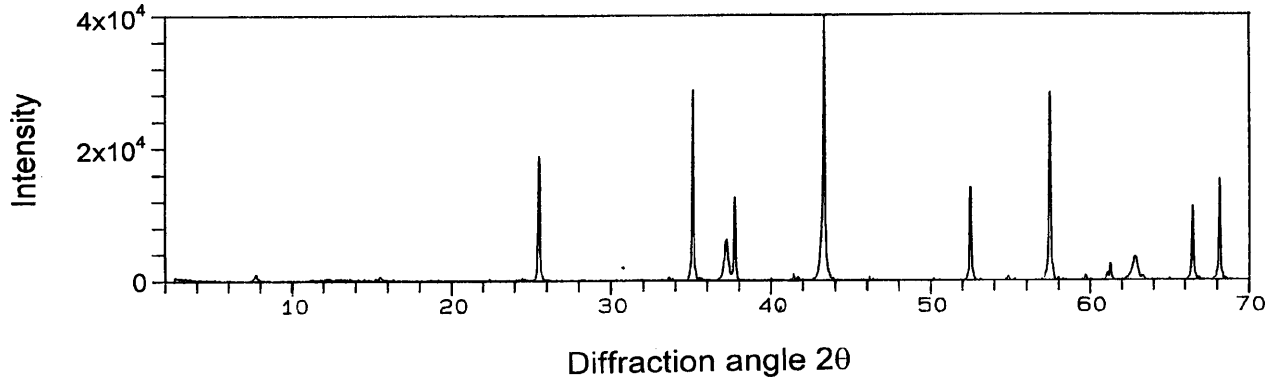


Fig.3.3 X-ray diffraction pattern of samples promoted with $La_2O_3$ (AK7 - AK9)

iii) Catalysts promoted with $La_2O_3$ (AK7 - AK9)

The X-ray diffraction pattern obtained for samples AK7 - AK9 is shown in Fig.3.3. The XRD pattern obtained for each sample was again indistinguishable. A crystalline NiO phase was identified in each case with peaks at $2\theta = 36.6^o$, $42.6^o$ and $62.4^o$. The presence of $\alpha$-$Al_2O_3$ was also confirmed by main peaks at $2\theta = 34.5^o$, $42.6^o$ and $57.7^o$. Peaks corresponding to $La_2O_3$ were not observed and there was no evidence of any NiO-$Al_2O_3$ compound formation or any phases resulting from the interaction of NiO and $La_2O_3$.

## 3.4 Catalyst Activation

Before studying the interaction of any reagent(s) with the catalysts, all samples were activated by two consecutive steps. These stages comprised of pre-treatment in helium followed by reduction in hydrogen.

### 3.4.1 Pre-treatment in helium

It is a common occurrence for catalysts to undergo some contamination during forming, transport and loading into the reactor. Therefore pre-treatment of the catalyst by heating it in situ under a flow of helium allows surface contaminants to be removed prior to reduction. Each of the samples, AK1-AK9, underwent the following pre-treatment procedure whenever in use. The catalyst (0.5 g) was heated in a 100% helium stream (25 $cm^3\ min^{-1}$, 1 bar, 10 K $min^{-1}$) from ambient to 873 K and maintained at that temperature for 2 hours to ensure the complete removal of any water. The temperature dependent product spectrum for sample AK1 is shown in Fig.3.4. The characteristics of this product spectrum were very similar for all 9 catalyst and therefore only this example will be presented. The main material desorbing was $CO_2$, for which three distinct peak maximum temperatures were observed. A small, peak occurred at 423 K, a broader peak followed at 610 K and finally a substantially larger peak was present at 730 K. These may be attributed to the presence of Ni or Al carbonates or hydroxycarbonates which may have been formed or may be due to contamination

which occurred during transport or storage. In all cases little or no water desorption was observed.

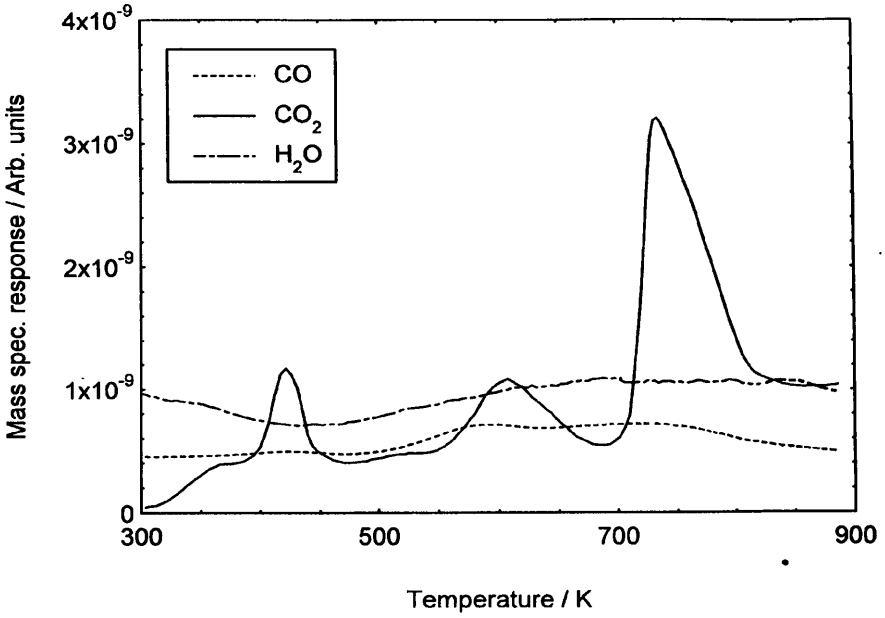


Fig.3.4 Heating sample AK1 in a 100% He stream (25 $cm^3$ $min^{-1}$)

### 3.4.2 Reduction of the Catalysts

The last stage in the preparation of $Ni/Al_2O_3$ catalysts is a reduction process. Here the active phase of the catalyst, the zero valent metal $Ni^0$ is generated by reduction of the $Ni^{2+}$ with a suitable reductant. In industrial reforming plants these are commonly hydrogen, ammonia or hydrocarbons which are added to the steam [1]. To facilitate these operations the catalyst should be reducible at relatively low temperatures. Highest activity normally results from the lowest possible reduction temperature giving complete reduction within a convenient period. Rapid reduction may lead to lower dispersions and poor activity at process conditions [2].

Throughout this study all catalysts were reduced in hydrogen. The following equation is considered to describe the process:

$$NiO + H_2 = Ni + H_2O \qquad (3.1)$$

The majority of published research concerns the reduction of bulk nickel oxide samples. Delmon et al [3] demonstrated that with bulk nickel oxide the the reduction reaction (3.1) proceeds via a shrinking core model, in which a layer of metallic nickel forms on the outside of a particle of agglomerated nickel oxide crystallites. This layer increases in thickness until all the oxide disappears. There is general agreement that chemical reduction follows the sequence (1) dissociation of hydrogen (2) surface diffusion of hydrogen atoms to a reactive centre (3) rupture of the Ni-O bond, producing $Ni^0$ atoms (4) nucleation of $Ni^0$ atoms into metallic nickel clusters (5) growth of nickel clusters into crystallites as the supply of hydrogen accelerates. Any one or combination of these steps, together with removal of water, may control the overall reaction rate [4].

A major complication arising for supported nickel catalysts is the interaction of nickel oxide with support components which influences the extent and kinetics of reduction and the thermal stability [5]. Richardson et al [6] used temperature-programmed reduction to show that nickel oxide reduction is also changed by the incorporation of small amounts of additive oxide promoters. By measuring the extent of reduction at given temperatures they found that oxides which are easier to reduce than nickel oxide, such as $Ag_2O$ and CuO, accelerate reduction of NiO, whereas oxides such as $Al_2O_3$ and $ZrO_2$, inhibit reduction.

A relatively recent and convenient method of investigating the reduction behaviour of catalysts is Temperature-Programmed Reduction (TPR) [7]. The main feature of the method is its capability of continuously monitoring the consecutive reactions of reducible species at increasing tempeartures. The technique is therefore useful since it determines the temperatures needed for complete reduction of a catalyst and can also provide information about any metal-support and metal-metal interactions which may have occurred.

All the catalysts in this study were reduced in hydrogen using the following procedure. The catalyst was firstly pre-treated in a helium stream as described in section 3.4.1. The sample was then cooled to ambient and the flow switched to a hydrogen-helium stream (5% $H_2$, 25 $cm^3$ $min^{-1}$, 1 bar). The temperature was raised to 873 K* at 3 K $min^{-1}$ under the hydrogen-helium stream and held at that temperature for 16 hours. The $H_2$ consumed and the $H_2O$ produced were continuously monitored during the reaction. In the following sections the temperature-programmed reduction spectra are discussed separately for each series of promoted catalysts.

i) Catalysts promoted with $Al_2O_3$ (AK1 - AK3)

Well defined temperature-programmed reduction profiles for samples AK1 - AK3 are presented in Figs.3.5(a)-(c). The onset of hydrogen consumption for each sample occurred at ~500 K and in each case a dominant peak maximum was observed at 685 K. A high temperature shoulder at ~800 K was also present for each sample. Samples AK1 and AK2 exhibited a broad shoulder of equal size, whereas for sample AK3 the shoulder had increased in size (~doubled) and its peak maximum had become clearer.

It has been known for some time that major differences in reduction of $Ni/Al_2O_3$ catalysts result from interaction of nickel oxide with the support (even with the nearly 'inert' α-alumina) which gives rise to the formation of nickel aluminium spinel:

$$NiO + Al_2O_3 \rightarrow NiAl_2O_4 \qquad (3.2)$$

It seems unlikely in this case, however, that the formation of nickel aluminium spinel is responsible for the difference in reduction kinetics observed. It has been widely reported that the formation of nickel aluminium spinel starts at temperatures above about 970 K [8] [9] [10], well above the calcination temperature employed during the

* For sample AK6 the temperature was raised to 1000K

preparation of the samples in this work. Cimino et al [11] found that it is possible to form a 'surface spinel' below 870 K, however this less well defined interaction occurred only between NiO and η- or γ-alumina. In the specific case of NiO on α-$Al_2O_3$, Gavalas et al [12] reported that calcination below 1123 K gives only NiO and only above 1123 K is some precursor of $NiAl_2O_4$ observed.

The improbability of any interaction between NiO and α-$Al_2O_3$ in samples AK1 - AK3 is further supported by the XRD data shown in Fig.3.1. None of the diffractograms show any evidence for the presence of $NiAl_2O_4$ or any $NiAl_2O_4$ precursors. It is most likely therefore that the presence of the high temperature shoulder in the reduction profiles is due to the interaction between NiO and the added amounts of $Al_2O_3$ promoter, which results in the formation of a Ni phase (possibly a precursor to $NiAl_2O_4$) which is more difficult to reduce. The fact that the size of the shoulder increases on icreasing the loading of $Al_2O_3$ promoter indicates a stronger interaction. The percentage of added promoter was very small in each case and so the concentration of any newly formed Ni phase will be very low and therefore undetectable by XRD.

ii) Catalysts promoted with MgO (AK4 - AK6)

The TPR profiles obtained for samples AK4 - AK6 are shown in Figs.3.6(a)-(c). These differ dramatically from those obtained for the $Al_2O_3$ promoted samples. The addition of 1 wt% of MgO of the NiO weight caused the dominant peak maximum now to shift to 700 K (cf. 685 K for $Al_2O_3$) again with a shoulder visible at ~815 K (Fig.3.6(a)). For 5wt% MgO addition the first maxima had moved to 735 K and had become less well pronounced, while the second shoulder was at ~840 K (Fig.3.6(b)). Addition of 10wt% MgO again caused the main peak maximum to shift to a higher temperature (~860 K) (Fig.3.6(c)).

Due to their similar structures, NiO and MgO are completely miscible and therefore have the propensity to form NiO-MgO solid solutions [13]. The formation of such solid solutions is well known for systems where NiO is supported on magnesia and the difficulty associated with their reduction has been reported [14] [15]. Studies carried

out by Narayanan and Sreekanth [14] on the NiO-MgO system showed that the interaction between NiO and MgO is a facile process which starts at 673 K and is further facilitated with increasing calcination temperature. Hahn et al [16] also reported that high temperatures favour the formation of nearly ideal solid solutions of nickel and magnesium oxide, whereas at low temperatures less well-crystallised or mixed spinels may be formed.

Since the MgO promoted catalysts prepared in this study were calcined at 823 K, the possibility of forming a nickel/magnesia phase is highly likely and the XRD data presented in Fig.3.2 did suggest the presence of both $MgNiO_2$ and $Mg_{.4}Ni_{.6}O$ phases. From the TPR profiles it is evident that on higher loading of MgO the NiO-MgO interaction becomes more pronounced and thus reduction becomes increasingly more difficult. This is reinforced by the increase observed in the reduction activation energies, displayed in Table 3.1.

iii) Catalysts promoted with $La_2O_3$ (AK7 - AK9)

The addition of $La_2O_3$ to the $NiO/Al_2O_3$ catalysts gave rise to a situation quite different from that produced by the addition of $Al_2O_3$ and MgO, as illustrated by the TPR profiles in Figs.3.7(a)-(c). Addition of 1wt% $La_2O_3$ of the NiO weight caused the dominant peak maximum to shift to a lower temperature at 673 K (cf. 685 K for $Al_2O_3$) and gave rise to two shoulders at ~510 K and ~770 K (Fig.3.7(a)). On addition of 5wt% $La_2O_3$ the main peak in the TPR profile was still present at 672 K, however both shoulders were now less well pronounced (Fig.3.7(b)). Increasing the $La_2O_3$ loading to 10wt% of the NiO resulted in the loss of the high temperature shoulder altogether, with the main peak maximum still present at 670 K (Fig.3.7(c)).

It appears that the addition of $La_2O_3$ to the $NiO/Al_2O_3$ catalysts may have given rise to a $Ni/La_2O_3$ phase which was more easily reduced, although there was no evidence in the XRD data (Fig.3.3) that any $NiO\text{-}La_2O_3$ compound formation had occurred. This may of course be due to the fact that the concentration of the phase was so small, given the small amounts of $La_2O_3$ added, that it was unable to be detected by means of XRD.

There was also no evidence of any NiO interaction with the $\alpha$-$Al_2O_3$ support and so the difference in reduction kinetics observed cannot be ascribed to the formation of $NiAl_2O_4$ or any precursors.

Table 3.1 presents a comparison of the temperatures corresponding to the maximum rate of reduction ($T_{max}$) of the prepared catalyst samples AK1 - AK9. The reduction activation energies ($E_r$) for each of the samples are also displayed. The reduction activation energy is determined from the temperature of the maximum rate of reduction by solving the following equation at that temperature

$$E_r/RT^2_m - [H_2]\, A_r/\beta\, e^{-Er/RTm} = 0 \qquad (3.3)$$

where $E_r$ is the reduction activation energy (J $mol^{-1}$), $A_r$ is the reduction pre-exponential factor, $T_m$ is the temperature of the maximum reduction rate (K), $\beta$ is the heating rate (K $s^{-1}$), R is the Boltzmann constant (J $K^{-1}$), and $[H_2]$ is the gas phase concentration of hydrogen. A pre-exponential term of $10^{13}$ $cm^3$ $mol^{-1}$ $s^{-1}$ is assumed.

Integration of the area under the $H_2$ curves in each reduction profile enabled the number of moles of $H_2$ consumed during the reduction rection to be calculated . Since the number of moles of NiO available for reduction is known, the extent of reduction for each sample was determined (see Appendix 1).

### 3.5 Total Surface Area (TSA) measurements

The TSA's of catalysts AK1-AK9 were determined using the following procedure. 0.3g of catalyst (300-350μm finings) was loaded into a quartz U-tube and the U-tube placed inside a cylindrical furnace. The sample was pre-treated for 2 hours under a $N_2$ stream (25 $cm^3$ $min^{-1}$, 1 bar) at 873 K and then cooled to ambient. Keeping the flow

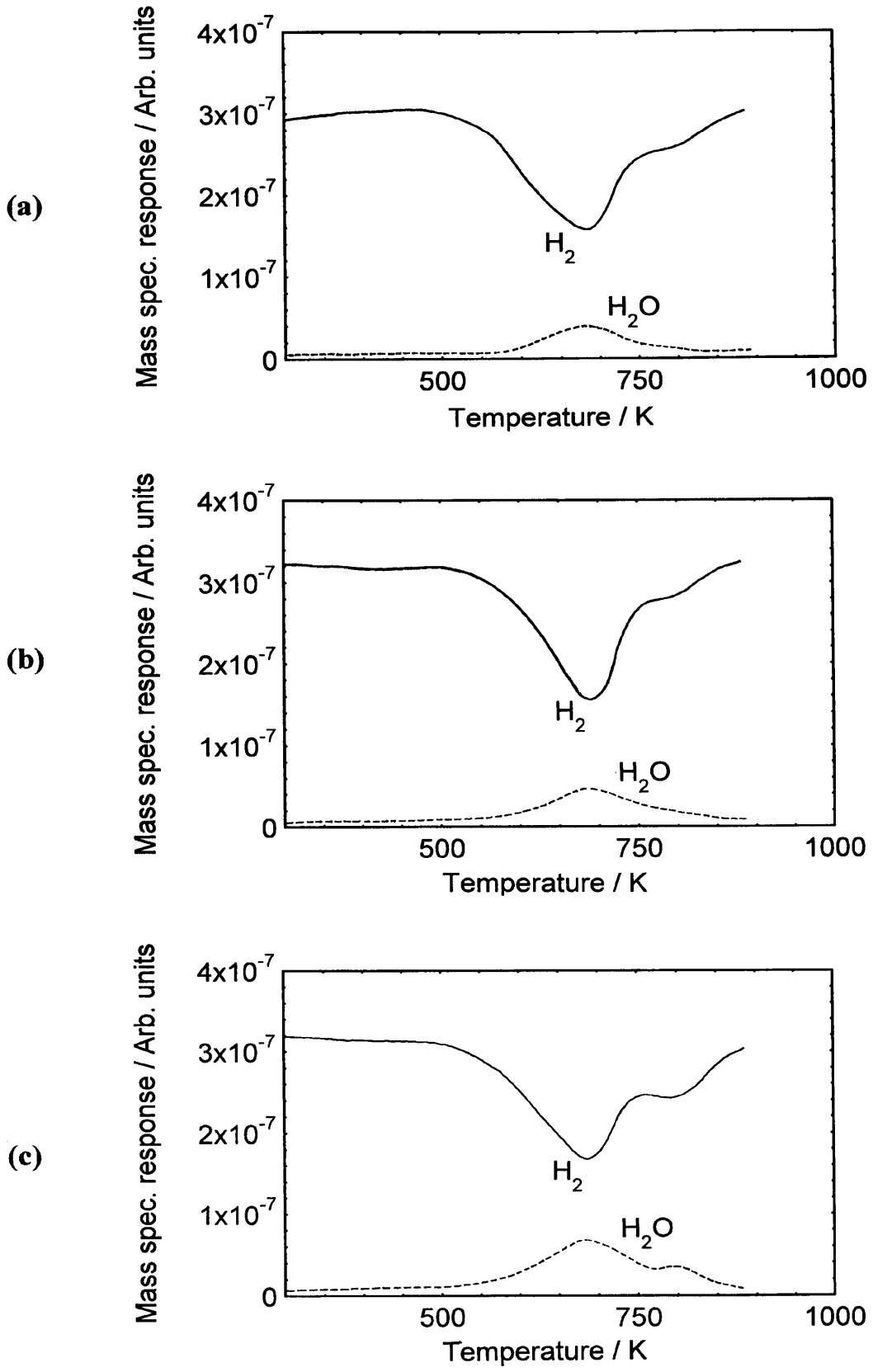


Fig.3.5 Temperature-programmed reduction profiles of $Al_2O_3$ promoted samples (a) AK1 (b) AK2 (c) AK3

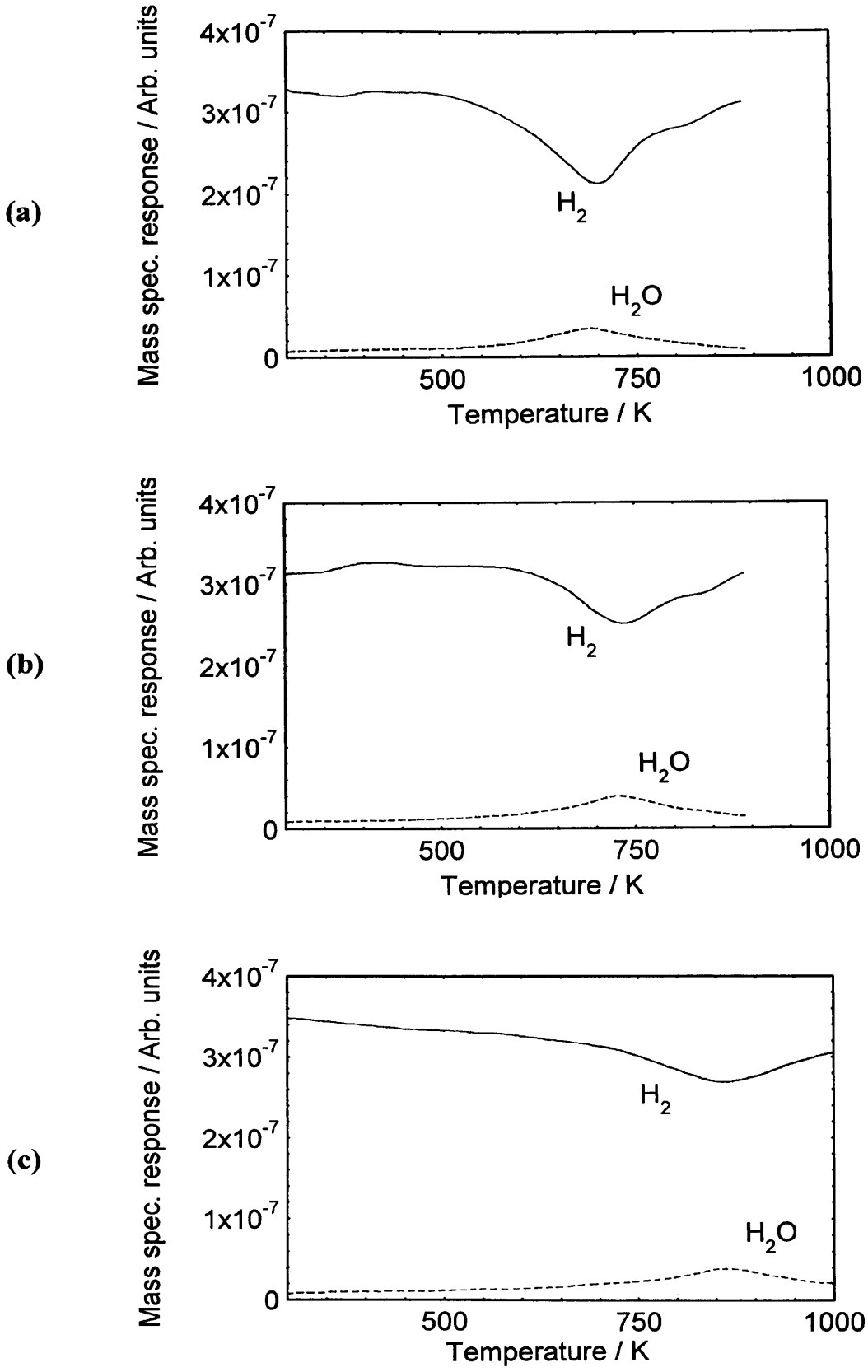


Fig.3.6 Temperature-programmed reduction profiles of MgO promoted samples (a) AK4 (b) AK5 (c) AK6

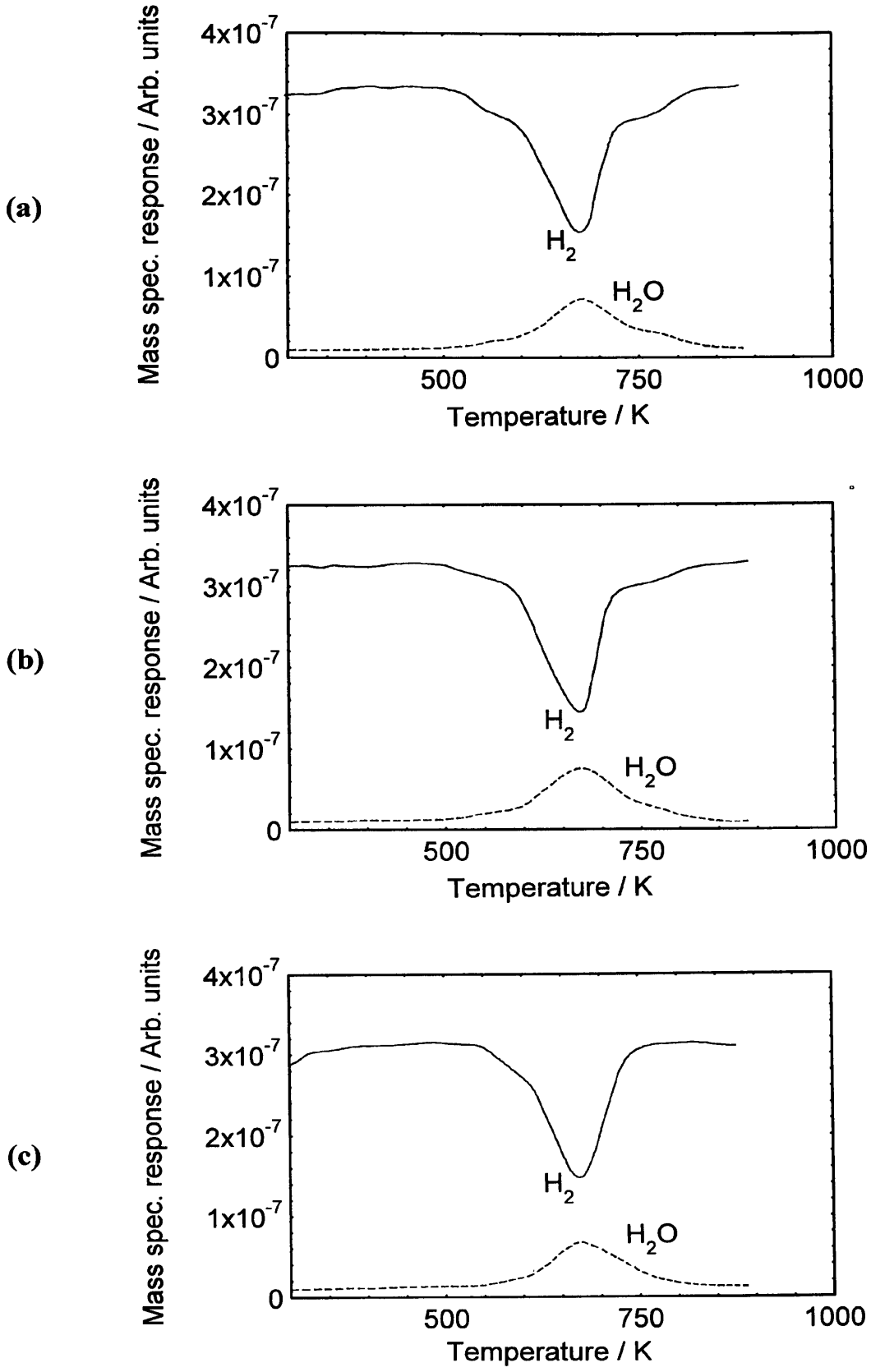


Fig.3.7 Temperature-programmed reduction profiles of $La_2O_3$ promoted samples (a) AK7 (b) AK8 (c) AK9

rate of $N_2$ constant (25 $cm^3$ $min^{-1}$, 1 bar), a helium stream was then introduced at a specific flow rate so as to achieve a $N_2$ partial pressure in the range $0.1<P_{N2}<0.3$.

| Catalyst | $T_{max}$ / K | $E_r$ / KJ $mol^{-1}$ | Extent of reduction / % |
|---|---|---|---|
| AK1 | 685 | 115 | 84 |
| AK2 | 685 | 115 | 81 |
| AK3 | 685 | 115 | 81 |
| AK4 | 700 | 117 | 72 |
| AK5 | 735 | 123 | 67 |
| AK6 | 860 | 144 | 61 |
| AK7 | 673 | 113 | 82 |
| AK8 | 672 | 112 | 79 |
| AK9 | 670 | 112 | 84 |

Table 3.1 Comparison of peak maximum reduction temperatures, reduction activation energies and extents of reduction for catalysts AK1 - AK9

After exiting the mixing chamber, the flow rate of the $He/N_2$ mixture was adjusted using a vent valve so that the mixture flowed at a rate of 25 $cm^3$ $min^{-1}$ at 1 bar through the sample-containing U-tube. The U-tube was then immersed in liquid nitrogen (77 K) and the uptake of $N_2$ monitored using a Thermal Conductivity Detector (TCD). This is shown schematically in Fig.3.8. At time $t_1$ the sample was immersed in liquid nitrogen and a change in the TCD response was observed, corresponding to the adsorption of $N_2$ by the sample at 77 K. After a certain time $t_2$, adsorption was complete and no further change in the TCD response was observed. Once this had occurred the U-tube was removed from the liquid nitrogen and was rapidly heated by placing it in a cylindrical furnace pre-set at 573 K. As soon as the sample became sufficiently warm any

adsorbed $N_2$ began to desorb, which was indicated by a change in the TCD response. This is represented in Fig.3.8 from time $t_3$ onwards. The above procedure was then repeated twice further at that particular $N_2$ partial pressure to obtain an average value for the amount of nitrogen adsorbed. In all, four partial pressures over the range $0.1<P_{N2}<0.3$ were used. The volume of $N_2$ desorbed from time $t_2$ onwards in Fig.3.8 was calculated by integrating the area under the peak and comparing this with the area produced when a known volume of nitrogen was injected into the $He/N_2$ stream and detected by the TCD.

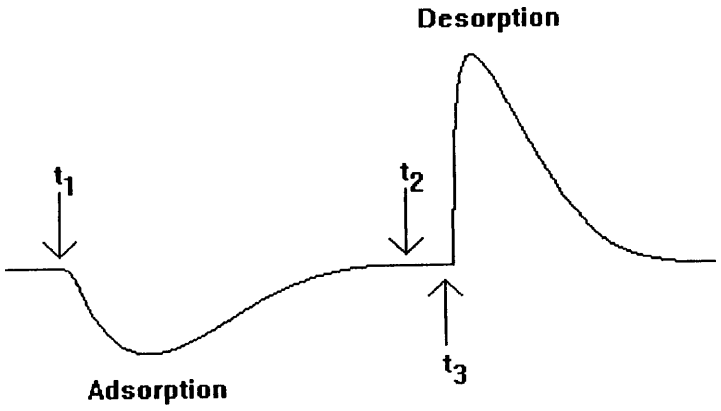


Fig.3.8 Schematic representation of the TCD response for a catalyst under a $N_2/He$ mixture

The TSA of the sample was then determined by using the Brunauer, Emmett and Teller [17] (BET) equation:

$$\frac{P}{(P_O - P)V_a} = \frac{1}{V_m C} + \frac{(C-1)}{V_m C}\frac{P}{P_O} \qquad (3.4)$$

where

$$C = exp\left(\frac{(q_1 - q_v)}{RT}\right)$$

P is the gas pressure, $P_o$ is the saturated vapour pressure of the liquid at the experimental temperature, $V_a$ is the amount of gas adsorbed per gram of catalyst, $V_m$ is

the amount of gas which gives monolayer coverage, $q_1$ is the heat of adsorption of the first layer, $q_v$ is equal to the latent heat of adsorption and T is the adsorption temperature.

By using equation 3.4 on the data obtained, a plot of $P/[(P_o-P)V_a]$ versus $P/P_o$ was obtained and is shown in Fig.3.9. This particular example is for catalyst AK1. Measurement of the gradient and the intercept enabled C and $V_m$ to be evaluated, from which the TSA of the catalyst was determined.

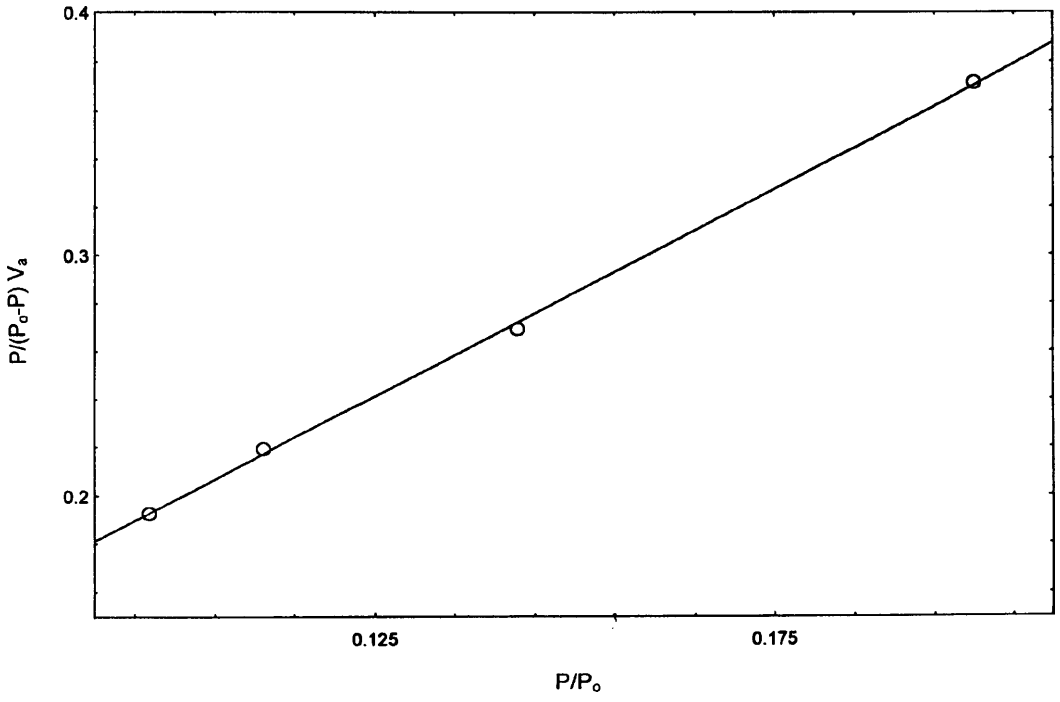


Fig.3.9 Linearisation of the data obtained using the BET equation

The parameter $V_m$ is related to the surface area equation

$$S = 4.371 \times V_m \qquad (3.5)$$

where S is the specific surface area ($m^2\ g^{-1}$) and $V_m$ is the monolayer capacity (ml $g^{-1}$). The factor 4.371 corresponds to the product of the cross-sectional area of a nitrogen atom and the molecular density of a close-packed monolayer. The cross-sectional area of a nitrogen molecule along its shortest axis is 16.2 x $10^{-20}$ $m^2$ $atom^{-1}$ and the molecular density of a close-packed layer of nitrogen molecules is ~2.7 x $10^{19}$ atoms $ml^{-1}$. Table 3.2 shows the results of TSA measurements carried out on samples AK1 - AK9. It can be seen that there is very little difference between the surface areas of each sample. This is not surprising since all were prepared using the same low area (~3$m^2\ g^{-1}$) $\alpha$-$Al_2O_3$ support.

| Catalyst | TSA / $m^2\ g^{-1}$ |
|---|---|
| AK1 | 2.5 |
| AK2 | 2.5 |
| AK3 | 2.9 |
| AK4 | 2.4 |
| AK5 | 2.7 |
| AK6 | 2.6 |
| AK7 | 2.5 |
| AK8 | 2.9 |
| AK9 | 2.8 |

Table 3.2 Total surface areas of catalysts AK1 - AK9 as measured by $N_2$ adsorption at 77 K.

### 3.6 Conclusions

1) XRD analysis of the promoted catalysts showed no indication of Ni-support interactions in any of the samples. Catalysts promoted with $Al_2O_3$ and $La_2O_3$ showed no evidence of Ni-$Al_2O_3$ or Ni-$La_2O_3$ compound formation. However XRD analysis of MgO promoted catalysts did suggest that $MgNiO_2$ and $Mg_{.4}Ni_{.6}O$ phases had been formed which was confirmed by temperature-programmed reduction.

2) Temperature-programmed reduction showed that the addition of $Al_2O_3$, MgO and $La_2O_3$ promoters had a profound effect on the nature of the nickel oxide catalyst presursors. This suggested that addition of $Al_2O_3$ and $La_2O_3$ to the catalysts may also have given rise to formation of Ni-$Al_2O_3$ and Ni-$La_2O_3$ phases which were present in too low a concentration to be detected by means of XRD.

3) Total surface area measurements of the prepared catalysts by $N_2$ adsorption at 77 K revealed areas ranging from 2.4 to 2.9 $m^2\ g^{-1}$, which was in good agreement with the surface area expected for $\alpha$-$Al_2O_3$ (~3$m^2\ g^{-1}$).

## References


[1] Rostrup-Nielsen, J.R., in 'Catalytic Steam Reforming', Springer-Verlag, 1984.

[2] Richardson, J.T., Lei, M., Turk, B., Forster, K. and Twigg. M.V., *Applied Catalysis A: General*, **110**, 217, 1994.

[3] Boldyrev, V.V., Bulens, M. and Delmon, B., The Control and Reactivity of Solids, Elsevier, Amsterdam, 1979.

[4] Coenen, J.W.E., Preparation of Catalysts II (B.Delmon, P. Grange, P. Jacobs, and G.Pocelet, Eds.), Elsevier, Amsterdam, 1979.

[5] Koga, Y. and Harrison, L.G. in 'Comprehensive Chemical Kinetics Vol. **21**', Bamford, C.H., Tipper, C.F.H. and Compton, R.G. (Eds.), Elsevier, Amsterdam, 1984.

[6] Richardson, J.T., Turk, B., Lei, M. and Forster, K., *Applied Catalysis A: General*, **83**, 87, 1992.

[7] Bhalia, S., Beltramini, J. and Do, D.D., *Catalysis Today*, **7**(3), 309, 1990.

[8] Takemura, Y., Yamamoto, K. and Morita, Y., *Int. Chem. Eng.*, **7**, 737, 1967.

[9] Blume, H., Becker, K., Engels, S., Hille, J., Maye, H. and Richter, K., *Z. anorg allg. Chem.*, **405**, 211, 1974.

[10] Alzamore, L.E., Ross, J.R.H., Kruissink, E.C.and van Reijnen, L.L., *J. Chem. Soc. Faraday Trans. I*, **77**, 665, 1981.

[11] Cimino, A., Lo Jacaono, M. and Schiarello, M., *J. Phys. Chem.*, **75**, 1044, 1971.

[12] Gavalas, G.R., Phichitkul, C. and Voecks, G.E., *J. Catal.*, **88**, 54, 1984.

[13] Nussler, H.B. and Kubaschewski, O., *Z. Phys. Chem. (NF)*, **121**, 187, 1980.

[14] Narayanan, S. and Sreekanth, G., *J. Chem. Soc. Faraday Trans.*, **89**(6), 943, 1993.

[15] Arena, F., Frusteri, F., Parmaliana, A. and Gordano, N., *React. Kinet. Catal. Lett.*, **42**, 121, 1990.

[16] Hahn, Jr., W.C. and Muan, A., *J. Phys. Chem. Solids*, **19**, 338, 1961.

[17] Brunauer, S., Emmett, P.H. and Teller, E., *J. Am. Chem. Soc.*, **60**, 309, 1938.

# 4

# DECOMPOSITION OF n-BUTANE OVER PROMOTED $NiO/Al_2O_3$ CATALYSTS AND OXIDATION OF CARBONACEOUS DEPOSITS

## 4.1 Introduction

The interaction of hydrocarbons with metal surfaces can result in a variety of reactions, one of which is the formation of filamentous carbon. This type of material is formed exclusively in systems where a catalyst is present and is believed to involve the interaction and subsequent decomposition of the hydrocarbon at particular faces of the metal [1]. Following hydrocarbon decomposition, carbon species diffuse through the catalyst particle and eventually precipitate at the rear surfaces to form the filament structure. The postulate that carbon diffusion through the catalyst particle is the rate-determining step is supported by the agreement between the measurements of activation energies for filament growth with those for carbon diffusion through the respective metals.

All hydrocarbons used as the reactant feed type in steam reforming have different reactivities and, most importantly, disparate tendencies to generate carbon. Heavy naphtha feedstocks in particular show a considerable propensity for carbon deposition [2]. Environmental legislation in North America has imposed ever more strict limits on emission of aromatics from car exhausts resulting in a reformulation of gasoline and a concomitant glut of $C_4$ hydrocarbons (butane). There is therefore an increasing amount of this valuable hydrocarbon available for transformation into hydrogen via steam reforming. Unfortunately, very little research exists concerning the interaction of butane with $Ni/Al_2O_3$ reforming catalysts.

The purpose of this chapter therefore, is to use temperature-programmed reaction (TPRn) of butane to investigate the kinetics and mechanism of the butane decomposition pathway over differently promoted $NiO/Al_2O_3$ catalysts. In the previous chapter it was shown that the addition of $Al_2O_3$, MgO and $La_2O_3$ to the $NiO/Al_2O_3$ catalysts had a profound effect on the nature of the Ni. Thus TPRn of butane will be used to determine whether the added promoters have any effect on the butane decomposition pathway and if they provide any resistance to carbon formation on the catalysts.

The nature of the carbon deposited by the TPRn reaction will be investigated using Temperature-programmed oxidation (TPO) which will evaluate its reactivity in $O_2$ and enable the amount of carbon removed to be deduced. Transmission electron microscopy (TEM) will be used to determine the morphology of carbonaceous deposits. Following the removal of carbon by TPO, the n-butane TPRn will be repeated to investigate whether regeneration effects the morphology of the nickel and if so, how this in turn influences the kinetics of the butane decomposition.

## 4.2 Studies carried out on $NiO/Al_2O_3$ promoted with 1wt% $Al_2O_3$ (AK1)

### 4.2.1 Temperature-programmed reaction (TPRn) of n-butane on AK1

The catalyst (0.5g) was firstly pre-treated by heating in a 100% helium stream (25 $cm^3$ $min^{-1}$, 1 bar, 10 K $min^{-1}$) from ambient to 873 K and was maintained at that temperature for 2 hours. After cooling to ambient under helium, the flow was switched to a hydrogen-helium stream (5% $H_2$, 25 $cm^3$ $min^{-1}$, 1 bar) and the catalyst was reduced by raising the temperature from ambient to 873 K at 3 K $min^{-1}$. The catalyst was held at 873 K for 16 hours under the hydrogen-helium stream. Following reduction, the flow was switched to helium once more and the sample cooled to ambient. The flow was then switched to an n-butane-helium stream (2% n-butane, 25 $cm^3$ $min^{-1}$, 1 bar) and the catalyst was heated under the flowing gas from ambient to 1023 K at a rate of 5 K

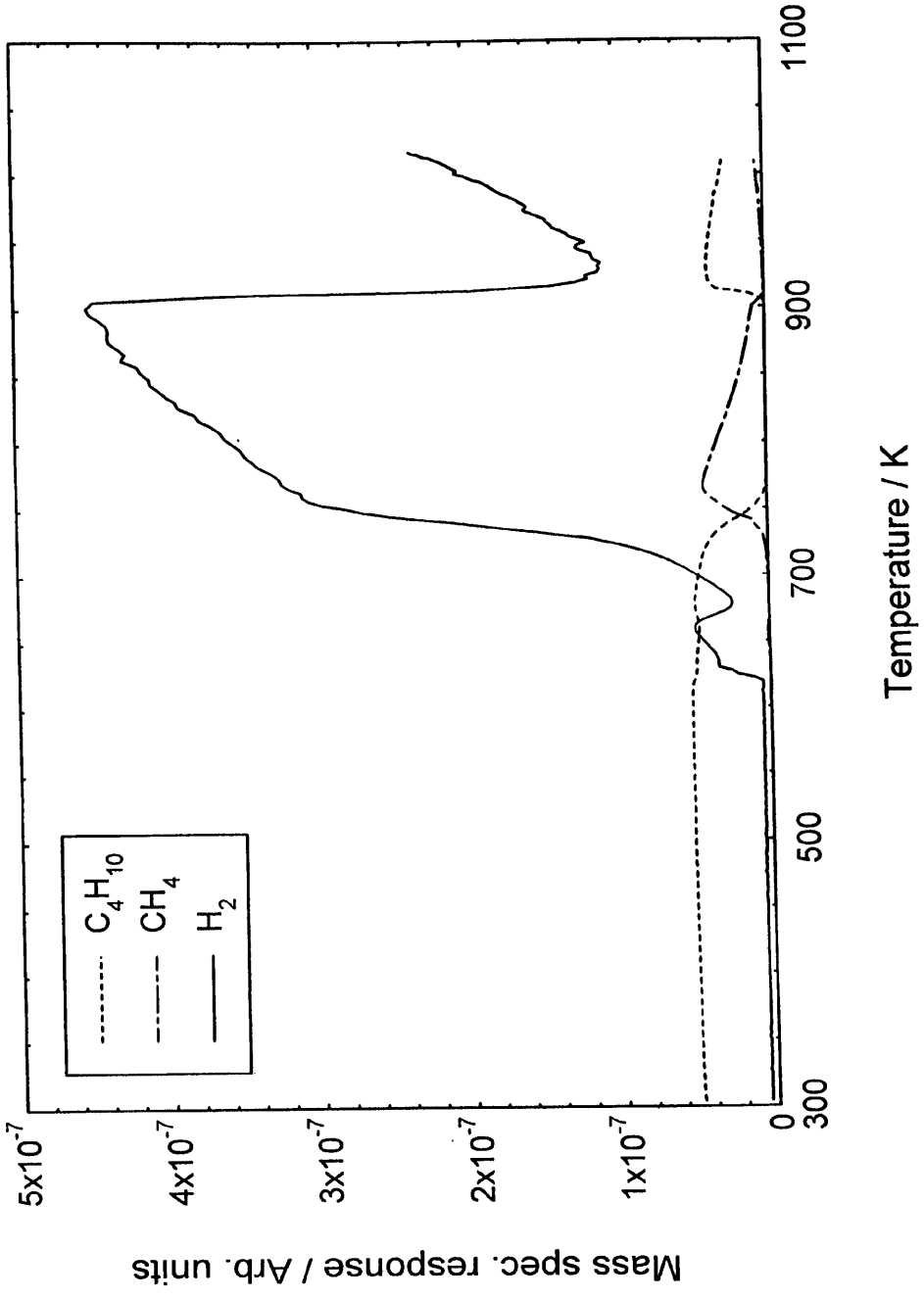


Fig.4.1 TPRn of n-butane on catalyst AK1

$min^{-1}$. The rate of the catalytic decomposition of n-butane was monitored by continuously following the hydrogen produced on the mass spectrometer.

The n-butane TPRn spectrum obtained for catalyst AK1 is shown in Fig. 4.1 No butane decomposition was observed below 620 K. The onset of hydrogen evolution occurred at 620 K giving rise to a small peak with a maximum at 660 K. Following the minimum at 678 K a rapid increase in hydrogen evolution was observed and a considerably larger peak was produced, which cut off sharply at 910 K. Methane was also formed from 725 K, maximising at 765 K and cutting off at the second minimum of $H_2$ evolution.

### 4.2.2 The morphology of the carbonaceous deposits

The morphology of the carbonaceous deposits generated by the decomposition of n-butane on AK1 was studied by transmission electron microscopy (TEM). The sample was prepared for microscopy as follows. Following the completion of the n-butane TPRn experiment, the flow was switched to helium and the sample was cooled to ambient. When completely cool, the carburized catalyst was discharged and pretreated by ultrasonic dispersion in ethanol. A small drop of the suspension was then deposited onto a holey carbon film supported by a copper grid and the ethanol evaporated to dryness. (All subsequent TEM samples were prepared in the same manner). The electron micrograph obtained is displayed in Fig.4.5. (See page 116)

It was found that the TPRn of n-butane up to 1023 K on sample AK1, produced filamentous carbon. The filaments had a central channel running down their length and were ~25 nm in diameter. Nickel crystallites were located at the top of the filaments and were encapsulated by carbon. Boellaard et al [3] described the existence of two types of filamentous carbon, between which there is a clear distinction. Primary filamentous carbon is characterised by a filament diameter which is equal to that of the nickel particle at the tip. Pyrolytic filamentous carbon is recognised by a filament diameter which exceeds the diameter of the original nickel particle, the nickel particle appearing 'trapped' within the pyrolytic carbon. In addition Rostrup-Nielsen [4] has

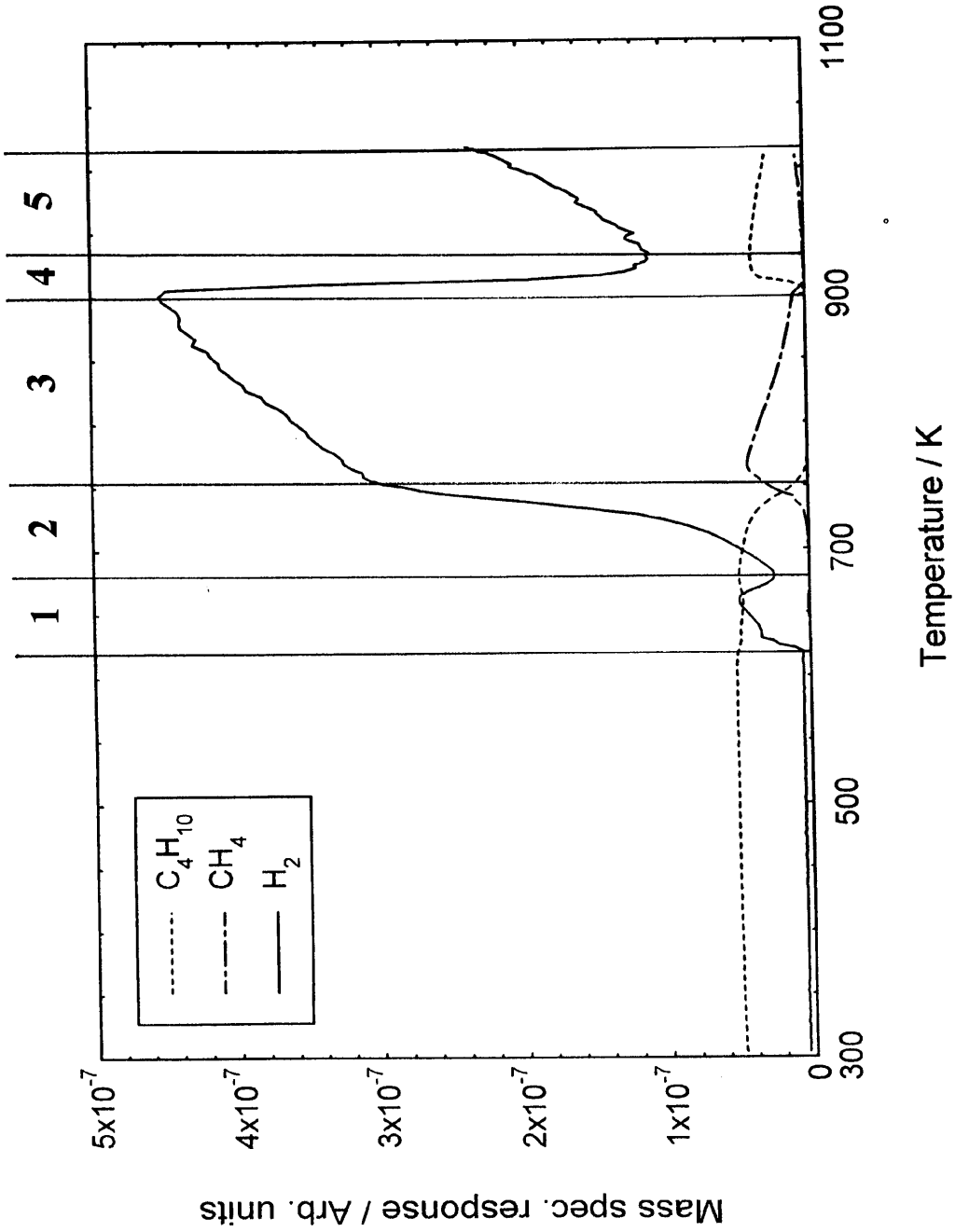


Fig.4.2 Temperature dependence of hydrogen evolution falling into 5 distinct regions

reported that pyrolitic filamentous carbon is formed by thermal cracking of hydrocarbons at temperatures above 870 K.

4.2.2.1 Explanation of the butane TPRn profile

As described in detail in Chapter 1, the mechanism of growth of carbon filaments is proposed to involve the diffusion of carbon through a metal particle and eventual precipitation at the rear of the metal crystallite [5]. This model can thus be used to satisfactorily explain the n-butane TPRn profile obtained for catalyst AK1. It is evident from Fig.4.1 that the temperature dependence of the hydrogen evolution falls into five distinct regions. These regions are clearly illustrated in Fig.4.2.

**Region 1** - The small peak observed between 620 and 680 K is due to encapsulation of the Ni by carbon (vide infra - Chapter 5, section 5.2.2). Over this temperature range the surface coverage of decomposition fragments can be expected to increase on the nickel component of the catalyst until the surface is completely poisoned by carbonaceous deposits. Further deposition will not occur until the carbon is removed by diffusion through the bulk of the nickel crystallite. Hadden et al [2] similarly found that initial dehydrogenation of 5% propane over a $Ni/Al_2O_3$ catalyst (10% w/w) commenced at 513 K showing a gradual increase until a temperature of 625 K was obtained, afterwhich a rapid increase in hydrogen production was observed. Integration of the area under the small $H_2$ peak in Region 1 (620 - 680 K) enabled the amount of hydrogen produced to be quantified and from this the amount of carbon deposited was determined. The amount of carbon formed was $7.2 \times 10^{19}$ atoms $g^{-1}_{cat}$ (Table 4.1). Throughout this chapter, carbon formed in Region 1 will be referred to as 'low temperature carbon' and will be expressed as such in tables. Tabulated results of the amounts of carbon formed will also be expressed as an approximate number of monolayers.

**Region 2** - It is likely that the large increase in rate of hydrogen production seen in Region 2 is associated with the increasing availability of surface metal sites, due to a rapid removal of surface carbonaceous species by diffusion through the nickel adsorbent. This diffusion process has been found to commence at temperatures as low as 640 K on nickel surfaces [6] and is believed to be the rate limiting step for carbon filament formation [5]. Further evidence for this conclusion was obtained by calculating the activation energy for the production of hydrogen, in the temperature range 680 - 730 K.

The rate of $H_2$ production can be written as

$$dH_2/dt = k\, P_{C4H10}.S \qquad (4.1)$$

where S is the number of sites on the nickel surface. Due to the large amount of $H_2$ formed, the rate of $H_2$ production can be considered to be zero order in S. Furthermore, since the conversion of butane is small in the region studied, $P_{C4H10}$ can be considered to be constant is constant. Therefore we can write

$$dH_2/dt = A\, e^{(-Ea/RT)} \qquad (4.2)$$

and thus

$$\ln(dH_2/dt) = \ln A - E_a/RT \qquad (4.3)$$

The activation energy for the production of hydrogen, $E_a$, was evaluated by plotting the logarithm of the rate of hydrogen production versus the reciprocal temperature which gave a straight line of slope $-E_a/R$ (Fig.4.3). The plot had a gradient of 18.7 which gave a value for $E_a$ of 155 kJ $mol^{-1}$. This is in good agreement with values obtained from previous studies of diffusion limited carbon filament formation, where the activation energy for diffusion of carbon through nickel has been reported to be in the range 125 - 155 kJ $mol^{-1}$ [5] [7].

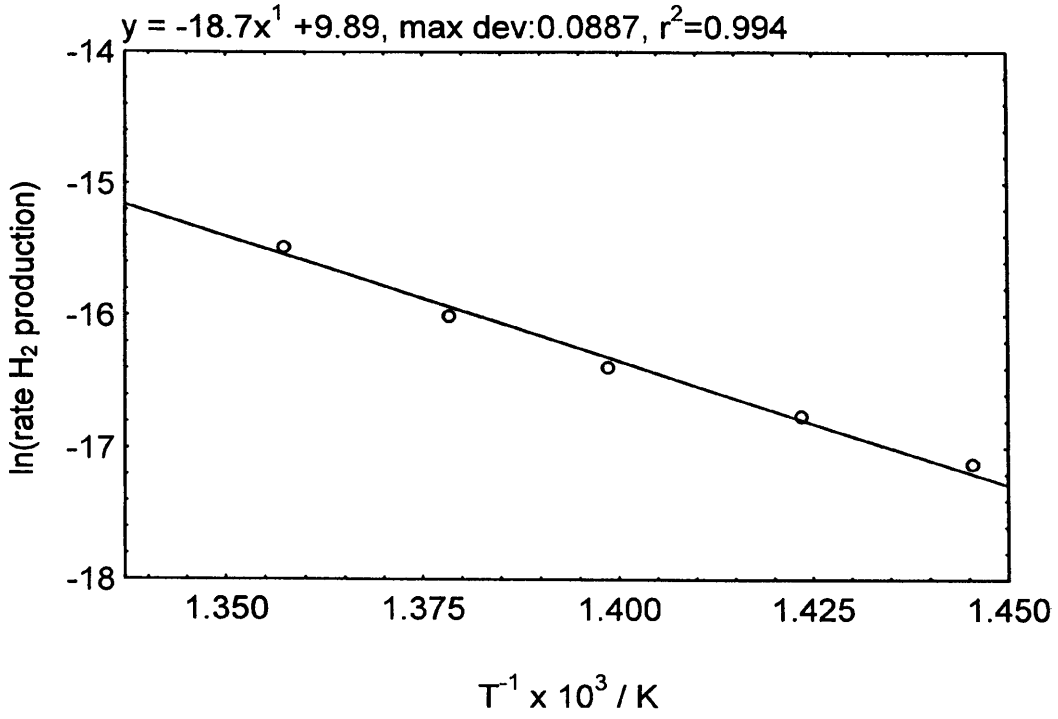


Fig.4.3 Plot of the logarithm of the rate of hydrogen production versus reciprocal temperature

**Region 3** - Between 760 and 900 K gas phase butane at the surface undergoes complete conversion and the rate becomes mass transport limited. This is coupled with the formation of methane. This formation of methane could be the result of the hydrogenation of surface carbon.

**Region 4** - A total cut-off in the rate of hydrogen formation is observed between 895 and 930 K suggesting that the Ni has become completely deactivated due to encapsulation by carbon. The dramatic decrease in rate therefore occurs because no surface metal sites are available for butane dehydrogenation reaction to continue. This is confirmed by the electron micrograph in Fig.4.5 which clearly shows that nickel particles are totally encapsulated. Lobo and Trimm [8] reported that at high temperature (823 - 923 K) adsorbed hydrocarbons may react into a film of nonreactive deposits which may encapsulate and deactivate the nickel surface. The phenomenon

was observed in studies of the decomposition of pure hydrocarbons which formed graphitic encapsulating carbon.

The total amount of carbon formed in Regions 2 - 4 (680 - 930 K) was calculated to be $2.6 \times 10^{21}$ atoms $g^{-1}_{cat}$ (Table 4.1). Carbon formed in these regions will be referred to as 'high temperature' carbon throughout this chapter.

**Region 5** - The increase in rate of $H_2$ production at such a high temperature can be attributed to gas phase cracking of the hydrocarbon feed. According to Rostrup-Nielsen [9] cracking reactions may start at temperatures above ~920 K which lead to the formation of olefins which may easily form carbon by the following reaction:

$$C_nH_m \rightarrow \text{'carbonaceous deposits'} + xH_2 \qquad (4.4)$$

The high temperature carbon or 'pyrolytic carbon' formed encapsulates the catalyst particles and is also deposited on the reactor wall. It has been reported that naphtha reformers with a completely deactivated nickel catalyst will work as a thermal cracker producing olefins [10].

Although the amount of carbon formed in Regions 1 - 4 is of primary interest, the total amount of carbon deduced from the TPRn profile, including that formed in Region 5, will also be quoted. In this case the amount was $3.3 \times 10^{21}$ atoms $g^{-1}_{cat}$ (Table 4.1).

### 4.2.3 Temperature-programmed oxidation (TPO) of carbon formed on AK1

The nature of the carbon formed on the catalysts by the temperature-programmed reaction of n-butane was investigated by removing it from the surface by temperature-programmed oxidation (TPO). The TPRn of n-butane was carried out as described in section 4.2.1. When complete the flow was switched from n-butane to helium and the catalyst cooled to ambient. The flow was then switched to an oxygen-helium stream

(5% $O_2$, 25 $cm^3min^{-1}$, 1 bar) and the temperature was raised from ambient to 1023 K at a rate of 5 K $min^{-1}$.

(See page 115)

The TPO profile obtained is shown in Fig.4.4. Both carbon dioxide and carbon monoxide were found to be the products of this reaction. The onset of $CO_2$ formation occurred at ~650 K and produced a sharp peak maximum at 826 K. CO formation began at ~700 K and showed a marked increase in rate at 825 K, with a sharp cut off at 950 K. The fact that no water was formed during the TPO reaction strongly suggests that the carbonaceous species formed are fully dehydrogenated.

The controlled oxidation of carbon filaments formed on Ni, Fe and Co catalysts carried out by Baker et al [11] revealed that they consisted of a duplex structure of two distinct types of carbon. They found that an inner core consisted of carbon which was easily oxidisable and was surrounded by a skin of more oxygen resistant material. This could suggest that the production of $CO_2$ observed in Fig.4.4 may well be due to the oxidation of the inner channel of the carbon filaments produced, which are clearly visible in the micrograph in Fig.4.5, and the CO is formed as a result of the outer core being oxidised. However the formation of both $CO_2$ and CO as gaseous products of carbon oxidation have never thus far been observed in the literature and therefore it is unlikely that this is the case. The formation of only $CO_2$ has been observed. Analysis of the $CO_2$ peak in the TPO profile reveals that at the peak maximum the partial pressure of $CO_2$ corresponds to $\cong$0.06 atm. Since the partial pressure of oxygen used for the gasification reaction was 0.05 atm, this suggests that the concentration of oxygen in the feed was too low to remove carbon as $CO_2$ only and a depletion of oxygen occurs which results in only a partial oxidation of the remaining carbon to form CO. This argument is supported by the mechanism suggested by Efstathiou et al [12]. In the case of carbon gasification with oxygen, there has not been reported in the literature a detailed kinetic model that describes the TPO process of filamentous carbon. However, Efstathiou et al [12] suggested that a mechanism similar to that proposed for the corresponding hydrogenation process might apply according to the elementary steps:

$$O_2 + 2(s) = 2O(s) \qquad (4.5)$$

$$C + O(s) \rightarrow CO(s) \qquad (4.6)$$

$$CO(s) + O(s) \rightarrow CO_2 + 2(s) \qquad (4.7)$$

where (s) is a site on the nickel surface. The fact that $CO_2$ is generated by the oxygen gasification reaction indicates that following the primary production of CO, $CO_2$ is formed by a secondary reaction of CO with adsorbed oxygen. If however the amount of oxygen is limited, the CO has no further oxygen to react with and the result obtained in Fig.4.4 is observed where the formation of CO is seen to follow that of $CO_2$. In future work these findings could be verified by simply gasifying the carbon formed using a higher concentration of oxygen in the feed and monitoring whether both $CO_2$ and CO are again gaseous products of the reaction.

From the TPO profile, the total amount of carbon oxidised was calculated to be 3.1 x $10^{21}$ atoms $g^{-1}_{cat}$, which indicates that virtually all of the carbon formed from the butane TPRn reaction was removed by oxidation (Table 4.1). A plot of the logarithm of the rate of gasification versus the reciprocal temperature enabled the activation energy for carbon oxidation to be determined (Fig.4.6). The value obtained was 161 kJ $mol^{-1}$ which was in good agreement with the value of the activation energy obtained earlier for the diffusion of carbon through nickel (155 kJ $mol^{-1}$). This result indicates that the gasification of filamentous carbon may well be the reverse of the formation process, as suggested by Figueiredo [13] and Baker [14]. They proposed that the diffusion of carbon through the nickel particle is a common step for both filament formation and gasification. The supply of carbon atoms to the exposed surface takes place by dissolution at the rear of the particle and diffusion through the nickel particle to the front of it. Here a surface reaction then takes place between the carbon species and dissociatively adsorbed reactant gas. The supply of carbon atoms to the exposed nickel surface by diffusion therefore causes the nickel particle to move in the opposite direction to that observed during the filament formation process. The possible

consequences of this phenomenon are reported later in Section 4.2.5, where the oxidation appears to have a profound effect on the surface morphology of the nickel and the subsequent kinetics of the repeated n-butane TPRn.

Unfortunately from the TPO profile obtained in Fig.4.4 it was not possible to conclusively identify the number of carbon species formed during the butane TPRn. However experiments presented in Chapter 5 do go on to identify several different carbon species formed at varying temperatures during the TPRn of butane - vide infra.

### 4.2.4 Re-reduction of catalyst AK1

Following the removal of carbon by TPO, the flow was switched to a helium stream and the sample was cooled to ambient under the flowing gas. When cool, the flow was then switched to a hydrogen-helium stream (5% $H_2$, 25 $cm^3$ $min^{-1}$, 1 bar) and the catalyst was reduced by raising the temperature from ambient to 1023 K at 3 K $min^{-1}$. The catalyst was held at this temperature for 16 hours under the hydrogen helium stream.

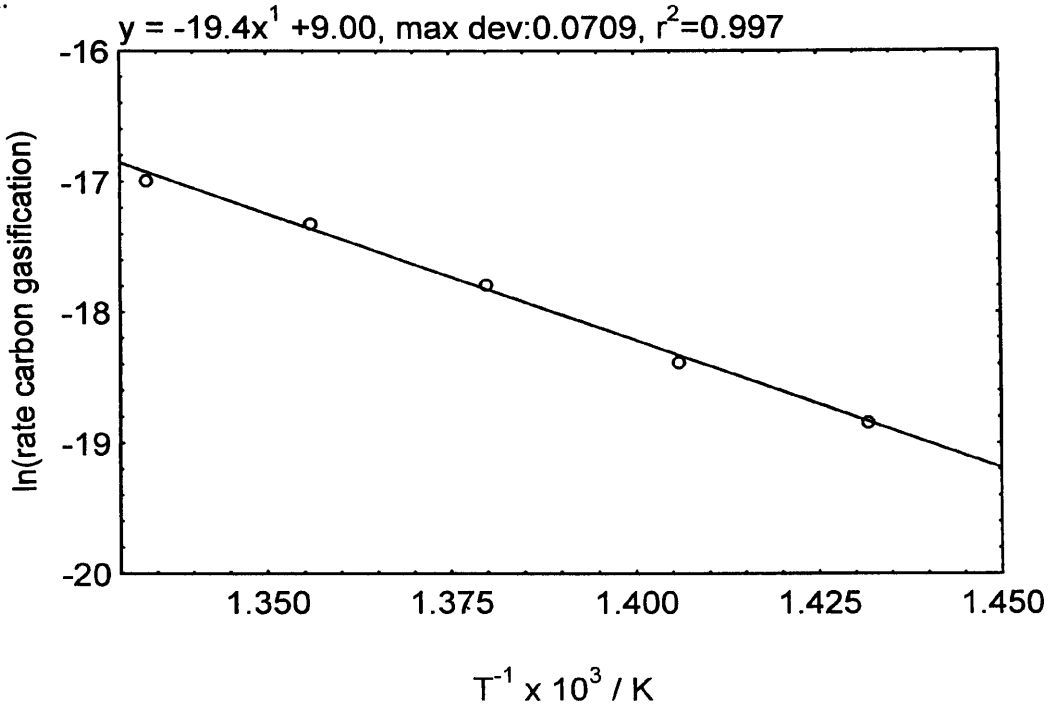


Fig.4.6 Plot of the logarithm of the rate of carbon gasification versus reciprocal temperature

The reduction profile obtained is shown in Fig.4.7. The profile differs markedly from the initial reduction profile obtained for catalyst AK1 (Fig.3.5(a)). The dominant peak maximum has now shifted to a higher temperature at 757 K and a second shoulder is visible at ~925 K.

It is well known that cyclic oxidation-reduction of supported catalysts can cause a redistribution of the metal components [15] as the TPR profile in Fig.4.7 suggests. Oxygen can often oxidise the metal component of the catalyst to alter the shape and size of the metal particles [16]. Subsequent reduction of the metal oxide in hydrogen may then lead to a redispersion of the metal constituent as smaller particles. If the oxidation of carbon filaments is indeed the reverse process of filament formation [13] [14] and the nickel particles do retrace their original path back down the filament, this would also result in a redispertion of nickel on the $Al_2O_3$ support producing a nickel surface of distinctly different morphology. Oxidation of the nickel to NiO during the TPO reaction and subsequent reduction in hydrogen are likely therefore to produce a different TPR profile. This is the case observed for all samples in this chapter. Zielinski [17] has also reported that small nickel oxide crystallites which occur on supported catalysts undergo reduction with less ease than large crystallites of nickel oxide. Thus the shift in temperature of the peak maxima in the re-reduction profiles could also be due to the presence of a larger number of small NiO crystallites.

### 4.2.5 TPRn of n-butane over re-reduced AK1

After reduction of the catalyst the flow was switched to helium and the sample was cooled to ambient. The flow was then switched to an n-butane-helium stream (2% n-butane, 25 $cm^3$ $min^{-1}$, 1 bar) and the catalyst was heated under the flowing gas from ambient to 1023 K at a rate of 5 K $min^{-1}$.

This second n-butane TPRn spectrum obtained for catalyst AK1 is shown in Fig.4.8. A completely different reaction profile was produced to that of the initial butane TPRn shown in Fig.4.1. In this case only two small, broad peaks were observed at ~630 K and ~800 K. A sharp increase in the rate of $H_2$ production was observed from ~850 K.

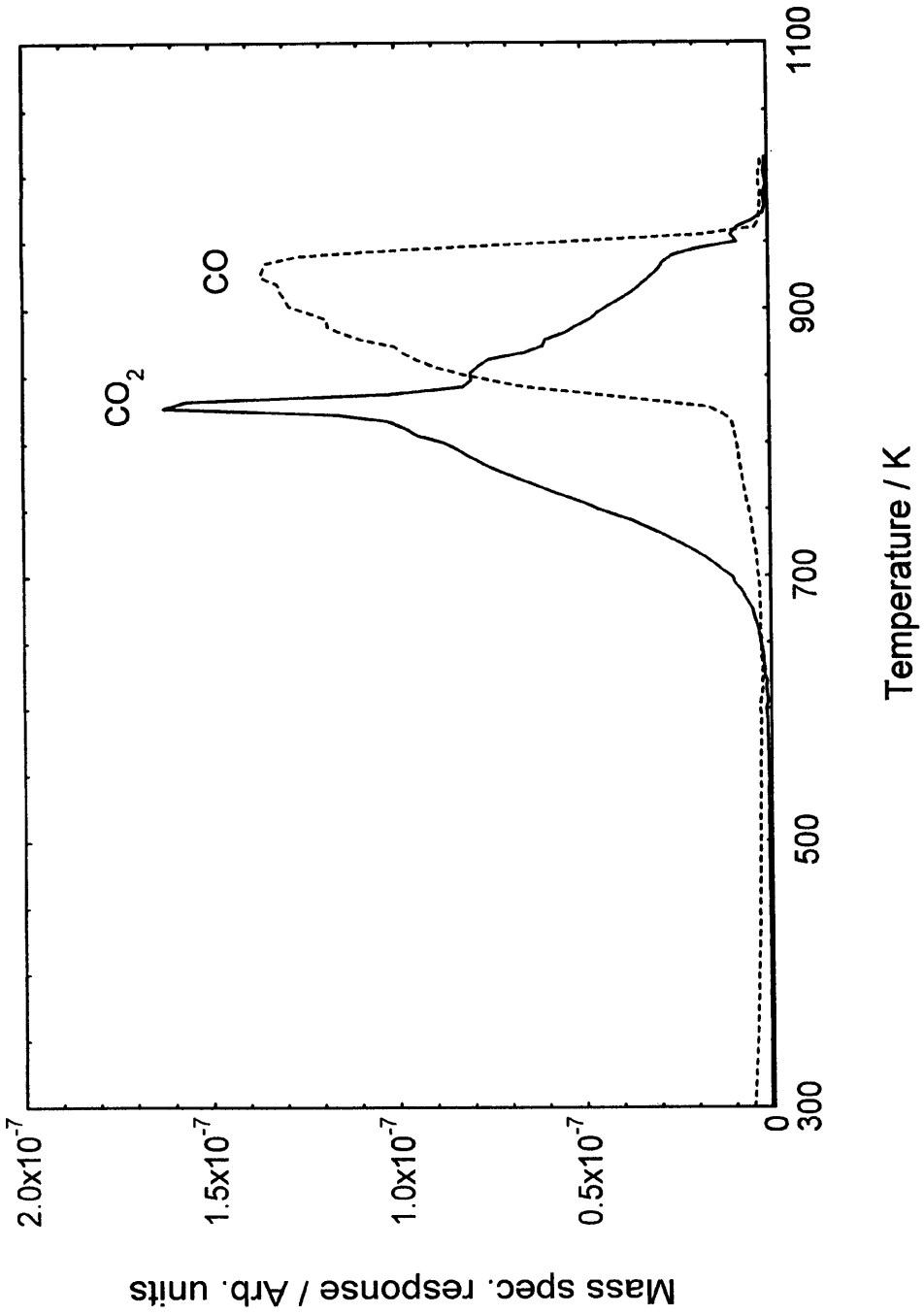


Fig.4.4 TPO of deposited carbon on catalyst AK1

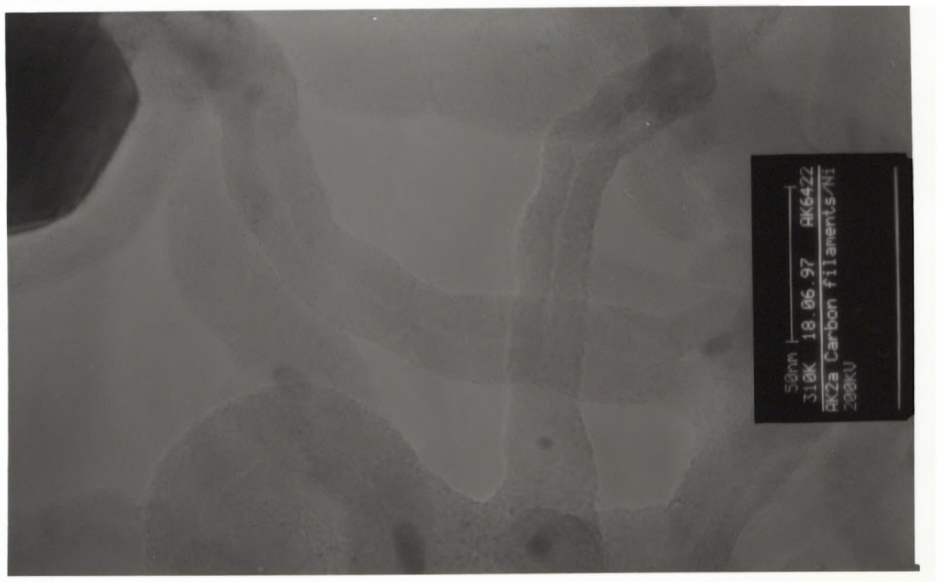


Fig.4.5 Transmission electron micrograph of carbon formed on catalyst AK1 (1023 K)

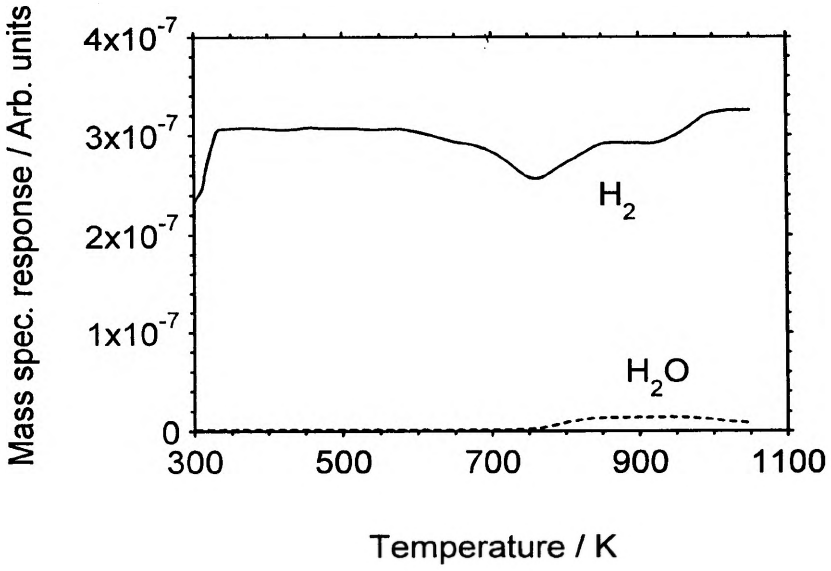


Fig.4.7 TPR profile of regenerated catalyst AK1

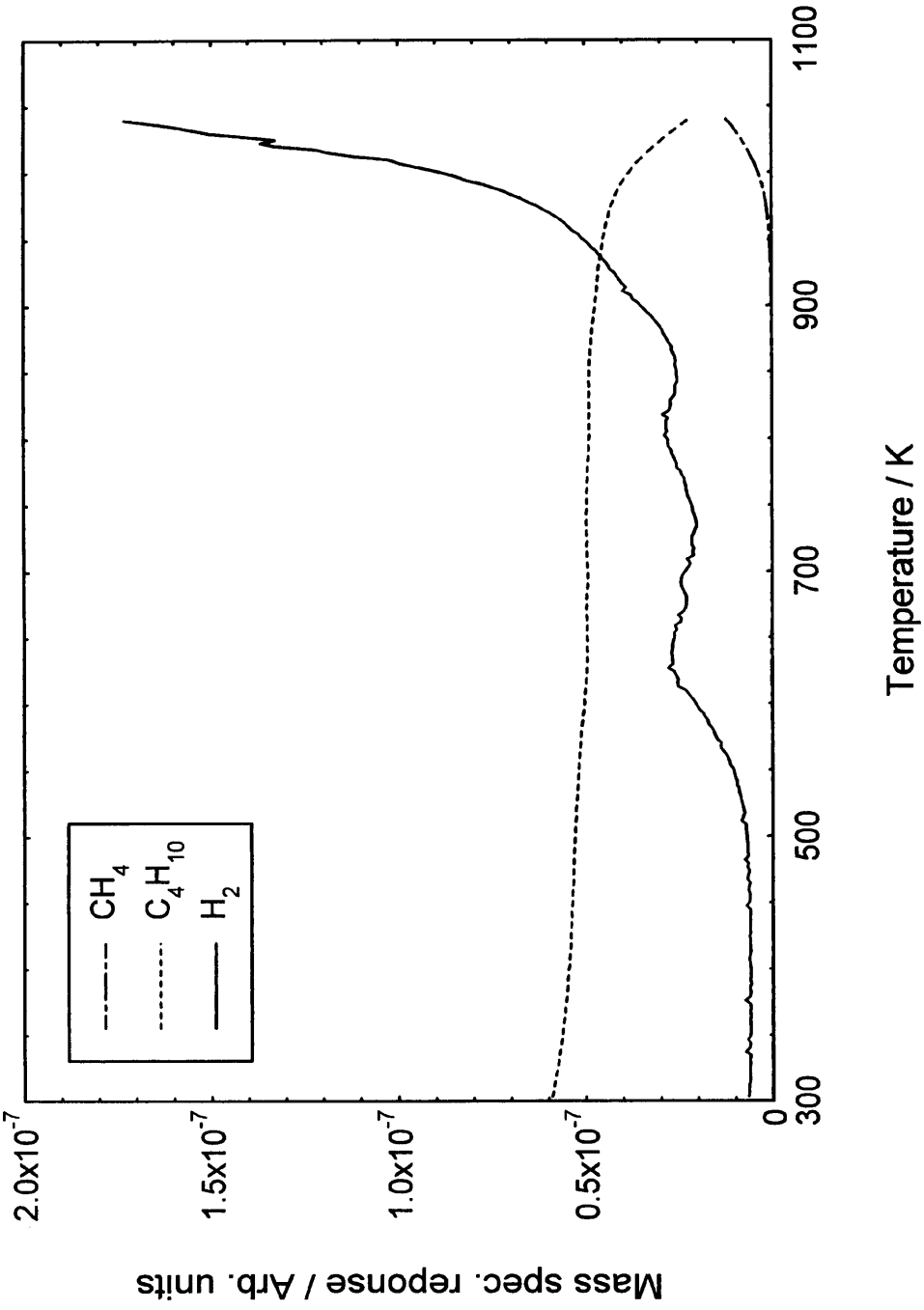


Fig.4.8 TPRn of n-butane on re-reduced catalyst AK1

An approximate deconvolution of the $H_2$ spectrum allowed the amount of carbon formed to be deduced. It should be noted that the amount of carbon formed by gas phase cracking at very high temperatures (>~900 K) was not quantified. The amount of 'low temperature' carbon associated with the first peak was calculated to be 1.6 x $10^{20}$ atoms $g^{-1}_{cat}$. The amount of 'high temperature' carbon associated with the second peak was 9.7 x $10^{19}$ atoms $g^{-1}_{cat}$ (Table 4.1). The absence of the large, high temperature $H_2$ peak as observed in the initial n-butane TPRn (Fig.4.1) suggests that the formation of filamentous carbon was severly inhibited in this case. The total amount of carbon formed up to ~900 K in this second TPRn is approximately 90% less than was formed in the initial TPRn. This remarkable decrease in the amount of carbon formed on the catalyst may therefore be a direct result of the redispersion of the nickel on the support caused by the carbon oxidation reaction. Let us consider the general mechanism proposed for the formation of filamentous carbon [18] [19] which includes:

1). dissociation of the hydrocarbon on the nickel surface to produce chemisorbed carbon atoms;
2). dissolution of carbon in the nickel and bulk and subsequent diffusion to the trailing faces;
3). reconstruction of the nickel crystallite with segregation of the carbon at the rear of the particle, the nickel particle becoming detached from the support matrix by the growing filament.

In the first stage it is assumed that the hydrocarbon is chemisorbed on a dual nickel site followed by successive α-scission of the C-C bonds [9]. The breakage of the carbon-carbon bond has been investigated in detail in connection with the hydrogenolysis reaction. Machiels et al [20] studied the hydrogenolysis at low temperatures of hydrocarbons higher than ethane and found that nickel selectively attacked the ends of the chains by successive α-scission, in contrast to platinum, for instance. Schouten et al [6] studied the interaction of methane with various surfaces of nickel by AES-LEED and found that on (100) and (110) planes, adsorption resulted in complete dissociation into adsorbed carbon atoms. Above ~620 K the carbon atoms were able to diffuse into the bulk nickel. In contrast, no adsorption was observed on the (111) plane. Martin et

al [21] reported the same trend for hydrogenolysis, the (111) plane being less active than other crystal planes. Yang et al [22] studied the segregation process during the growth of filamentous carbon and similarly found that Ni(100) and (110) faces, most abundant at the metal/gas interface, were the most active for hydrocarbon decomposition while the Ni(111) and (311) faces, most abundant at the metal/carbon interface, provided the strongest epitaxial covalent bonds with the basal plane of graphite.

It was described earlier that the oxidation of carbon filaments is believed to be the reverse of the filament forming process whereby carbon diffuses back through the nickel crystallites which retrace their original path by moving in the opposite direction back down the filament [13] [14]. Once oxidation of the filaments is complete it is highly unlikely that the nickel crystallites come to rest on the support as they were originally and therefore the nickel will have a completely different surface morphology. This redispersion of nickel caused by the oxidation results in a completely different distribution of Ni crystallographic faces on the surface which, if predominantly Ni (111), will inhibit the adsorption and subsequent decomposition of butane.

Recent investigations of the interactions of hydrocarbons with well characterised metal surfaces have enabled the intermediate species formed at at the surface of the metal to be identified. Work carried out by Somorjai and his co-workers [23] led to the postulation of the existence of an ethylidyne intermediate from the adsorption of ethylene and acetylene on Pt(111). Initially an arrangement is formed where each carbon atom is bonded to a corresponding metal atom as depicted in Fig.4.9(a). On heating, this conformation is transformed into a structure known as ethylidyne where one of the carbon atoms is attached to three metal atoms as illustrated in Fig.4.9(b). Marshall et al [24] used DRIFTS to study the adsorption of alkenes, ethene and propene on $Ni/Al_2O_3$ at 298 K and also reported the formation of alkylidyne intermediates. They found that the adsorption of ethene and propene gave rise to the corresponding alkylidyne whereas but-1-ene adsorption formed a mixed phase of trans-and gauche-butylidyne conformers. The structures of these various hydrocarbon species are illustrated in Fig.4.10. In each case however, the alkylidyne species proved to be

unstable at ambient temperatures and decomposed to lower hydrocarbon fragments. Ethylidyne was found to decay to a surface methyl species (and then, they presume, surface carbon) while propylidyne decomposed firstly to ethylidyne and in turn to a surface methyl. The mixed phase of trans- and gauche- butylidyne conformers were found to decompose at substantially different rates forming again ethylidyne. If the carbon oxidation reaction causes a redispersion of Ni on the surface it is likely that a redispersion of the $Al_2O_3$ promoter also occurs. As a result the $Al_2O_3$ may block a substantial number of Ni ensembles required for the formation of ethylidyne, by doing so further suppressing the formation of carbon.

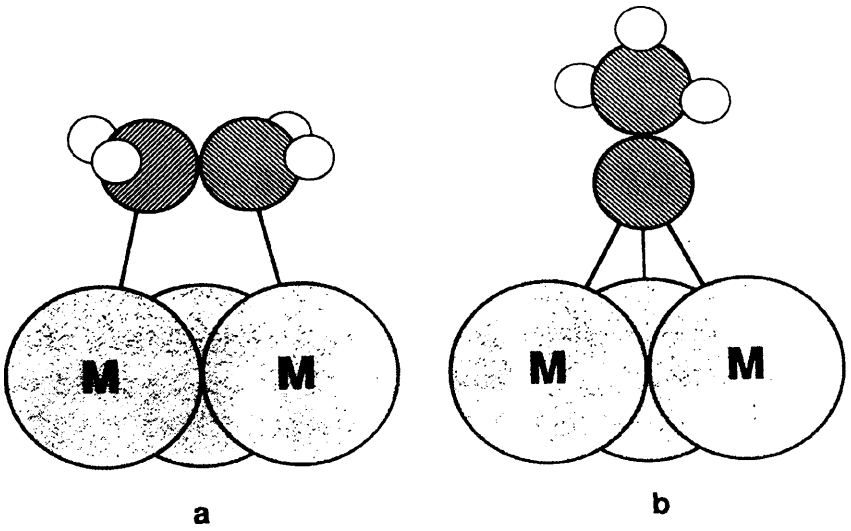


Fig.4.9 Structural arrangement for (a) hydrocarbon bonded parallel to metal surface and (b) hydrocarbon bonded to metal in the ethylidyne conformation

## 4.3 Studies carried out on $NiO/Al_2O_3$ promoted with 5wt% $Al_2O_3$ (AK2)

### 4.3.1 TPRn of n-butane on AK2

The experiment was carried out using the same procedure as detailed in Section 4.2.1. The n-butane TPRn spectrum obtained for catalyst AK2 is shown in Fig.4.11. The reaction profile is very similar to that obtained for sample AK1 (Fig.4.1). The onset of

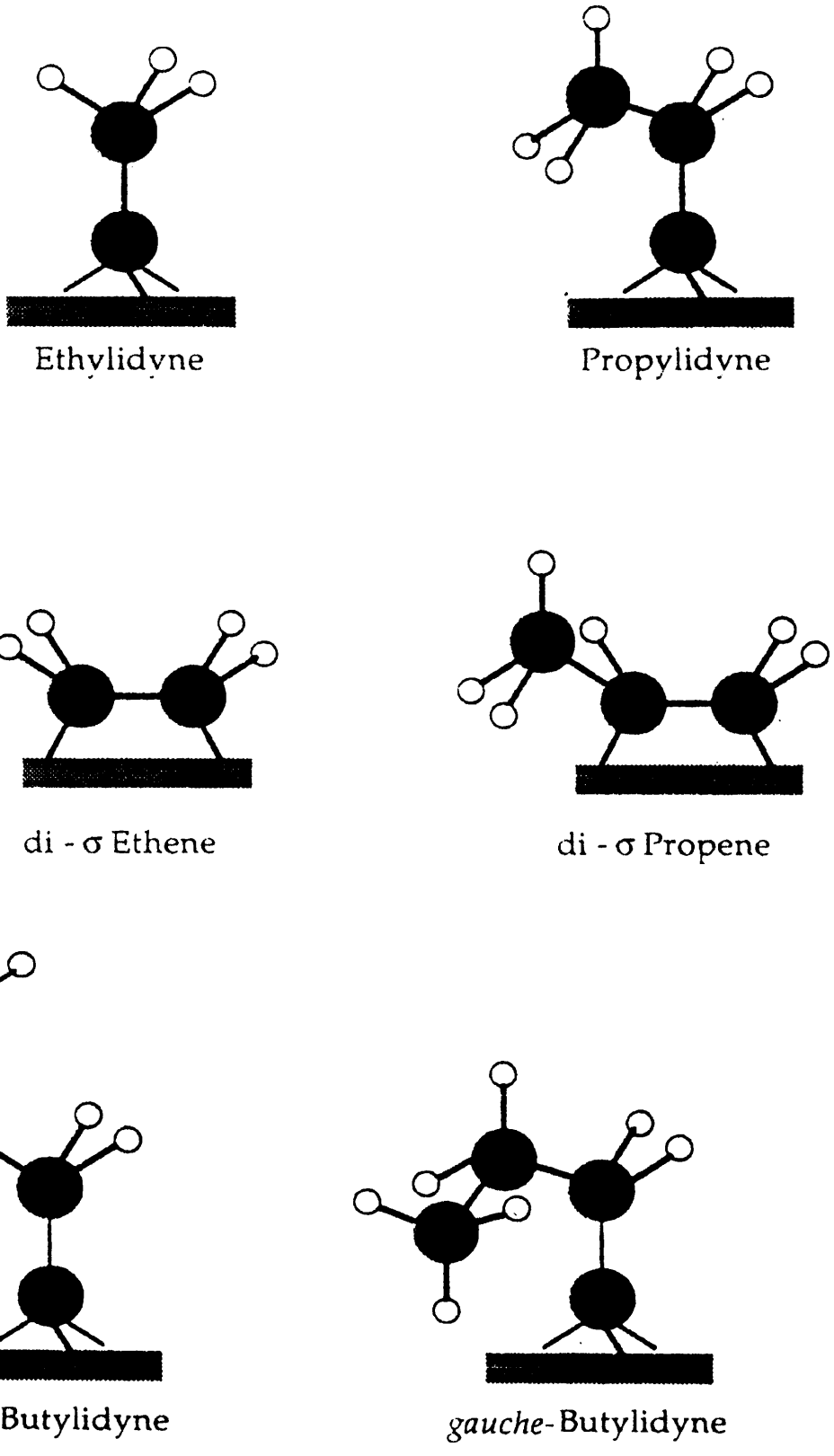


Fig.4.10 Illustrative structures of the various surface hydrocarbon species identified by Marshall et al [24]

hydrogen evolution commenced at 640 K with a peak maximum at 653 K followed by a minimum at 680 K. A further rise in $H_2$ evolution followed, producing a substantailly larger peak which cut off sharply at 891 K. Methane formation commenced at 740 K, maximising at 794 K and cut off at the second minimum of $H_2$ evolution.

### 4.3.2 The morphology of the carbonaceous deposits

The morphology of the carbonaceous deposits generated by n-butane decomposition was studied by TEM. The electron micrograph obtained is displayed in Fig.4.13. Carbon filaments were again produced which had a central channel running down their lengths. The widths of the filaments ranged from ~30 - 100 nm and nickel particles were again present at the tops of the filaments. The nickel particles were encapsulated by carbon.

The temperature dependence of hydrogen evolution in the butane TPRn profile for sample AK2 again falls into 5 distinct regions. Since the profile for sample AK2 is very similar to that obtained for AK1, the features in each region can be explained using the same arguments as were detailed in Section 4.2.2.1, viz:-

**Region 1** - The small peak observed between 640 and 680 K is due to the encapsulation of nickel by carbon. The amount of carbon formed in this region was calculated to be $6.4 \times 10^{19}$ atoms $g^{-1}_{cat}$ (Table 4.1).

**Region 2** - The exponential increase in the rate of hydrogen production is due the diffusion of surface carbonaceous species through the nickel which is the rate limiting step for carbon filament formation. The activation energy for the production of hydrogen in the temperature range 680 - 730 K was calculated to be 137 kJ $mol^{-1}$, which again is in good agreement with literature values for the diffusion of carbon through nickel [5] [7].

**Region 3** - Between 775 and 900 K the rate is mass transport limited. The formation of methane is also observed which may be due to hydrogenation of surface carbon.

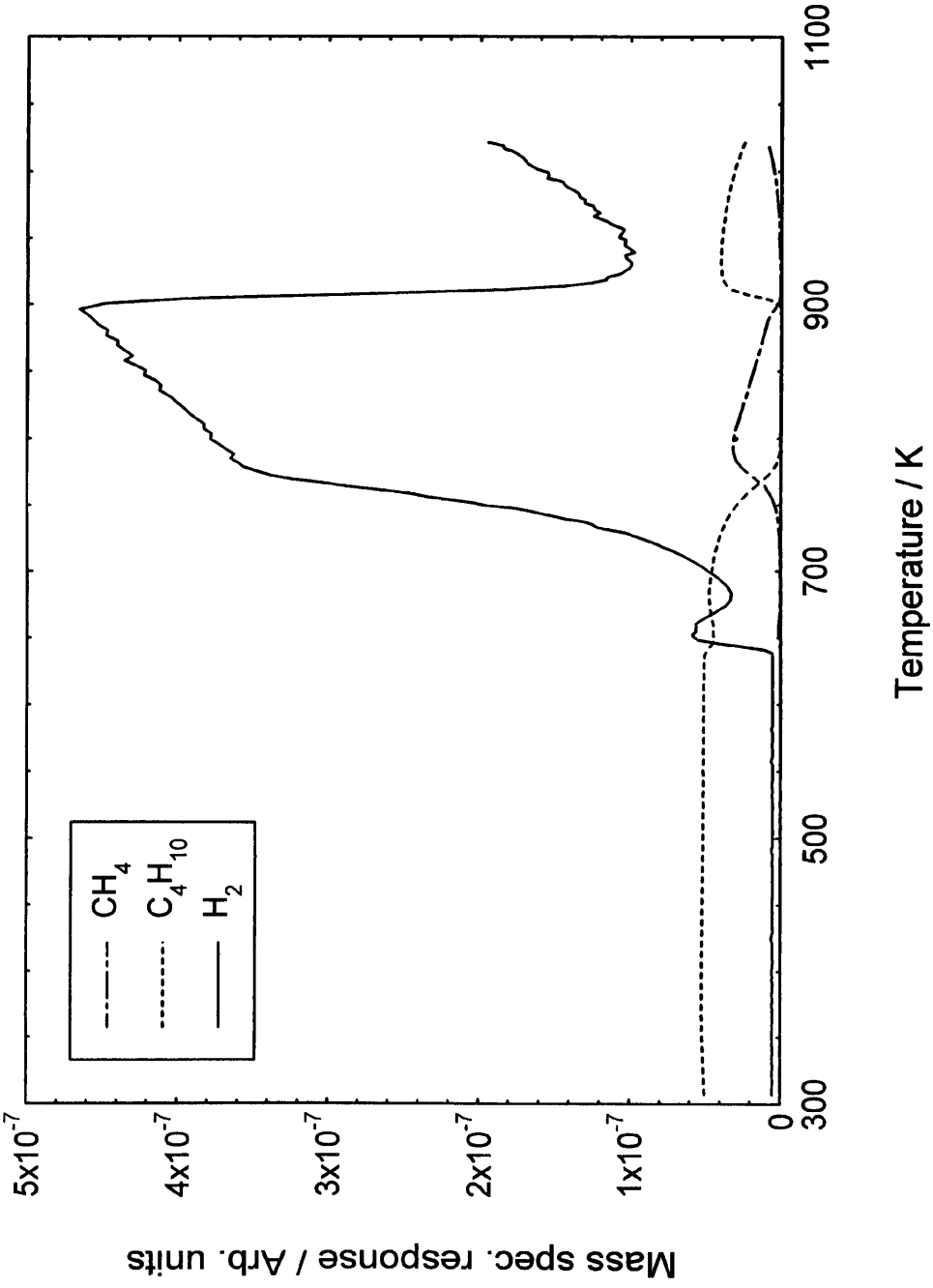


Fig.4.11 TPRn of n-butane on catalyst AK2

**Region 4** - A total cut-off in the rate of hydrogen formation is observed between 900 and 930 K because nickel has become deactivated due to encapsulation by carbon.

The amount of carbon formed between 680 and 930 K was calculated to be 2.6 x $10^{21}$ atoms $g^{-1}_{cat}$ (Table 4.1).

**Region 5** - The increase in the rate of hydrogen production observed from 930 K onwards is due to gas phase cracking of the hydrocarbon feed.

The total amount of carbon deduced from the TPRn profile was 3.4 x $10^{21}$ atoms $g^{-1}_{cat}$ (Table 4.1).

The remarkably similar kinetics of the decomposition reaction observed for samples AK1 and AK2 and the similar amounts of carbon formed in each case show that increasing the amount of $Al_2O_3$ promoter to 5wt% has little effect on the decomposition pathway of butane.

### 4.3.3 TPO of carbon formed on AK2

The TPO experiment was carried out using the same procedure as detailed in Section 4.2.3. The TPO profile obtained is shown in Fig.4.12. Again there are similarities between this and the TPO profile obtained for catalyst AK1 (Fig.4.5). Both carbon dioxide and carbon monoxide were produced during the reaction. $CO_2$ was formed with an onset temperature of ~670 K with a marked peak at 792 K. CO evolution also began at ~670 K and showed a considerable increase in rate at 795 K with a sharp cut off occurring at 950 K. A second sharp $CO_2$ peak was observed at the CO cut off.

The production of both $CO_2$ and CO is again attributed to oxygen depletion, as was observed for sample AK1. In Fig.4.13 the partial pressure at the peak maximum of the $CO_2$ peak corresponds to $\cong$0.06 atm. whereas the partial pressure of oxygen used for the gasification reaction corresponded to 0.05 atm. Thus the concentration of oxygen in the feed was insufficient to completely oxidise carbon to $CO_2$ and therefore the production

of CO was also observed. The total amount of carbon oxidised was calculated to be 3.6 x $10^{21}$ atoms $g^{-1}_{cat}$ (Table 4.1) which again indicates that all the carbon formed in the TPRn reaction was gasified. The activation energy for carbon oxidation was calculated to be 121 kJ $mol^{-1}$.

### 4.3.4 Re-reduction of catalyst AK2

The catalyst was re-reduced using the same procedure as detailed in Section 4.2.4. The reduction profile obtained is shown in Fig.4.14. Again the reduction profile differs markedly from the initial reduction profile obtained for catalyst AK2 (Fig.3.5(b)). The dominant peak maximum has now shifted to a higher temperature at 810 K and a second shoulder is present at ~950 K.

### 4.3.5 TPRn of n-butane over re-reduced AK2

The TPRn experiment was carried out using the same procedure as detailed in section 4.2.5. The reaction profile obtained is shown in Fig.4.15. A considerably different profile was produced to that of the initial butane TPRn shown in Fig.4.11. In this case a small, low temperature $H_2$ peak was produced at 625 K however the large, high temperature $H_2$ peak observed previously was absent. A sharp increase in the rate of $H_2$ evolution was observed from ~900 K onwards.

Approximate deconvolution of the $H_2$ spectrum shown in Fig.4.15 allowed the amount of carbon formed to be determined. The amount of carbon associated with the small, low temperature $H_2$ peak was calculated to be 3.8 x $10^{19}$ atoms $g^{-1}_{cat}$. The amount of high temperature carbon formed was 7.4 x $10^{19}$ atoms $g^{-1}_{cat}$ (Table 4.1). The total amount of carbon formed up to ~900 K in this case therefore was approximately 96% less than was observed in the initial TPRn (Fig.4.11). This result is very similar to the one observed for sample AK1 where 90% less carbon was formed during the second TPRn.

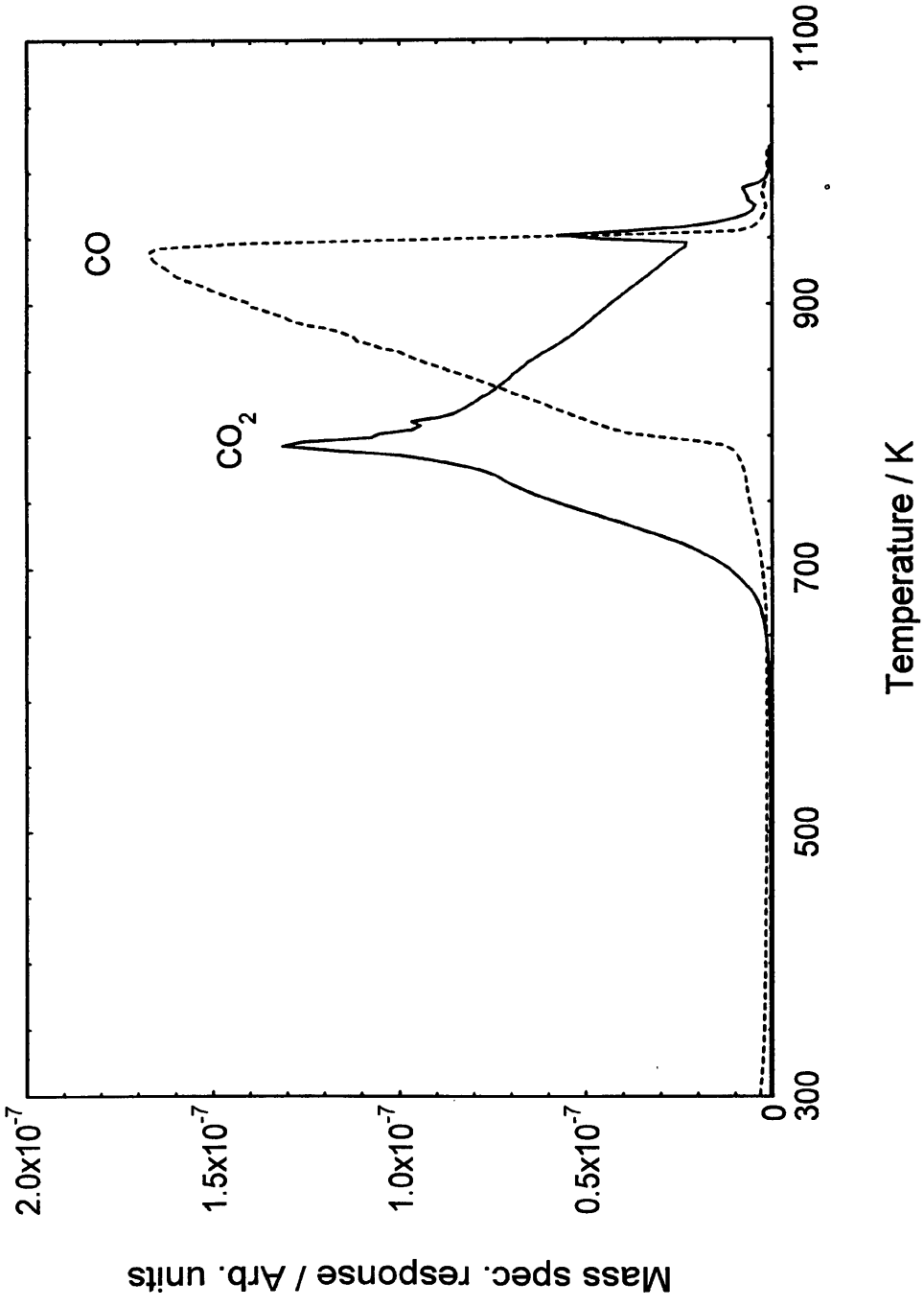


Fig.4.12 TPO of deposited carbon on catalyst AK2

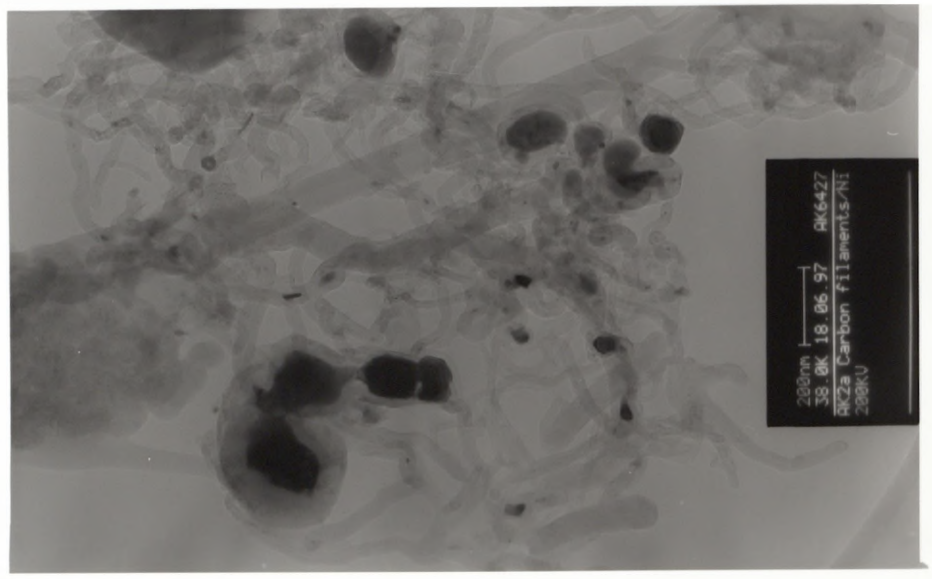


Fig.4.13 Transmission electron micrograph of carbon formed on catalyst AK2 (1023 K)

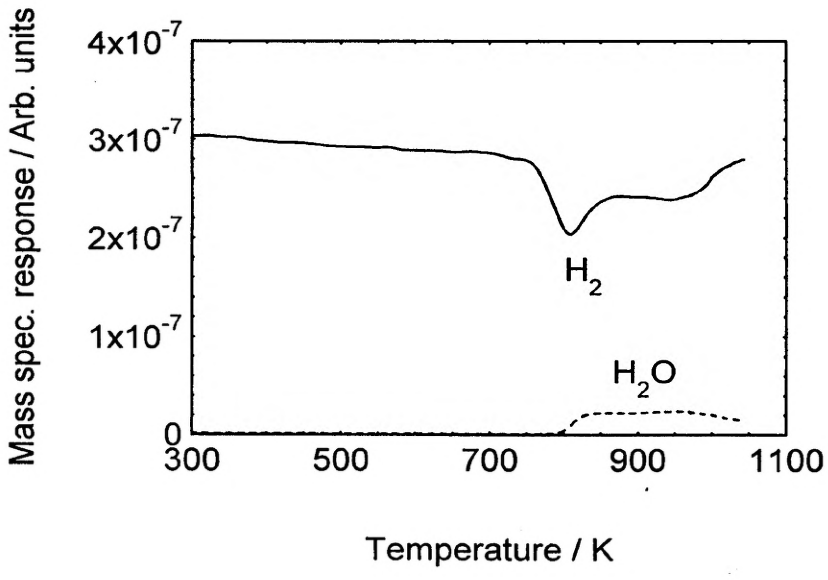


Fig.4.14 TPR profile of regenerated catalyst AK2

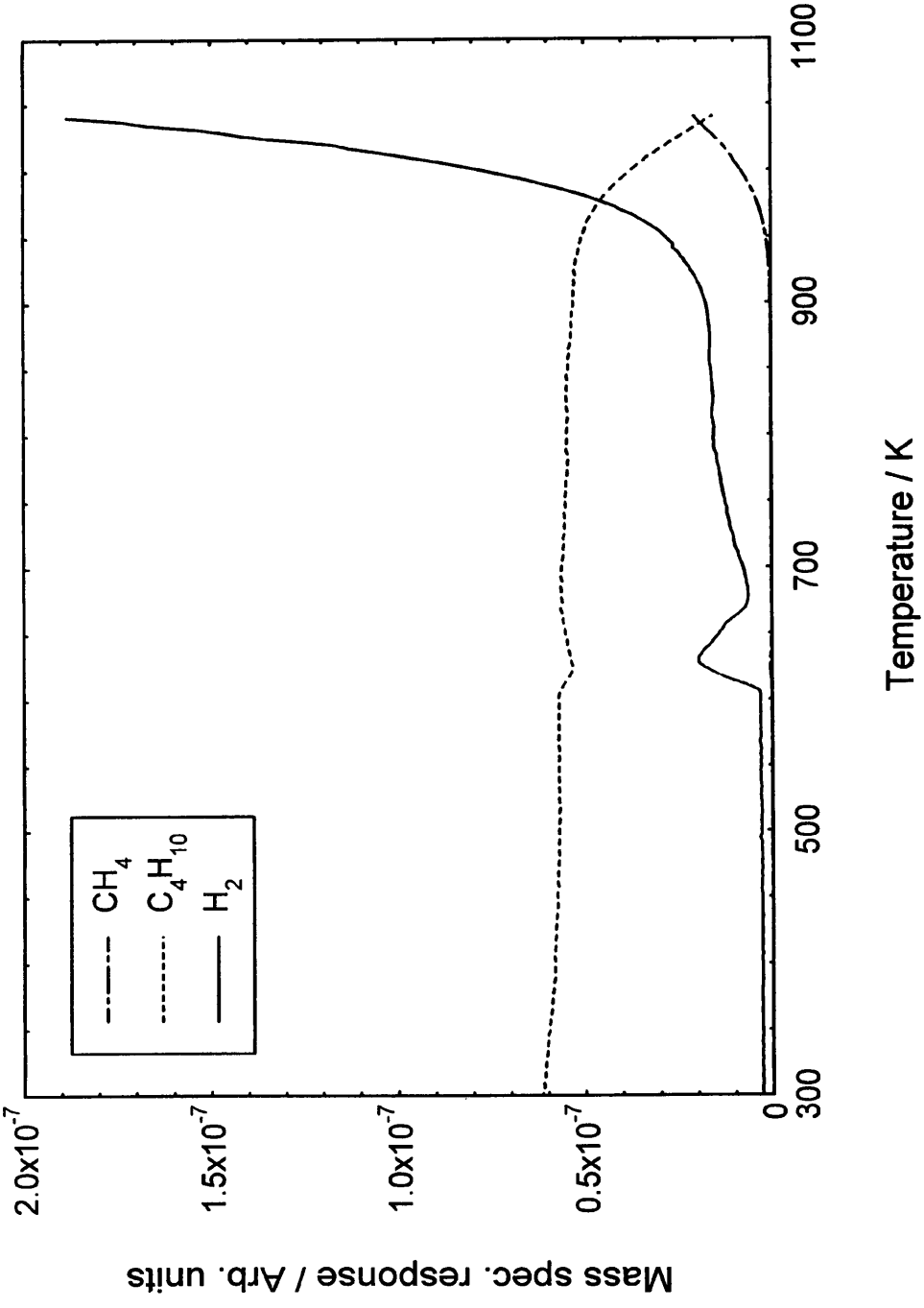


Fig.4.15 TPRn of n-butane on re-reduced catalyst AK2

The change in kinetics of the butane decomposition observed in Fig.4.15 can again be attributed to a redispersion of the nickel caused by the oxidation reaction, as was observed for sample AK1. The different surface morphology of the Ni and site blocking effects of $Al_2O_3$ appear to be major factors in suppressing the formation of carbon.

## 4.4 Studies carried out on $NiO/Al_2O_3$ promoted with 10wt% $Al_2O_3$ (AK3)

### 4.4.1 TPRn of n-butane on AK3

The TPRn experiment was carried out using the same procedure as detailed in Section 4.2.1. The TPRn profile obtained is shown in Fig.4.16. It can be clearly seen that the reaction profile exhibits similar features both the n-butane TPRn profiles obtained for catalyst AK1 (Fig.4.1) and catalyst AK2 (Fig.4.11). The onset of hydrogen evolution began at 574 K, a slightly lower temperature than observed for samples AK1 and AK2. A peak maximum was observed at 622 K followed by a minimum at 667 K. A further rise in $H_2$ occurred producing a large peak which cut off sharply at 925 K. Methane formation started at 722 K maximising at 778 K and cut off at the second minimum of $H_2$ evolution.

### 4.4.2 The morphology of the carbonaceous deposits

The morphology of the carbonaceous deposits generated by the decomposition of n-butane was studied by TEM. The electron micrograph is displayed in Fig.4.18. Carbon filaments were produced, the widths of which ranged from ~30 - 60 nm. Central channels running down the length of the filaments were visible. The nickel particles were encapsulated by carbon.

The temperature dependence of hydrogen evolution in the butane TPRn profile for sample AK3 again falls into 5 distinct regions which are very similar to those observed for samples AK1 and AK2. Therefore the features can be explained using the same

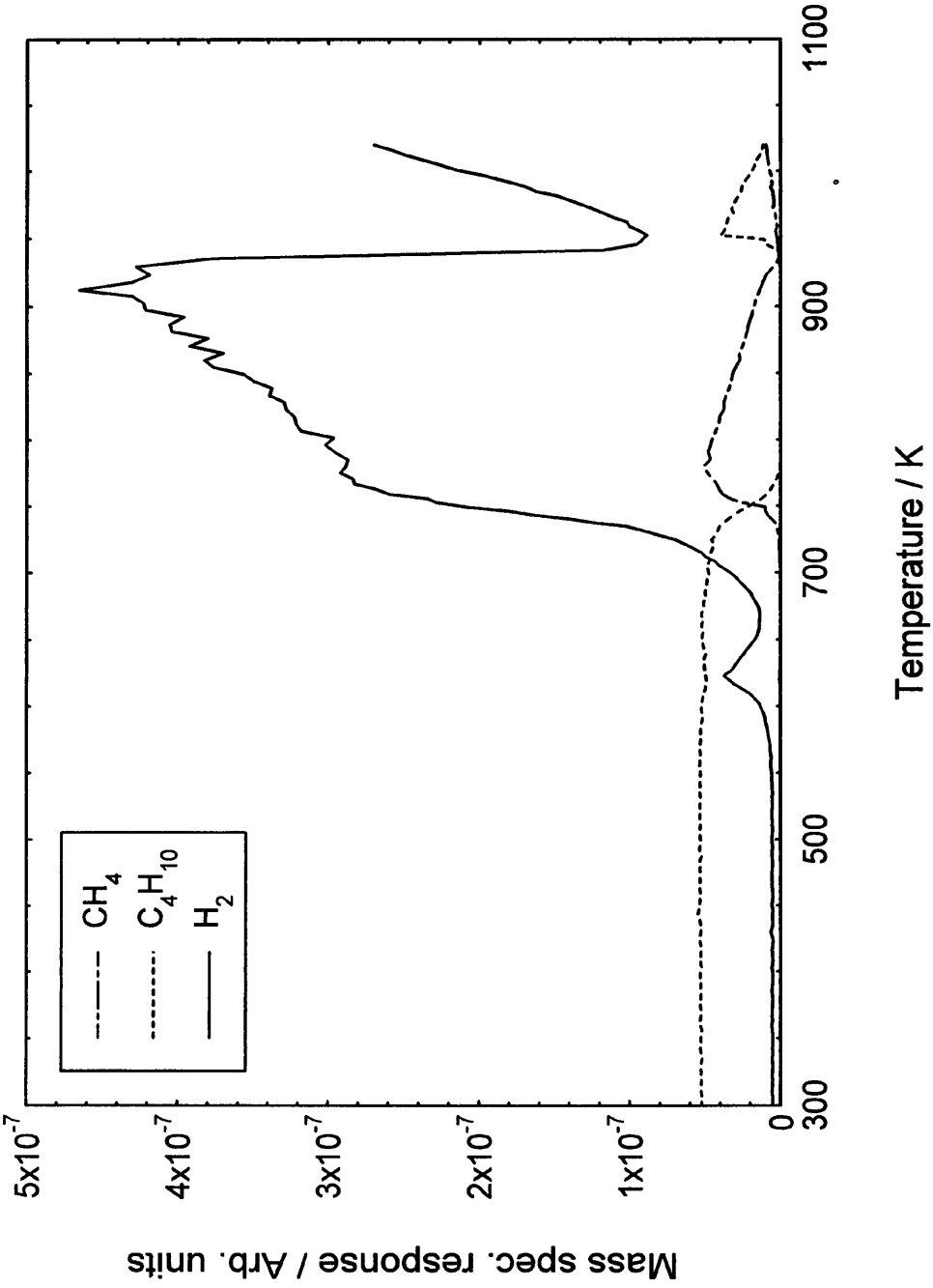


Fig.4.16 TPRn of n-butane on catalyst AK3

arguments as previously (Section 4.2.2.1) based on the mechanism of growth of carbon filaments. It appears that the presence of $Al_2O_3$ promoter in samples AK1 - AK3, even with increasing loading, has little effect on the decomposition pathway of butane and thus the amount of carbon formed at this stage. The amount of low temperature carbon formed between 570 and 670 K on sample AK3 was calculated to be 5.6 x $10^{19}$ atoms $g^{-1}_{cat}$ and the amount of high temperature carbon formed between 670 and 940 K was 2.8 x $10^{21}$ atoms $g^{-1}_{cat}$. The total amount of carbon formed was 3.5 x $10^{21}$ atoms $g^{-1}_{cat}$. These amounts are very similar to those calculated for samples AK1 and AK2 (Table 4.1) The activation energy for the production of hydrogen between 680 - 730 K was calculated to be 147 kJ $mol^{-1}$.

### 4.4.3 TPO of carbon formed on AK3

The TPO experiment was carried out using the same procedure as detailed in Section 4.2.3. The TPO profile obtained is shown in Fig.4.17. Similarities between this and the TPO profiles obtained for both catalysts AK1 (Fig.4.4) and AK2 (Fig.4.12) are again evident. In this case $CO_2$ production began at ~650 K and showed a peak maximum at 829 K. CO evolution began at ~750 K and a sharp increase in rate was observed at 820 K. A sharp cut off in CO evolution occurred at 1005 K. The production of both $CO_2$ and CO is again attributed to the depletion of oxygen (partial pressure of $CO_2$ at the peak maximum $\cong$0.05 atm.) as was observed for samples AK1 and AK2. The activation energy for the gasification of carbon was calculated to be 160 kJ $mol^{-1}$. The amount of carbon removed by oxidation was 3.6 x $10^{21}$ atoms $g^{-1}_{cat}$ (Table 4.1) indicating all the carbon formed by the butane TPRn had been gasified.

### 4.4.4 Re-reduction of catalyst AK3

The re-reduction of sample AK3 was carried out using the same procedure as detailed in Section 4.2.4. The reduction profile obtained is shown in Fig.4.19. Once again the reduction profile differs markedly from the initial reduction profile obtained for catalyst AK3 (Fig.3.5(c)). The dominant peak maximum has in this case shifted to the higher temperature of 813 K and a second shoulder is visible at ~890 K.

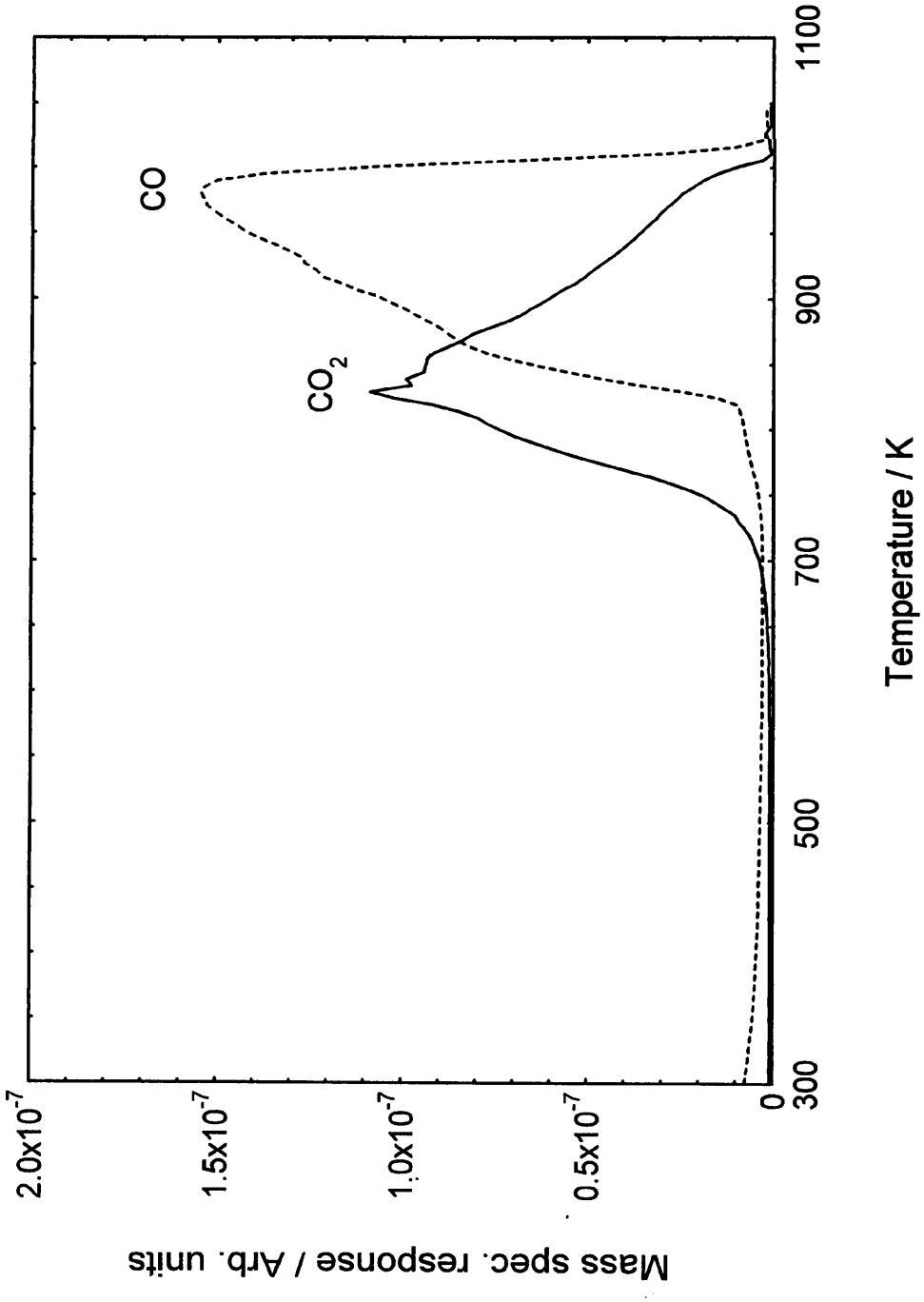


Fig.4.17 TPO of deposited carbon on catalyst AK3

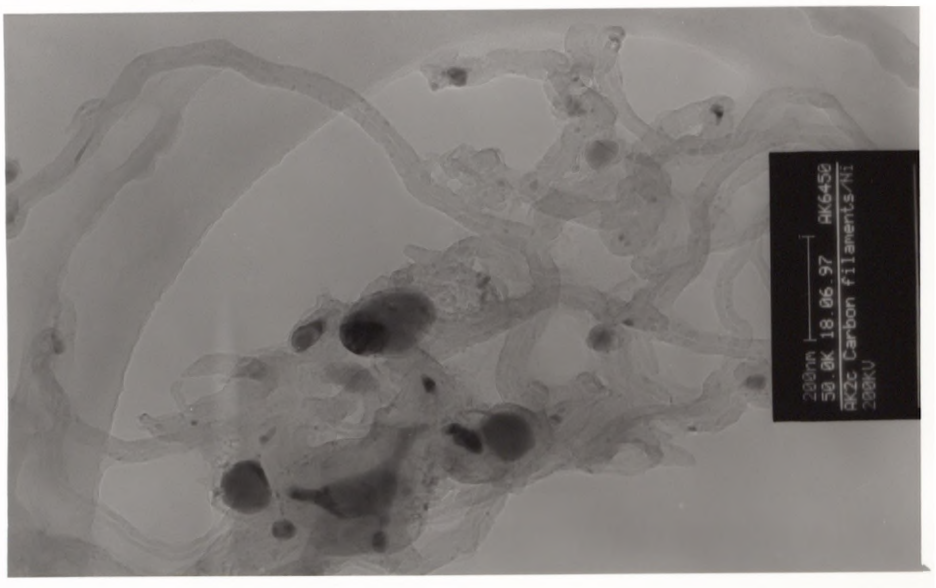

Fig.4.18 Transmission electron micrograph of carbon formed on catalyst AK3 (1023 K)

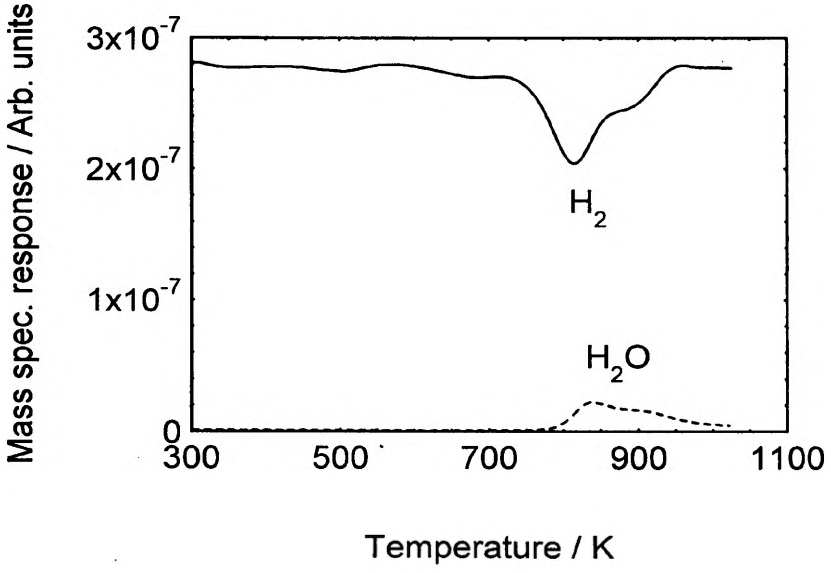


Fig.4.19 TPR profile of regenerated catalyst AK3

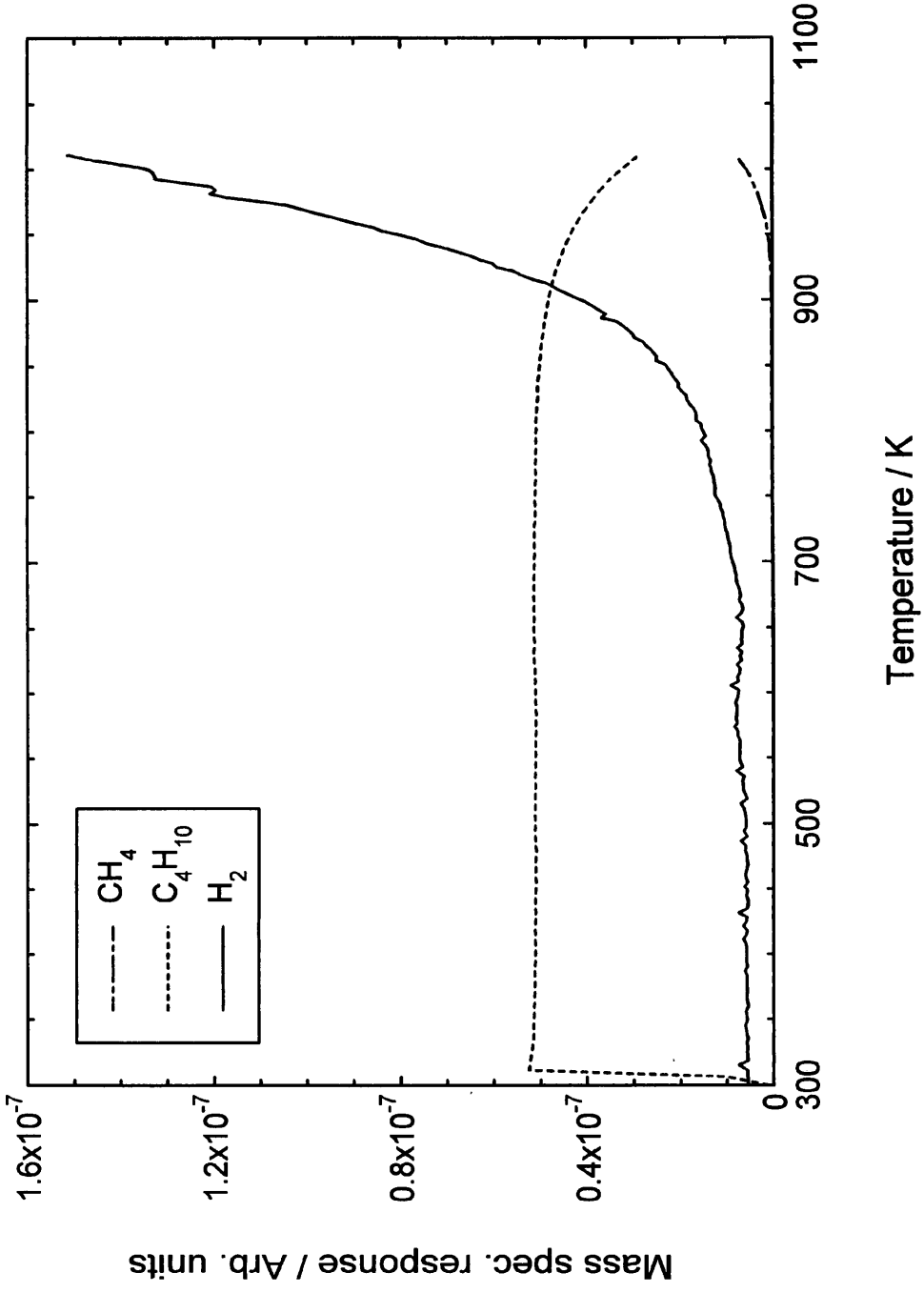


Fig.4.20 TPRn of n-butane on re-reduced catalyst AK3

Table 4.1

The amounts of carbon formed and gasified on $Al_2O_3$ promoted $NiO/Al_2O_3$ catalysts (AK1 - AK3)

| | FIRST BUTANE TPRn | | | | | | SECOND BUTANE TPRn | | |
|---|---|---|---|---|---|---|---|---|---|
| Sample | Amount of low temp. carbon formed/ atoms $g^{-1}_{cat}$ | $E_{act}$ for diffusion of carbon through Ni/ kJ $mol^{-1}$ | Amount of high temp. carbon formed/ atoms $g^{-1}_{cat}$ | Total amount of carbon formed/ atoms $g^{-1}_{cat}$ | $E_{act}$ for gasification of carbon/ kJ $mol^{-1}$ | Total amount of carbon oxidised/ atoms $g^{-1}_{cat}$ | Amount of low temp. carbon formed/ atoms $g^{-1}_{cat}$ | Amount of high temp. carbon formed/ atoms $g^{-1}_{cat}$ | Reduction in amount of carbon formed / % |
| **AK1** | $7.2 \times 10^{19}$ (3 monolayers)* | 155 | $2.6 \times 10^{21}$ (104 monolayers) | $3.3 \times 10^{21}$ (132 monolayers) | 161 | $3.1 \times 10^{21}$ (124 monolayers) | $1.6 \times 10^{20}$ (6 monolayers) | $9.7 \times 10^{19}$ (4 monolayers) | 90 |
| **AK2** | $6.4 \times 10^{19}$ (3 monolayers)* | 137 | $2.6 \times 10^{21}$ (104 monolayers) | $3.4 \times 10^{21}$ (136 monolayers) | 121 | $3.6 \times 10^{21}$ (144 monolayers) | $3.8 \times 10^{19}$ (2 monolayers) | $7.4 \times 10^{19}$ (3 monolayers) | 96 |
| **AK3** | $5.6 \times 10^{19}$ (2 monolayers)* | 147 | $2.8 \times 10^{21}$ (97 monolayers) | $3.5 \times 10^{21}$ (121 monolayers) | 160 | $3.6 \times 10^{21}$ (124 monolayers) | $1.6 \times 10^{19}$ (0.6 monolayers) | $8.0 \times 10^{19}$ (3 monolayers) | 97 |

Mass of each catalyst used = 0.5g  Total surface areas: AK1 = 2.5 $m^2 g^{-1}$; AK2 = 2.5 $m^2 g^{-1}$; AK3 = 2.9 $m^2 g^{-1}$

*Number of monolayers of carbon calculated on the basis of the total surface area of the catalyst, taking monolayer coverage to be $10^{15}$ atoms $cm^{-2}$
(This will obviously represent a lower limit since the Ni area is less)

### 4.4.5 TPRn of n-butane over re-reduced AK3

The TPRn experiment was carried out using the same procedure as detailed in Section 4.2.5. The TPRn profile obtained for catalyst AK3 is shown in Fig.4.20. Again a completely different reaction profile was produced to that of the initial butane TPRn shown in Fig.4.16. In this case there does appear to be a small, very broad low temperature peak. However, the large, high temperature $H_2$ peak present in Fig.4.16 was now absent. A gradual increase in the rate of $H_2$ evolution was observed from ~700 K which increased sharply from ~850 K onwards.

The $H_2$ spectrum in Fig.4.20 was again approximately deconvoluted. The amount of low temperature carbon formed between 500 and 700 K was $1.6 \times 10^{19}$ atoms $g^{-1}_{cat}$ and the amount of high temperature carbon formed between 700 and 900 K was $8.0 \times 10^{19}$ atoms $g^{-1}_{cat}$ (table 4.1). The total amount of carbon formed up to ~900 K in this case was approximately 97% less than in the initial TPRn (Fig.4.16). This result is again very similar to those observed for both samples AK1 and AK2 where the amount of carbon produced during the second butane TPRn was 90 and 96% less respectively. Therefore, as for samples AK1 and AK2, the change in kinetics of the butane TPRn and subsequent suppression of carbon formation can be attributed to the redispersion of nickel caused by the oxidation reaction and the blocking of Ni ensembles by $Al_2O_3$.

## 4.5 Conclusions

1) The TPRn of butane carried out on fresh catalysts promoted with 1, 5 and 10wt% $Al_2O_3$ produced $H_2$ spectra which were remarkably similar, indicating that in each case the promoter had little effect on the kinetics of decomposition. It therefore seems that although the promoters had a profound effect on the nature of the nickel oxide catalyst precursors, as shown by temperature-programmed reduction in Chapter 3, they had little effect on the dehydrogenational activity of Ni once formed after the reduction. It could be concluded from this that the promoters are associated with the oxide support after

reduction and only become involved with the Ni again after oxidation of the carbon, which results in a redistribution of the Ni on the support. The total amount of carbon formed in each case was equivalent, indicating that increasing the amount of promoter had no effect on suppressing the formation of carbon.

2) The activation energy for the production of hydrogen was calculated in each case and values obtained were in good agreement with those in the literature for the diffusion of carbon through nickel. This suggested that carbon filaments were being formed by the butane TPRn and this was confirmed by transmission electron microscopy.

3) It was found in each case that all the deposited carbon was gasified by temperature programmed oxidation. The activation energy calculated for the gasification of carbon gave values which were comparable to those obtained for the diffusion of carbon through nickel. This suggested that the gasification of carbon filaments may be the reverse process of filament formation, where the nickel particle retraces its original path back down the filament. This leads to a redistribution of Ni on the surface.

4) Repetition of the butane TPRn on each catalyst regenerated by oxidation produced completely different $H_2$ spectra compared to those for the initial TPRns, which showed a dramatic decrease in the amount of carbon formed. The difference in the kinetics of decomposition was attributed to a redispersion of Ni on the support caused by the oxidation and re-reduction, resulting in a distinctly different Ni surface morphology. It is possible that a redistribution of Ni crystallographic faces on the surface to predominantly Ni(111) was responsible for inhibiting the adsorption and subsequent decomposition of butane.

5) In each case after carbon oxidation, a redispersion of $Al_2O_3$ promoter may also have been responsible for blocking specific nickel ensembles required for the formation of ethylidyne, which further inhibited the formation of carbon. The decrease in carbon formation observed during the second TPRn was 90, 96 and 97% respectively for

samples containing 1, 5 and 10wt% of $Al_2O_3$ indicating that each loading of $Al_2O_3$ had a comparable effect.

## 4.6 Studies carried out on $NiO/Al_2O_3$ promoted with 1wt% MgO (AK4)

### 4.6.1 TPRn of n-butane on AK4

The TPRn experiment was carried out using the same procedure as detailed in Section 4.2.1. The TPRn profile obtained is shown in Fig.4.21. The onset of $H_2$ evolution occurred at ~500 K giving rise to a small peak with a maximum at 620 K. Following a minimum at 650 K a sharp rise in $H_2$ was again observed, the large peak cutting off sharply at 920 K. Methane formation began at 715 K maximising at 762 K and expired at the second minimum of $H_2$ evolution.

### 4.6.2 The morphology of the carbonaceous deposits

The morphology of the carbonaceous deposits generated by the decomposition of n-butane was studied by TEM. The electron micrograph is displayed in Fig.4.23. Carbon filaments were again produced which had similar characteristics to those formed on the $Al_2O_3$ promoted samples. The filaments had a central channel running down their lengths and nickel particles were situated at their tops. The filaments had an average diameter of ~30 nm. The nickel particles were again encapsulated by carbon.

The butane TPRn profile obtained for sample AK4 exhibited very similar features to the profiles produced for samples AK1 - AK3 in that the temperature dependence of hydrogen evolution again fell into 5 distinct regions. The profile can therefore again be explained by the model described for carbon filament formation as in Section 4.2.2.1.

The amount of carbon formed at low temperature between 500 and 650 K was calculated to be $6.8 \times 10^{19}$ atoms $g^{-1}_{cat}$. The amount of carbon formed between 650 and 940 K was $2.6 \times 10^{21}$ atoms $g^{-1}_{cat}$. The total amount of carbon formed was $3.6 \times 10^{21}$ atoms $g^{-1}_{cat}$ (Table 4.2). The activation energy for the production of hydrogen in the

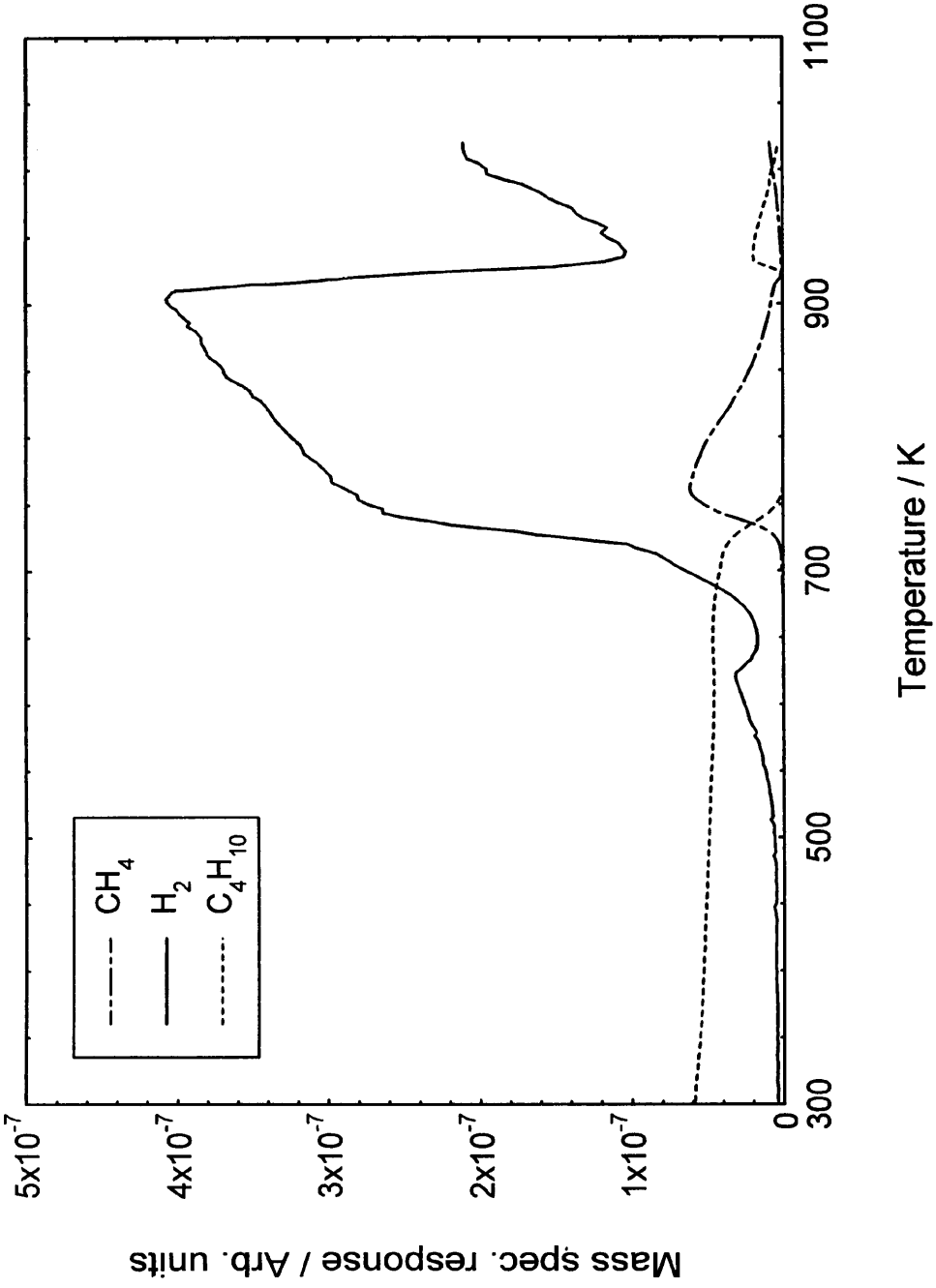


Fig.4.21 TPRn of n-butane on catalyst AK4

temperature range 680 - 730 K was calculated to be 133 kJ $mol^{-1}$ which was again in good agreement with values reported in the literature for the diffusion of carbon through nickel [5] [7]. The similarity of the TPRn profile in Fig.4.21 with those obtained for the $Al_2O_3$ promoted samples (AK1 - AK3, Figs. 4.1, 4.11, 4.16) and the comparable amount of carbon formed show that the presence of 1wt% MgO does little to alter the kinetics of the butane decomposition and suppress carbon formation.

### 4.6.3 TPO of carbon formed on AK4

The TPO experiment was carried out using the same procedure as detailed in Section 4.2.3. The TPO profile obtained is shown in Fig.4.22. $CO_2$ evolution commenced at ~630 K and produced a sharp peak maximum at 829 K. CO formation began at ~700 K and showed a substantial increase in rate 830 K. A sharp cut off in CO production occurred at 985 K.

The TPO profile again shows a clear similarity to the TPO profiles obtained for the $Al_2O_3$ promoted samples. The formation of both $CO_2$ and CO as gaseous products of the reaction are again the result of oxygen depletion (partial pressure of $CO_2$ at the peak maximum $\cong$0.07 atm). The activation energy for the oxidation of carbon was calculated to be 115 kJ $mol^{-1}$. The amount of carbon removed by oxidation was 4.0 x $10^{21}$ atoms $g^{-1}_{cat}$ which showed that all the carbon formed had been gasified (Table 4.2).

### 4.6.4 Re-reduction of catalyst AK4

The re-reduction of catalyst AK4 was carried out using the same procedure as detailed in Section 4.2.4. The profile obtained is shown in Fig.4.24. This profile differed from the initial reduction profile obtained for catalyst AK4 (Fig.3.6(a)) in that the dominant peak maximum had shifted to a higher temperature at 780 K and the second shoulder had also shifted to ~900 K.

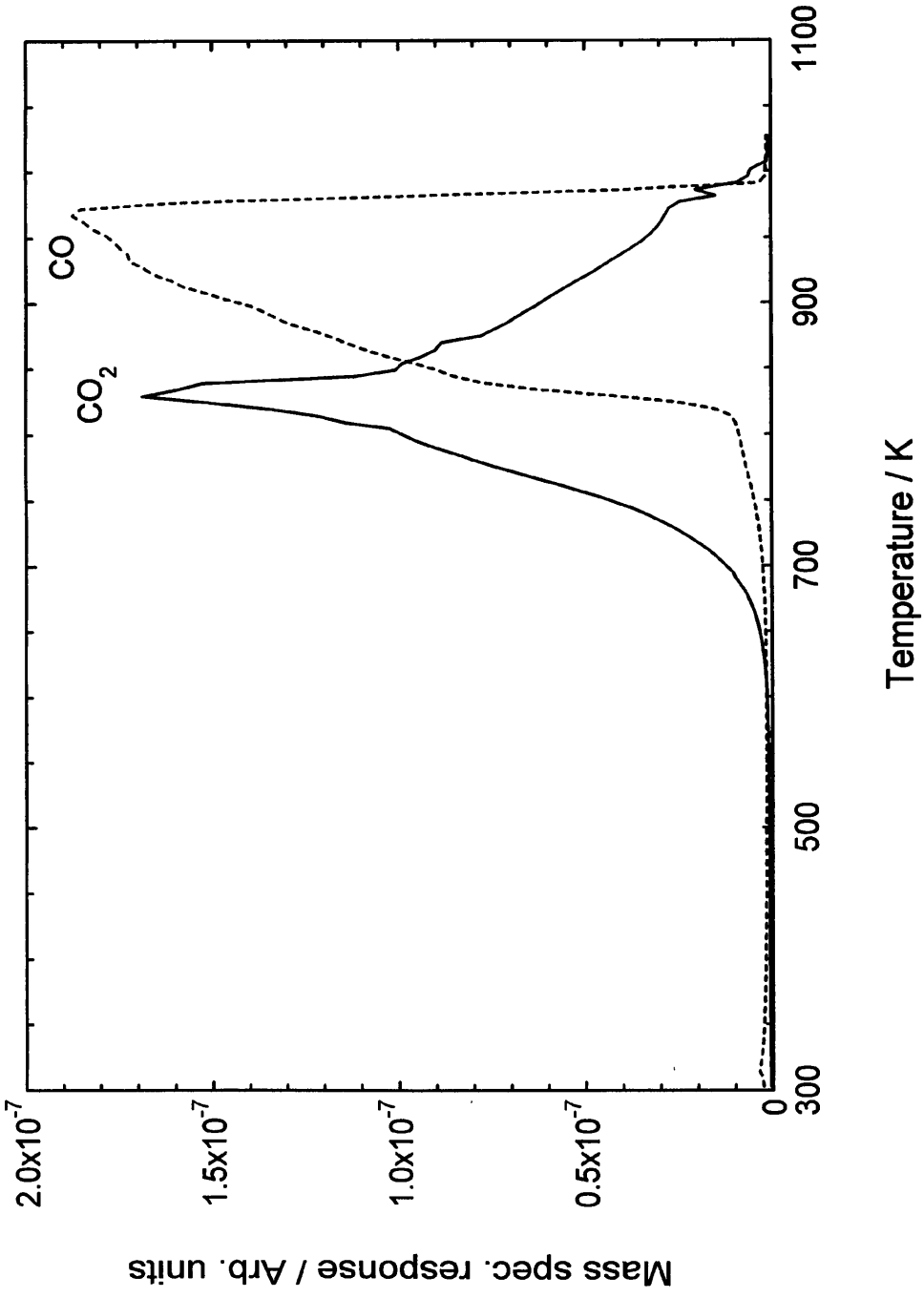


Fig.4.22 TPO of deposited carbon on catalyst AK4

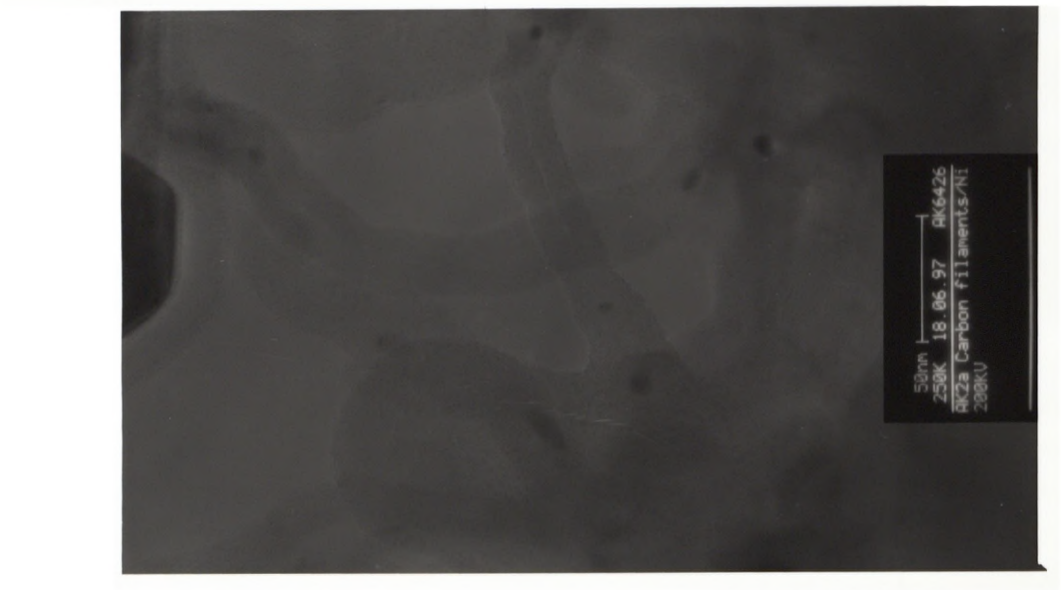


Fig.4.23 Transmission electron micrograph of carbon formed on catalyst AK4 (1023 K)

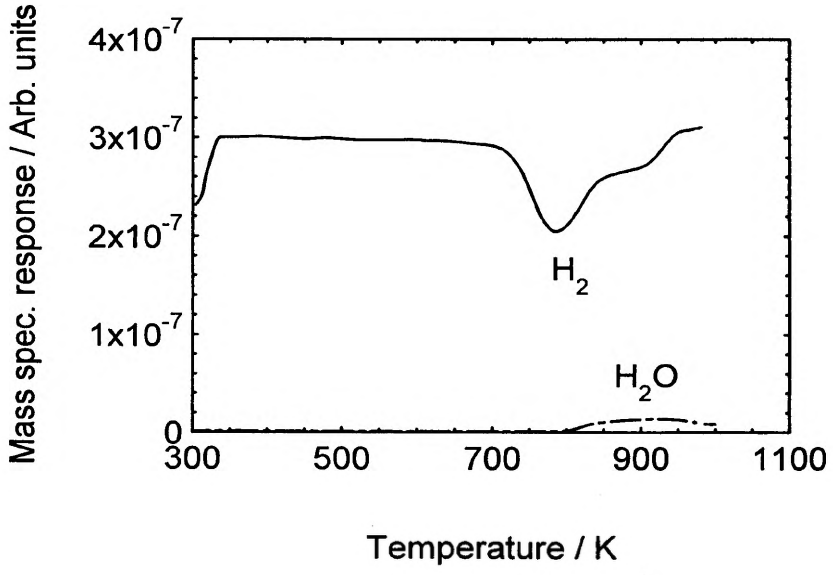


Fig.4.24 TPR profile of regenerated catalyst AK4

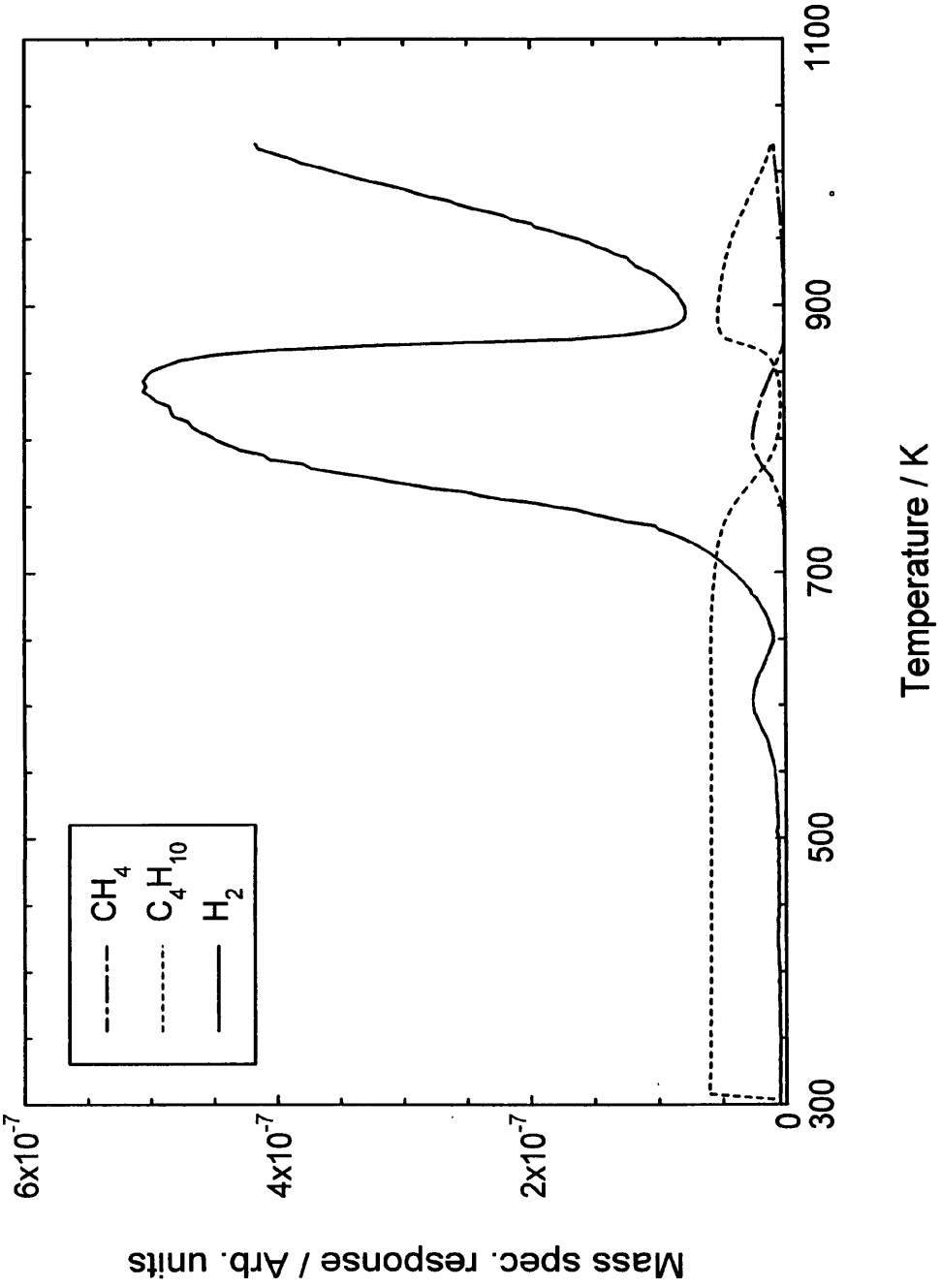


Fig.4.25 TPRn of n-butane on re-reduced catalyst AK4

### 4.6.5 TPRn of of n-butane over re-reduced AK4

The TPRn experiment was carried out using the same procedure as detailed in Section 4.2.5. The TPRn profile obtained for catalyst AK4 is shown in Fig.4.25. Again a different profile was obtained compared to the initial TPRn shown in Fig.4.21. This time a broad, low temperature $H_2$ peak was produced with a maximum at ~600 K. This was followed by a sharp rise in $H_2$ at ~650 K producing a large peak with a maximum at 840 K which again cut off sharply at ~850 K. Methane formation commenced at 735 K maximising at 800 K and expired at 870 K.

The amount of carbon formed at low temperature between 550 - 650 K was calculated to be 2.8 x $10^{19}$ atoms $g^{-1}_{cat}$. The amount of high temperature carbon formed between 650 -900K was 2.2 x $10^{21}$ atoms $g^{-1}_{cat}$. The total amount of carbon formed from this butane TPRn up to ~900 K was approximately 16% lower than the amount formed from the initial TPRn (Fig.4.21). This decrease was not as dramatic as was observed for the sample doped with 1wt% $Al_2O_3$, where 90% less carbon was formed. Although MgO does alter the kinetics of the butane decomposition the second time around, the presence of 1wt% MgO is not as effective as 1wt% $Al_2O_3$ in suppressing the formation of carbon. It seems therefore that not only does the redispersion of nickel influence the decomposition pathway of butane on regenerated catalysts, the promoters also play an important role. The results observed in this case suggest that the dispersion of 1wt% MgO is not as great as that of 1wt% $Al_2O_3$ following oxidation and therefore a lesser number of nickel ensembles required for the formation of ethylidyne are blocked.

## 4.7 Studies carried out on $NiO/Al_2O_3$ promoted with 5wt% MgO (AK5)

### 4.7.1 TPRn of n-butane on AK5

The TPRn experiment was carried out using the same procedure as detailed in Section 4.2.1. The TPRn profile obtained is shown in Fig.4.26. $H_2$ evolution commenced at 570 K with a peak maximum occurring at 614 K followed by a minimum at 655 K. A

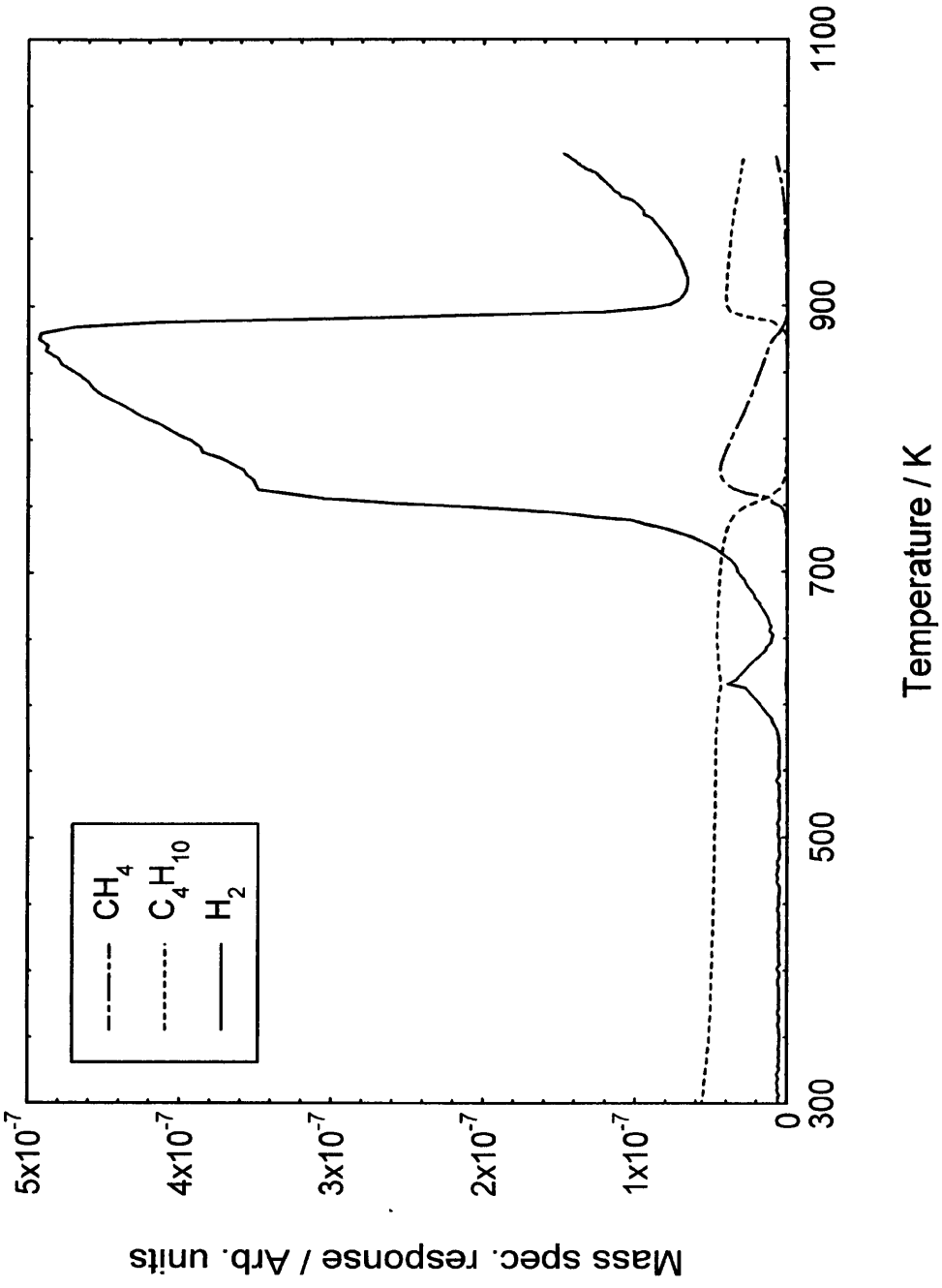


Fig.4.26 TPRn of n-butane on catalyst AK5

sharp rise in $H_2$ production was then observed producing a much larger peak which cut off sharply at 875 K. Methane formation occurred from 740 K, rose to a maximum at 773 K and cut off at the second minimum of $H_2$ evolution.

### 4.7.2 The morphology of the carbonaceous deposits

The morphology of the carbonaceous deposits generated by the decomposition of n-butane was studied by TEM. The electron micrograph is displayed in Fig.4.28. The carbon filaments produced again contained a central channel running down their length. The width of the filaments was ~30 nm. The nickel particles were again encapsulated by carbon.

The butane TPRn profile obtained for sample AK5 shows that the presence of 5wt% MgO has little influence on the kinetics of decomposition. The temperature dependence of $H_2$ evolution again falls into 5 distinct regions which can again be elucidated as in Section 4.2.2.1. The amount of low temperature carbon formed between 570 and 650 K was calculated to be $4.0 \times 10^{19}$ atoms $g^{-1}_{cat}$. The amount of high temperature carbon formed between 650 and 900 K was $2.4 \times 10^{21}$ atoms $g^{-1}_{cat}$. The total amount of carbon formed was $3.1 \times 10^{21}$ atoms $g^{-1}_{cat}$ (Table 4.2). The activation energy for the production of hydrogen in the temperature range 700 - 740 K was calculated to be 130 kJ $mol^{-1}$. The amount of carbon formed in this case was of the same order as observed in each corresponding TPRn up until now, showing that increasing the amount of MgO to 5wt% has no effect in suppressing the formation of carbon.

### 4.7.3 TPO of carbon formed on AK5

The TPO experiment was carried out using the same procedure as detailed in Section 4.2.3. The TPO profile obtained is shown in Fig.4.27. In this case a somewhat anomalous result was obtained which had not been previously observed. $CO_2$ evolution began at ~650 K and 5 peak maxima were observed at 802, 845, 874, 924 and 962 K.

The production of CO commenced at ~720 K and showed two maxima at 900 and 944 K. A sharp CO cut off was observed at 960 K which coincided with the last peak maximum observed for $CO_2$.

The fact that both $CO_2$ and CO were products of the TPO was again attributed to the depletion of oxygen (partial pressure of $CO_2$ at the peak maximum $\cong$0.05 atm). The activation energy for the gasification of carbon was calculated to be 150 kJ $mol^{-1}$. The amount of carbon removed by oxidation was 3.0 x $10^{21}$ atoms $g^{-1}_{cat}$ (Table 4.2) indicating that all the carbon had reacted. No conclusive explanation can be provided for the anomalous appearance of the TPO profile obtained in this case, although it may simply be a function of the distribution of particle sizes.

### 4.7.4 Re-reduction of catalyst AK5

Re-reduction of sample AK5 was carried out using the same procedure as detailed in Section 4.2.4. The reduction profile obtained is shown in Fig.4.29. In this case a shift in peak maxima was again observed compared to the initial reduction profile obtained for catalyst AK5 (Fig.3.6(b)). The first peak maximum had now shifted to a higher temperature at ~820 K with a second peak maximum present at ~950 K.

### 4.7.5 TPRn of n-butane over re-reduced AK5

The TPRn experiment was carried out using the same procedure as detailed in Section 4.2.5. The TPRn profile obtained is shown in Fig.4.30. The reaction profile obtained again differed from the first TPRn profile obtained for catalyst AK5 (Fig.4.26). In this case $H_2$ evolution began at ~520 K and a slight increase in rate was observed until ~640 K. Following this a sharp increase in $H_2$ was observed and a large peak was produced with a peak maximum at 840 K. It was not until ~950 K that the formation of methane was observed.

The $H_2$ spectrum was approximately deconvoluted and the amounts of carbon formed calculated. The amount formed at low temperature between 500 and 700 K was 4.2 x

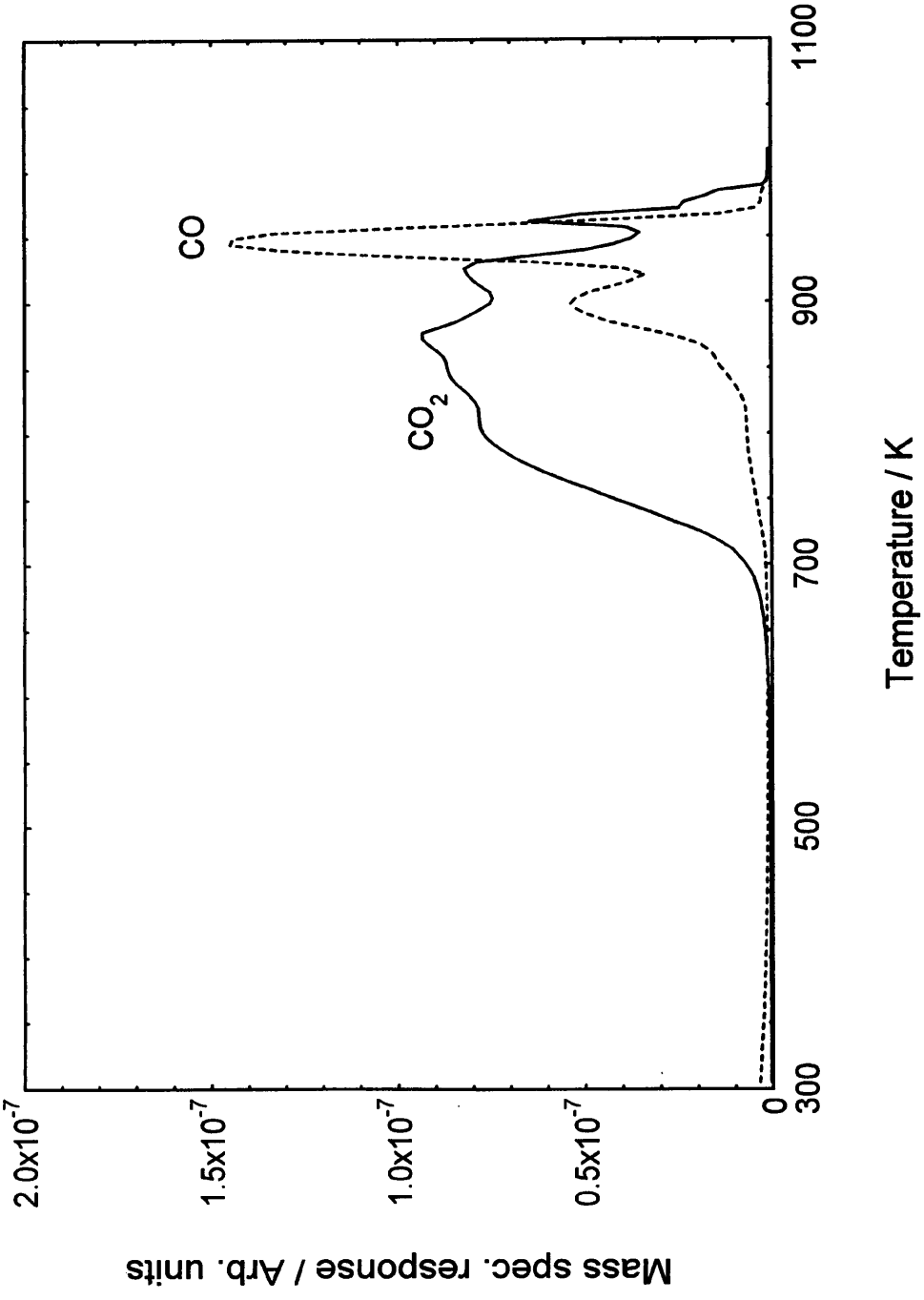


Fig.4.27 TPO of carbon deposited on catalyst AK5

Fig.4.28 Transmission electron micrograph of carbon formed on catalyst AK5 (1023 K)

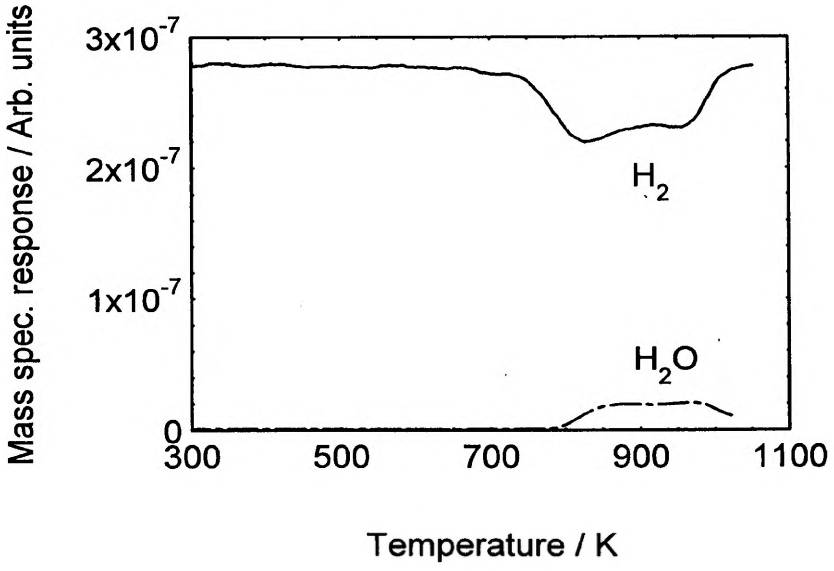


Fig.4.29 TPR profile of regenerated catalyst AK5

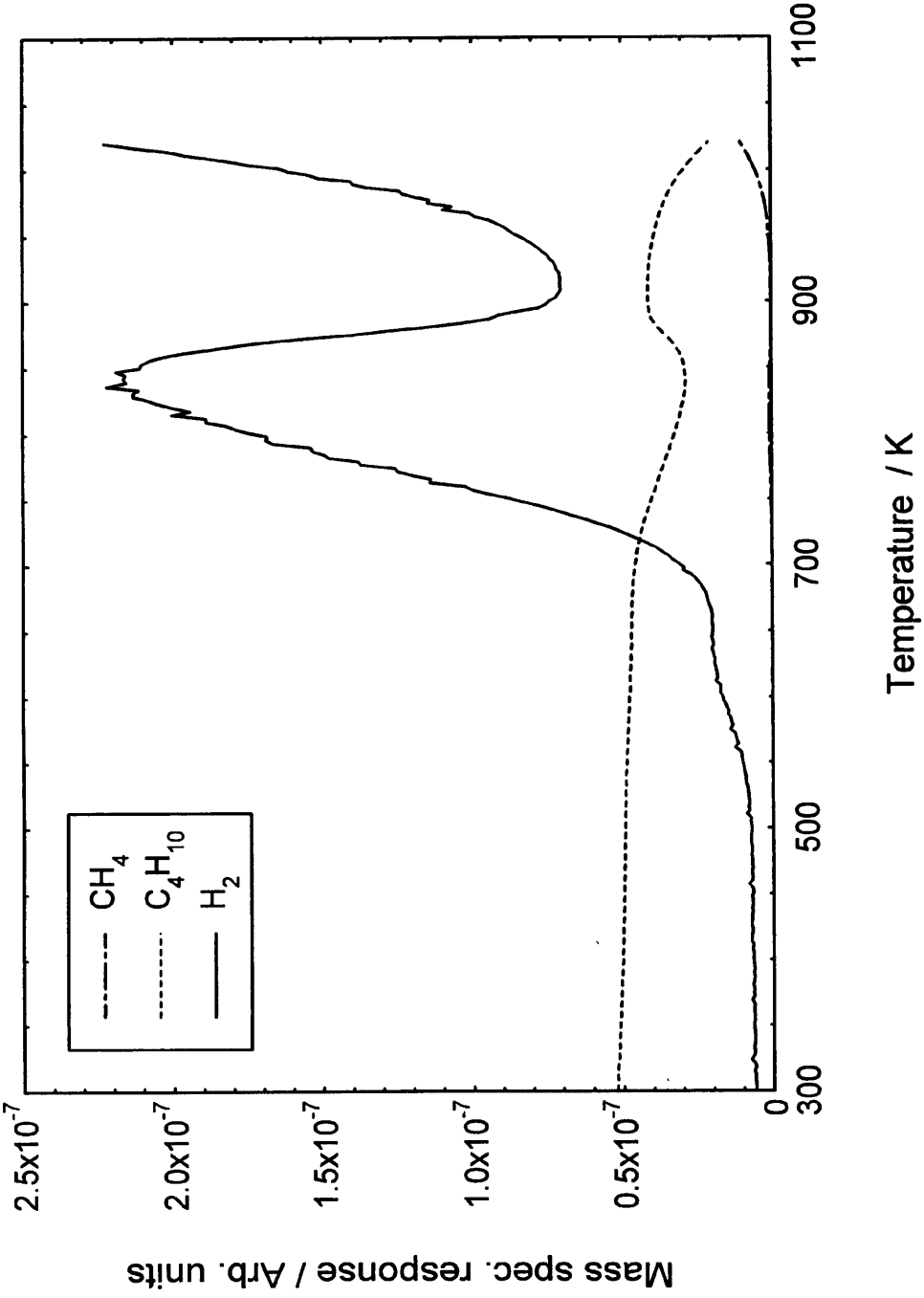


Fig.4.30 TPRn of n-butane on re-reduced catalyst AK5

$10^{19}$ atoms $g^{-1}_{cat}$. Between 700 and 900 K, the amount of high temperature carbon formed was 1.0 x $10^{21}$ atoms $g^{-1}_{cat}$ (Table 4.2). The total amount of carbon formed up to ~900 K in this case was approximately 57% less compared to the amount formed in the initial TPRn (Fig.4.26). Only 16% less carbon formation was observed for the 1wt% MgO doped sample, which indicates that increasing the amount of MgO from 1wt% to 5wt% results in a greater dispersion and more nickel ensembles being blocked.

## 4.8 Studies carried out on $NiO/Al_2O_3$ promoted with 10wt% MgO (AK6)

### 4.8.1 TPRn of n-butane on AK6

The TPRn experiment was carried out using the same procedure as detailed in Section 4.2.1.* The TPRn profile obtained is shown in Fig.4.31. Again similarities between this and the TPRn profiles obtained for sample AK4 (Fig.4.21) and AK5 (Fig.4.26) are evident. A small $H_2$ peak was initially observed, the onset of which occurred at 610 K with a peak maximum at 617 K. Following the minimum at 650 K a sharp rise in $H_2$ production occurred yet again and as previously cut off sharply, this time at 878 K. Methane was formed from 748 K maximising at 784 K and cut off at the second minimum of $H_2$ evolution.

### 4.8.2 The morphology of the carbonaceous deposits

The morphology of carbonaceous deposits generated by the decomposition of n-butane was studied by TEM. The electron micrograph is displayed in Fig.4.33. Carbon filaments produced contained a central channel running down their lengh. The average width of the filaments was ~40 nm. The nickel particles were again encapsulated by carbon.

The butane TPRn profile obtained for sample AK6 again shows that the temperature dependence of $H_2$ evolution falls into 5 distinct regions which can again be elucidated as in Section 4.2.2.1. The amount of low temperature carbon formed between 600 and

* Reduction temperature for sample AK6 was raised to 1000K

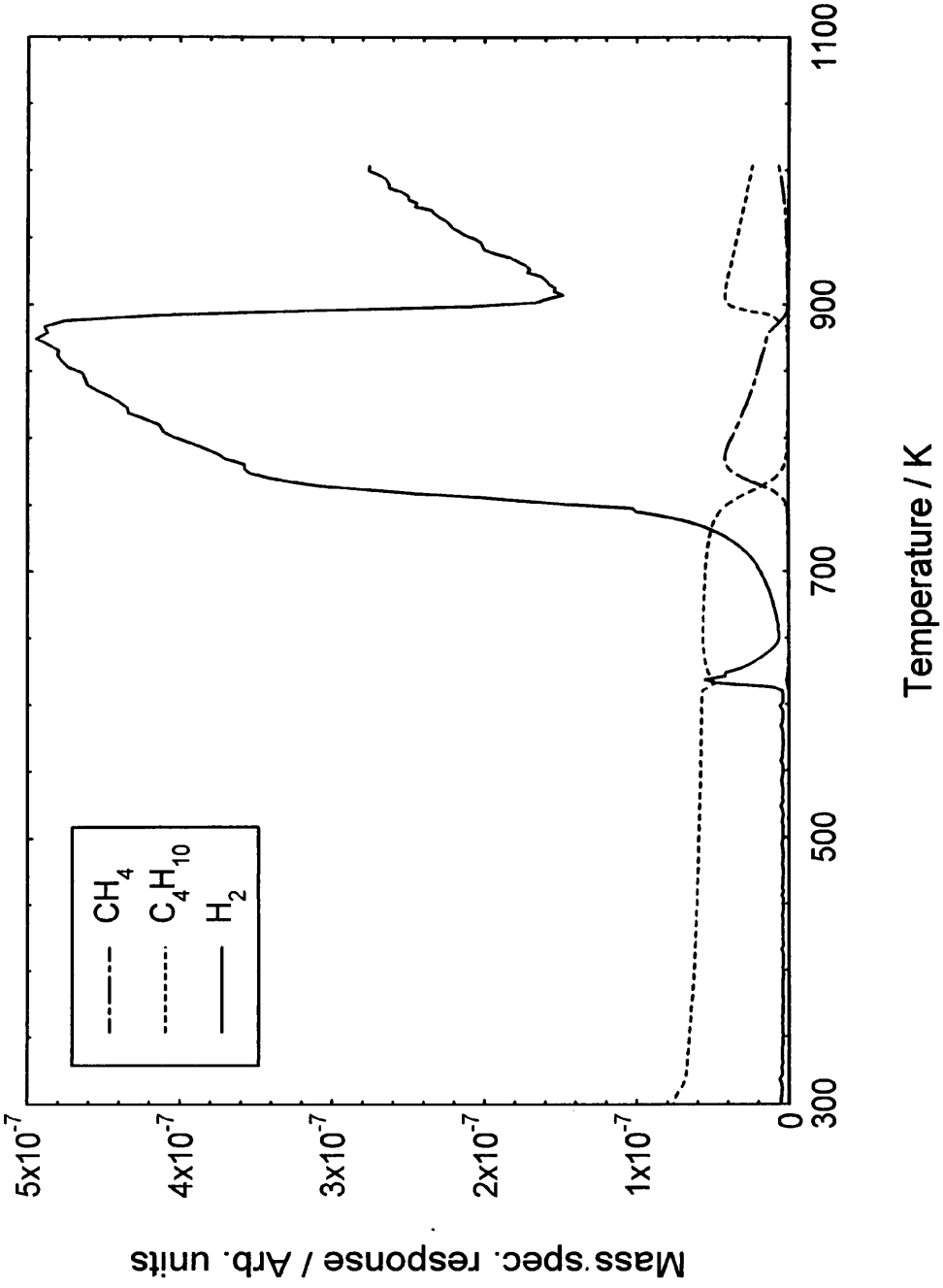


Fig.4.31 TPRn of n-butane on catalyst AK6

650 K was calculated to be 3.8 x $10^{19}$ atoms $g^{-1}_{cat}$. The amount of high temperature carbon formed between 650 and 900 K was 2.4 x $10^{21}$ atoms $g^{-1}_{cat}$. The total amount of carbon formed was 3.3 x $10^{21}$ atoms $g^{-1}_{cat}$ (Table 4.2). The activation for the production of hydrogen in the temperature range 700 - 750 K was calculated to be 140 kJ $mol^{-1}$. The similarity of the butane TPRn profile obtained for sample AK6 with those obtained for samples AK4 and AK5 shows that even the addition of 10wt% MgO appears to have little effect on the kinetics of decomposition. The total amount of carbon formed on sample AK6 is also very similar to the amounts formed on both the 1wt% and 5wt% MgO doped samples.

### 4.8.3 TPO of carbon formed on AK6

The TPO experiment was carried out using the same procedure as detailed in Section 4.2.3. The TPO profile obtained is shown in Fig.4.32. The onset of $CO_2$ evolution began at ~650 K and a sharp peak maximum was observed at 798K. The onset of CO evolution began at ~700K and a sharp increase in rate occurred at 798 K. A peak maximum occurred at 926 K followed by a sharp cut off at 980 K. A second $CO_2$ peak was observed at the CO cut off.

Depletion of oxygen was again responsible for the production of CO following $CO_2$ (partial pressure of $CO_2$ at the peak maximum $\cong$0.06 atm). The activation energy for the gasification of carbon was calculated to be 131 kJ $mol^{-1}$. The amount of carbon removed by oxidation was calculated to be 3.5 x $10^{21}$ atoms $g^{-1}_{cat}$ (Table 4.2) indicating that all the carbon formed was gasified.

### 4.8.4 Re-reduction of catalyst AK6

The re-reduction of catalyst AK6 was carried out using the same procedure as detailed in Section 4.2.4. The reduction profile obtained is shown in Fig.4.34. In this case, as in the initial reduction profile obtained for sample AK6 (Fig.3.6(c)), a broad peak maximum is observed at ~860 K with the addition of a slight shoulder visible at ~940 K.

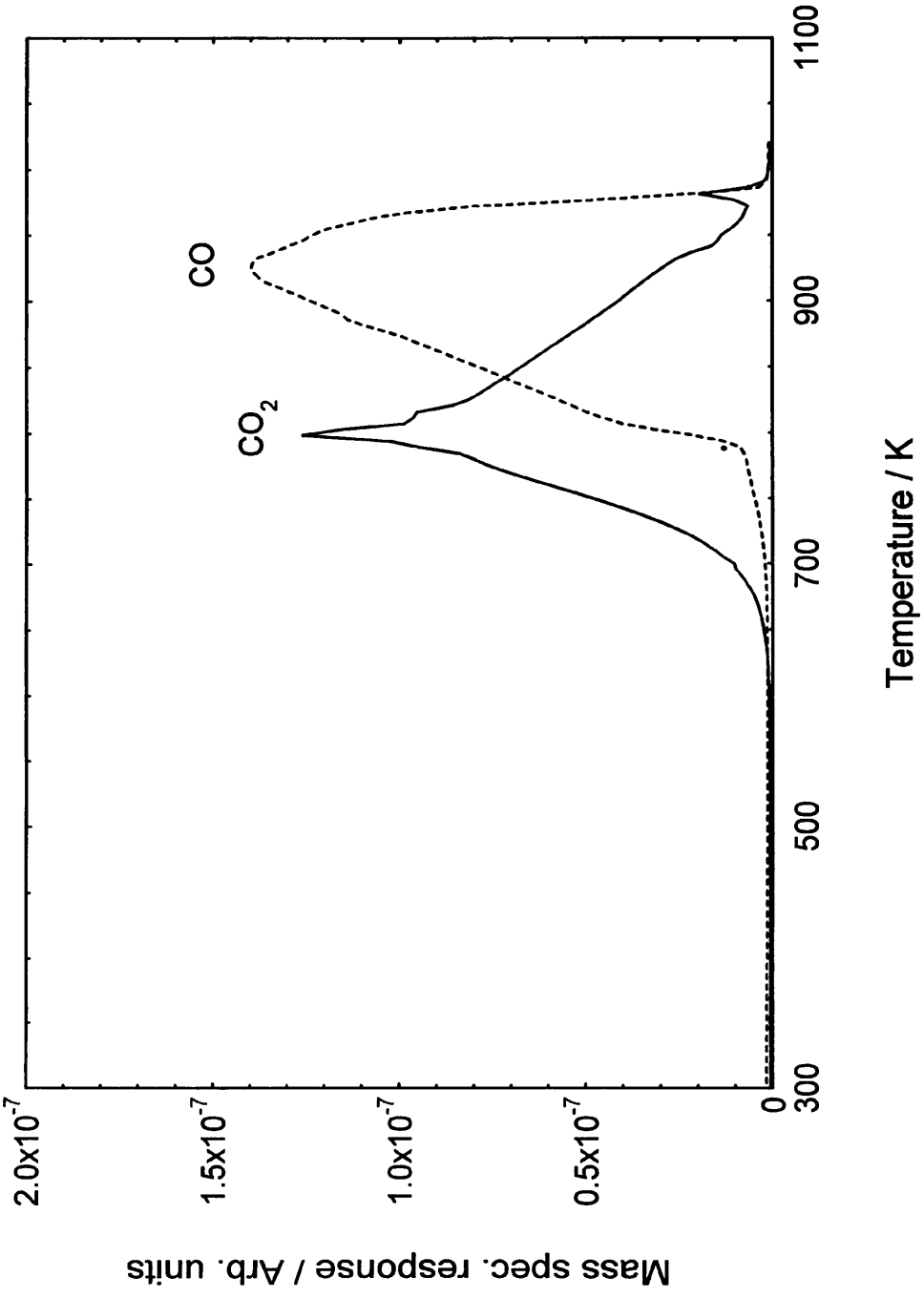


Fig.4.32 TPO of deposited carbon on catalyst AK6

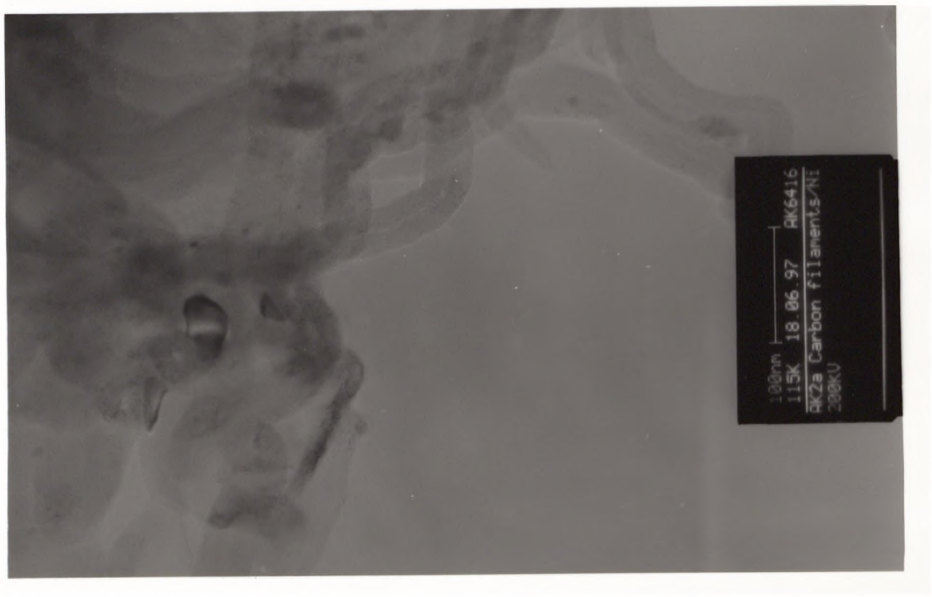


Fig.4.33 Transmission electron micrograph of carbon formed on catalyst AK6 (1023 K)

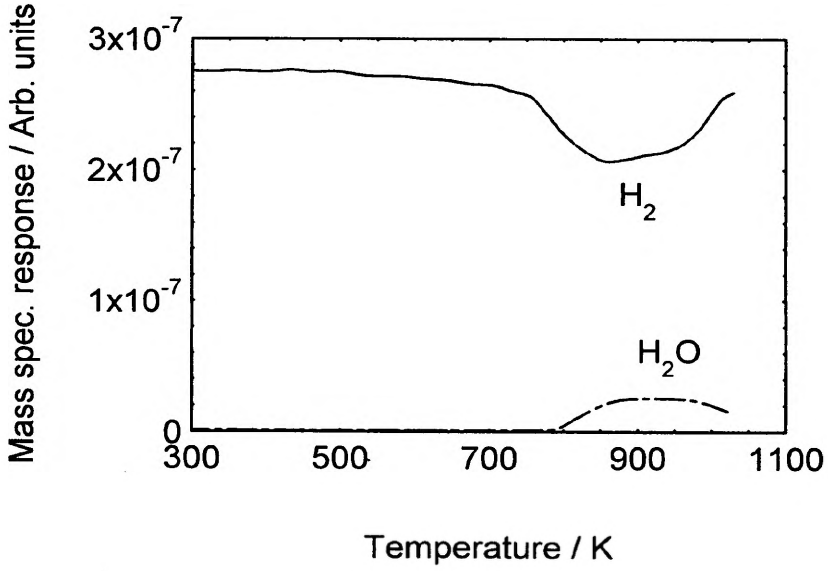


Fig.4.34 TPR profile of regenerated catalyst AK6

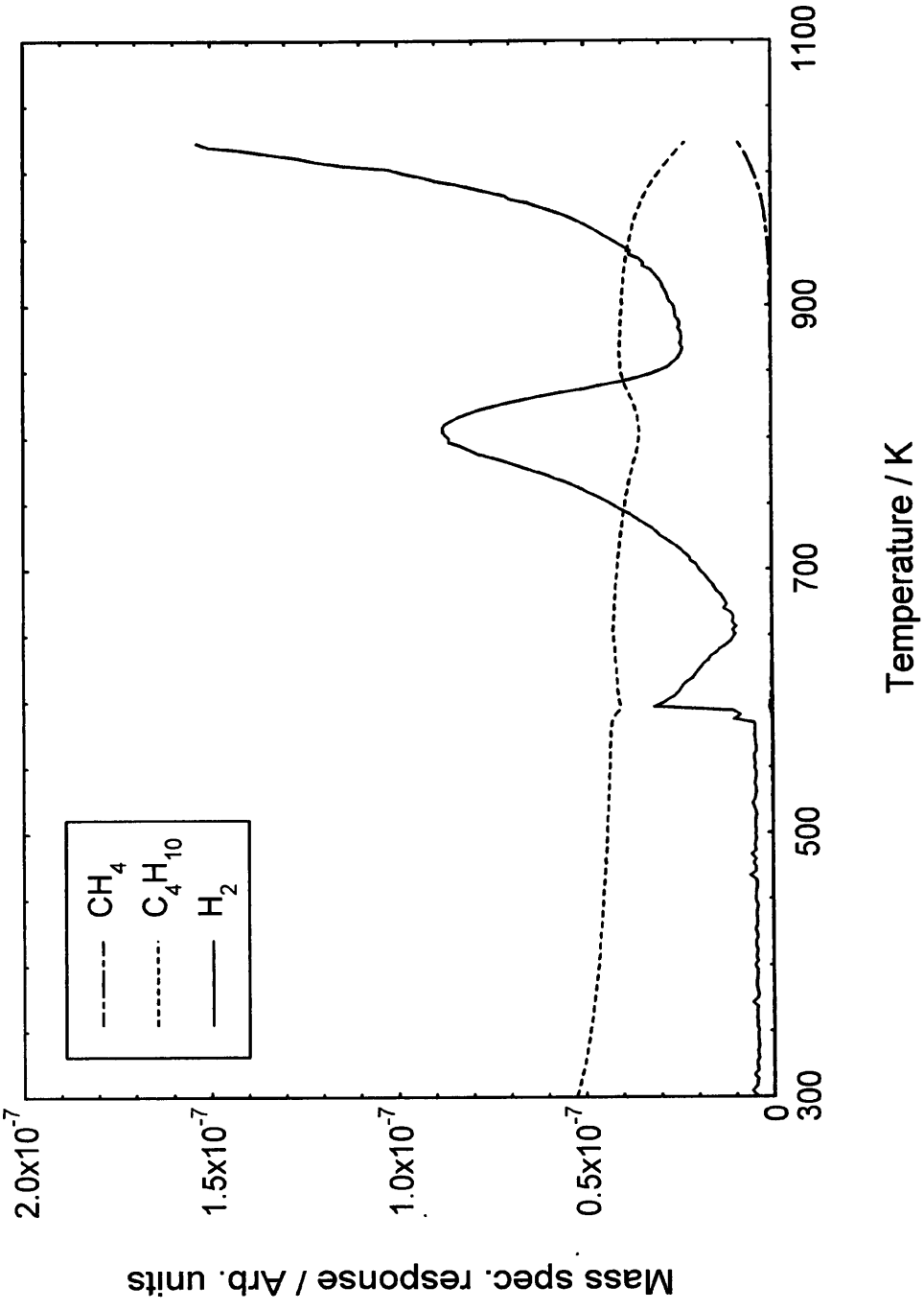


Fig.4.35 TPRn of n-butane on re-reduced catalyst AK6

Table 4.2

The amounts of carbon formed and gasified on MgO promoted $NiO/Al_2O_3$ catalysts (AK4 - AK6)

| | FIRST BUTANE TPRn | | | | | | SECOND BUTANE TPRn | | |
|---|---|---|---|---|---|---|---|---|---|
| Sample | Amount of low temp. carbon formed/ atoms $g^{-1}_{cat}$ | $E_{act}$ for diffusion of carbon through Ni/ kJ $mol^{-1}$ | Amount of high temp. carbon formed/ atoms $g^{-1}_{cat}$ | Total amount of carbon formed/ atoms $g^{-1}_{cat}$ | $E_{act}$ for gasification of carbon/ kJ $mol^{-1}$ | Total amount of carbon oxidised/ atoms $g^{-1}_{cat}$ | Amount of low temp. carbon formed/ atoms $g^{-1}_{cat}$ | Amount of high temp. carbon formed/ atoms $g^{-1}_{cat}$ | Reduction in amount of carbon formed / % |
| **AK4** | $6.8 \times 10^{19}$ (3 monolayers)* | 133 | $2.6 \times 10^{21}$ (108 monolayers) | $3.6 \times 10^{21}$ (150 monolayers) | 115 | $4.0 \times 10^{21}$ (167 monolayers) | $2.8 \times 10^{19}$ (1 monolayer) | $2.2 \times 10^{21}$ (92 monolayers) | 16 |
| **AK5** | $4.0 \times 10^{19}$ (1 monolayer)* | 130 | $2.4 \times 10^{21}$ (89 monolayers) | $3.1 \times 10^{21}$ (115 monolayers) | 150 | $3.0 \times 10^{21}$ (111 monolayers) | $4.2 \times 10^{19}$ (2 monolayers) | $1.0 \times 10^{21}$ (37 monolayers) | 57 |
| **AK6** | $3.8 \times 10^{19}$ (1 monolayer)* | 140 | $2.4 \times 10^{21}$ (92 monolayers) | $3.3 \times 10^{21}$ (127 monolayers) | 131 | $3.5 \times 10^{21}$ (135 monolayers) | $3.8 \times 10^{19}$ (1 monolayer) | $3.0 \times 10^{20}$ (12 monolayers) | 82 |

Mass of each catalyst used = 0.5g  Total surface areas: AK4 = 2.4 $m^2 g^{-1}$; AK5 = 2.7 $m^2 g^{-1}$; AK6 = 2.6 $m^2 g^{-1}$

*Number of monolayers of carbon calculated on the basis of the total surface area of the catalyst, taking monolayer coverage to be $10^{15}$ atoms $cm^{-2}$

### 4.8.5 TPRn of n-butane over re-reduced AK6

The TPRn experiment was carried out using the same procedure as detailed in section 4.2.5. The TPRn profile obtained for catalyst AK6 is shown in Fig.4.35. As in the first TPRn profile obtained for sample AK6 (Fig.4.31), a small $H_2$ peak was initially observed with a sharp peak maximum at 598 K. Following a minimum at 650 K an increase in $H_2$ was observed and a larger $H_2$ peak was produced with a peak maximum at 805 K. The size of this second $H_2$ peak however was significantly smaller than that observed in the initial TPRn in Fig.4.31. The onset of methane formation did not occur until ~925 K.

The amount of carbon formed at low temperature between ~600 and 650 K was 3.8 x $10^{19}$ atoms $g^{-1}_{cat}$. The amount of high temperature carbon formed between 650 and 900K was 3.0 x $10^{20}$ atoms $g^{-1}_{cat}$ (Table 4.3). The total amount of carbon formed in this case up to ~900 K, compared to the initial TPRn was approximately 82% less and therefore provides further evidence that inceasing the loading of MgO promoter has a greater effect on suppressing the amount of carbon formed. It can be concluded that the increased loading of MgO again leads to a greater dispersion on the surface and thus alters the kinetics of butane decomposition by blocking a greater number of nickel ensembles. Nevertheless, each loading of MgO proved to be less effective at suppressing carbon formation than even 1wt% $Al_2O_3$, which suggests that a significantly greater dispersion of $Al_2O_3$ was attained following the oxidation of carbon.

## 4.9 Conclusions

1) The remarkable similarity of the initial butane TPRn profiles obtained for MgO promoted samples to those promoted with $Al_2O_3$, indicated that the presence of MgO had a negligible effect on the kinetics of butane decomposition. It can therefore again be concluded that although the MgO promoters had a profound effect on the NiO

catalyst precursors, they had little effect on the dehydrogenational activity of Ni once formed after reduction. The total amounts of carbon formed on the MgO promoted samples were comparable to the amounts formed on the $Al_2O_3$ promoted samples, confirming that each loading of MgO provided no resistance to carbon formation

2) The activation energy calculated for the gasification of carbon in each case gave values in good agreement with those for the diffusion of carbon through nickel, suggesting again that the gasification of filaments may be the reverse process of filament formation.

3) Repetition of the butane TPRn on each regenerated catalyst produced significantly different $H_2$ spectra compared to those for the initial TPRn, which again suggested that oxidation had caused a redistribution of the Ni on the support which markedly altered the kinetics of the decomposition. The presence of predominantly Ni(111) on the surface may again have inhibited the adsorption and subsequent decomposition of butane. A decrease in the amount of carbon formed was observed, however the difference was not as great as observed for the $Al_2O_3$ promoted samples, where an average 94% reduction was observed. This suggested therefore that as well as a redistribution of Ni on the surface, the promoters play a significant role in the reduction of carbon formation on regenerated samples.

4) The percentage reduction in the amount of carbon formed ranged from 16% for the 1wt% MgO promoted sample to 82% for the 10wt% MgO promoted sample indicating that, in the case of MgO, increasing the amount of promoter did have a significant effect on supressing the amount of carbon formed on regenerated samples. This was attributed to a greater dispersion of the higher loading of MgO which was able to block a greater number of nickel ensembles required for ethylidyne formation.

5) The fact that a 90% reduction in carbon formation was observed for the 1wt% $Al_2O_3$ promoted sample implied that a greater dispersion of 1wt% $Al_2O_3$ was achieved by oxidation than each loading of MgO.

## 4.10 Studies carried out on $NiO/Al_2O_3$ promoted with 1wt% $La_2O_3$ (AK7)

### 4.10.1 TPRn of n-butane on AK7

The TPRn experiment was carried out using the same procedure as detailed in Section 4.2.1. The TPRn profile obtained is shown in Fig.4.36. The onset of $H_2$ evolution occurred at ~600 K and a small peak was produced with a minimum at ~680 K. A sharp rise in $H_2$ then occurred, giving rise to a considerably larger peak which cut off sharply at 885 K. Methane formation began at 725 K maximising at 762 K and then cut off at the second minimum of $H_2$ evolution.

### 4.10.2 Morphology of the carbonaceous deposits

The morphology of carbonaceous deposits generated by the decomposition of n-butane was studied by TEM. The electron micrograph is displayed in Fig.4.38. Carbon filaments were produced which had a central channel running down their length. The average diameter of the filaments was ~25 nm. The nickel particles were encapsulated by carbon.

The butane TPRn profile obtained for sample AK7 shows similar features to those produced in the TPRn profiles produced for all the $Al_2O_3$ and MgO promoted samples. This suggests that, like $Al_2O_3$ and MgO, 1wt% $La_2O_3$ has little effect on the kinetics of butane decomposition. The temperature dependence of $H_2$ evolution again falls into 5 distinct regions and each region is explained as previously in Section 4.2.2.1. The amount of low temperature carbon formed between 550 and 680 K was calculated to be $5.2 \times 10^{19}$ atoms $g^{-1}_{cat}$. The amount of high temperature carbon formed between 680 and 900 K was $2.6 \times 10^{21}$ atoms $g^{-1}_{cat}$. The total amount of carbon formed was $3.0 \times 10^{21}$ atoms $g^{-1}_{cat}$ (Table 4.3). The activation energy for the production of hydrogen in the temperature range 700 - 740 K was calculated to be 160 kJ $mol^{-1}$ which again showed good agreement with values reported in the literature for the diffusion of carbon through nickel [5] [7].

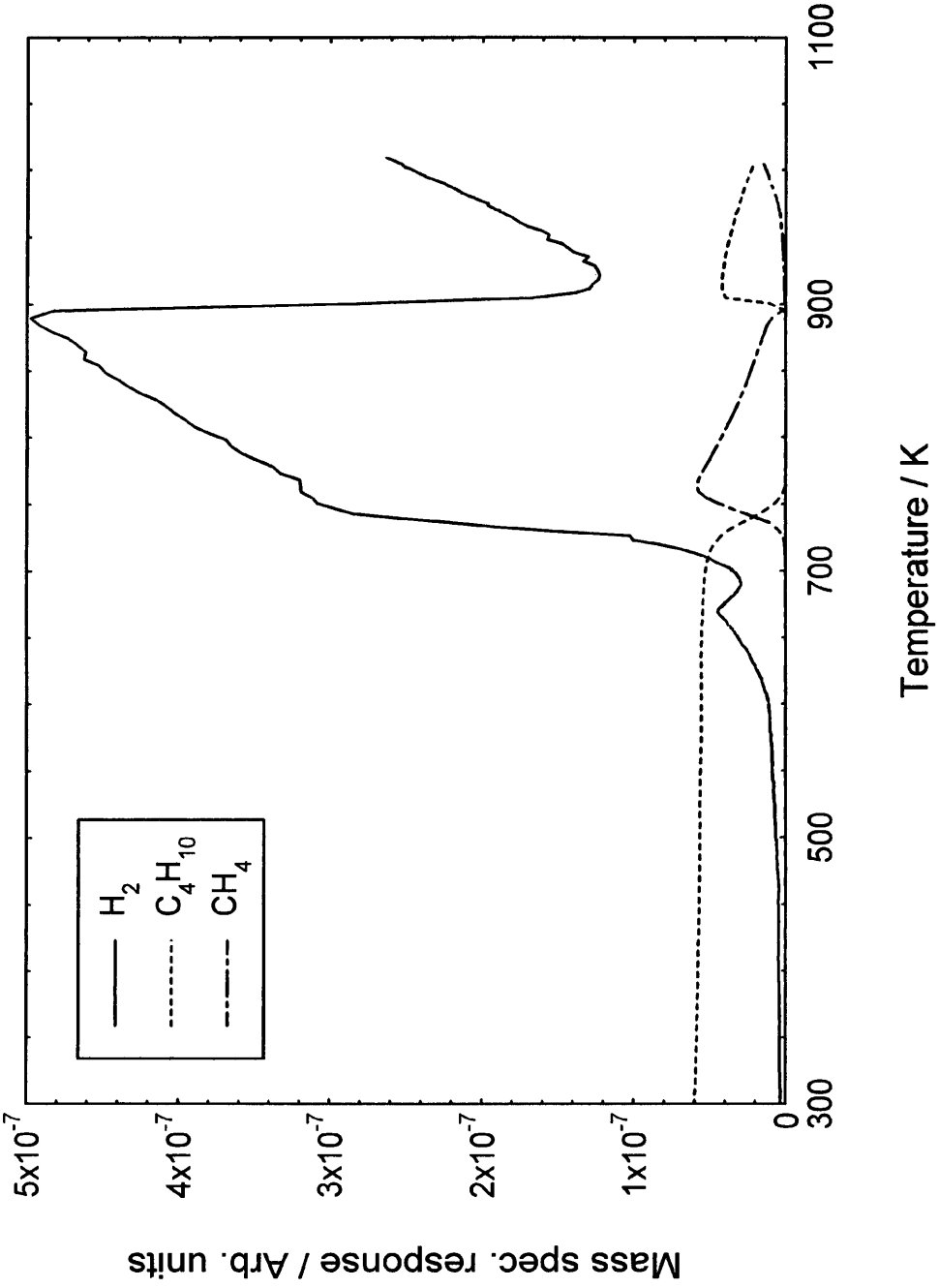


Fig.4.36 TPRn of n-butane on catalyst AK7

### 4.10.3 TPO of carbon formed on AK7

The TPO experiment was carried out using the same procedure as detailed in Section 4.2.3. The TPO profile obtained is shown in Fig.4.37. $CO_2$ evolution began at ~650 K and produced a sharp peak maximum at 807 K. CO formation began at ~700 K with a marked increase in rate occurring at 810 K and a sharp cut off at 950 K.

The TPO profile obtained in this case again shows similarities with the TPO profiles obtained for the $Al_2O_3$ and MgO promoted samples. $CO_2$ and CO were again gaseous products of the TPO reaction and this was again as a result of oxygen depletion ($CO_2$ partial pressure at the peak maximum ≅0.07 atm). The activation energy for the gasification of carbon was calculated 136 kJ $mol^{-1}$. The amount of carbon removed by oxidation was calculated to be 3.2 x $10^{21}$ atoms $g^{-1}_{cat}$ (Table 4.3), indicating that all the carbon produced by the butane TPRn was oxidised.

### 4.10.4 Re-reduction of catalyst AK7

The re-reduction of catalyst AK7 was carried out using the same procedure as detailed in Section 4.2.4. The reduction profile obtained is shown in Fig.4.39. This profile differed from the initial reduction profile obtained for catalyst AK7 (Fig.3.7(a)). In this case the dominant peak maximum had shifted to a markedly higher temperature at ~780 K and a second, broader peak was now present at ~910 K.

### 4.10.5 TPRn of n-butane over re-reduced AK7

The TPRn experiment was carried out using the same procedure as detailed in Section 4.2.5. The TPRn profile obtained for catalyst AK7 is shown in Fig.4.40 and differed markedly from the initial butane TPRn profile (Fig.4.36). The onset of $H_2$ production began at ~510 K and a slight increase in the rate of $H_2$ production was observed up to 630 K. A sharp increase in $H_2$ was then observed and a larger peak was produced with a peak maximum at 780 K. The onset of methane formation occurred at ~925 K.

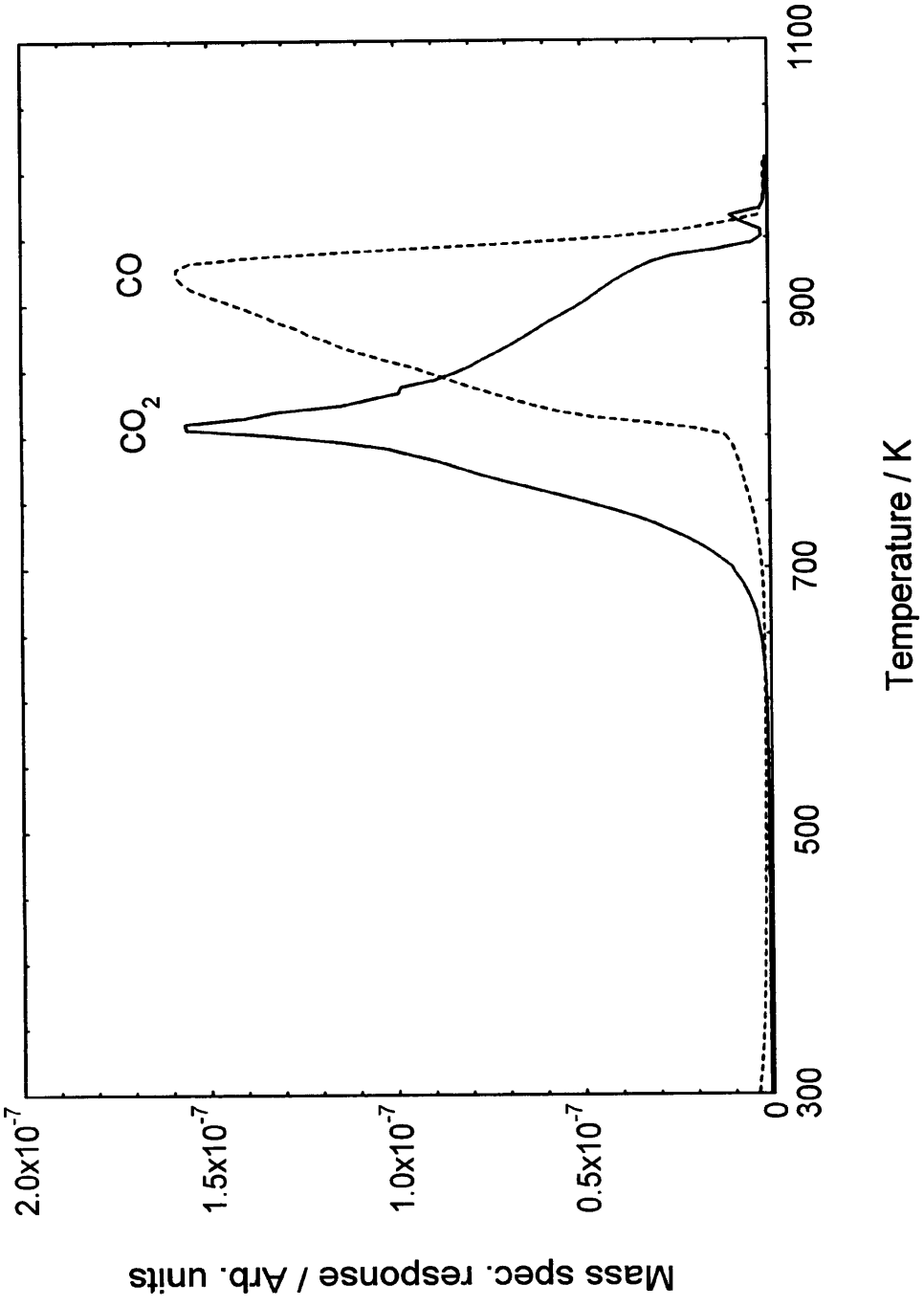


Fig.4.37 TPO of deposited carbon on catalyst AK7

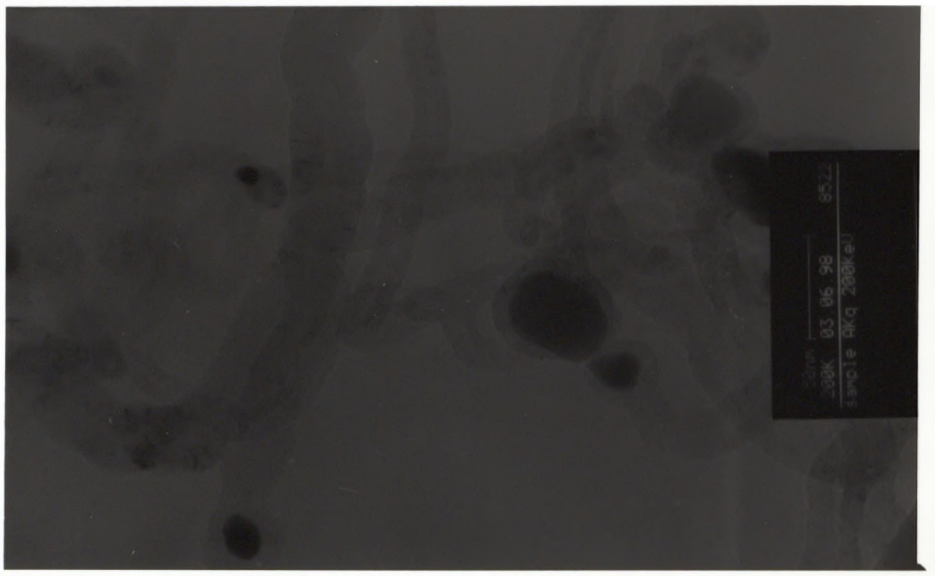

Fig.4.38 Transmission electron micrograph of carbon formed on catalyst AK7 (1023 K)

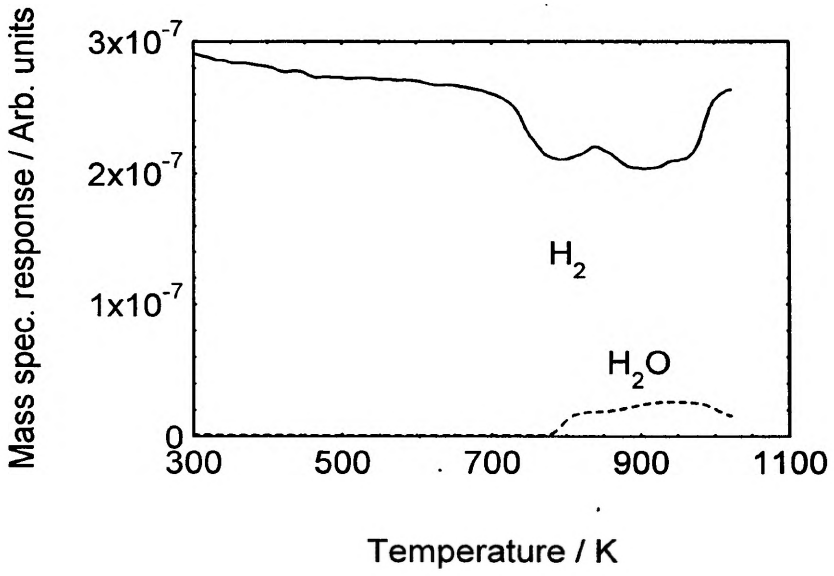


Fig.4.39 TPR profile of regenerated catalyst AK7

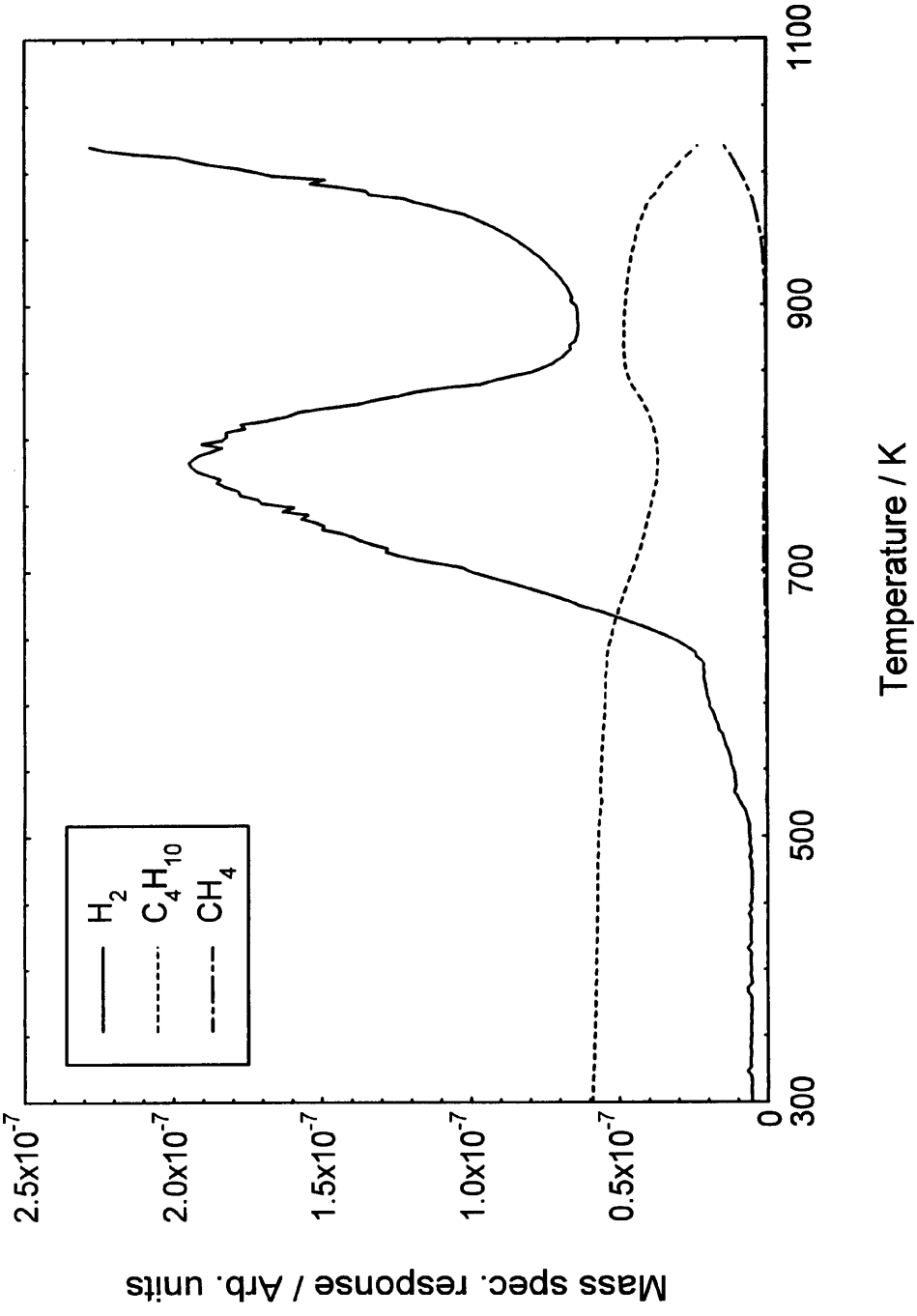


Fig.4.40 TPRn of n-butane on re-reduced catalyst AK7

The $H_2$ spectrum was approximately deconvoluted to determine the amount of carbon formed at low temperature between 500 and 700 K, which was 5.2 x $10^{19}$ atoms $g^{-1}_{cat}$. The amount of high temperature carbon formed between 600 and 900 K was 1.0 x $10^{21}$ atoms $g^{-1}_{cat}$ (Table 4.3). Compared to the initial butane TPRn (Fig.4.36), approximately 60% less carbon was formed up to ~900 K in this case. This shows that the addition of 1wt% $La_2O_3$ has a comparable effect to 5wt% MgO, which suppressed carbon formation by a similar amount. Of the three promoters however, 1wt% $Al_2O_3$ still appears to have the most appreciable effect in reducing carbon formation, due to its greater dispersion on the surface.

## 4.11 Studies carried out on $NiO/Al_2O_3$ promoted with 5wt% $La_2O_3$ (AK8)

### 4.11.1 TPRn of n-butane on AK8

The TPRn experiment was carried out using the same procedure as detailed in section 4.2.1. The TPRn profile is shown in Fig.4.41. Again similarities between this profile and the first TPRn profile obtained for AK7 (Fig.4.31) are evident. The evolution of $H_2$ began at ~600 K and a small peak was produced with a minimum at ~680 K. This was followed by a sharp rise in $H_2$ production, the large peak cutting off at 875 K. Methane was formed from ~710 K, reaching a maximum at 770 K and again cut off at the second minimum of $H_2$ evolution.

### 4.11.2 The morphology of the carbonaceous deposits

The morphology of carbonaceous deposits generated by the decomposition of n-butane was studied by TEM. The electron micrograph is displayed in Fig.4.43. carbon filaments were produced which had an average diameter of ~40 nm. Central channels running down the length of the filaments were present. Nickel particles were again encapsulated by carbon.

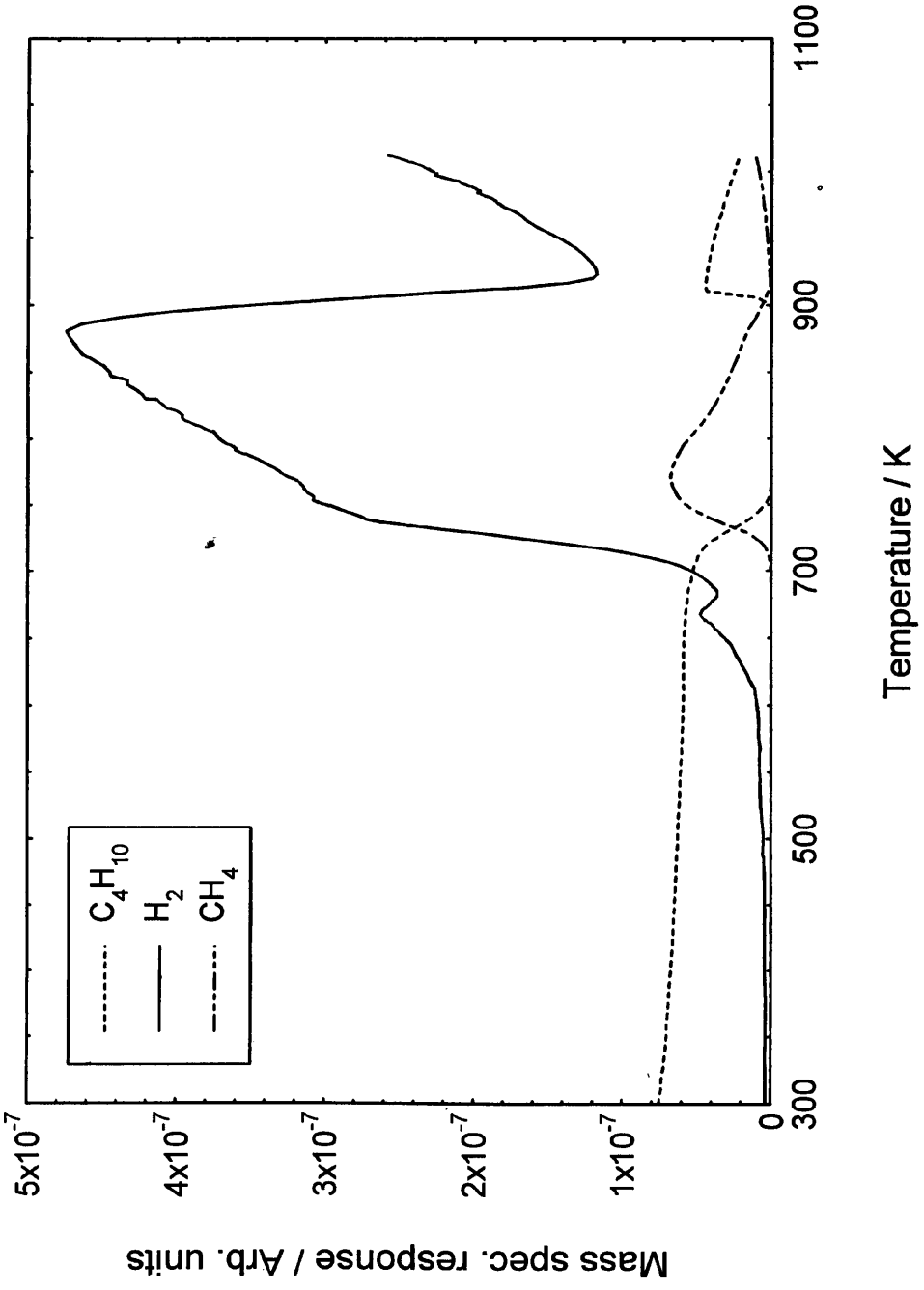


Fig.4.41 TPRn of n-butane on catalyst AK8

From the butane TPRn profile in Fig.4.41, it is evident that increasing the loading of $La_2O_3$ to 5wt% has little effect on the kinetics of decomposition. The TPRn profile obtained again shows that the temperature dependence of $H_2$ evolution falls into 5 distinct regions, each of which are explained as previously in Section 4.2.2.1. The amount of low temperature carbon formed between 550 and 680 K was $5.0 \times 10^{19}$ atoms $g^{-1}_{cat}$, while the amount formed at high temperature between 680 and 920 K was $2.8 \times 10^{21}$ atoms $g^{-1}_{cat}$. The total amount of carbon formed was $3.2 \times 10^{21}$ atoms $g^{-1}_{cat}$ (Table 4.3). The activation energy for the production of hydrogen in the temperature range 700 - 730 K was calculated to be 154 kJ $mol^{-1}$.

### 4.11.3 TPO of carbon formed on AK8

The TPO experiment was carried out using the same procedure as detailed in Section 4.2.3. The TPO profile obtained is shown in Fig.4.42. The onset of $CO_2$ evolution occurred at ~630 K producing a sharp peak maximum at 836 K. CO formation commenced at ~700 K and a sharp increase in rate was observed at 820 K. A sharp cut off in CO evolution occurred at 950 K.

The production of both $CO_2$ and CO is again attributed to oxygen depletion (partial pressure of $CO_2$ at the peak maximum $\cong$0.06 atm). The activation energy for the gasification of carbon was calculated to be 134 kJ $mol^{-1}$. The amount of carbon removed by oxidation was $3.3 \times 10^{21}$ atoms $g^{-1}_{cat}$ which indicates that all the carbon formed by the TPRn has been oxidised (Table 4.3).

### 4.11.4 Re-reduction of catalyst AK8

The re-reduction of sample AK8 was carried out using the same procedure as detailed in Section 4.2.4. The reduction profile obtained is shown in Fig.4.44. In this case two peak maxima were observed at 782 K and ~940 K, unlike in the initial reduction profile obtained for catalyst AK8 (Fig.3.7(b)) where only one dominant peak maximum was present at 672 K.

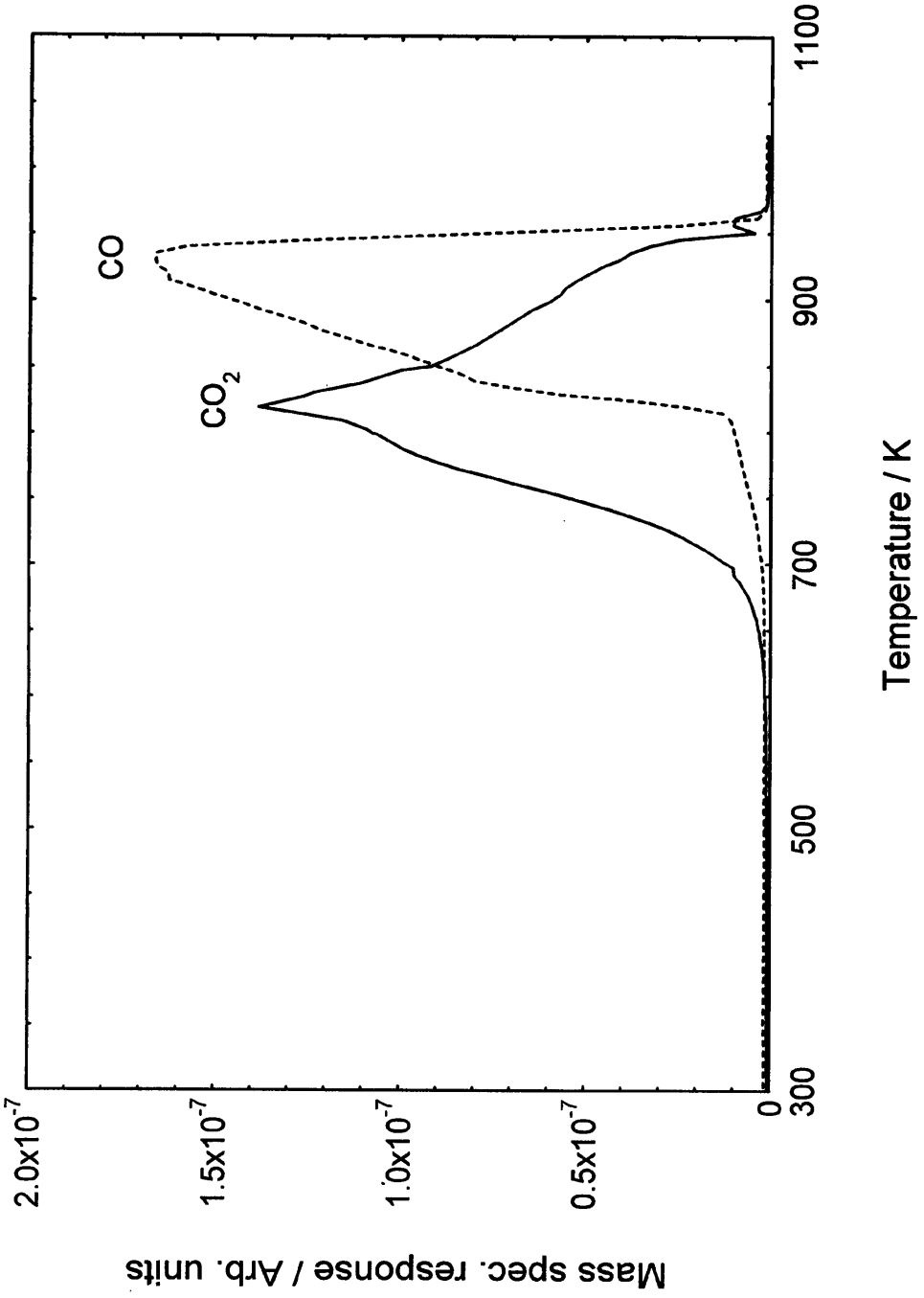


Fig.4.42 TPO of deposited carbon on catalyst AK8

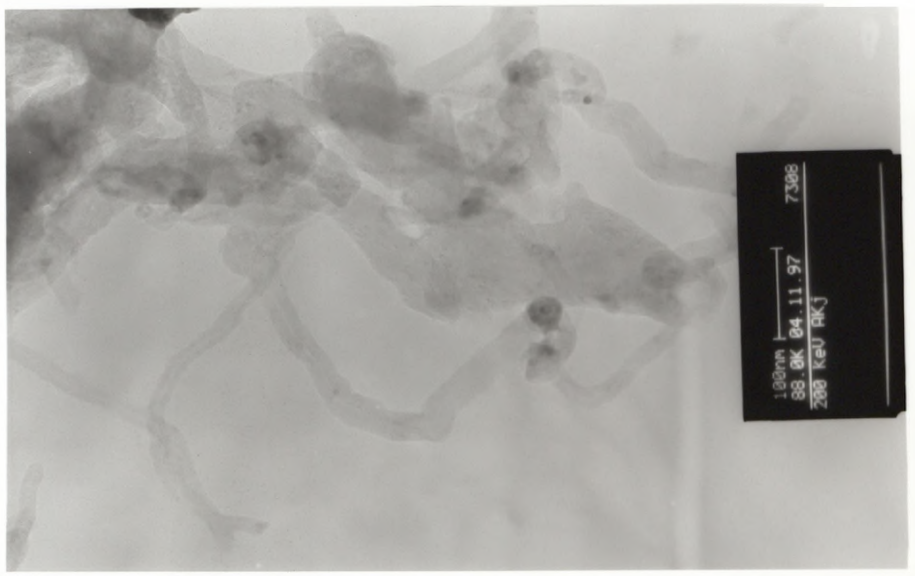

Fig.4.43 Transmission electron micrograph of carbon formed on catalyst AK8 (1023 K)

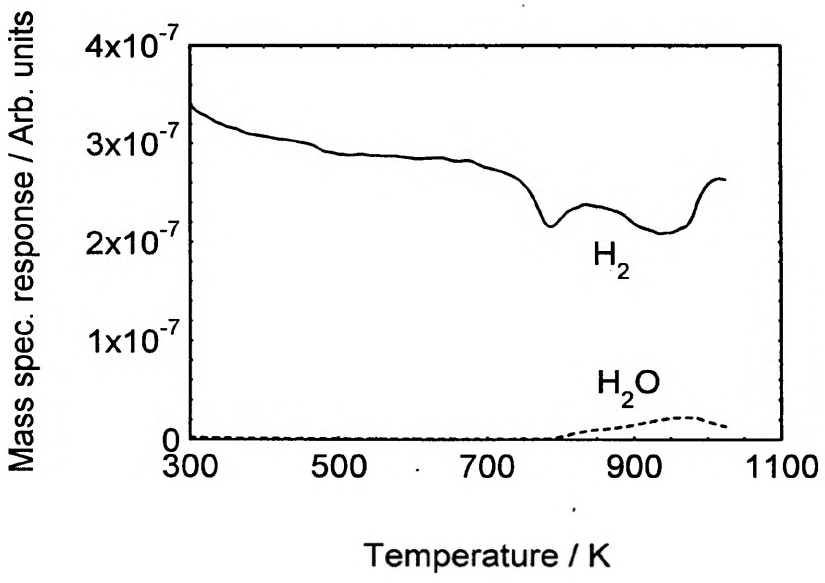


Fig.4.44 TPR profile of regenerated catalyst AK8

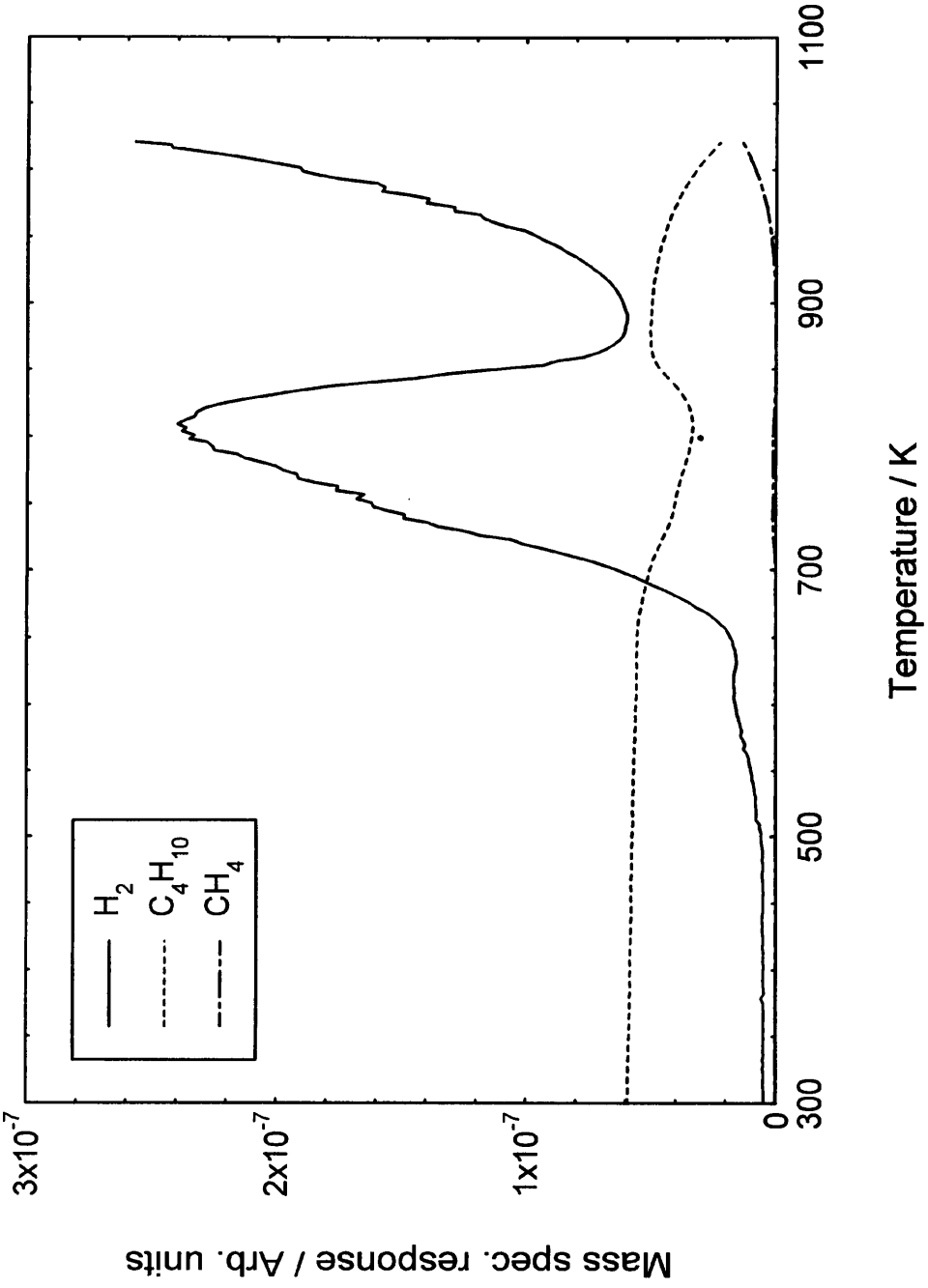


Fig.4.45 TPRn of n-butane on re-reduced catalyst AK8

### 4.11.5 TPRn of n-butane over re-reduced AK8

The TPRn experiment was carried out using the same procedure as detailed in Section 4.2.5. The TPRn profile obtained for catalyst AK8 is shown in Fig.4.45 and was very similar to the TPRn profile obtained for re-reduced AK7 (Fig.4.40). The onset of $H_2$ evolution occurred at ~500 K and again a slight increase in $H_2$ was observed up to ~615 K. A sharp increase in $H_2$ was then observed from ~650 K and a large $H_2$ peak was produced with a peak maximum at 815 K. Following a minimum at 900 K a second sharp increase in $H_2$ evolution was observed. The onset of methane formation occurred at ~920 K.

The amount of low temperature carbon formed between 500 and 650 K was calculated to be 4.2 x $10^{19}$ atoms $g^{-1}_{cat}$. The amount of high temperature carbon formed between 650 and 900 K was 1.1 x $10^{21}$ atoms $g^{-1}_{cat}$ (Table 4.3). The total amount of carbon formed in this second TPRn up to ~900 K was 60% less than in the initial TPRn (Fig.4.40), indicating that following regeneration, the dispersion of 5wt% $La_2O_3$ was similar to that of 1wt% $La_2O_3$ and therefore had a comparable effect in supressing carbon formation.

## 4.12 Studies carried out on $NiO/Al_2O_3$ promoted with 10wt% $La_2O_3$ (AK9)

### 4.12.1 TPRn of n-butane on AK9

The TPRn experiment was carried out using the same procedure as detailed in Section 4.2.1. The TPRn profile obtained is shown in Fig.4.46 and is very similar to the profiles obtained for both other $La_2O_3$ promoted samples (AK7 and AK8, Figs.4.36 and 4.41). In this case $H_2$ evolution again commenced at ~600 K producing a small peak with a minimum at ~670 K. A sharp increase in $H_2$ evolution was then observed and a large $H_2$ peak was produced which cut off sharply at 890 K. The onset of methane formation occurred at 740 K reaching a maximum at 775 K and then cut off at the second minimum of $H_2$ evolution.

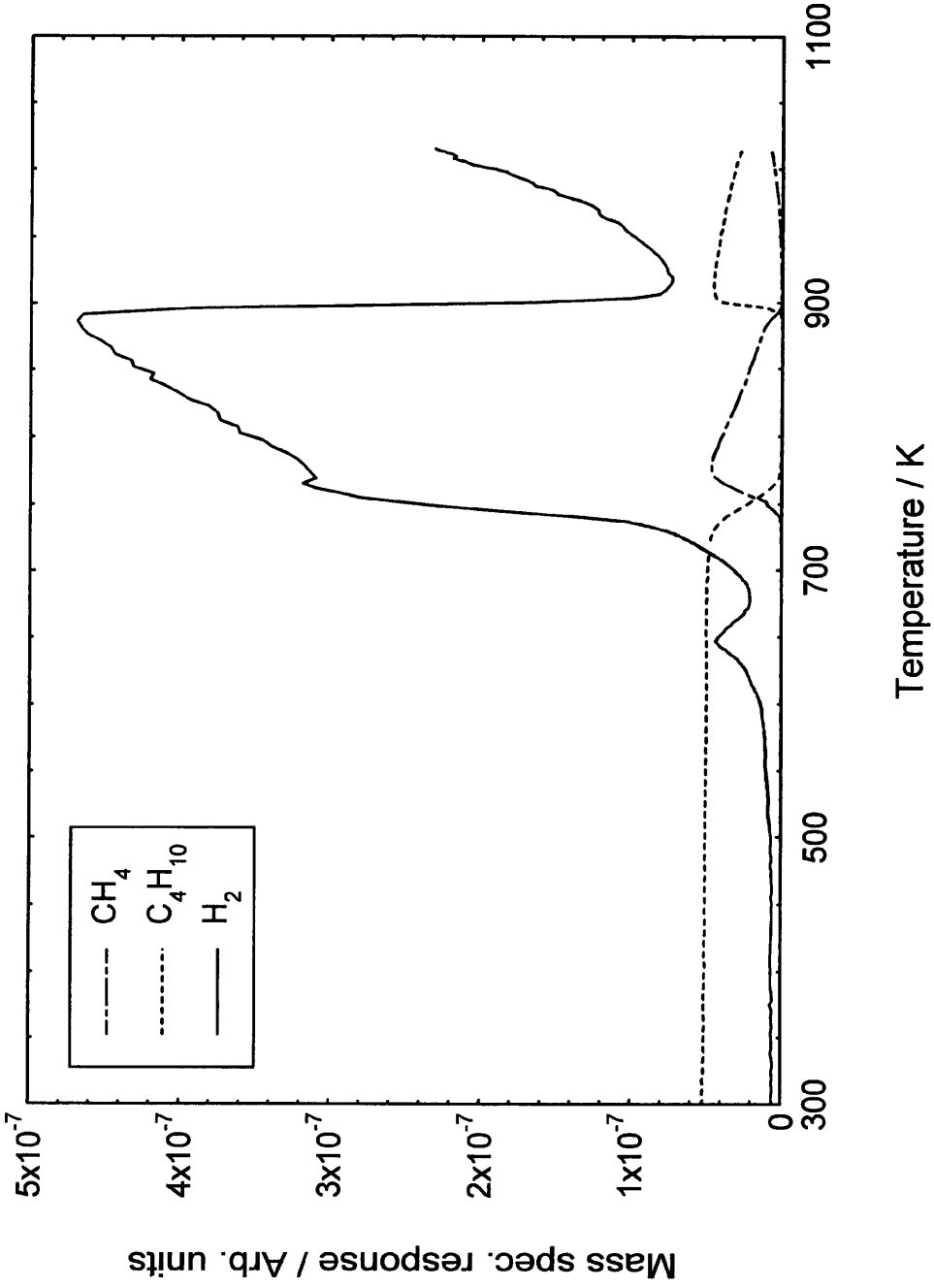


Fig.4.46 TPRn of n-butane on catalyst AK9

### 4.12.2 The morphology of the carbonaceous deposits

The morphology of carbonaceous deposits generated by the decomposition of n-butane was studied by TEM. The electron micrograph is displayed in Fig.4.48. Carbon filaments were again produced with an average width of ~30nm. Central channels running down the length of the filaments were visible. The nickle particles were again encapsulated by carbon.

As in all the prior initial TPRn profiles, the temperature dependence of $H_2$ evolution again fell into 5 destinct regions, which are explained as in Section 4.2.2.1. The amount of low temperature carbon formed between 550 and 680 K was 5.2 x $10^{19}$ atoms $g^{-1}_{cat}$. The amount of high temperature carbon formed between 680 and 910 K was 2.5 x $10^{21}$ atoms $g^{-1}_{cat}$. The total amount of carbon formed was 3.0 x $10^{21}$ atoms $g^{-1}_{cat}$ (Table 4.3). The activation energy for the production of hydrogen in the temperature range 700 -740 K was 147 kJ $mol^{-1}$. Once again it was apparent that increasing the amount of $La_2O_3$ to 10wt% had little effect on the kinetics of butane decomposition and in suppressing carbon formation.

### 4.12.3 TPO of carbon formed on AK9

The TPO experiment was carried out using the same procedure as detailed in Section 4.2.3. The TPO profile obtained is shown in Fig.4.47. $CO_2$ evolution began at ~620 K and two peak maxima were produced at 838 and 900 K. The onset of CO evolution occurred at ~700 K with a sharp increase in rate at 830 K and a sharp cut off at 900 K.

The production of both $CO_2$ and CO was again attributed to oxygen depletion (partial pressure of $CO_2$ at the peak maximum $\cong$0.07 atm). The activation energy for the gasification of carbon was calculated to be 160 kJ $mol^{-1}$. The total amount of carbon removed by oxidation was 3.1 x $10^{21}$ atoms $g^{-1}_{cat}$ (Table 4.3).

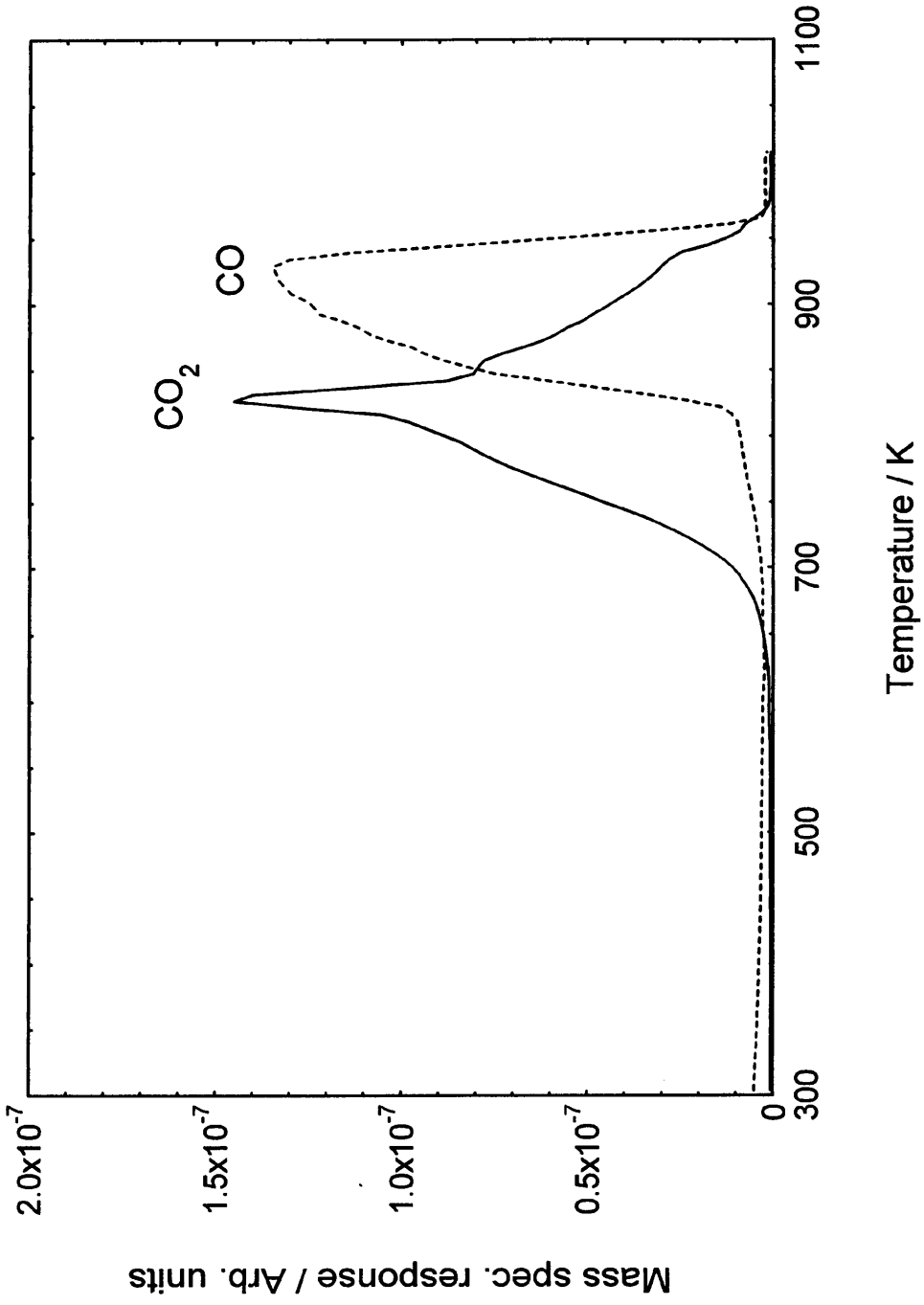


Fig.4.47 TPO of deposited carbon on catalyst AK9

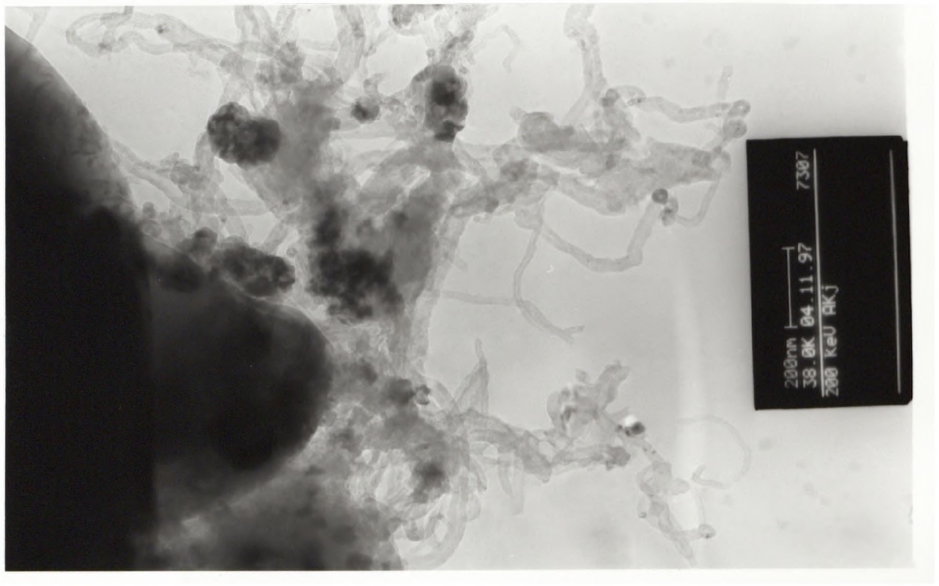

Fig.4.48 Transmission electron micrograph of carbon formed on catalyst AK9 (1023 K)

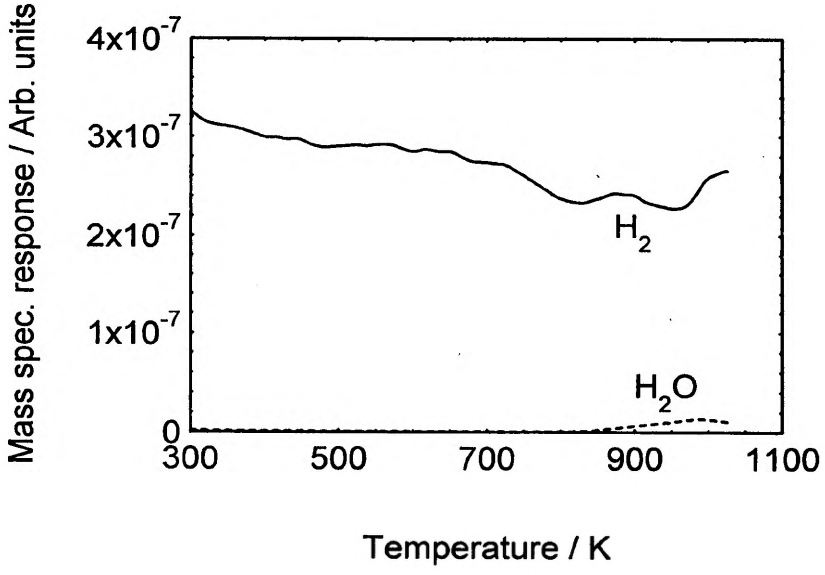


Fig.4.49 TPR profile of regenerated catalyst AK9

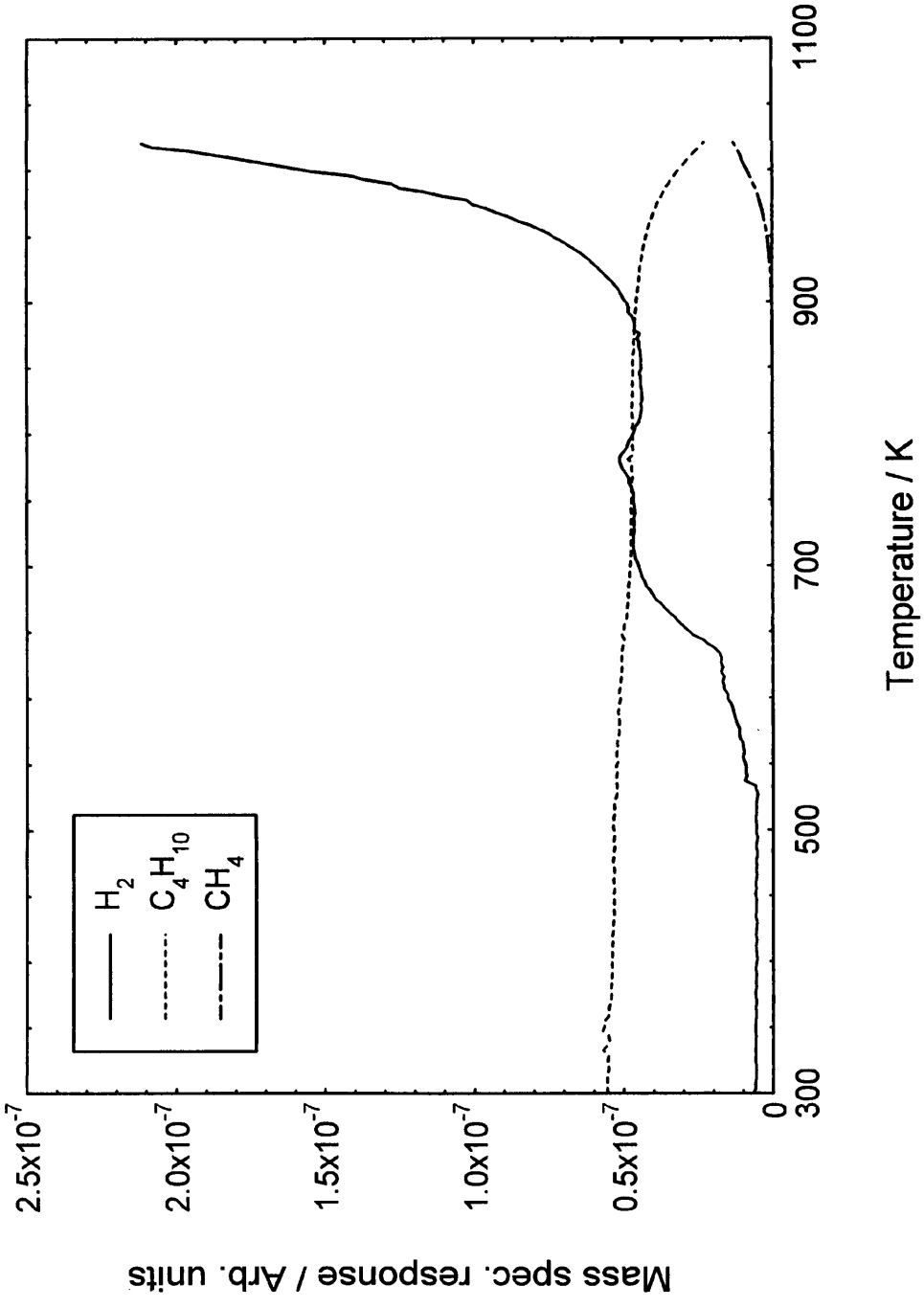


Fig.4.50 TPRn of n-butane on re-reduced catalyst AK9

Table 4.3

The amounts of carbon formed and gasified on $La_2O_3$ promoted $NiO/Al_2O_3$ catalysts (AK7 - AK9)

| | FIRST BUTANE TPRn | | | | | | SECOND BUTANE TPRn | | |
|---|---|---|---|---|---|---|---|---|---|
| Sample | Amount of low temp. carbon formed/ atoms $g^{-1}_{cat}$ | $E_{act}$ for diffusion of carbon through Ni/ kJ $mol^{-1}$ | Amount of high temp. carbon formed/ atoms $g^{-1}_{cat}$ | Total amount of carbon formed/ atoms $g^{-1}_{cat}$ | $E_{act}$ for gasification of carbon/ kJ $mol^{-1}$ | Total amount of carbon oxidised/ atoms $g^{-1}_{cat}$ | Amount of low temp. carbon formed/ atoms $g^{-1}_{cat}$ | Amount of high temp. carbon formed/ atoms $g^{-1}_{cat}$ | Reduction in amount of carbon formed / % |
| **AK7** | $5.2 \times 10^{19}$ (2 monolayers)* | 160 | $2.6 \times 10^{21}$ (104 monolayers) | $3.0 \times 10^{21}$ (120 monolayers) | 136 | $3.2 \times 10^{21}$ (128 monolayers) | $5.2 \times 10^{19}$ (2 monolayers) | $1.0 \times 10^{21}$ (40 monolayers) | 60 |
| **AK8** | $5.0 \times 10^{19}$ (2 monolayers)* | 154 | $2.8 \times 10^{21}$ (97 monolayers) | $3.2 \times 10^{21}$ (110 monolayers) | 134 | $3.3 \times 10^{21}$ (114 monolayers) | $4.2 \times 10^{19}$ (1 monolayer) | $1.1 \times 10^{21}$ (38 monolayers) | 60 |
| **AK9** | $5.2 \times 10^{19}$ (2 monolayers)* | 147 | $2.5 \times 10^{21}$ (89 monolayers) | $3.0 \times 10^{21}$ (107 monolayers) | 160 | $3.1 \times 10^{21}$ (110 monolayers) | $3.0 \times 10^{19}$ (2 monolayers) | $3.6 \times 10^{20}$ (13 monolayers) | 85 |

Mass of each catalyst used = 0.5g  Toatal surface areas: AK7 = 2.5 $m^2 g^{-1}$; AK8 = 2.9 $m^2 g^{-1}$; AK9 = 2.8 $m^2 g^{-1}$

*Number of monolayers of carbon calculated on the basis of the total surface area of the catalyst, taking monolayer coverage to be $10^{15}$ atoms $cm^{-2}$

### 4.12.4 Re-reduction of catalyst AK9

The re-reduction of catalyst AK9 was carried out using the same procedure as detailed in Section 4.2.4. The reduction profile obtained is shown in Fig.4.49. In this case two broader $H_2$ peak maxima were observed at ~800 and 958 K, unlike in the initial reduction profile obtained for catalyst AK9 (Fig.3.7(c)), where a single sharp peak maximum at 670 K was observed.

### 4.12.5 TPRn of n-butane over re-reduced AK9

The TPRn experiment was carried out using the same procedure as detailed in Section 4.2.5. The TPRn profile obtained for catalyst AK9 is shown in Fig.4.50. Compared to the second TPRn profiles obtained for AK7 (Fig.4.40) and AK8 (Fig.4.45), this profile differed significantly. A slight increase in $H_2$ was observed between 530 and 630 K, however as seen in both Figs.4.40 and 4.45, a second larger $H_2$ peak was not produced in this case. The rate of $H_2$ production increased slightly from 630 to ~700 K, afterwhich the rate remained fairly constant until ~900 K, afterwhich a sharp increase in $H_2$ was observed. The onset of methane formation again occurred at ~925 K.

The $H_2$ spectrum was approximately deconvoluted to enable the amounts of carbon to be determined. The amount of carbon formed at low temperature between 530 and 700 K was calculated to be $3.0 \times 10^{19}$ atoms $g^{-1}_{cat}$. The amount of carbon formed at high temperature between 700 and 900 K was calculated to be $3.6 \times 10^{20}$ atoms $g^{-1}_{cat}$ (Table 4.3). The addition of 10wt% $La_2O_3$ appeared to have a greater effect on suppressing the formation of carbon on the regenerated catalyst, the amount of carbon formed up to ~900 K being approximately 85% less than in the initial butane TPRn (Fig.4.46).

## 4.13 Conclusions

1) The TPRn of butane carried out on fresh catalysts promoted with 1, 5 and 10wt% $La_2O_3$ produced very similar $H_2$ spectra, which indicated that in each case the promoter

had little effect on the kinetics of decomposition. The similarity of these TPRn profiles with those obtained for the $Al_2O_3$ and MgO promoted samples showed conclusively that none of the promoters initially had any significant effect on the decomposition pathway of butane. In Chapter 3 temperature-programmed reduction revealed that all the promoters had a profound effect on the nature of the NiO catalyst precursors, but had negligible effect on the dehydrogenational activity of Ni once formed after reduction.

2) For all the promoted catalysts, the activation energy for gasification of carbon gave values which were comparable to the diffusion of carbon through nickel. In each case this suggested that the gasification of carbon filaments may be the reverse of filament formation.

3) Repetition of the butane TPRn on the regenerated $La_2O_3$ promoted catalysts gave rise to $H_2$ spectra which were significantly different to those obtained for the original TPRn indicating that the kinetics of decomposition had changed. This was again believed to be due to the redistribution of nickel on the support caused by the oxidation and the blocking of specific nickel ensembles by $La_2O_3$.

4) The amounts of carbon formed was significantly less on regenerated samples, the greatest reduction being observed for the 10wt% $La_2O_3$ promoted sample where 85% less carbon was formed. The inhibiting effect of $La_2O_3$ on carbon formation was found to be similar to that of MgO which suggests that the dispersion of both promoters was similar following regeneration. However, the greatest inhibition of carbon formation was observed for the $Al_2O_3$ promoted samples, indicating that the dispersion of $Al_2O_3$ following regeneration was greater than that of both MgO and $La_2O_3$. This resulted in a greater proportion of nickel ensembles being blocked which inhibited the formation of ethylidyne on the surface.

## References


[1] Baker,R.T.K., Kim, M.S. and Rodriguez, N.M., *J. Catal.*, **131**, 60, 1991.

[2] Hadden, R.A., Howe, J.C. and Waugh, K.C. in 'Catalyst Deactivation', Bartholomew, C.H. and Butt, J.B. (Eds.), Elsevier Science Publishers B.V., Amsterdam, 1991.

[3] Boellard, E., De Bokx, P.K., Kock, A.J.H.M. and Geus, J.M., *J.Catal.*, **96**, 481, 1985.

[4] Rostrup-Nielsen, J.R. and Tøttrup, P.B. in 'Proc. Symp. Sci. Catal. Its Appl. Ind. 1979', p.379, Fert. (Plann. Dev.) India Ltd. Sindri, India.

[5] Trimm, D.L., *Catal. Rev. Sci. Eng.*, **16**, 155, 1977.

[6] Schouten, F.C., Gijzeman, O.C.J. and Bootsma, G.A., *Surf. Sci.*, **87**, 1, 1979.

[7] Diamond, S., PhD Thesis, University of Illinois, 1965.

[8] Lobo, L.S. and Trimm, D.L., *J. Catal.*, **29**, 15, 1973.

[9] Rostrup-Nielsen, J.R., Catalytic Steam Reforming, Springer-Verlag, 1984.

[10] Froment, G.F., *Chem. Eng. Sci.* **36**, 1271, 1981.

[11] Baker, R.T.K., Barber, M.A., Harris, P.S., Feates, F.S. and Waite, R.J., *J. Catal.*, **26**, 51, 1972.

[12] Goula, M.A., Lemonidou, A.A. and Efstathiou, A.M., *J. Catal.*, **161**, 626, 1996.

[13] Figueiredo, J.L., Bernardo, C.A., Chludzinski, J.J. and Baker, R.T.K., *J.Catal*, **110**, 127, 1988.

[14] Baker, R.T.K. in 'Catalyst Deactivation', Bartholomew, C.H. and Butt, J.B. (Eds.), Elsevier Science Publishers B.V., Amsterdam, 1991.

[15] Petersen, E.E. and Bell, A.T. (Eds.), 'Catalyst Deactivation', Chemical Industries, Vol.30, Marcel Dekker, New York, 1987.

[16] Somorjai, G.A. in 'Surface Chemistry and Catalysis', 452, Wiley-Interscience, 1994.

[17] Zielinski, J., *J. Catal.*, **76**, 157, 1982.

[18] Figueiredo, J.L. in 'Progress in Catalyst Deactivation', Nato Advanced Study Institute Series, 45, 1982.

[19] Rostrup-Nielsen, J.R. and Trimm, D.L., *J. Catal.*, **48**, 155, 1977.

[20] Machiels, C.J. and Anderson, R.B., *J. Catal.*, **58**, 268, 1979.

[21] Martin, G.A. and Dalmon, D.A., *C. R. Acad. Sci. Ser. C.*, **286**, 127, 1978.

[22] Yang, R.T. and Chen, J.P., *J. Catal.*, **115**, 52, 1989.

[23] Koestner, R.J., Frost, J.C., Stair, P.C., Van Hove, M.A. and Somorjai, G.A., *Surf. Sci.*, **116**, 85, 1982.

[24] Marshall, P.R., McDougall, G.S. and Hadden, R.A., *Topics in Catalysis* **1**, 9, 1994.

# 5

# GASIFICATION AND CHARACTERISATION OF CARBONACEOUS DEPOSITS FORMED AT VARYING TEMPERATURES ON PROMOTED $NiO/Al_2O_3$ CATALYSTS

## 5.1 Introduction

The deactivation of supported nickel catalysts in steam reforming is due foremost to carbon deposition, which poisons the active nickel surface and further causes blockage of pore mouths of the catalyst support and even its physical disintegration [1]. The carbon produced, however, can exist on the metal surfaces of nickel catalysts in a variety of forms. It is well known that hydrocarbon exposure to nickel crystallites at elevated temperatures (>700 K) can rapidly produce a mass of long-growing carbon filaments [2] [3] which have been identified in numerous experiments analyzed by transmission electron microscopy. However, other very reactive forms of surface carbon can also exist, since carbon atoms chemisorbed on nickel surfaces are believed to play a role in the mechanism of hydrocarbon steam reforming [4] [5].

The nature of carbonaceous deposits formed on nickel catalysts at particular temperatures can be characterised by their reactivity with a suitable gas during temperature-programmed surface reaction (TPSR). Such removal of carbon by reaction with $O_2$ has recieved relatively minor attention, whereas gasification with $H_2O$ and $H_2$ has been more widely studied [6] [7] [8]. In one of the most detailed studies carried out by McCarty et al [6], carbon deposits formed by exposure to ethylene, depending primarily on the temperature during deposition, exhibited seven reactive states during TPSR with 1-atm $H_2$. These included two very reactive states of chemisorbed carbon, a carbon film, nickel carbide and two types of filamentous carbon.

In Chapter 4, only carbon formed at high temperature (1023 K) on the promoted NiO catalysts was gasified by reaction with oxygen. TEM revealed this carbon to be filamentous in nature. In the present chapter, carbon is to be deposited on the catalysts again by the temperature-programmed reaction of n-butane, which will be aborted at three different temperatures: 673, 773 and 873 K. The carbon will then be gasified by reaction with oxygen (temperature-programmed oxidation (TPO)) in order to provide information about the nature of the carbon deposited and to determine the amount of carbon present. This will indicate whether the presence of the different promoters provides any resistance to carbon formation at various temperatures and if they have any influence in determining the nature of carbon species formed. TEM will be employed to investigate the morphology of the carbonaceous deposits. Temperature-programmed hydrogenation (TPH) of deposited carbon species will also be carried out in order to provide a comparison with the results obtained from the TPO experiments.

It was seen in the previous chapter that the $Al_2O_3$, MgO and $La_2O_3$ promoters initially had little effect on the decomposition pathway of n-butane on each of the catalysts. In this chapter therefore, only the $NiO/Al_2O_3$ samples promoted with 5wt% of each promoter were investigated, namely AK2, AK5 and AK8.

## 5.2 Studies carried out on $NiO/Al_2O_3$ promoted with 5wt% $Al_2O_3$ (AK2)

### 5.2.1 Deposition of carbon by TPRn of n-butane

Carbon was deposited on catalyst AK2 by the TPRn of n-butane as follows. The catalyst (0.5 g) was firstly pre-treated by heating in a 100% helium stream (25 $cm^3$ $min^{-1}$, 1 bar, 10 K $min^{-1}$) from ambient to 873 K and was maintained at that temperature for 2 hours. After cooling to ambient under helium, the flow was switched to a hydrogen-helium stream (5% $H_2$, 25 $cm^3$ $min^{-1}$, 1 bar) and the catalyst was reduced by raising the temperature to 873 K at 3 K $min^{-1}$. The catalyst was held at 873 K for 16 hours under the hydrogen-helium stream. Following reduction, the flow was switched to helium once more and the sample cooled to ambient. The flow was then switched to

an n-butane-helium stream (2% n-butane, 25 $cm^3$ $min^{-1}$, 1 bar) and the catalyst was heated under the flowing gas from ambient to 673 K at a rate of 5 K $min^{-1}$.

The same procedure as above was repeated on two further fresh samples of catalyst AK2, however this time the butane TPRn was stopped at 773 K for one sample and 873 K for the other.

### 5.2.2 Carbonaceous deposits formed via n-butane TPRn up to 673 K

#### 5.2.2.1 The morphology of the carbonaceous deposit

The morphology of the carbonaceous deposit formed via n-butane TPRn up to 673 K was studied by TEM. In all cases sample preparation for microscopy was carried out as described previously in Section 4.2.2. The electron micrograph obtained is shown in Fig.5.1. Upon inspection a 'film' surrounding the large nickel crystallite in the foreground was clearly visible. It therefore appears that n-butane TPRn up to 673 K produces a carbon species which entirely encapsulates the nickel. This reasonably explains the decrease in the rate of $H_2$ production observed at 680 K in the n-butane TPRn profile shown in Fig.4.1, Chapter 4. At this temperature the surface coverage of decomposition fragments can be expected to increase on the nickel component of the catalyst until the surface is completely poisoned by the carbon. Thus the nickel surface is no longer available for butane dehydrogenation to continue and the rate of $H_2$ production decreases. Further deposition only occurs when the carbon is removed by diffusion through the bulk of the nickel crystallite, which has been found to occur at temperatures >~640 K [9]. This can then lead to the formation of carbon filaments [10].

#### 5.2.2.2 Gasification of deposited carbon by TPO

On completion of the n-butane TPRn at 673 K, the flow was switched to helium and the sample was cooled to ambient. When cool, the flow was then switched to an oxygen-helium stream (5% $O_2$, 25 $cm^3$ $min^{-1}$, 1 bar) and the temperature was raised from

(See page 191)

ambient to 1023 K at a rate of 5 K $min^{-1}$. The carbon TPO profile is shown in Fig.5.2. The oxidation of carbonaceous species began at ~500 K and $CO_2$ was the only gaseous product of the reaction. Different states of carbon were identified by maxima in the rate of $CO_2$ production which were observed at 588 and 690 K. This confirmed that two dominant carbon species were present which exhibited different activities for reaction with $O_2$. An approximate deconvolution of the of the $CO_2$ spectrum provided the amounts of both types of carbon formed. These species designated as $C^1$ and $C^2$ in accordance with their reactivity order, were present in amounts 3.0 x $10^{19}$ atoms $g^{-1}_{cat}$ and 3.5 x $10^{19}$ atoms $g^{-1}_{cat}$. The total amount of carbon deduced from the TPO experiment was 6.5 x $10^{19}$ atoms $g^{-1}_{cat}$ (Table 5.1 - N.B. Tabulated results also present the amounts of carbon formed in terms of monolayers). This amount of carbon is therefore consistent with the formation of an encapsulating film, as observed by TEM (Fig.5.1). McCarty et al [6] described the presence of what they called a 'surface carbon film' on $Ni/Al_2O_3$ which was formed from ethylene at the lower temperature of 573 K. Based on TPH experiments, they deduced that the amount of carbon deposited did not exceed 4 monolayers and therefore suggested that the material was most likely to be an amorphous carbon film. Barbier et al [11] also carried out the TPO of carbon deposited on $Ni/Al_2O_3$ form the hydrogenolysis of cyclopentane at 693 K and found that reaction with oxygen produced a single $CO_2$ peak with $T_{max}$ at 633 K. They suggested that this carbonaceous species was a very reactive bidimensional carbon. The two states of carbon identified from the TPO experiment in Fig.5.2 implies that the carbon film encapsulating the nickel is heterogeneous in nature. It is therefore likely that the carbon species is present as two layers which exhibit a different reactivity to oxidation and thus give rise to two $CO_2$ peaks in the TPO experiment.

### 5.2.3 Carbonaceous deposits formed via n-butane TPRn up to 773 K

#### 5.2.3.1 Morphology of the carbonaceous deposit

The electron micrograph of carbon produced by n-butane TPRn up to 773 K is displayed in Fig.5.3. The carbon deposit was found to consist of short, carbon filaments with well faceted, pear shaped nickel particles located at the top of the

filaments. The micrograph confirms therefore, that the carbon film identified in Section 5.2.2 is a precursor to the formation of the carbon fibrils observed. The diffusion of carbon through the bulk of nickel crystallites can occur at temperatures as low as ~640 K [9] and the formation of carbon filaments has been reported to take place at temperatures >720 K [10] which agrees well with our observations. The widths of the filaments formed were governed by the size of the associated nickel particles and were typically in the range 25 - 40 nm. It was significant that the filaments did not have a hollow appearance, a central core being clearly absent. This is in agreement with the observations reported by Tracz et al [12]. They examined carbon deposited on $Ni/Al_2O_3$ catalysts during the steam reforming of n-butane using High Resolution Electron Microscopy, and found that at 773 K filaments possessing no central channel were generated. These filaments were described as 'true' filaments which had carbon layers aligned perfectly to the shape of the nickel particle. The fact that no carbon deposit was visible at the metal/gas interface in the TEM in Fig.5.3 was evidence that the filaments formed do not deactivate the catalyst.

### 5.2.3.2 Gasification of deposited carbon by TPO

The oxidation of carbonaceous deposits formed via n-butane TPRn up to 773 K was carried out as described in Section 5.2.2.2. The TPO profile obtained is shown in Fig.5.4. Again the only gaseous product of the reaction was $CO_2$. The onset of $CO_2$ evolution began at ~600 K in this case and this time only a single, large peak was produced with a maximum at 785 K. The amount of carbon formed, labelled $C^3$, was calculated to be $3.6 \times 10^{20}$ atoms $g^{-1}_{cat}$ (Table 5.1). The TPO profile also indicated that these filaments formed at 773 K are not gasified as easily as the surface carbon deposited at 673 K. The presence of a single $CO_2$ peak suggests the presence of only one dominant type of carbonaceous species, which ties in with the TEM results which showed filaments containing no central core. However it is not clear from the TEM if the carbon is graphitic in nature. Tracz et al [12] observed that the structure of carbon filaments formed on $Ni/Al_2O_3$ by the steam reforming of n-butane at 773 K showed only initial stages of ordering of short carbon layers which showed a partially

amorphous structure. They also reported that filaments formed exhibited a higher degree of graphitization with increasing temperature.

### 5.2.4 Carbonaceous deposits formed via n-butane TPRn up to 873 K

#### 5.2.4.1 Morphology of the carbonaceous deposit

The electron micrograph of carbon produced by n-butane TPRn up to 873 K is displayed in Fig.5.5. In this case a high density of long carbon filaments was observed, which had diameters ranging from 25 - 40 nm. Unlike the filaments produced at 773 K, the filaments this time exhibited a hollow appearance, the presence of a central channel clearly evident. Nickel particles were again situated at the top of filaments. Comparison of the filament structures obtained at 773 K and 873 K suggests that the 'true' filaments undergo a transition into 'tubular' filaments. This step-wise change of filament structures at increasing temperatures has been reported by Tracz et al [12]. They reported that the 'tubes' formed at 873 K possessed a higher degree of graphitization than filaments formed at 773 K, with the carbon layers in the tubes arranged more or less parallel to the tube axis. Unfortunately this cannot be seen in the TEM shown in Fig.5.5.

#### 5.2.4.2 Gasification of deposited carbon by TPO

The TPO of carbonaceous deposits formed by n-butane TPRn up to 873 K was carried out as detailed in Section 5.2.2.2. The TPO profile obtained is shown in Fig.5.6. In this case both $CO_2$ and CO were gaseous products of the reaction. The onset of $CO_2$ evolution began at ~600 K and produced a sharp peak maximum at 839 K. CO formation commenced at ~700 K and showed a marked increase in rate at 840 K with a sharp cut off at 925 K. A similar phenomenon was observed in Chapter 4, when carbon formed at 1023 K was gasified with oxygen. In this case it also appears that the formation of both $CO_2$ and CO is caused by the depletion of oxygen. The partial pressure of $CO_2$ in the spectrum at the peak maximum corresponds to $\cong$0.06 atm, whereas the partial pressure of oxygen used for the gasification corresponded to 0.05

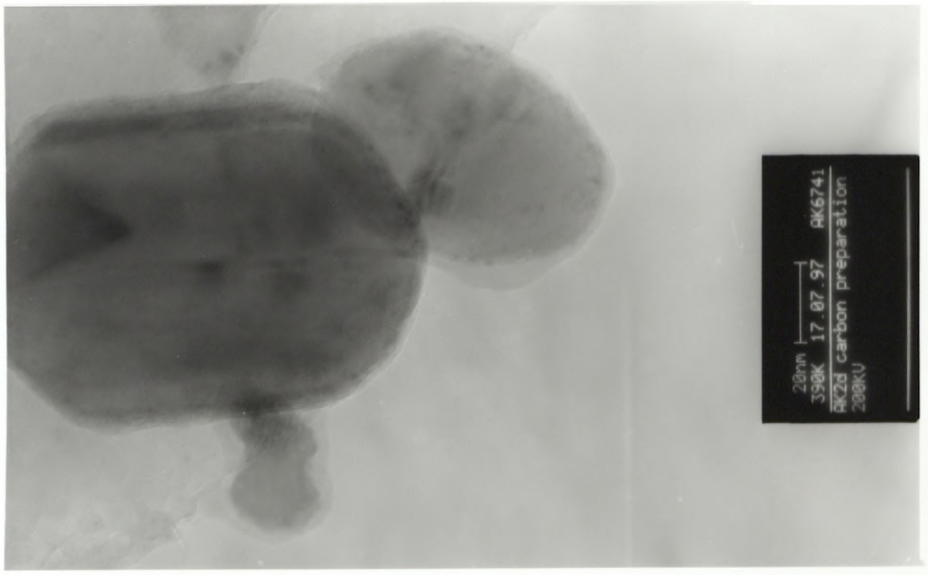


Fig.5.1 Electron micrograph of carbon formed on AK2 from n-butane at 673 K

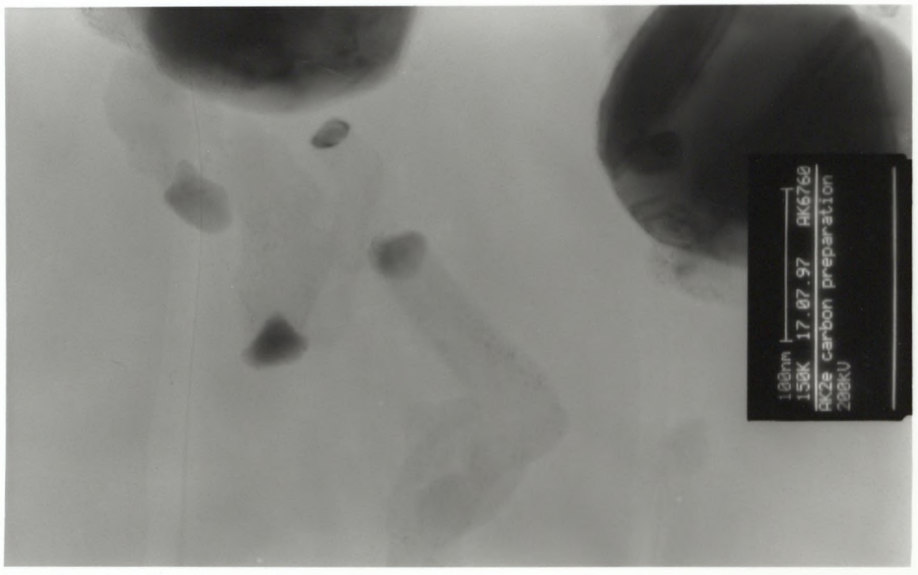


Fig.5.3 Electron micrograph of carbon formed on AK2 from n-butane at 773 K

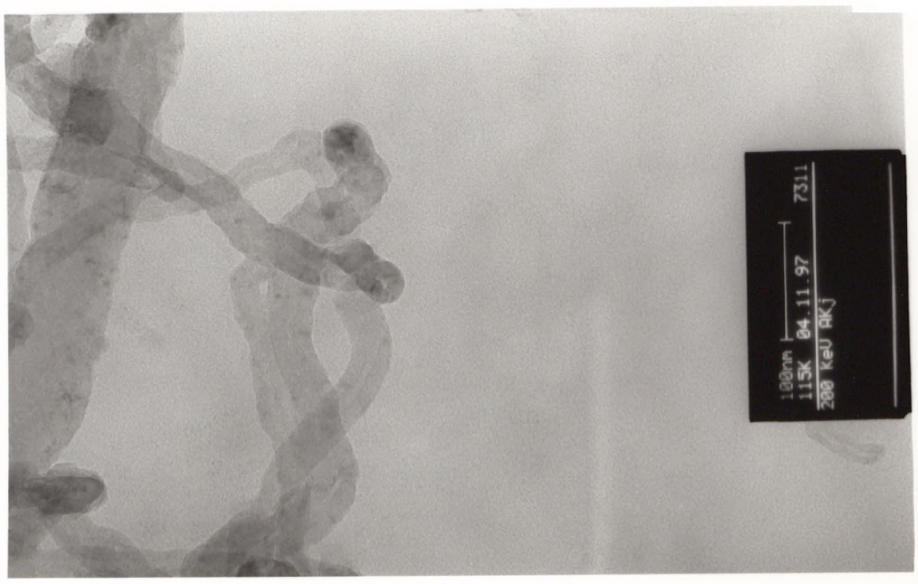


Fig.5.5 Electron micrograph of carbon formed on AK2 from n-butane at 873 K

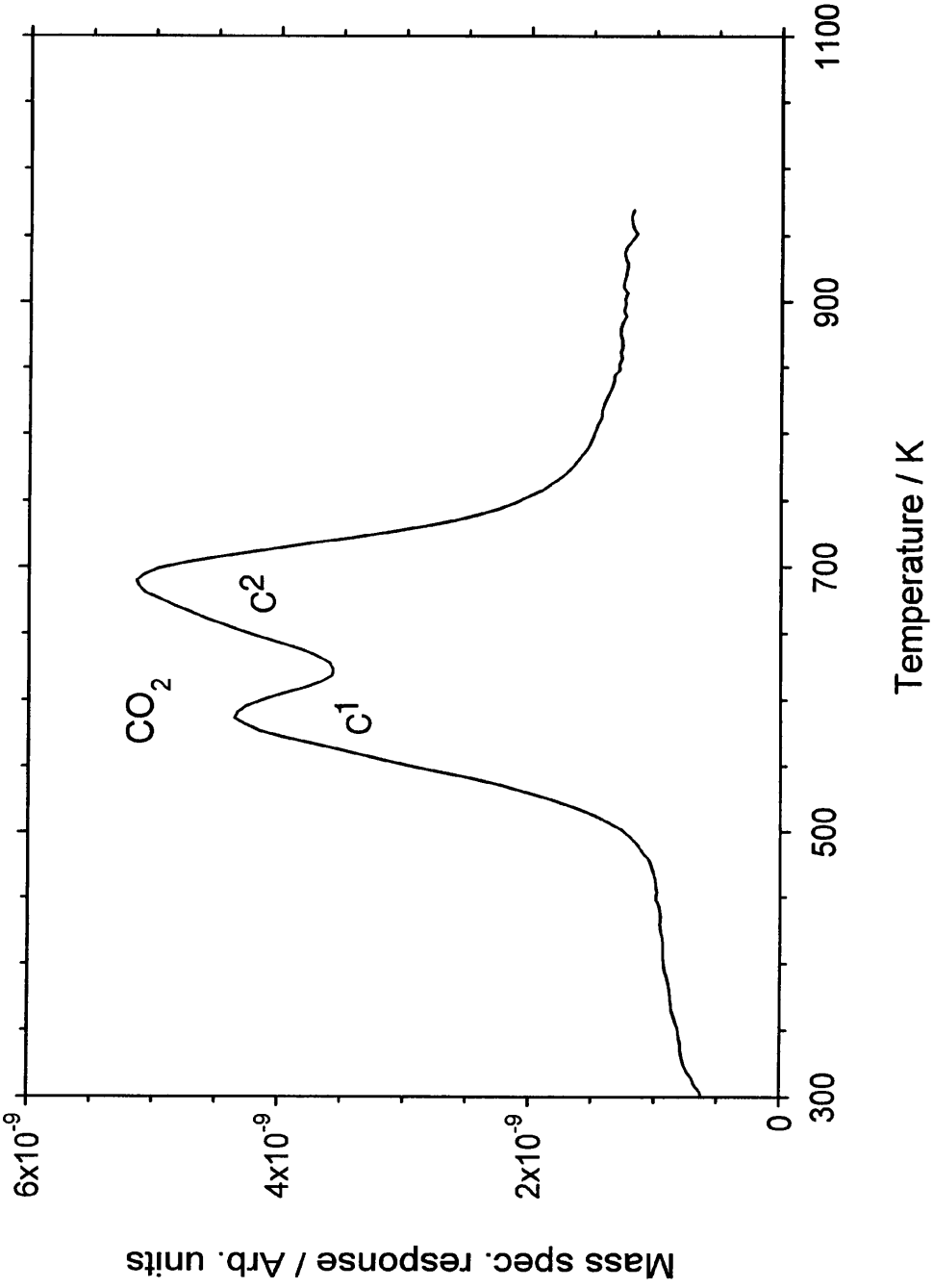


Fig.5.2 TPO of carbon formed on AK2 from n-butane at 673 K

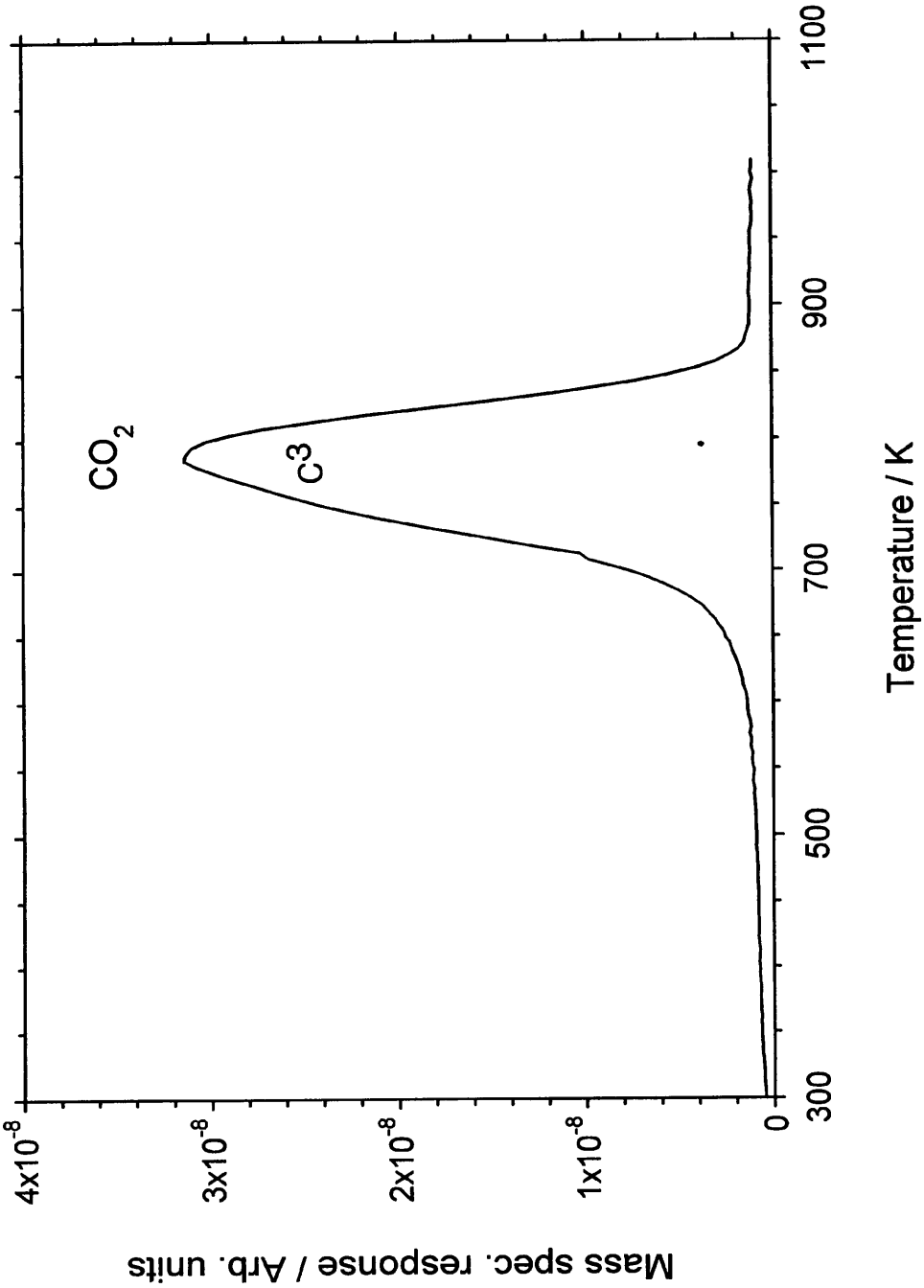


Fig.5.4 TPO of carbon formed on AK2 from n-butane at 773 K

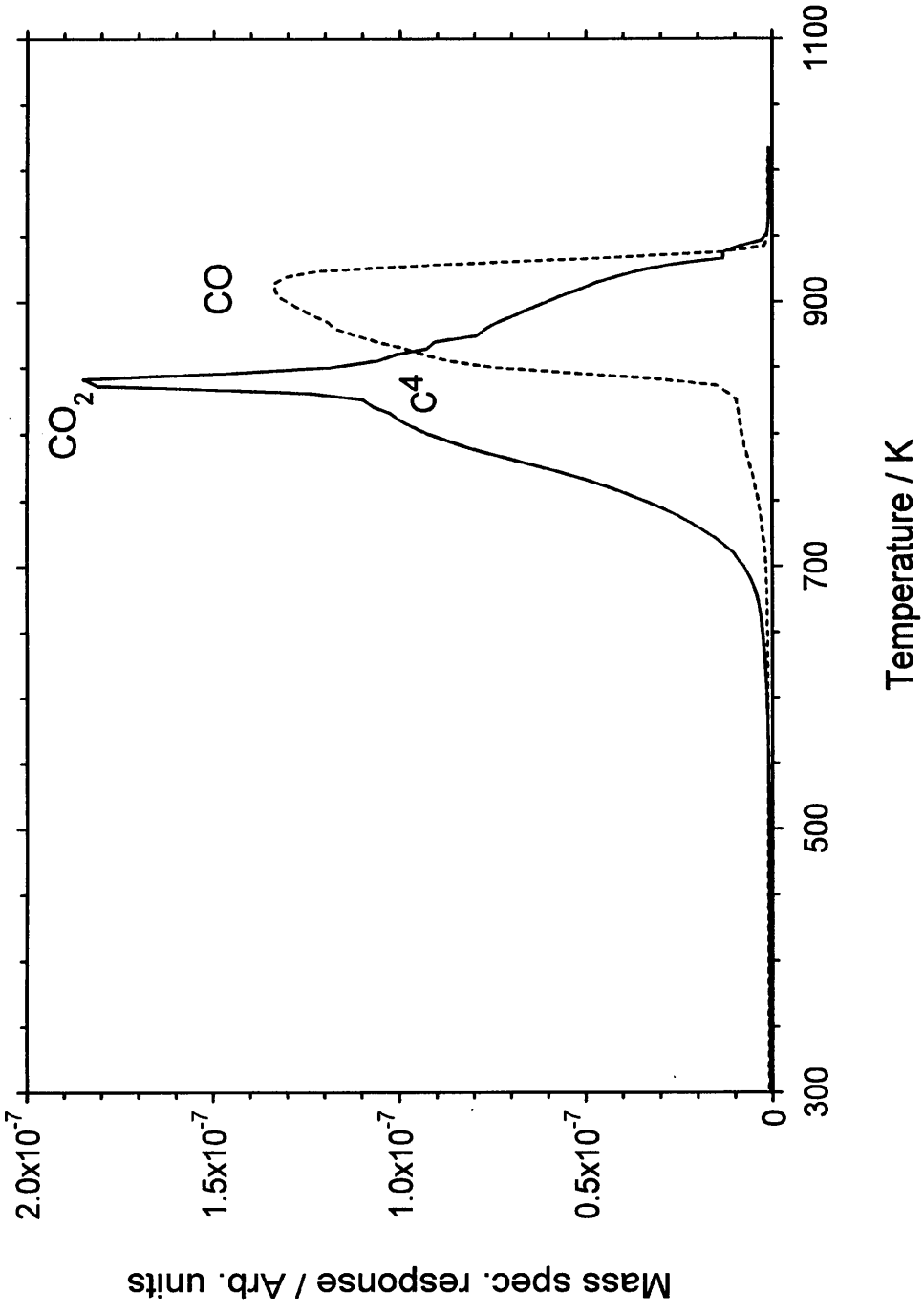


Fig.5.6 TPO of carbon formed on AK2 from n-butane at 873 K

Table 5.1

The amounts of carbon species formed on catalyst AK2 from the TPRn of n-butane at different temperatures

| Butane TPRn temperature/ K | Carbon species | $CO_2$ $T_{max}$/K | CO $T_{max}$/K | Amount of carbon formed/atoms $g^{-1}_{cat}$ | Total amount of carbon formed/atoms $g^{-1}_{cat}$ | Monolayers of carbon formed* |
|---|---|---|---|---|---|---|
| 673 | $C^1$ | 588 | - | $3.0 \times 10^{19}$ | $6.5 \times 10^{19}$ | 3 |
| | $C^2$ | 690 | - | $3.5 \times 10^{19}$ | | |
| 773 | $C^3$ | 785 | | $3.6 \times 10^{20}$ | $3.6 \times 10^{20}$ | 14 |
| 873 | $C^4$ | 839 | 910 | $2.5 \times 10^{21}$ | $2.5 \times 10^{21}$ | 100 |

Total surface area = 2.5 $m^2$ $g^{-1}$ Mass of catalyst = 0.5g

*Number of monolayers of carbon formed calculated on the basis of the total surface area of the catalyst, taking monolayer coverage to be $10^{15}$ atoms $cm^{-2}$

atm. It is not clear from the TPO spectrum in Fig.5.6. how many states of carbon are present at 873 K. The formation of 'tubular' carbon filaments, as evidenced by the electron micrograph in Fig.5.5, suggests that two dominant types of could be present, one corresponding to the inner, more reactive core and the other corresponding to the harder, less reactive outer shell. Baker et al [13] found this to be the case when oxidising carbon filaments formed on Ni catalysts from acetylene at different temperatures. This however could not be distinguished from our TPO profile. Later in the chapter, temperature-programmed hydrogenation (TPH) of the same high temperature carbon formed from n-butane is carried out in order to obtain a comparison with the TPO results and to see whether it provides any information about the types of carbon species present. The total amount of carbon formed, $C^4$, calculated from the TPO experiment, was found to be $2.5 \times 10^{21}$ atoms $g^{-1}_{cat}$ (Table 5.1).

## 5.3 Studies carried out on $NiO/Al_2O_3$ promoted with 5wt% MgO (AK5)

### 5.3.1 Deposition of carbon by n-butane TPRn

Carbon was deposited on catalyst AK5 by the TPRn of n-butane using the same procedure as described in section 5.2.1. The TPRn was again carried out three times each time on a fresh catalyst sample. The reaction was aborted at 673, 773 and 873 K.

### 5.3.2 Carbonaceous deposits formed via n-butane TPRn up to 673 K

#### 5.3.2.1 The morphology of the carbonaceous deposit

The electron micrograph of carbon formed by n-butane TPRn up to 673 K is shown in Fig.5.7. The micrograph showed similar features to the one obtained for catalyst AK2 (Fig.5.1). Again large nickel crystallites were present which were surrounded by what appeared to be a film. As previously there was no presence of carbon filaments.

5.3.2.2 Gasification of deposited carbon by TPO

Gasification of carbon by TPO was carried out using the same procedure as described in Section 5.2.2.2. The carbon TPO profile is shown in Fig.5.8 in which $CO_2$ was again the only gaseous product of the reaction. Oxidation of the carbonaceous species commenced at ~500 K, as for sample AK2 (Fig.5.2), and two maxima in the rate of $CO_2$ production were again produced at 570 and 700 K. The temperatures of these peak maxima were similar to those observed for sample AK2. Again an approximate deconvolution of the $CO_2$ spectrum enabled the amounts of both types of carbon, labelled as $C^{1}$' and $C^{2}$', to be deduced. The amounts were 3.6 x $10^{19}$ atoms $g^{-1}_{cat}$ and 3.0 x $10^{19}$ atoms $g^{-1}_{cat}$ respectively. The total amount of carbon formed was 6.6 x $10^{19}$ atoms $g^{-1}_{cat}$ (Table 5.2). It can thus be concluded that the TPRn of n-butane up to 673 K produces an encapsulating film on catalyst AK5, which again consists of layers of carbon which exhibit different reactivities in oxygen. The similarity of the findings in this case compared with those for sample AK2 lead to the conclusion that the presence of MgO appears to have no effect in determining the nature or amount of carbon formed from n-butane at this low temperature.

5.3.3 Carbonaceous deposits formed via n-butane TPRn up to 773 K

5.3.3.1 Morphology of the carbonaceous deposit

The electron micrograph of carbon produced by n-butane TPRn up to 773 K is displayed in Fig.5.9. As observed for sample AK2, the carbon deposit consisted of short filaments which had a diameter of ~40 nm. A well faceted, pear shaped nickel particle is clearly visible at the top of the filament in the centre of the photograph. Again the filaments can be described as 'true' since they did not appear hollow and there was no presence of a central channel. No carbon deposit was visible at the metal/gas interface.

5.3.3.2 Gasification of deposited carbon by TPO

The oxidation of carbon formed from n-butane TPRn up to 773 K was carried out as described in Section 5.2.2.2. The TPO profile obtained is shown in Fig.5.10 where $CO_2$ was the only gaseous product of the reaction. The onset of $CO_2$ evolution again began at ~600 K and a single large peak was produced whose maximum was at 756 K. This temperature was similar to that of the $CO_2$ peak maximum observed for sample AK2 (Fig.5.4). The amount of carbon formed in this case, $C^{3}$', was calculated to be 3.2 x $10^{20}$ atoms $g^{-1}_{cat}$ (Table 5.2). These findings coupled with the transmission electron micrograph of the carbonaceous deposit (Fig.5.9) show that the TPRn of n-butane up to 773 K on sample AK5 produces one dominant type of carbon, which appears to be of the same type as that observed on sample AK2 at the same temperature. This would again suggest that the presence of MgO has no effect on the amount or nature of the carbon formed from n-butane at 773 K.

5.3.4 Carbonaceous deposits formed via n-butane TPRn up to 873 K

5.3.4.1 Morphology of the carbonaceous deposit

The electron micrograph of carbon produced by n-butane TPRn up to 873 K is displayed in Fig.5.11. As was observed for sample AK2 at 873 K (Fig.5.5), a high density of long carbon filaments was also observed in this case. The average width of the filaments was ~25 nm and this time they clearly possessed a central channel running down their lengths. Nickel particles were again situated at the tops of the filaments.

5.3.4.2 Gasification of deposited carbon by TPO

The TPO of carbon formed by n-butane TPRn up to 873 K was carried out as detailed in Section 5.2.2.2. The TPO profile is shown in Fig.5.12. The profile obtained was very similar to the one obtained for sample AK2 (Fig.5.6). Both $CO_2$ and CO were again produced. The onset of $CO_2$ evolution began at ~600 K and produced a sharp peak maximum at 820 K. CO formation began at ~700 K and showed a marked

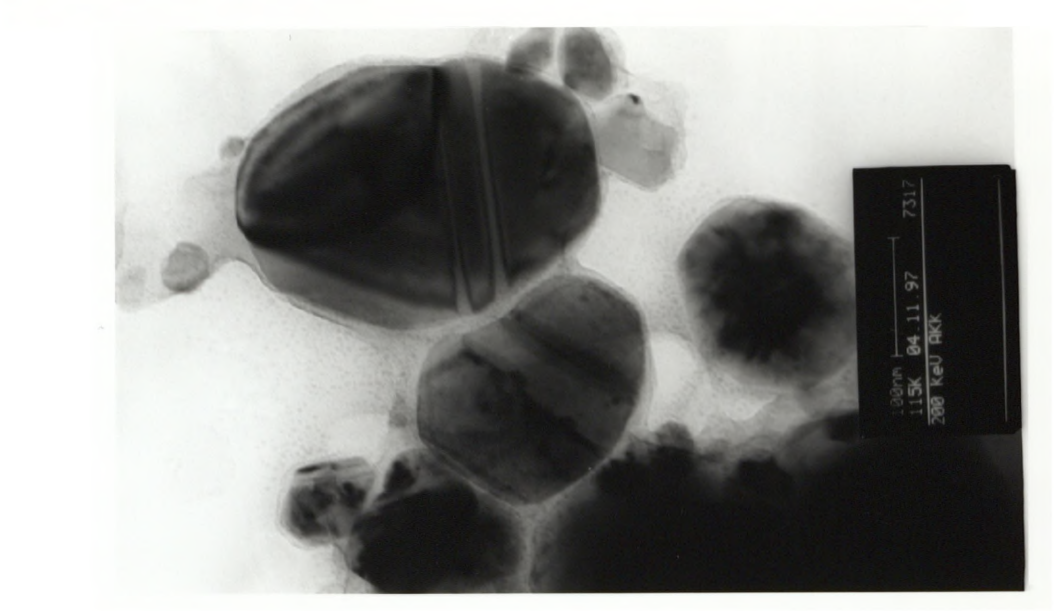


Fig.5.7 Electron micrograph of carbon formed on AK5 from n-butane at 673 K

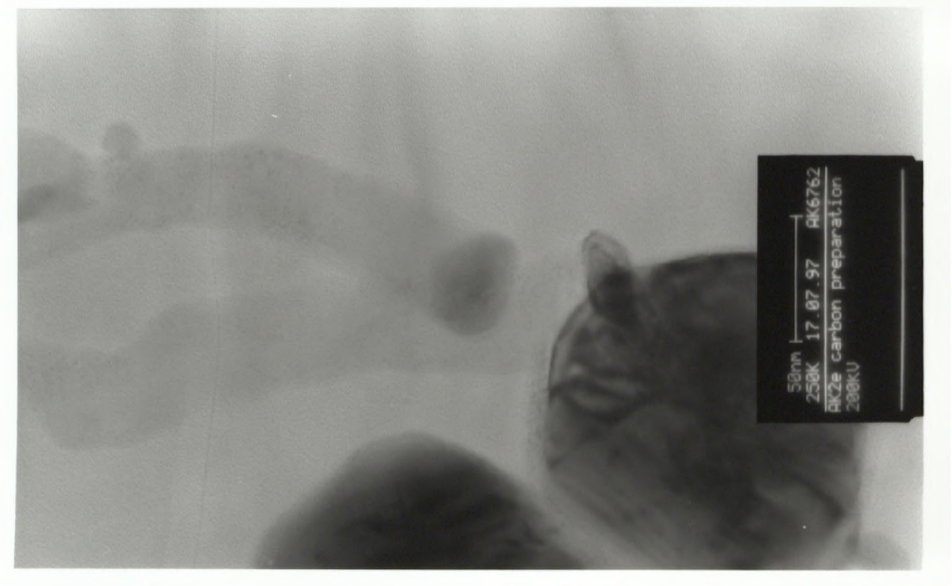


Fig.5.9 Electron micrograph of carbon formed on AK5 from n-butane at 773 K

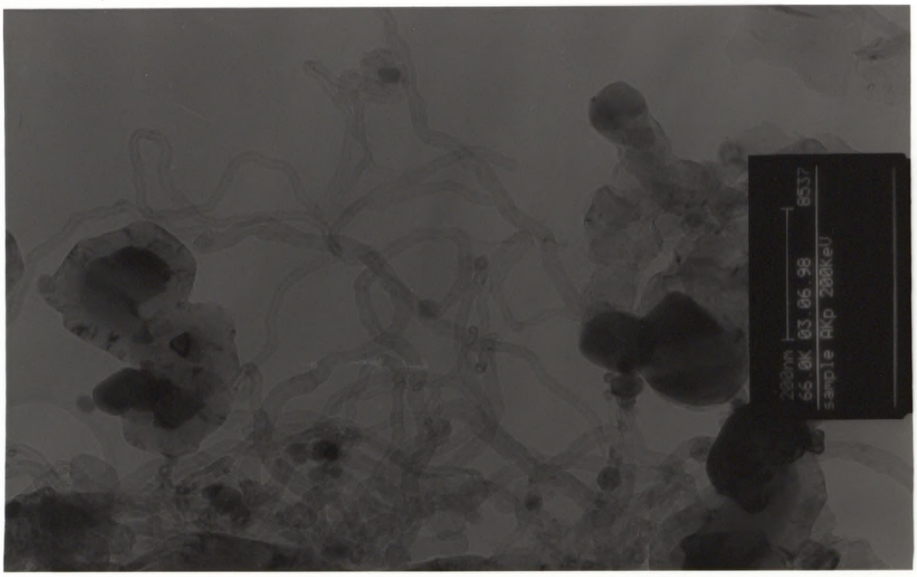


Fig.5.11 Electron micrograph of carbon formed on AK5 from n-butane at 873 K

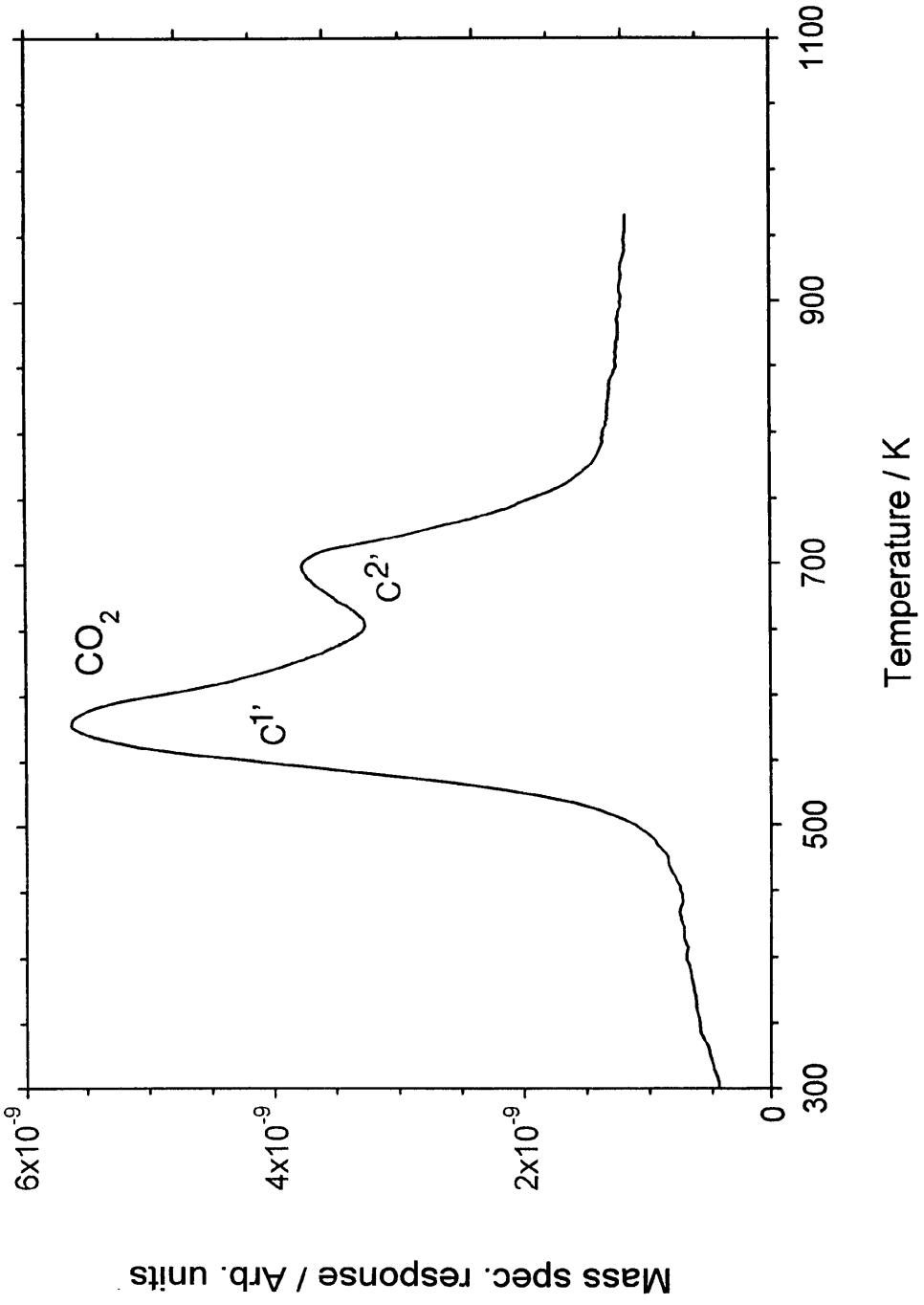


Fig.5.8 TPO of carbon formed on AK5 from n-butane at 673 K

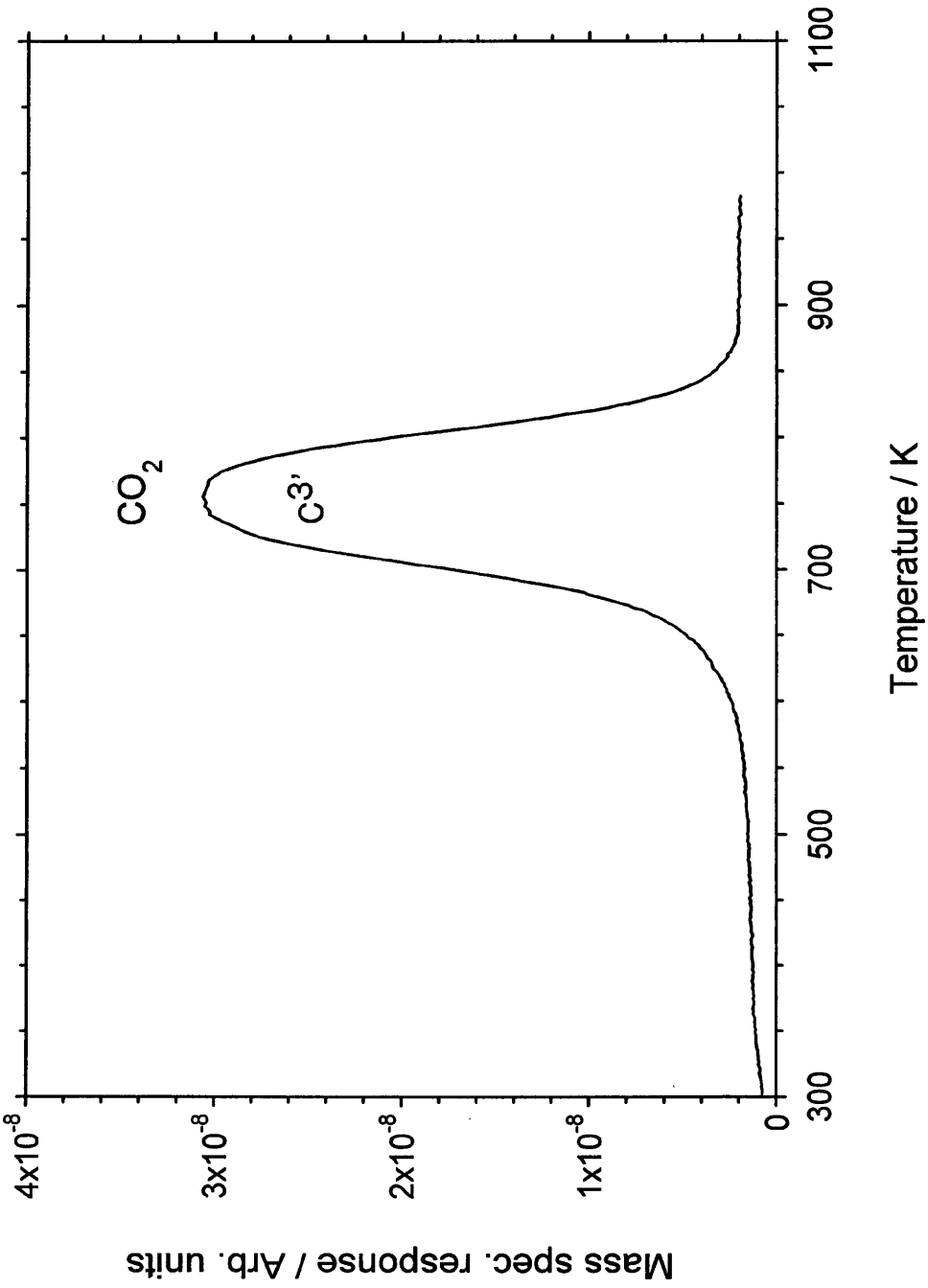


Fig.5.10 TPO of carbon formed on AK5 from n-butane at 773 K

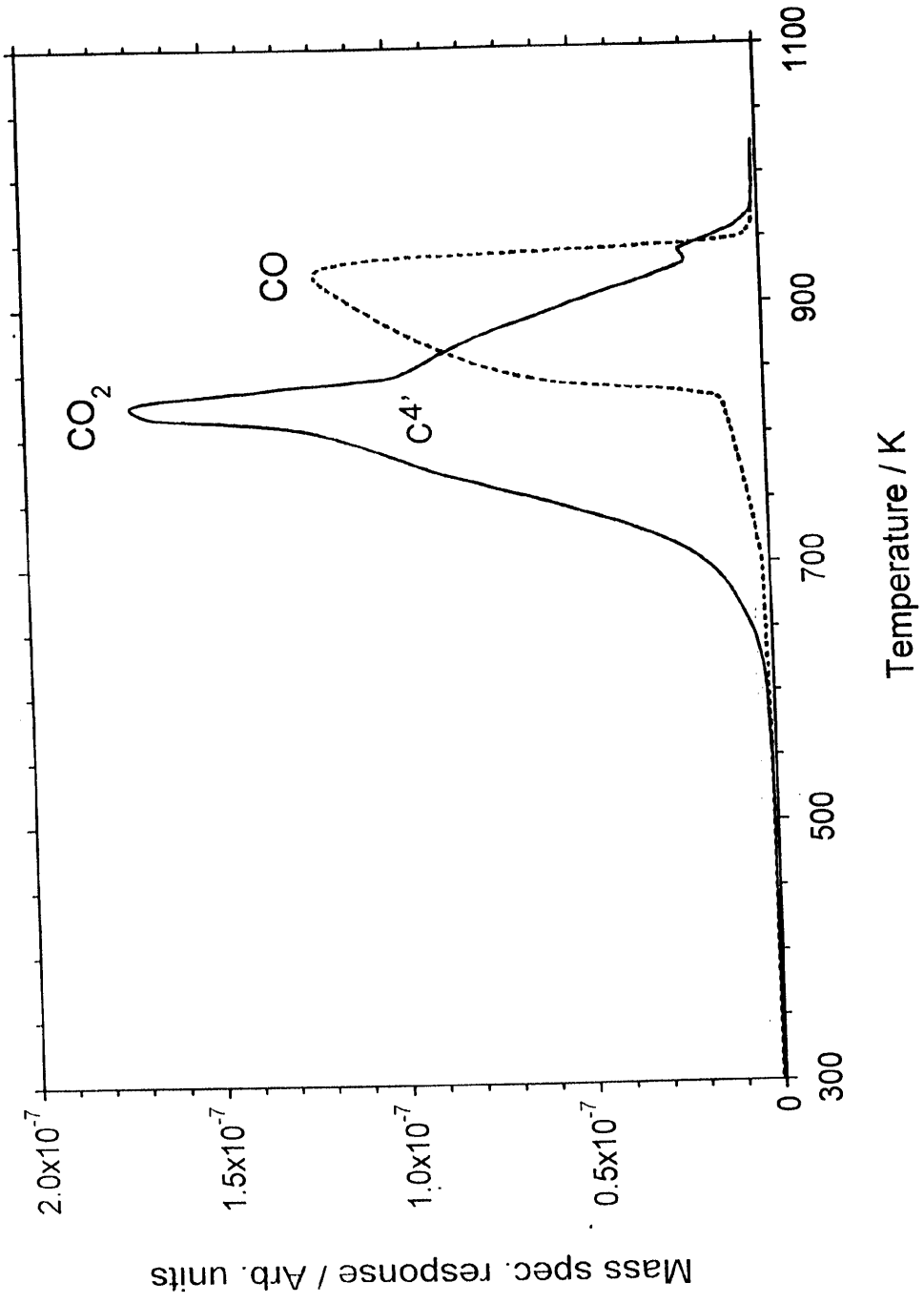


Fig.5.12 TPO of carbon formed on AK5 from n-butane at 873 K

Table 5.2

The amounts of carbon species formed on catalyst AK5 from the TPRn of n-butane at different temperatures

| Butane TPRn temperature/ K | Carbon species | $CO_2$ $T_{max}$/K | CO $T_{max}$/K | Amount of carbon formed/atoms $g^{-1}_{cat}$ | Total amount of carbon formed/atoms $g^{-1}_{cat}$ | Monolayers of carbon formed* |
|---|---|---|---|---|---|---|
| 673 | $C^{1,}$ | 570 | - | $3.6 \times 10^{19}$ | $6.6 \times 10^{19}$ | 2 |
| | $C^{2,}$ | 700 | - | $3.0 \times 10^{19}$ | | |
| 773 | $C^{3,}$ | 756 | | $3.2 \times 10^{20}$ | $3.2 \times 10^{20}$ | 12 |
| 873 | $C^{4,}$ | 820 | 925 | $2.4 \times 10^{21}$ | $2.4 \times 10^{21}$ | 89 |

Total surface area = 2.7 $m^2 g^{-1}$ Mass of catalyst = 0.5g

*Number of monolayers of carbon formed calculated on the basis of the total surface area of the catalyst, taking monolayer coverage to be $10^{15}$ atoms $cm^{-2}$

increase in rate at 825 K with a sharp cut off at 940 K. The partial pressure of $CO_2$ in the profile at the peak maximum corresponds to ≅0.06 atm. which again suggests that depletion of oxygen has occurred, hence the formation of both $CO_2$ and CO. Again the number of carbon species present could not be distinguished from the TPO profile. The amount of carbon formed, $C^{4'}$, was calculated to be 2.4 x $10^{21}$ atoms $g^{-1}_{cat}$ (Table 5.2).

## 5.4 Studies carried out on $NiO/Al_2O_3$ promoted with 5wt% $La_2O_3$ (AK8)

### 5.4.1 Deposition of carbon by n-butane TPRn

Carbon was deposited on catalyst AK8 by the TPRn of n-butane using the same procedure as described in Section 5.2.1. The TPRn was carried out three times, each time on a fresh catalyst sample. The TPRn was stopped at 673, 773 and 873 K.

### 5.4.2 Carbonaceous deposits formed via n-butane TPRn up to 673 K

#### 5.4.2.1 The morphology of the carbonaceous deposit

The electron micrograph of carbon formed by n-butane TPRn up to 673 K is shown in Fig.5.13. The micrograph showed similar features to those obtained for both samples AK2 (Fig.5.1) and AK5 (Fig.5.7). In this case the nickel crystallites visible were again surrounded by a faint film. No carbon filaments were present.

#### 5.4.2.2 Gasification of deposited carbon by TPO

Gasification of carbon by TPO was carried out using the same procedure as detailed in Section 5.2.2.2. The TPO profile produced is shown in Fig.5.14. As was observed in the TPO profiles for samples AK2 (Fig.5.2) and AK5 (Fig.5.8), $CO_2$ alone was the gaseous product of this reaction. Oxidation of the carbon species again commenced at ~500 K and, as observed for samples AK2 and AK5, two $CO_2$ peak maxima were

produced at 578 and 685 K suggesting the presence of two types of carbon. Again the temperatures of these peak maxima were similar to those observed for samples AK2 and AK5. Deconvolution of the $CO_2$ profile enabled the amounts of both types of carbon, labelled $C^{1}$'' and $C^{2}$'', to be deduced. The amounts were 3.7 x $10^{19}$ atoms $g^{-1}_{cat}$ and 3.1 x $10^{19}$ atoms $g^{-1}_{cat}$ respectively. The total amount of carbon formed was 6.8 x $10^{19}$ atoms $g^{-1}_{cat}$ (Table 5.3) It is thus evident again that the nature of the carbon species formed on catalyst AK8 from n-butane at 673 K is identical to that produced on samples AK2 and AK5. The presence of $La_2O_3$ also appears to little influence on the nature or amount of carbon formed from n-butane at low temperature.

### 5.4.3 Carbonaceous deposits formed via n-butane TPRn up to 773 K

#### 5.4.3.1 The morphology of the carbonaceous deposit

The electron micrograph of carbon produced by n-butane TPRn up to 773 K is displayed in Fig.5.15. As observed for both samples AK2 and AK5, the carbon deposit consisted of short filaments whso width ranged from ~20 - 50 nm. The filaments contained no central channel and well faceted, pear shaped nickel partcles were clearly visible at the tops. No carbon was visible at the metal/gas interface.

#### 5.4.3.2 Gasification of deposited carbon by TPO

The oxidation of carbon formed from n-butane TPRn up to 773 K was carried out as detailed in Section 5.2.2.2. The TPO profile obtained is shown in Fig.5.16. The profile was similar to those obtained for samples AK2 (Fig.5.4) and AK5 (Fig.5.10) in that only a single $CO_2$ peak was produced, with a maximum at 770 K in this case. The amount of carbon, $C^{3}$'', was calculated to be 3.8 x $10^{20}$ atoms $g^{-1}_{cat}$ (Table 5.3). These results together with the electron micrograph (Fig.5.14) indicate that the same dominant type of carbon is formed on catalyst AK8 as is formed on both AK2 and AK5 from the TPRn of butane up to 773 K.

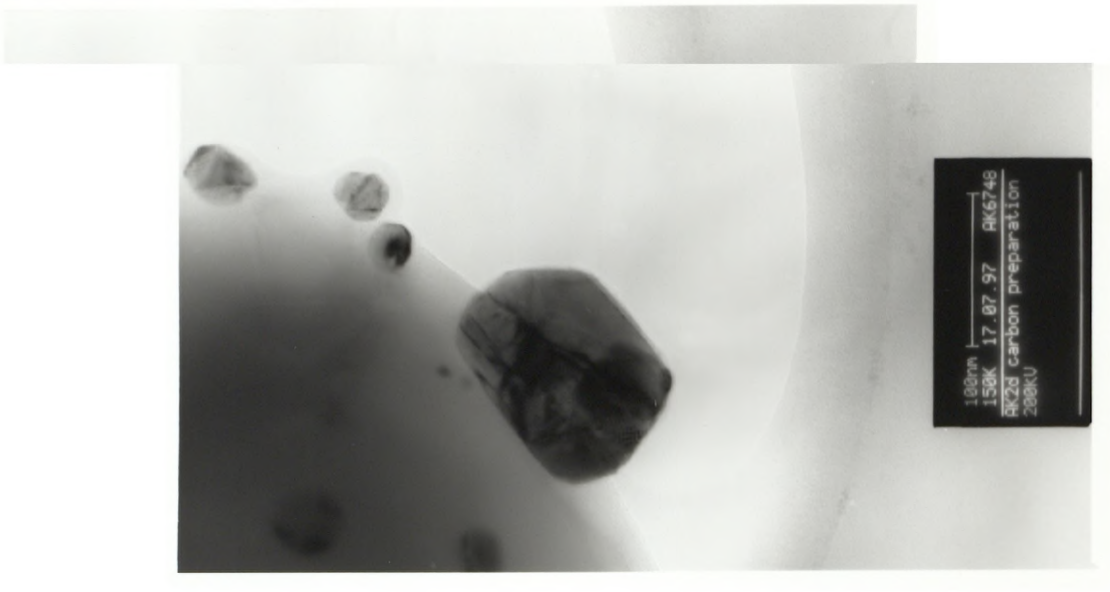


Fig.5.13 Electron micrograph of carbon formed on AK8 from n-butane at 673 K

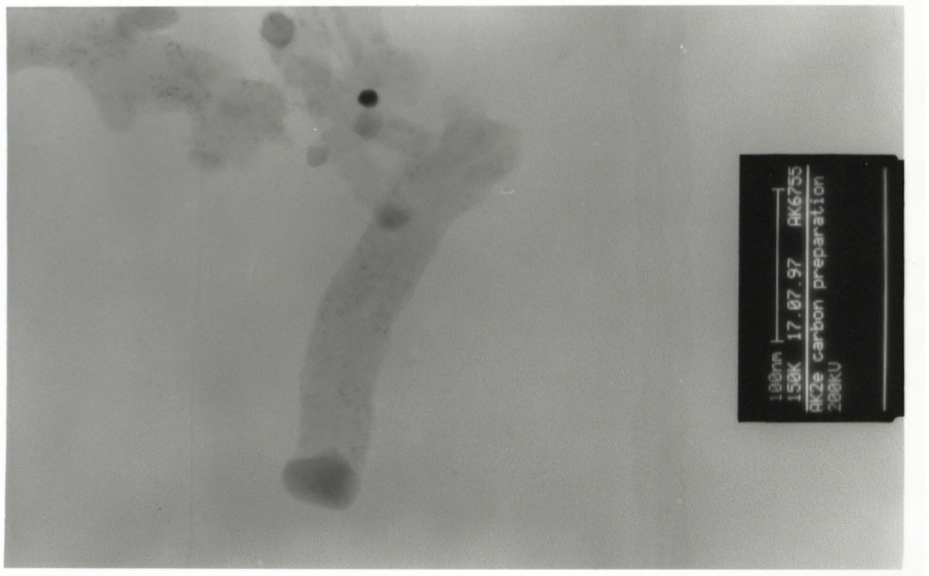


Fig.5.15 Electron micrograph of carbon formed on AK8 from n-butane at 773 K

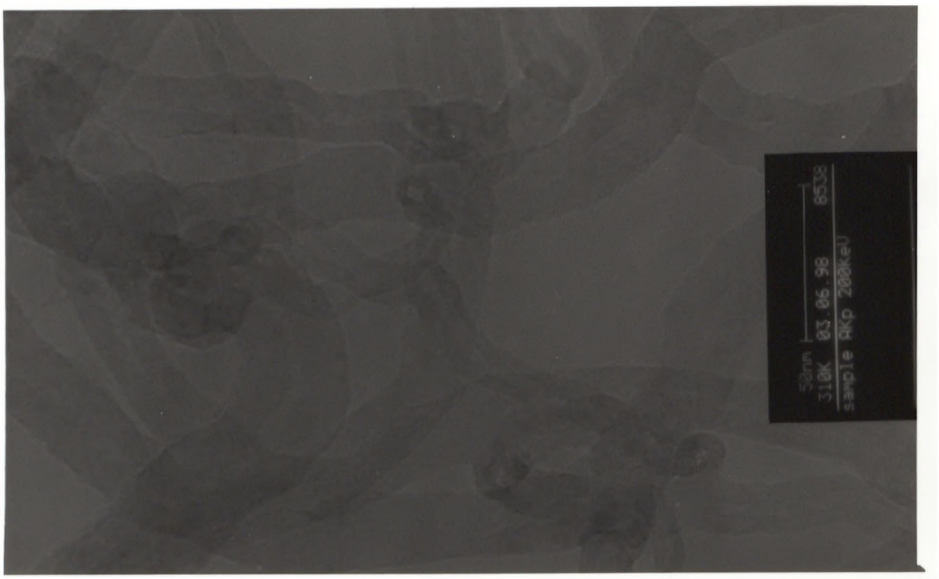


Fig.5.17 Electron micrograph of carbon formed on AK8 from n-butane at 873 K

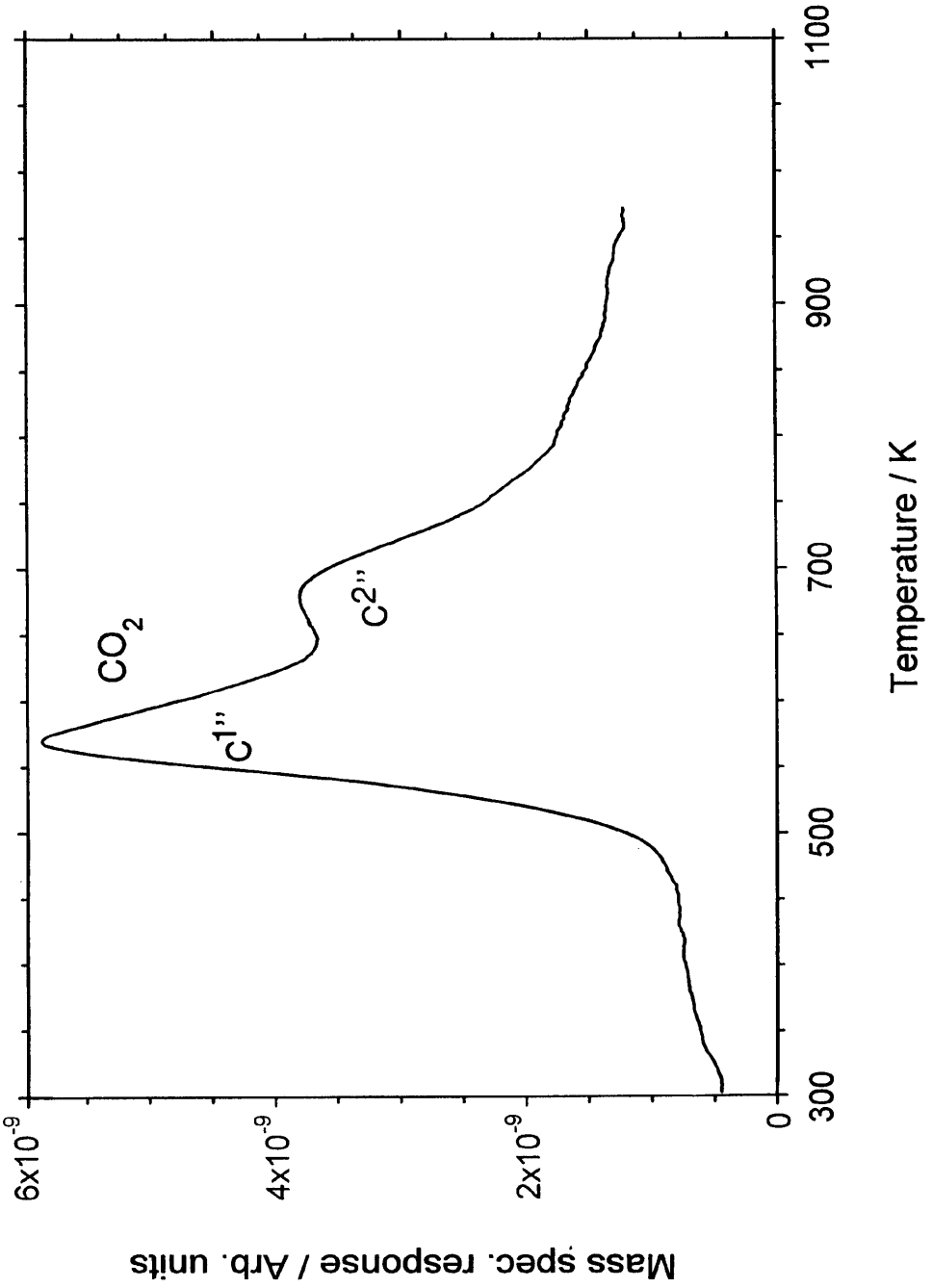


Fig.5.14 TPO of carbon formed on AK8 from n-butane at 673 K

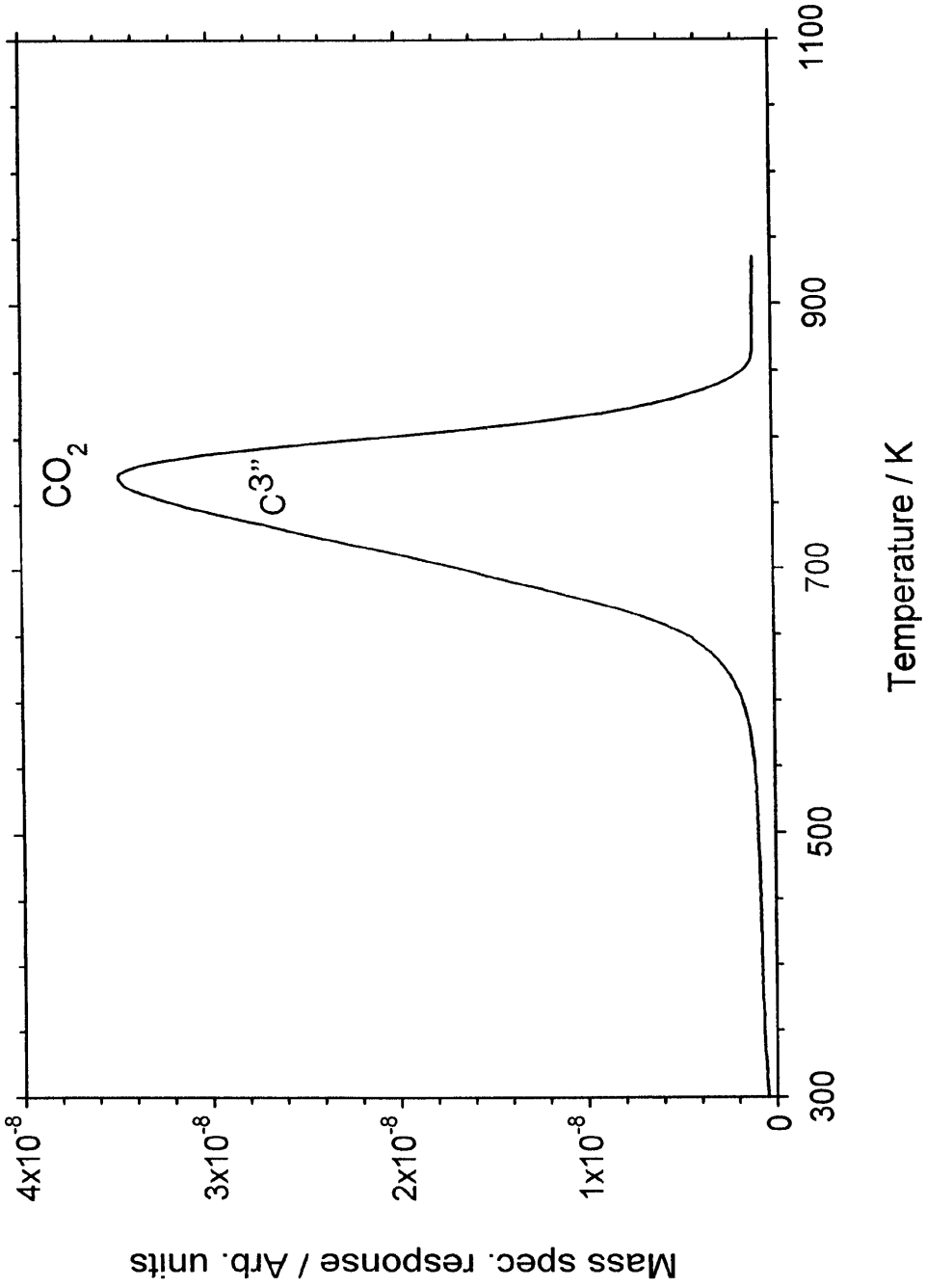


Fig.5.16 TPO of carbon formed on AK8 from n-butane at 773 K

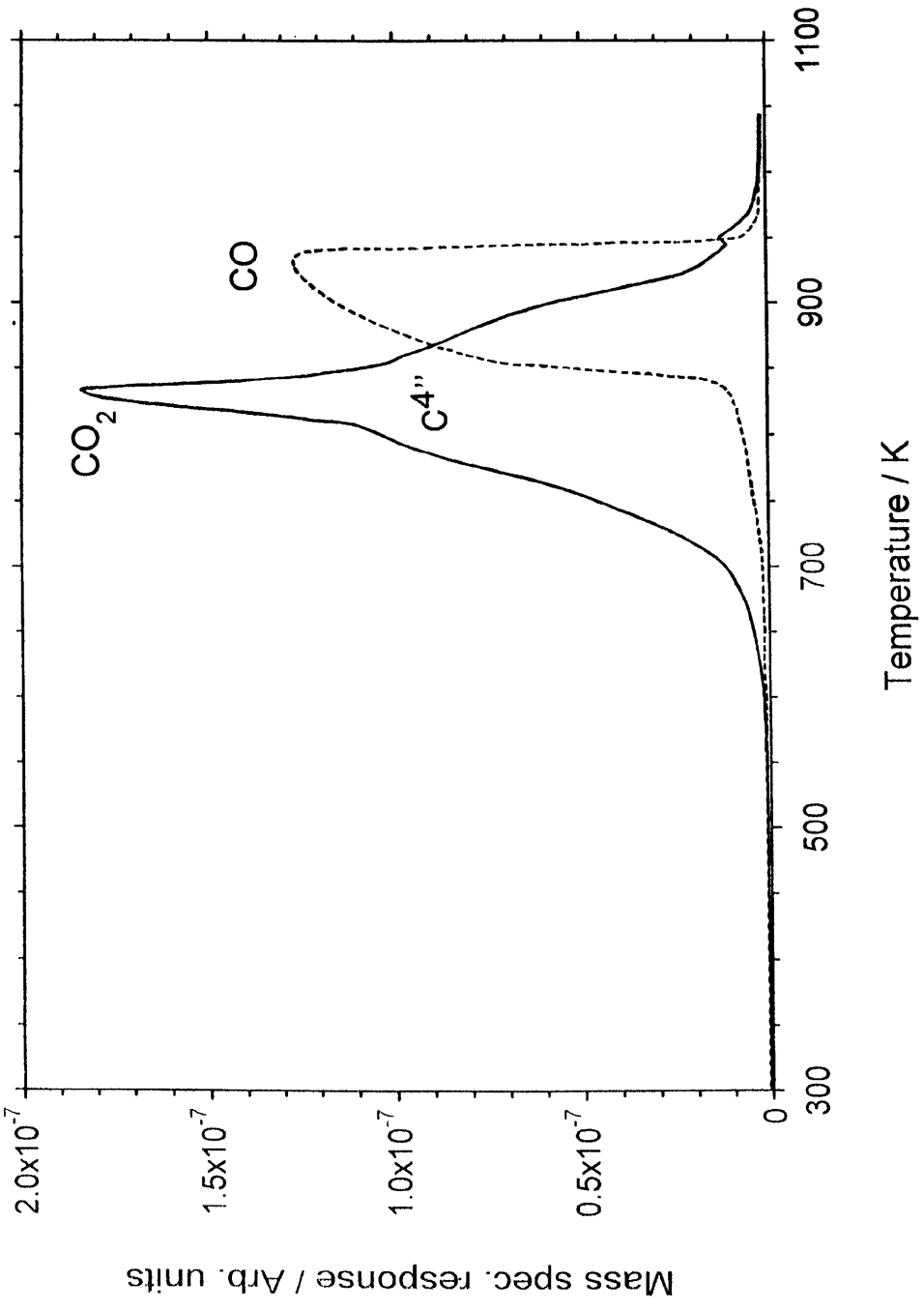


Fig.5.18 TPO of carbon formed on AK8 from n-butane at 873 K

Table 5.3

The amounts of carbon species formed on catalyst AK8 from the TPRn of n-butane at different temperatures

| Butane TPRn temperature/ K | Carbon species | $CO_2$ $T_{max}$/K | CO $T_{max}$/K | Amount of carbon formed/atoms $g^{-1}_{cat}$ | Total amount of carbon formed/atoms $g^{-1}_{cat}$ | Monolayers of carbon formed* |
|---|---|---|---|---|---|---|
| 673 | $C^{1,,}$ | 578 | - | $3.7 \times 10^{19}$ | $6.8 \times 10^{19}$ | 2 |
| | $C^{2,,}$ | 685 | - | $3.1 \times 10^{19}$ | | |
| 773 | $C^{3,,}$ | 770 | | $3.8 \times 10^{20}$ | $3.8 \times 10^{20}$ | 13 |
| 873 | $C^{4,,}$ | 832 | 935 | $2.3 \times 10^{21}$ | $2.3 \times 10^{21}$ | 79 |

Total surface area = 2.9 $m^2 g^{-1}$ Mass of catalyst = 0.5g

*Number of monolayers of carbon formed calculated on the basis of the total surface area of the catalyst, taking monolayer coverage to be $10^{15}$ atoms $cm^{-2}$

### 5.4.4 Carbonaceous deposits formed via n-butane TPRn up to 873 K

#### 5.4.4.1 Morphology of the carbonaceous deposit

The electron micrograph of carbon produced by n-butane up to 873 K is displayed in Fig.5.17. As was observed for both samples AK2 (Fig.5.5) and AK5 (Fig.5.11), a high density of long carbon filaments was observed which had an average diameter of ~25 nm. A central channel running down their lengths was clearly visible and nickel particles were again situated at the tops of the filaments.

#### 5.4.4.2 Gasification of deposited carbon by TPO

The TPO of carbon formed by n-butane TPRn up to 873 K was carried out as detailed in Section 5.2.2.2. The TPO profile is shown in Fig.5.18. This profile again exhibited very similar features to the corresponding TPO profiles obtained for samples AK2 (Fig.5.6) and AK8 (Fig.5.12). The onset of $CO_2$ evolution began at ~600 K and produced a sharp peak at 832 K. CO formation commenced at ~700 K and again showed a marked increase in rate at 835 K with a sharp cut off at 945 K. The production of both $CO_2$ and CO in the TPO profile can again be attributed to the depletion of oxygen, the $CO_2$ partial pressure at the peak maximum corresponding to $\cong$0.06 atm. The amount of carbon formed, labelled $C^{4,,}$, was calculated to be 2.3 x $10^{21}$ atoms $g^{-1}_{cat}$ (Table 5.3).

## 5.5 Temperature-Programmed Hydrogenation (TPH) of carbonaceous deposits

### 5.5.1 Introduction

Up until now, the amounts and kinds of carbonaceous deposits formed on catalysts AK2, AK5 and AK8 by n-butane TPRn have been probed by the TPO technique. This revealed (coupled with TEM investigations) that for each of the catalysts studied, two types of surface carbon were formed from n-butane TPRn up to 673 K, 'true' carbon

filaments consisting of one type of carbon were formed from n-butane TPRn up to 773 K, and long 'tubular' carbon filaments were formed from n-butane TPRn up to 873 K. The amounts of each type of carbon formed were also found to be almost the same for each catalyst studied. It has, however, been reported by Efstathiou et al [14] that the high exothermicity of the carbon gasification reaction with oxygen can lead to features in the TPO profile which may not be genuine and therefore such features and their interpretation (ie. kinds of carbon species formed) have to be cautiously considered. It was therefore decided to carry out a temperature-programmed hydrogenation (TPH) of carbon deposited via n-butane TPRn at 673, 773 and 873 K, as in the experiments prior, in which the carbonaceous species would be characterised by their reactivity in $H_2$ to form $CH_4$. By following the $CH_4$ response obtained during the TPH reaction, the amount and kinds of carbon would again be determined and then be used in comparison to the deductions made from the TPO experiments described earlier.

All three samples studied in this chapter produced similar carbon TPO profiles for all the temperature regimes studied, suggesting that the carbon species produced on each sample did not significantly differ. The TPH sudies were therefore only carried out on sample AK2.

### 5.5.2 Deposition of carbon on AK2 by the TPRn of n-butane

Carbon was deposited on sample AK2 by n-butane TPRn using the same procedure as described in section 5.2.1. The TPRn was again carried out three times, each time on a fresh catalyst sample. The reaction was aborted at 673, 773 and 873 K.

#### 5.5.2.1 TPH of carbon deposited by n-butane TPRn up to 673K

On completion of the n-butane TPRn at 673 K, the flow was switched to helium and the sample was cooled to ambient. When cool, the flow was then switched to a hydrogen-helium stream (5% $H_2$, 25 $cm^3$ $min^{-1}$, 1 bar) and the temperature was raised from ambient to 1023 K at a rate of 5 K $min^{-1}$. The carbon TPH profile is shown in Fig.5.19.

The hydrogenation of carbonaceous species commenced at ~450 K and $CH_4$ was the only gaseous product of the reaction. Again different states of carbon were identified by maxima in the rate of $CH_4$ production, two of which occurred at 640 K and 770 K. These temperatures were higher than those observed for the two $CO_2$ peaks obtained during the corresponding TPO reaction (Fig.5.2). An approximate deconvolution of the $CH_4$ spectrum provided the amount of both types of carbon formed. These species, designated as $C^1$ and $C^2$ in accordance with their reactivity order, were present in amounts 2.3 x $10^{19}$ atoms $g^{-1}_{cat}$ and 3.0 x $10^{19}$ atoms $g^{-1}_{cat}$ respectively. The total amount of carbon deduced from the TPH experiment was 5.3 x $10^{19}$ atoms $g^{-1}_{cat}$ (Table 5.4). The $CO_2$ response obtained during the TPO experiment shown in Fig.5.2 also revealed two distinct peaks, thus there is very good agreement between the TPH and TPO experiments concerning the number of carbon species identified based on their reactivities towards hydrogenation and oxidation.

5.5.2.2 TPH of carbon deposited by n-butane TPRn up to 773 K

The hydrogenation of carbon formed by n-butane TPRn up to 773 K was carried out as described in section 5.5.2.1. The TPH profile is shown in Fig.5.20 where $CH_4$ was again the only gaseous product of the reaction. The onset of $CH_4$ evolution began at ~630 K and a single, large peak was produced with a maximum at 830 K, indicating the presence of one dominant type of carbon species. This is in agreement with the result obtained for the corresponding TPO reaction (Fig.5.4) which also produced a single $CO_2$ peak with a maximum at 785 K. The total amount of carbon, $C^3$, calculated from the TPH experiment was 9.4 x $10^{19}$ atoms $g^{-1}_{cat}$ (Table 5.4). The fact that the peak maximum temperature of the $CH_4$ formed in the TPH reaction (830 K) was higher than the peak maximum temperature of the $CO_2$ formed in the corresponding TPO reaction (785 K), indicates that the carbonaceous species formed at 773 K is less reactive towards hydrogenation than oxidation. The amount of carbon species calculated based on the TPH experiment (9.4 x $10^{19}$ atoms $g^{-1}_{cat}$) was significantly smaller than the amount calculated based on the TPO experiment (3.6 x $10^{20}$ atoms $g^{-1}_{cat}$). This suggests that the carbon species has not been completely hydrogenated and is most likely due to the lack of hydrogen present on the surface at this temperature. According to studies

carried out by Bianchi and Gass [15], the prevailing mechanism of the carbon hydrogenation process is assumed to be the stepwise addition of hydrogen atoms to the carbon atoms to form $CH_4$. Hydrogen atoms are formed on the metal surface via a dissociation step of gaseous $H_2$:

$$H_{2\,(gas)} = 2\,H_{(ads)} \qquad (5.1)$$

$$C_{(ads)} + H_{(ads)} \rightarrow CH_{(ads)} \qquad (5.2)$$

$$CH_{(ads)} + H_{(ads)} \rightarrow CH_{2\,(ads)} \qquad (5.3)$$

$$CH_{2\,(ads)} + H_{(ads)} \rightarrow CH_{3\,(ads)} \qquad (5.4)$$

$$CH_{3\,(ads)} + H_{(ads)} \rightarrow CH_{4\,(ads)} \qquad (5.5)$$

$$CH_{4\,(ads)} \rightarrow CH_{4\,(gas)} \qquad (5.6)$$

However, TPD studies of hydrogen on $Ni/Al_2O_3$ carried out have reported that hydrogen desorption occurs at temperatures ranging from 300 - 600 K [16] [17]. Therefore in the temperature region where hydrogenation of the carbon takes place, it is likely that the amount of hydrogen available on the surface is limited.

5.5.2.3 TPH of carbon deposited by n-butane TPRn up to 873 K

The TPH of carbon formed by the TPRn of n-butane up to 873 K was carried out as described in section 5.5.2.1. The TPH profile is shown in Fig.5.21. The onset of $CH_4$ evolution commenced at ~675 K and produced a sharp peak with a maximum at 950 K. A shoulder was also clearly visible at ~830 K. From this result we can conclude that the $CH_4$ response corresponds to the hydrogenation of two carbonaceous species. (The number of carbonaceous species could not be conclusively distinguished from the corresponding TPO experiment shown in Fig.5.6). This agrees with the electron micrograph of the carbonaceous deposit (Fig.5.5) which clearly showed filaments consisting of both an outer shell and an inner core. An approximate deconvolution of the $CH_4$ spectrum enabled the amount of each carbon to be deduced. The amount of carbon labelled $C^{4a}$ corresponded to $6.1 \times 10^{18}$ atoms $g^{-1}_{cat.}$ The amount of carbon, $C^{4b}$, calculated was $1.6 \times 10^{19}$ atoms $g^{-1}_{cat.}$ The total amount of carbon therefore

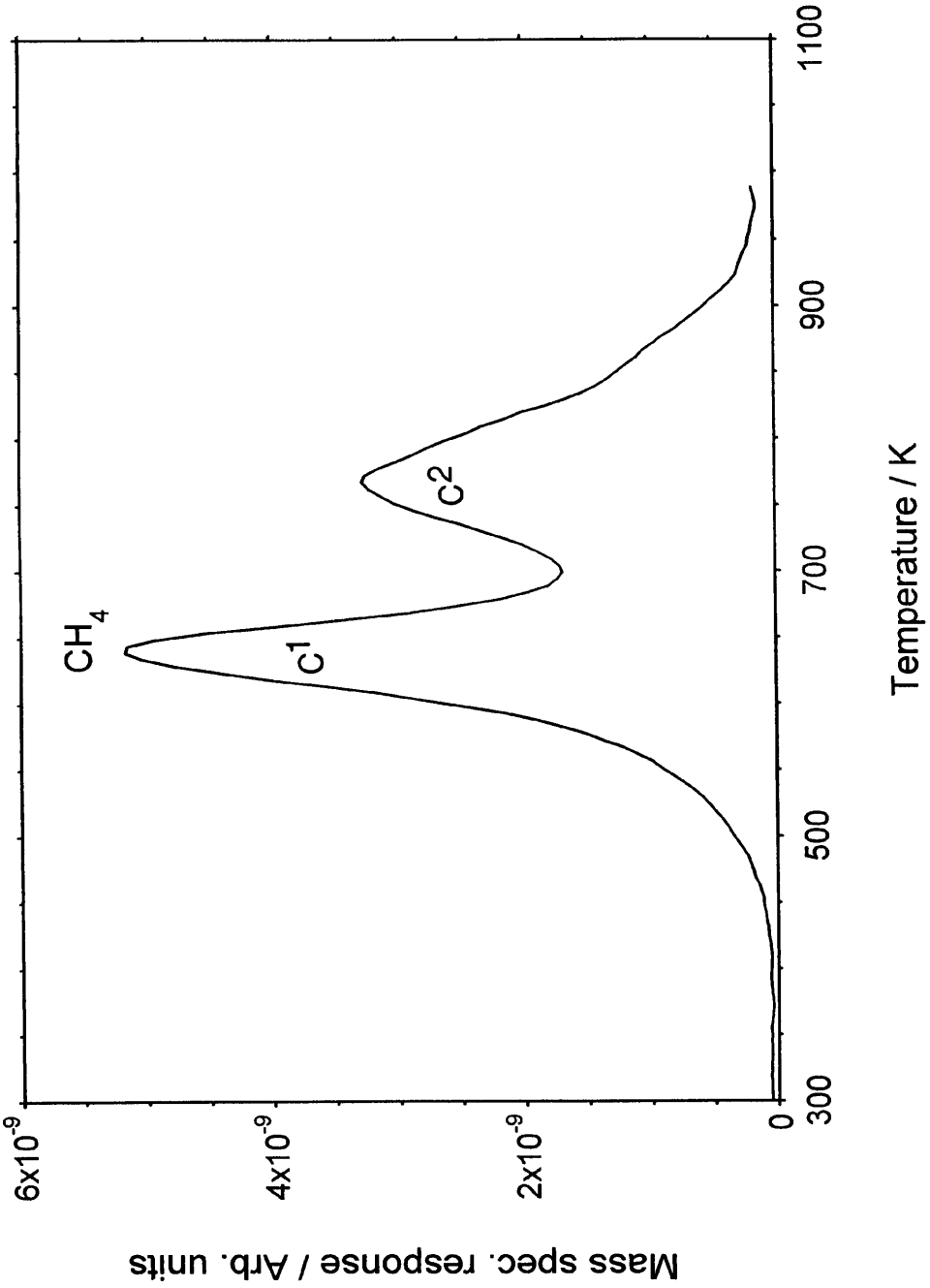


Fig.5.19 TPH of carbon formed on AK2 from n-butane at 673 K

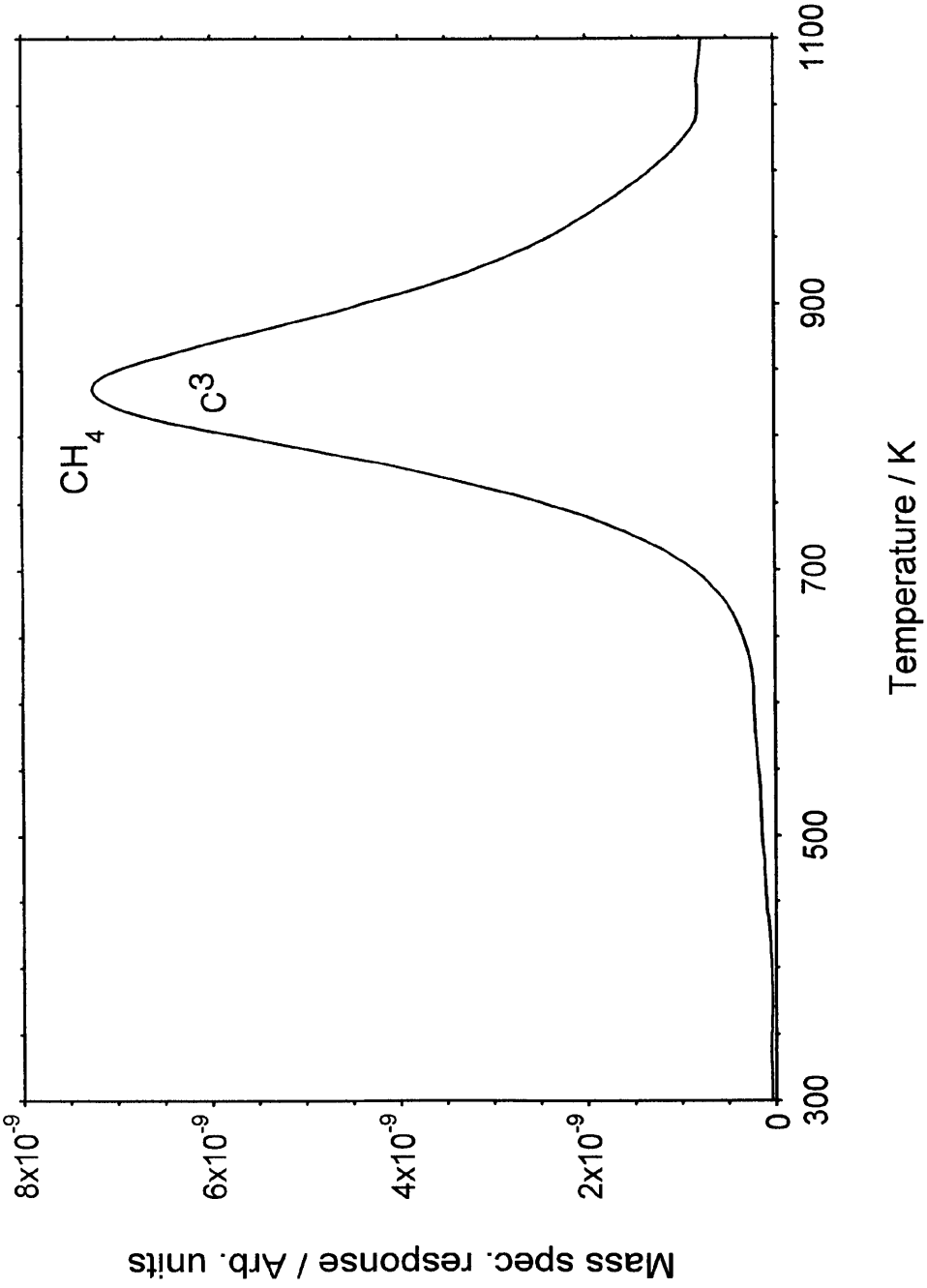


Fig.5.20 TPH of carbon formed on AK2 from n-butane at 773 K

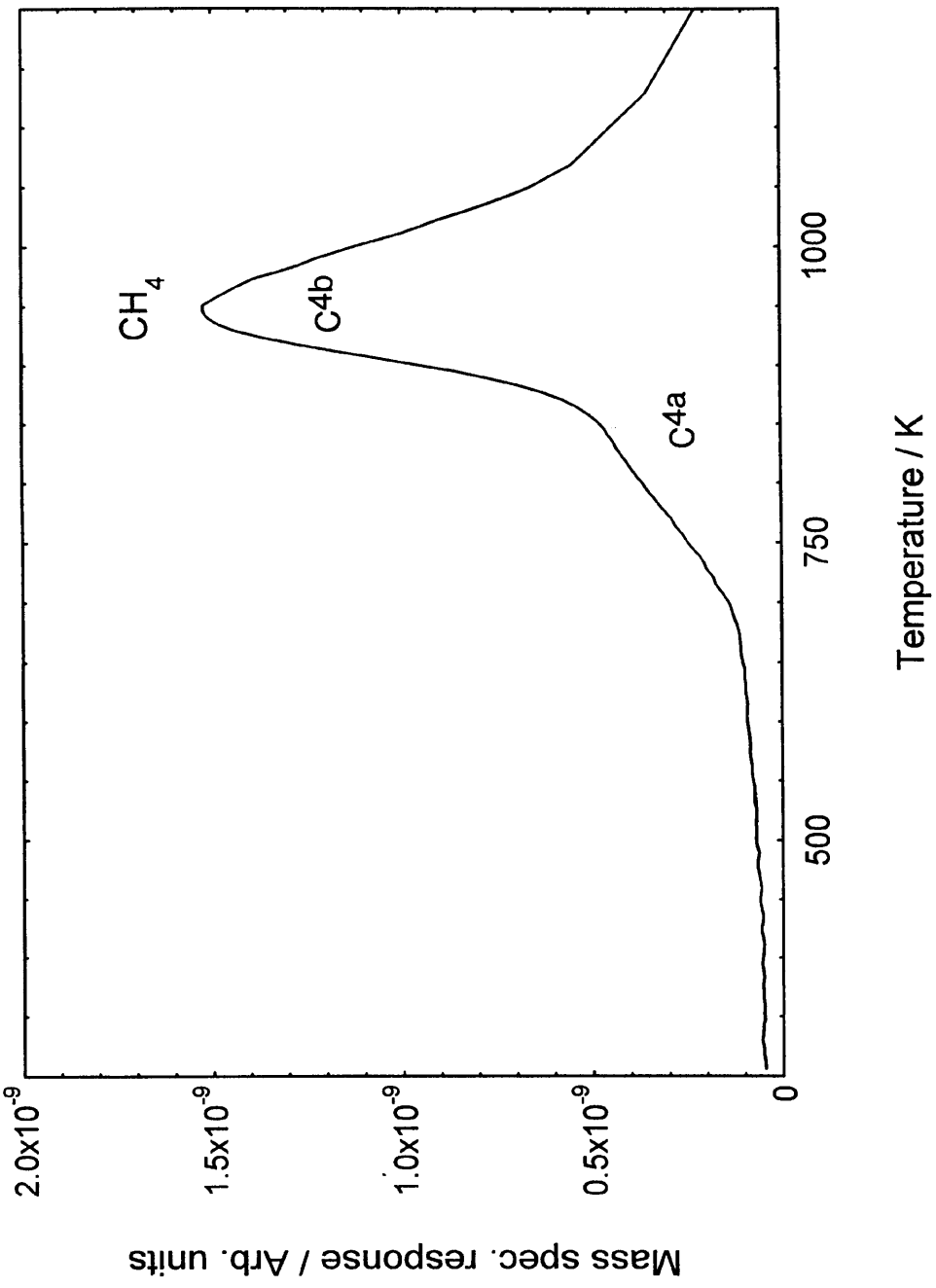


Fig.5.21 TPH of carbon formed on AK2 from n-butane at 873 K

Table 5.4

The amounts of carbon species formed on catalyst AK2 from the TPRn of n-butane at different temperatures

| Butane TPRn temperature/ K | Carbon species | $CH_4$ $T_{max}$/K | Amount of carbon formed/atoms $g^{-1}_{cat}$ | Total amount of carbon formed/atoms $g^{-1}_{cat}$ | Monolayers of carbon formed* |
|---|---|---|---|---|---|
| 673 | $C^1$ | 640 | $2.3 \times 10^{19}$ | $5.3 \times 10^{19}$ | 2 |
| | $C^2$ | 770 | $3.0 \times 10^{19}$ | | |
| 773 | $C^3$ | 830 | $9.4 \times 10^{19}$ | $9.4 \times 10^{19}$ | 4 |
| 873 | $C^{4a}$ | 830 | $6.1 \times 10^{18}$ | $2.2 \times 10^{19}$ | 1 |
| | $C^{4b}$ | 950 | $1.6 \times 10^{19}$ | | |

Total surface area = 2.5 $m^2 g^{-1}$ Mass of catalyst = 0.5g

*Number of monolayers of carbon formed calculated on the basis of the total surface area of the catalyst, taking monolayer coverage to be $10^{15}$ atoms $cm^{-2}$

corresponded to 2.2 x $10^{19}$ atoms $g^{-1}_{cat}$ (Table 5.4). This amount is considerably smaller than the amount deduced from the corresponding TPO experiment (2.5 x $10^{21}$ atoms $g^{-1}_{cat}$ - Fig.5.6) and suggests once more that only some of the carbon has been hydrogenated. This apparent inactivity of the carbon towards hydrogenation can again be attributed to the negligible amount of $H_{(ads)}$ available on the surface, since most would have desorbed at the hydrogenation temperature employed. The $CH_4$ response obtained in Fig.5.21 is in good agreement with the results obtained by McCarty et al [6] who hydrogenated carbon formed on a $Ni/Al_2O_3$ by exposure to ethylene at 873 K. They also reported that two dominant types of carbon were present which produced two $CH_4$ peaks at 820 and 950 K on reaction with hydrogen. The lower temperature $CH_4$ peak repesented what they called the δ' carbon state and the higher temperature peak represented the δ carbon state, both of which were associated with filamentous carbon (identified by TEM). They suggested that the δ' carbon state was the soft, more reactive core of the filaments, whereas the δ state was the hard outer shell of the filaments and possibly also the encapsulating carbon which is often observed surrounding nickel particles during high temperature exposure to hydrocarbons.

## 5.6 Conclusions

1) Transmission electron microscopy revealed that TPRn of n-butane carried out on differently promoted $NiO/Al_2O_3$ catalysts up to 673 K produced an encapsulating carbon film which surrounded the Ni particles. For each of the samples, TPO of the carbonacious deposit revealed the presence of two species of carbon, suggesting that the encapsulating film may consist of two carbon layers which exhibit different reactivities towards oxidation. TPH of the carbonaceous deposit confirmed the presence of two carbon species. From the TPO experiments comparable amounts of carbon were calculated to be present on each of the catalysts; 3 monolayers on AK2, 2 monolayers on AK5 and 2 monolayers on AK8. This indicated that the presence of different promoters has little effect on the nature and amount of carbon formed at this temperature.

2) TEM showed that TPRn of n-butane up to 773 K produced short, 'true' carbon filaments which were partially amorphous. TPO and TPH of the deposited carbon confirmed the presence of one dominant type of carbonaceous species. The amounts of carbon calculated from the TPO experiments revealed that similar amounts were present on each catalyst; 14 monolayers on AK2, 12 monolayers on AK5 and 13 monolayers on AK8. This again showed that the promoters had no effect on the type or amount of carbon formed at this temperature.

3) TEM revealed that TPRn of n-butane up to 873K produced 'tubular' carbon filaments which consisted of a duplex structure of an outer carbon skin and an inner carbon channel. This indicated that 'true' carbon filaments formed at lower temperatures undergo a transition into 'tubular' filaments at higher temperatures. TPH of the deposited carbon produced two $CH_4$ peaks confirming the presence of two dominant carbon species. These were believed to correspond to the inner core and outer skin of the filaments and possibly encapsulating carbon which is formed at temperatures >~800 K. The amounts of carbon formed on each of the samples was comparable; 100 monolayers on AK2, 89 monolayers on AK5 and 79 monolayers on AK8. This again showed that the promoters had little influence on the nature and amount of carbon formed.

## References


[1] Bartholomew, C.H., *Catal. Rev.-Sci. Eng.*, **24**, 67,1982.

[2] Baker, R.T.K. and Harris, P.S., The Formation of Filamentous Carbon in 'Chemistry and Physics of Carbon'; Walker, P.Jr., Thrower, P.A., Eds.; Marcel Dekker: New York, Vol.14, 1978.

[3] Trimm, D.L., *Catal. Rev.*, **16**, 155, 1977.

[4] Rostrup-Nielsen, J.R. and Trimm, D.L., *J. Catal.*, **48**, 155, 1977.

[5] Munster, P. and Grabke, H.J., *J. Catal.*, **72**, 279, 1981.

[6] McCarty, J.G., Hou, P.Y., Sheridan, D. and Wise, H. in 'Coke Formation on Metal Surfaces'; (Albright, L.F. and Baker, R.T.K. Eds.), ACS Symposium Series 202, p.253. Am. Chem. Soc., Washington, D.C., 1982.

[7] Figueiredo, J.L. and Trimm, D.L., *J. Catal.*, **40**, 158, 1975.

[8] Baker, R.T.K., in 'Catalyst Deactivation 1991', Bartholomew, C.H. and Butt, J.B. (Eds.), Elsevier Science Publishers B.V., Amsterdam, 1991.

[9] Shouten, F.C., Gijzeman, O.L.J. and Bootsma, G.A., *Surf. Sci.*, **87**, 1, 1979.

[10] Rostrup-Nielsen, J.R., in 'Catalytic Steam Reforming', Springer-Verlag, 1984.

[11] Barbier, J., Duprez, D. and Fadili, K., *Ind. Eng. Chem. Res.*, **36**, 3180, 1997.

[12] Tracz, E., Scholtz, R. and Borowiecki, T., *Applied Catalysis*, **66**, 133, 1990.

[13] Baker, R.T.K., Barber, M.A., Harris, P.S., Feates, F.S. and Waite, R.J., *J. Catal.*, **26**, 51, 1972.

[14] Goula, M.A., Lemonidou, A.A. and Efstathiou, A.M., *J. Catal.*, **161**, 626, 1996.

[15] Bianchi, D. and Gass, J.L., *J. Catal.*, **123**, 298, 1990.

[16] Smeds, S., Salmi, T., Lindfors, L.P. and Krause, O., *Applied Catalysis A: General*, **144**, 177, 1996.

[17] Weatherbee, G.D. and Bartholomew, C.H., *J. Catal.*, **87**, 55, 1984.

# 6

# THE EFFECT OF POTASSIUM ADDITION TO A $NiO/Al_2O_3$ CATALYST AS A MEANS OF PROVIDING RESISTANCE TO CARBON FORMATION

## 6.1 Introduction

The beneficial effect of potassium incorporation into nickel steam reforming catalysts was discussed in detail in Chapter 1, as a means of increasing the catalyst's resistivity to carbon formation [1]. This positive effect of alkali doping was pioneered by ICI some 40 years ago who developed a range of industrial catalysts known as series 46-1 for the reforming of naphtha feedstocks. Indeed potassium promotion is still the most common method employed in the world today to prevent the formation of carbon in industrial steam reformers [2].

The ICI 46-1 series of catalysts use potash in their formulation which is hydrolysed to form KOH, the effective carbon-removing agent which is very mobile on the catalyst surface (see Section 1.11.5). The process is complex however and catalyst formulation has to be carried out with much care in order to achieve optimum performance and a lifespan of several years [2].

The aim of this chapter is to dope a $NiO/Al_2O_3$ catalyst, previously prepared, with potassium by the simple method of post-impregnation and to investigate what influence the alkali has on the catalyst's resistivity to carbon formation. TPRn will be used again to determine the kinetics of n-butane decomposition and TPO will be used to determine the nature and amount of any carbon formed by the TPRn reaction. The morphology of carbonaceous species deposited at various stages during the TPRn will be determined by TEM. As in Chapter 4, following the carbon TPO reaction, the catalyst will be re-

reduced and the butane TPRn will be carried out again in order to investigate whether regeneration has any subsequent effect on the kinetics of butane decomposition.

## 6.2 Catalyst preparation

Catalyst AK2 (15% NiO / $\alpha$-$Al_2O_3$ + 5% $Al_2O_3$) was promoted with 3wt% potassium by the method of post-impregnation. A detailed description of the preparation method can be found in Chapter 2, section 2.1.2.

## 6.3 Catalyst Pre-treatment and reduction.

Prior to reduction, the catalyst (0.5 g) was heated in a 100% helium stream (25 $cm^3$ $min^{-1}$, 1 bar, 10 K $min^{-1}$) from ambient to 873 K and maintained at that temperature for 2 hours to ensure the removal of contaminants and water. The temperature dependent product spectrum is shown in Fig.6.1. The profile is very similar to the one obtained for potassium free AK2 (Fig.3.4). The main material desorbing in this case was again $CO_2$, for which three peak maximum temperatures were observed at 475, 578 and 688 K. These can again be attributed to the presence of metal carbonates or hydroxycarbonates which may have been formed or may be due to contamination during storage. No desorption of water was observed.

Following the pre-treatment in helium, the sample was cooled to ambient and the flow switched to a hydrogen-helium stream (5% $H_2$, 25 $cm^3$ $min^{-1}$, 1 bar). The sample was then reduced by raising the temperature from ambient to 873 K at 3 K $min^{-1}$ under the hydrogen-helium stream and held at that temperature for 16 hours. The $H_2$ consumed and the $H_2O$ produced were monitored continuously during the reaction. The temperature-programmed reduction spectrum obtained is displayed in Fig.6.2.

A single dominant peak maximum was observed at 655 K (cf. 685 K for the potassium-free AK2 (Fig.3.5(b))) and the high temperature shoulder observed for potassium-free

AK2 had now disappeared. This result indicates that the presence of potassium has removed the high temperature reduction phase resulting from the interaction between NiO and $Al_2O_3$, replacing it with a phase which is easier to reduce.

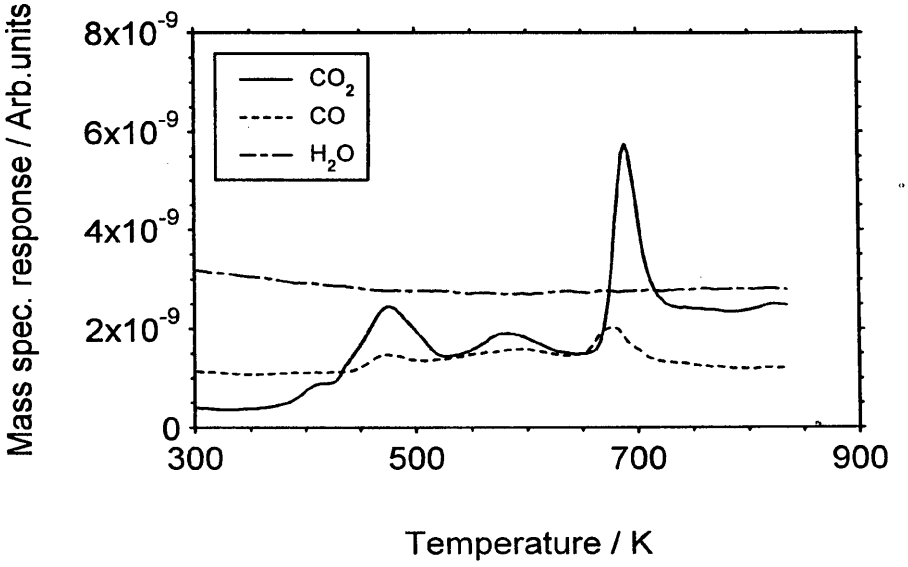


Fig.6.1 Heating potassium promoted AK2 in a 100% helium stream

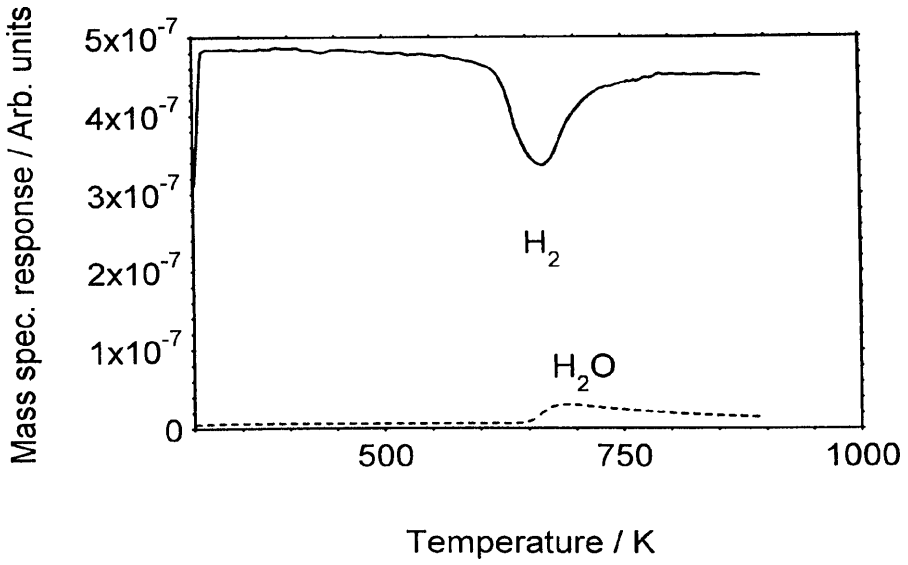


Fig.6.2 TPR profile of potassium promoted AK2

### 6.4 Temperature-programmed reaction (TPRn) of n-butane

The TPRn of n-butane was carried out to investigate whether the addition of potassium would act to modify the kinetics of the decomposition reaction and thereby reduce the amount of carbon accumulated on the potassium promoted catalyst. The n-butane TPRn reaction was carried out under identical conditions as for the potassium free sample, AK2 (Chapter 4, Section 4.2.1).

Following reduction of the catalyst, the flow was switched to a butane-helium stream (2% n-butane, 25 $cm^3$ $min^{-1}$, 1 bar) and the catalyst was heated under the flowing gas from ambient to 1023 K at a rate of 5 K $min^{-1}$. The rate of the catalytic decomposition of n-butane was monitored by continuously following the hydrogen produced on the mass spectrometer. The n-butane TPRn spectrum obtained is shown in Fig.6.3. Comparison of the TPRn profile obtained in this case with the one obtained for potassium free AK2 (Fig.4.1) shows dramatic differences between the two. The onset of $H_2$ production for the potassium promoted sample began at ~ 600 K, however no low temperature peak was observed as for sample AK2. A marked increase in $H_2$ evolution then occurred at ~ 675 K producing a large peak with a maximum at 793 K. In this case a mass transport limitation of the rate was not observed. Methane formation for the potassium promoted sample was observed only at high temperature, commencing at 900 K. The activation energy, $E_a$, for the production of hydrogen in the temperature range 680 - 730K was calculated. In this case a finite amount of $H_2$ was produced and therefore the conversion of butane was taken into consideration. Referring to Fig.6.3

$h_1 \alpha$ rate of $H_2$ production

$h_2' \alpha$ initial conc$^n$ $C_4H_{10}$

$h_2'' \alpha$ conc$^n$ $C_4H_{10}$ at exit

We can therefore say that

$$h_1 = k (h_2' + h_2''/2).S \qquad (6.1)$$

where

S is the the number of sites on the nickel surface. S $\alpha$ area under the curve at any time.

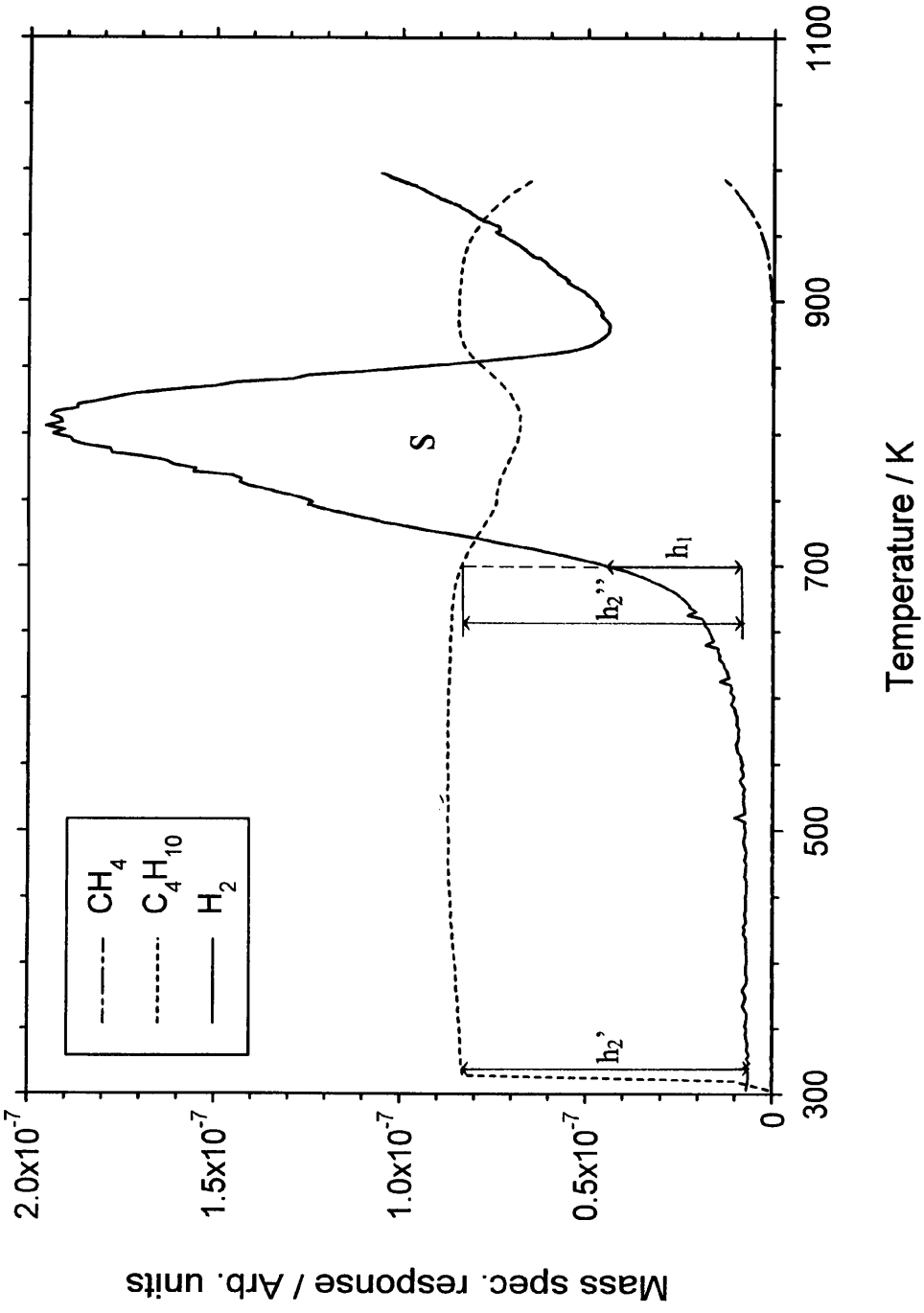


Fig.6.3 TPRn of n-butane over potassium promoted AK2

Hence $$h_1/(h_2' + h_2''/2).S = k \qquad (6.2)$$

$$h_1/(h_2' + h_2''/2).S = A\, e^{(-Ea/RT)} \qquad (6.3)$$

$$\ln(h_1/(h_2' + h_2''/2).S) = \ln A - E_a/RT \qquad (6.4)$$

By plotting $\ln(h_1/(h_2' + h_2''/2).S)$ versus reciprocal temperature, a straight line of slope $-E_a/R$ was produced, as shown in Fig.6.4. The value of $E_a$ obtained was 126 kJ $mol^{-1}$, which was in good agreement with values of diffusion of carbon through nickel from previous studies [3].

A very significant difference between the two TPRn profiles was that the rate of n-butane decomposition on the potassium promoted sample was significantly slower than on the unpromoted sample. At 700 K, the rates of carbon deposition on the alkali promoted and alkali free catalysts were calculated to be $7.9 \times 10^{16}$ carbon atoms $sec^{-1}$ and $1.5 \times 10^{17}$ carbon atoms $sec^{-1}$ respectively. The amount of carbon produced in each case was quantified by integrating the area under the $H_2$ curves. The total amount of carbon formed on potassium promoted AK2 was calculated to be $6.1 \times 10^{20}$ atoms $g^{-1}_{cat}$. In contrast, the total amount of carbon formed on potassium free AK2 was $3.4 \times 10^{21}$ atoms $g^{-1}_{cat}$. The presence of the potassium had therefore caused the amount of carbon deposited to decrease by approximately 82%.

Hadden et al [4] similarly reported a reduction in the accumulation of carbonaceous deposits from the decomposition of propane on a potassium promoted commercial $NiO/\alpha Al_2O_3$ catalyst, compared to that observed on the unpromoted material. They found that the alkali limited the rate of the hydrocarbon decomposition reaction and suggested that the potassium promoter may limit the rate of the decomposition reaction by reducing the number of active sites available for adsorption of the hydrocarbon on the nickel surface. In addition the alkali may interfere with the decomposition pathway of the adsorbed hydrocarbon species in such a way that the extent of dehydrogenation or carbon-carbon bond cleavage is reduced. Windham et al [5] observed this type of effect

when ethylene and potassium were coadsorbed onto a Pt(111) single crystal. They suggested that geometric (ensemble size) effects due to K blocking sites required for ethylene decomposition were largely responsible for the decrease in the amount of dehydrogenation occurring. Blackmond et al [6], studying the influence of Cs promotion on $Rh/Al_2O_3$ catalysts, also suggested that adsorbed alkali may serve to dilute the metal surface thereby suppressing certain types of adsorption which require ensembles of adjacent metal atoms.

As described in Chapter 4, Somorjai et al [7] studied the adsorption of ethylene and acetylene on Pt(111) and postulated that initiallly, an arrangement is formed where each carbon atom is bonded to a corresponding metal atom (See Fig.4.9). On heating, this arrangement transforms into an ethylidyne species where one of the carbon atoms is attached to an ensemble of three metal atoms (Fig.4.9). Marshall et al [8] also found that hydrocarbons adsorbed on $Ni/Al_2O_3$ gave rise to ethylidyne intermediate which then decomposed to form a surface methyl species and then surface carbon. The fact that the formation of an ethylidyne species requires a particular ensemble of 3 metal atoms suggests that the presence of a potassium atoms on the surface acts by blocking these ensembles thereby inhibiting the formation of ethylidyne.

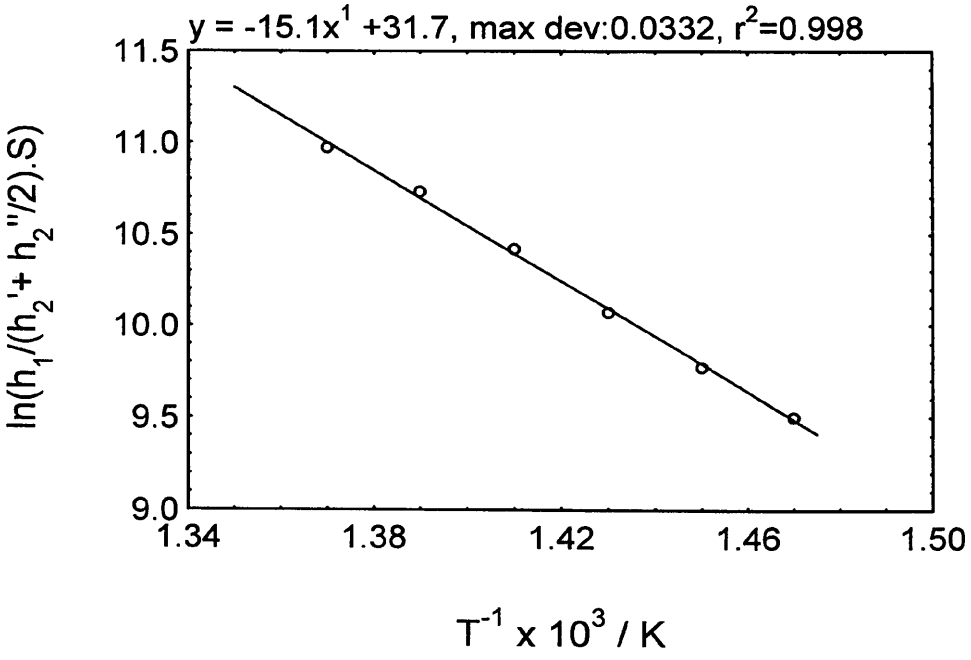


Fig.6.4 Plot of the $\ln(h_1/(h_2'+ h_2''/2).S)$ versus reciprocal temperature

## 6.5 The morphology of the carbonaceous deposits

The morphology of the carbonaceous deposits generated by the decomposition of n-butane up to 1023 K on potassium promoted AK2 was studied by TEM. The TPRn reaction was also aborted at both 723 K and 793 K and the carbon species formed at these temperatures was studied. Sample preparation was carried out using the same procedure as detailed in Section 4.2.2.

### 6.5.1 Carbon species formed at 723 K

The electron micrograph obtained is displayed in Fig.6.5. Ni crystallites were clearly visible with an average diameter of 100 nm, however there was no evidence of the presence of filamentous carbon at this temperature. The micrograph does suggest the presence of a thin film of material surrounding some of the crystallites. This may be a similar type of carbon film which was identified on catalyst AK2 at 673 K in Chapter 5, Section 5.2.2.

### 6.5.2 Carbon species formed at 793 K

The electron micrograph obtained is displayed in Fig.6.6. In this case the presence of carbon filaments was evident, which had an average width of ~ 25 nm. Unfortunately it was difficult to tell from the micrograph whether the filaments were 'true' filaments, as described by Tracz et al [9], or 'tubular' filaments with channels running through their centres.

### 6.5.3 Carbon species formed at 1023 K

The electron micrograph obtained is displayed in Fig 6.7. In this case the carbon filaments formed were clearly tubular in nature possessing central channels running down their lengths. The filaments had an average width of ~ 25 nm.

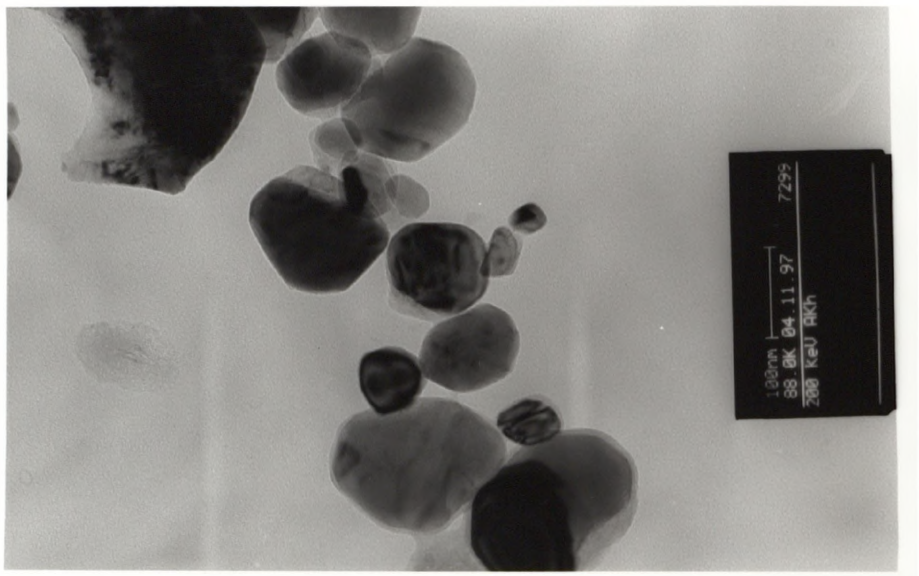


Fig.6.5 Electron micrograph of carbon formed on potassium promoted AK2 at 723 K

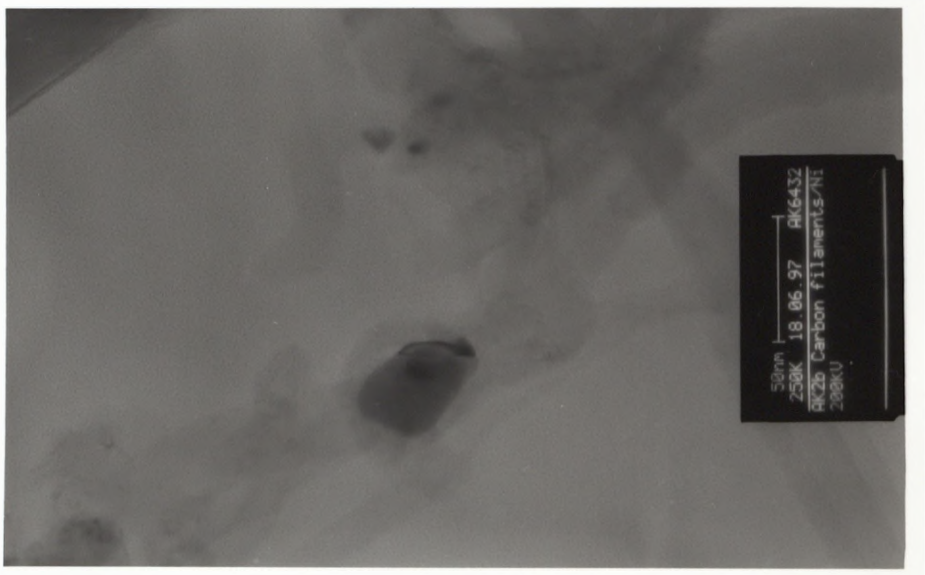


Fig 6.6 Electron micrograph of carbon formed on potassium promoted AK2 at 793 K

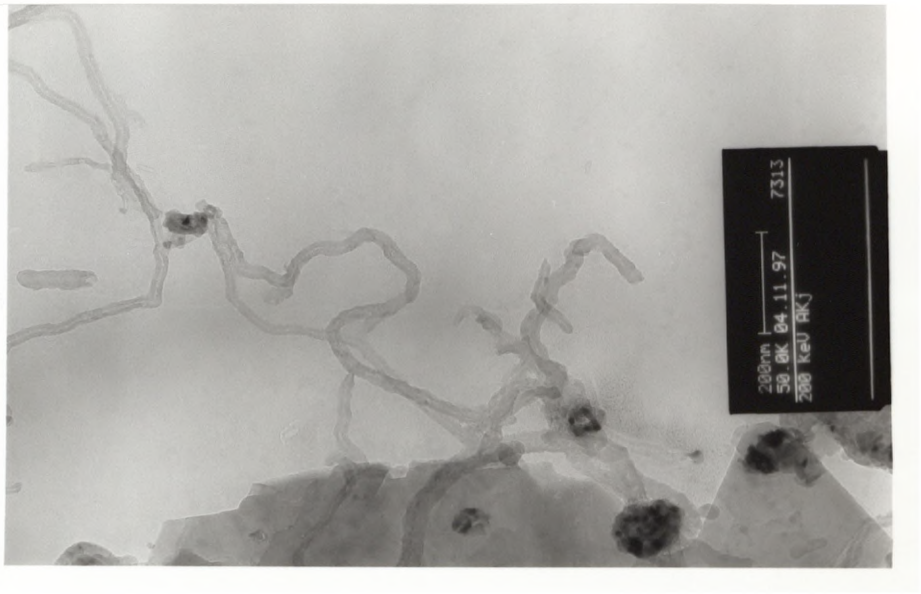


Fig.6.7 Electron micrograph of carbon formed on potassium promoted AK2 at 1023 K

## 6.6 Temperature-programmed oxidation (TPO) of carbon formed on potassium promoted AK2

The TPRn of n-butane was carried out as described in section 6.4. The flow was then switched from n-butane to helium and the catalyst cooled to ambient. Following this the flow was switched to an oxygen-helium stream (5% $O_2$, 25 $cm^3$ $min^{-1}$, 1 bar) and the temperature was raised from ambient to 1023 K at a rate of 5 K $min^{-1}$.

The TPO profile is shown in Fig.6.8. $CO_2$ was found to be the only gaseous product of this reaction. The onset of $CO_2$ evolution began at ~ 600 K afterwhich a marked increase in rate was observed which gave rise to a large peak with a maximum at 750 K and a distinct shoulder at ~ 820 K, which suggested that two types of carbonaceous species were present. A major difference in this TPO profile compared to that of the TPO of carbon formed on potassium free AK2 (Fig.4.4) was that no CO evolution was

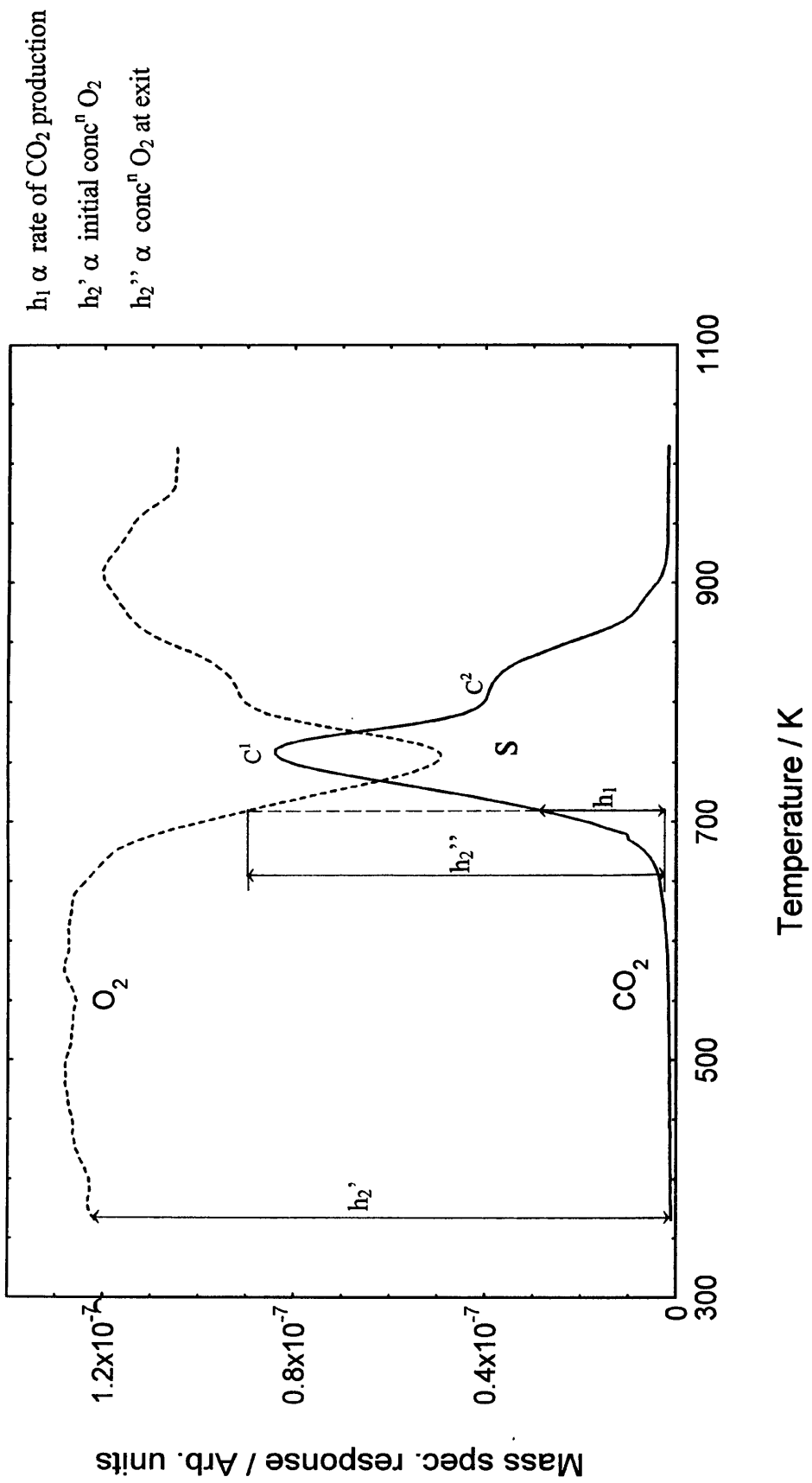


Fig.6.8 TPO of deposited carbon on potassium-promoted AK2

observed. The partial pressure of $CO_2$ at the peak maximum in Fig.6.8 corresponded to ≅0.03 atm which implied that a depletion of oxygen did not occur in this case. This was to be expected since the amount of carbon formed on the potassium promoted sample was markedly lower than on potassium free AK2 and therefore the concentration of oxygen in the feed was high enough to completely oxidise the deposited carbon to $CO_2$. The $CO_2$ spectrum was approximately deconvoluted and the amounts of both types of carbon was calculated. These species designated as $C^1$ and $C^2$ in accordance with their reactivity order, were present in amounts 4.0 x $10^{20}$ atoms $g^{-1}_{cat}$ and 2.5 x $10^{20}$ atoms $g^{-1}_{cat}$ respectively. The total amount of carbon oxidised was 6.5 x $10^{20}$ atoms $g^{-1}_{cat}$ (Table 6.1) which confirmed that all the carbon had been removed. The activation energy, $E_a$, for the gasification of carbon was calculated by plotting $\ln(h_1/(h_2'+ h_2''/2).S)$ versus reciprocal temperature as shown in Fig.6.9. This gave a straight line of slope $-E_a/R$. The value of $E_a$ obtained was 195 kJ $mol^{-1}$.

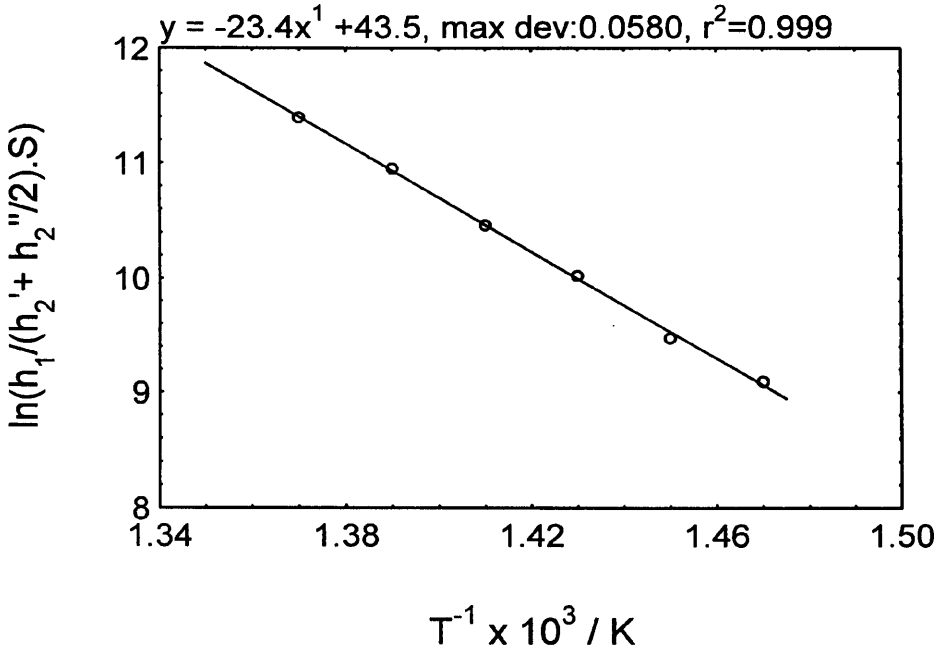


Fig.6.9 Plot of $\ln(h_1/(h_2'+ h_2''/2).S)$versus reciprocal temperature

The TPO profile in Fig.6.8 clearly showed that two types of carbonaceous species were present which exhibited different activities for reaction with $O_2$. These two carbon

species may correspond to the inner core and outer skin of the filaments, which can be seen clearly in the electron micrograph in Fig.6.7. According to Baker et al [10] the inner core is more reactive and therefore more easily oxidisable, whereas the outer core is harder to oxidise. Efstathiou et al [11], who carried out the oxidation of carbon formed on $Ni/CaO-Al_2O_3$ catalysts from $CH_4$ at 1023 K, also found that oxidation produced a $CO_2$ peak at 883 K with a distinct shoulder at 973 K, which indicated the presence of two types of carbon. They assigned the high temperature $CO_2$ peak to amorphous and or/graphitic forms of carbon whereas the carbon species oxidised at lower temperature was suggested to be filamentous in form. Duprez et al [12] found that filamentous carbon oxidised at lower temperatures on potassium promoted catalysts ($T_{max} \sim 730$ K) than on the same unpromoted catalysts ($T_{max} \sim 873$ K). Similar behaviour has also been reported by Demicheli et al [13] who suggested that some potassium may be inserted between the nickel particle and the filament, thus modifying the rate of carbon oxidation at the nickel/carbon interface. This may therefore explain the difference in temperature of the $CO_2$ peak maxima observed in our case and the work of Efstathiou et al [11].

### 6.7 Re-reduction of the catalyst

Following the removal of carbon by TPO, the flow was switched to a helium stream and the sample was cooled to ambient under the flowing gas. When cool, the flow was then switched to a hydrogen-helium stream (5% $H_2$, 25 $cm^3$ $min^{-1}$, 1 bar) and the catalyst was reduced by raising the temperature from ambient to 1023 K at 3 K $min^{-1}$. The catalyst was held at this temperature for 16 hours under the hydrogen-helium stream.

The reduction profile obtained is shown in Fig.6.10. The profile differed markedly from the initial reduction profile obtained for the catalyst (Fig.6.2). Two broader peaks were now visible at the higher temperatures of ~ 825 K and ~ 920 K. A similar result was observed in Chapter 4 when catalysts were re-reduced following carbon oxidation. In this case, as in Chapter 4, the change in the reduction spectrum was believed to be

due to the redispersion of the nickel component caused by the oxidation reaction resulting in a totally different surface morphology. The fact that two peaks were observed the second time around may be a function of the distribution of NiO crystallite sizes.

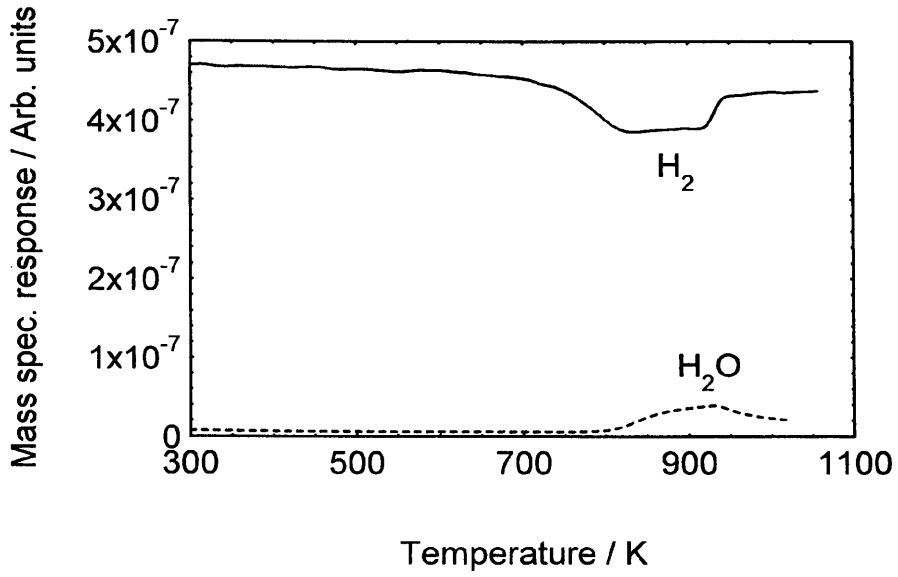


Fig.6.10 TPR profile of regenerated, potassium promoted AK2

## 6.8 TPRn of n-butane over the re-reduced catalyst

After the re-reduction of the catalyst, the flow was switched to helium and the sample was cooled to ambient. The flow was then switched to an n-butane-helium stream (2% n-butane, 25 $cm^3$ $min^{-1}$, 1 bar) and the catalyst was heated under the flowing gas from ambient to 1023 K at a rate of 5 K $min^{-1}$.

The second butane TPRn profile is shown in Fig.6.11 and differs dramatically from the initial butane TPRn shown in Fig.6.3. In this case a small, broad $H_2$ peak was produced between ~ 550 and 670 K, however the large $H_2$ peak observed in the initial TPRn was now absent. The amount of carbon associated with the small peak was calculated to be 3.0 x $10^{19}$ atoms $g^{-1}_{cat}$. Comparing the amount of carbon formed up to 900 K in the first

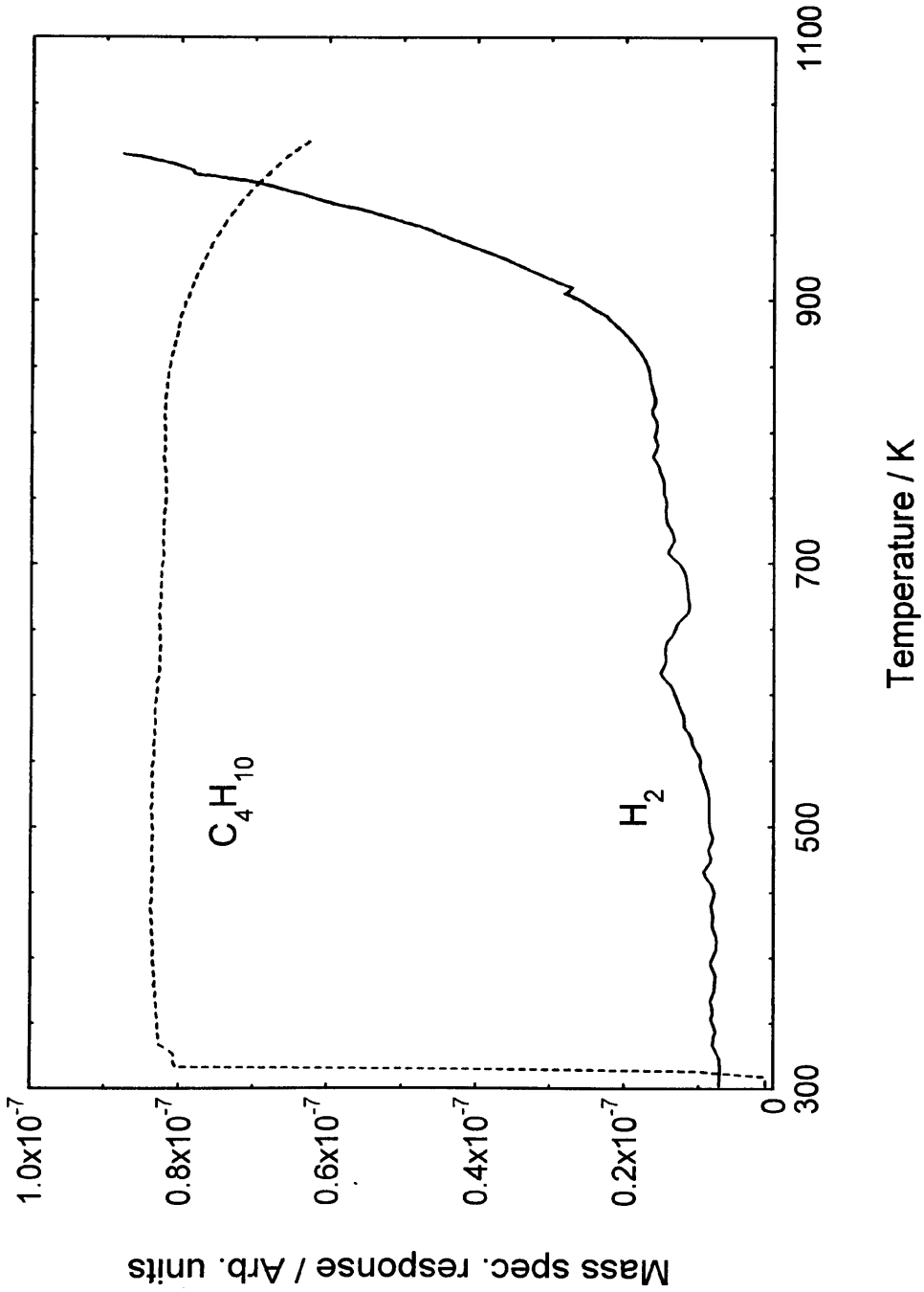


Fig.6.11 TPRn of n-butane on re-reduced potassium promoted AK2

Table 6.1

Comparison of the amounts of carbon formed and gasified on potassium promoted AK2 and potassium free AK2

| | FIRST BUTANE TPRn | | | | | SECOND BUTANE TPRn | |
|---|---|---|---|---|---|---|---|
| Sample | Amount of carbon formed up to 900K/ atoms $g^{-1}_{cat}$ | $E_{act}$ for diffusion of carbon through Ni/ kJ $mol^{-1}$ | Total amount of carbon formed/ atoms $g^{-1}_{cat}$ | $E_{act}$ for gasification of carbon/ kJ $mol^{-1}$ | Total amount of carbon oxidised/ atoms $g^{-1}_{cat}$ | Amount of carbon formed up to 900K/ atoms $g^{-1}_{cat}$ | Reduction in amount of carbon formed / % |
| **K promoted AK2** | $4.8 \times 10^{20}$ (20 monolayers)* | 126 | $6.1 \times 10^{20}$ (24 monolayers) | 195 | $6.5 \times 10^{20}$ (26 monolayers) | $3.0 \times 10^{19}$ (1 monolayer) | 94 |
| **AK2** | $2.7 \times 10^{21}$ (108 monolayers)* | 137 | $3.4 \times 10^{21}$ (136 monolayers) | 121 | $3.6 \times 10^{21}$ (144 monolayers) | $1.1 \times 10^{20}$ (4 monolayers) | 96 |

Total surface areas = 2.5 $m^2 g^{-1}$ Mass of each catalyst used = 0.5g

*Number of monolayers of carbon calculated on the basis of the total surface area of the catalyst, taking monolayer coverage to be $10^{15}$ atoms $cm^{-2}$

and second TPRn profiles, we can see that approximately 94% less carbon was produced during the second TPRn on the regenerated catalyst (Table 6.1). It is apparent that the same phenomena had occurred here as in Chapter 4, namely a redispersion of nickel caused by the oxidation, which results in a distinctly different nickel surface morphology. In Chapter 4 it was discussed how the adsorption and decomposition of hydrocarbons on nickel appear to be structure sensitive, Ni(100) and (110) being most active for hydrocarbon decomposition [14]. It would appear therefore that a completely different distribution of nickel crystallographic faces on the surface may be responsible for inhibiting the adsorption and subsequent decomposition of the hydrocarbon which results in a decrease in the amount of carbon was formed. This may be coupled with the blocking of nickel ensembles by potassium and $Al_2O_3$ promoter which further inhibits the adsorption of the hydrocarbon and the formation of ethylidyne.

## 6.9 Conclusions

1) The addition of potassium to a $NiO/Al_2O_3$ catalyst prepared previously was found to have a dramatic effect on suppressing the formation of carbon. This was attributed to the potassium limiting the rate of hydrocarbon decomposition by blocking specific nickel ensembles required for the adsorption of n-butane and formation of ethylidyne intermediate.

2) Oxidation of carbon deposited by butane TPRn up to 1023 K on the potassium promoted catalyst revealed the existence of 2 species of carbon. This suggested that the two types of carbon may correspond to the inner core and outer skin which make up the filaments and possibly also encapsulating carbon which is known to form at temperatures >~800K.

3) Following regeneration of the carbided catalyst by oxidation, repetition of the butane TPRn revealed that the amount of carbon formed had again decreased. The difference in the kinetics of butane decomposition observed was attributed to a redispersion of

nickel on the surface caused by the oxidation reaction and the blocking of nickel ensembles by redispersed potassium and $Al_2O_3$ promoter.

## References


[1] Mross, W.D., *Catal. Rev. Sci. Eng.*, **25**, 591, 1983.

[2] Twigg, M.V., in 'Catalyst Handbook' (2nd Edition), Wolfe Publishing, London, 1989.

[3] Trimm, D.L., *Catal. Rev. Sci. Eng.*, **16**, 155, 1977.

[4] Hadden, R.A., Howe, J.C. and Waugh, K.C. in 'Catalyst Deactivation', Bartholomew, C.H. and Butt, J.B. (Eds.), Elsevier Science Publishers B.V., Amsterdam, 1991.

[5] Windham, R.G. and Koel, B.E., *J. Phys. Chem.*, **94**, 1489, 1990.

[6] Blackmond, D.G., Williams, J.A., Kesraoui, S. and Blazewick, D.S., *J. Catal.*, **101**, 496, 1986.

[7] Koestner, R.J., Frost, J.C., Stair, P.C., Van Hove, M.A. and Somorjai, G.A., *Surf. Sci.*, **116**, 85, 1982.

[8] Marshall, P.R., McDougall, G.S. and Hadden, R.A., *Topics in Catalysis* **1**, 9, 1994.

[9] Tracz, E., Scholtz, R. and Borowiecki, T., *Applied Catalysis*, **66**, 133, 1990.

[10] Baker, R.T.K., Barber, M.A., Harris, P.S., Feates, F.S. and Waite, R.J., *J. Catal.*, **26**, 51, 1972.

[11] Goula, M.A., Lemonidou, A.A. and Efstathiou, A.M., *J. Catal.*, **161**, 626, 1996.

[12] Duprez, D., Fadili, K. and Barbier, J., *Ind. Eng. Chem. Res.*, **36**, 3180, 1997.

[13] Demicheli, M.C., Duprez, D., Barbier, J., Ferretti, O.A. and Ponzi, E.N., *J. Catal.*, **145**, 437, 1994.

[14] Yang, R.T. and Chen, J.P., *J. Catal.*, **115**, 52, 1989.

# 7

# CONCLUSIONS

Nine NiO/α-$Al_2O_3$ catalysts containing 15wt% NiO and promoted with either $Al_2O_3$, MgO or $La_2O_3$ were prepared by the technique of wet impregnation (Section 2.1, Chapter 2). Characterisation by X-ray diffraction (XRD) and Temperature-Programmed Reduction (TPR) revealed that the promoters had a profound effect on the nature of the NiO precursor, most likely caused by a promoter-NiO interaction during preparation which resulted in a Ni phase which was more difficult to reduce. The most dramatic results were observed for the MgO promoted samples and was due to the formation of NiO-MgO solid solutions. On higher loadings of MgO the catalyst reduction became increasingly more difficult.

Temperature-Programmed Reaction (TPRn) of 2% n-butane carried out on each catalyst up to 1023K revealed that the kinetics of butane decomposition were remarkably similar for each of the promoted samples. This indicated that although the promoters had a profound effect on the nature of the NiO catalyst precursors, they had little effect on the dehydrogenational activity of the Ni once formed after reduction. The total amount of carbon formed on each of the promoted catalysts was also found to be very similar, in the order of $3 \times 10^{21}$ monolayers, which showed that the promoters initially had no effect on suppressing the formation of carbon. This indicated that the promoters may become associated with the oxide support following reduction and become involved with the Ni again only after oxidation of the carbon formed, which results in a redistribution of the Ni and promoters on the support.

Transmission Electron Microscopy (TEM) revealed that the carbon formed on each catalyst by butane TPRn was filamentous in nature. The activation energy for the production of hydrogen in the temperature range 680 – 730K was also determined for each catalyst. The values obtained were in good agreement with those in the literature for the diffusion of carbon through Ni (125 – 155kJ $mol^{-1}$), which is considered to be the rate determining step for the formation of carbon filaments. The nature of carbonaceous species formed by butane TPRn at different and fixed temperatures was characterised by their reactivity with $O_2$ and $H_2$ and by TEM. These revealed that at

673 K Ni particles are encapsulated by a film consisting of two types of carbon. Once the surface is completely poisoned, diffusion of the carbon through nickel occurs and, at 773 K, short partially amorphous filaments consisting of one type of carbon are the dominant carbon species. These filaments then undergo a transition into tubular carbon filaments at 873 K which consist of a duplex structure of an outer carbon skin and inner carbon channel.

Temperature-Programmed Oxidation (TPO) resulted in complete gasification of the carbon deposited on each of the catalysts. The activation energy calculated for the oxidation of carbon was nearly the same as that obtained earlier for the diffusion of carbon through nickel. This therefore suggests that the gasification of carbon may be the reverse process of filament formation, whereby the nickel particle retraces its original path back up the filament.

Repetition of butane TPRn on regenerated catalysts yielded significantly different results from those obtained originally on the freshly reduced samples. This time the kinetics of butane decomposition were dramatically altered and the amount of carbon formed on the regenerated samples was also considerably less. This was thought to be due to a redistribution of Ni crystallographic faces on the surface to predominantly Ni(111), which inhibited the adsorption and subsequent decomposition of butane. A redispersion of the promoters following oxidation was also found to play a major role in suppressing the formation of carbon. The decomposition of butane is believed to occur via an unstable butylidyne intermediate which 'topples' on the Ni surface, requiring specific Ni ensembles to decompose it to lower hydrocarbon fragments, (the ethylidyne intermediate) through to a surface methyl and finally surface carbon. The greatest inhibition of carbon formation was observed for the $Al_2O_3$ promoted samples, indicating that following regeneration the dispersion of $Al_2O_3$ was greater than that of both MgO and $La_2O_3$. This resulted in a greater proportion of Ni ensembles being blocked which inhibited the formation of ethylidyne on the surface. The addition of 3wt% potassium to the 5wt% $Al_2O_3$ promoted catalyst was found to reduce carbon accumulation by decreasing the rate of hydrocarbon decomposition. This was again attributed to potassium blocking specific Ni ensembles required for the adsorption of butane and the subsequent formation of ethylidyne from the butylidyne.

# Appendix 1

Calculation of the extent of reduction of the catalyst

$NiO + H_2 = Ni + H_2O$

Mass of catalyst used = 0.5g; NiO loading = 15wt%

$\therefore$ Number of moles NiO = $1 \times 10^{-3}$ moles

$n = (PV/RT)$ where n = number of moles of $H_2$ consumed

P = partial pressure of $H_2$ / atm

V = volume / $cm^3$

R = gas constant / $cm^3$ atm $K^{-1}$ $mol^{-1}$

T = temperature / K

eg. For catalyst AK1

Integral area under $H_2$ curve / $H_2$ calibration height = t / min

Flow rate of $H_2$ = 25 $cm^3$ $min^{-1}$ $\therefore V = 25 \times t$

$$n = \frac{0.05 \times ((4.125 \times 10^{-6} / 2.550 \times 10^{-7}) \times 25)}{82.06 \times 295}$$

$n = 8.4 \times 10^{-4}$ moles

Extent of reduction = $(8.4 \times 10^{-4} / 1 \times 10^{-3}) \times 100 = 84\%$